POLITECNICO DI MILANO

SCHOOL OF CIVIL, ENVIRONMENTAL AND URBAN ENGINEERING

DEPARTMENT OF CIVIL & ENVIRONMENTAL ENGINEERING

MASTER THESIS

STRUCTURAL ASSESSMENT OF AN INDUSTRIAL RC STRUCTURE DAMAGED DURING 2010 CHILE EARTHQUAKE

Ricardo A. SOTILLO BASTIAN

Advisor:
Prof. Maria G. MULAS

Co-Advisors:
Prof. Paolo MARTINELLI

Milano – December 15th, 2020

ABSTRACT IN ENGLISH

The Maule earthquake is the largest seismic event that has ever struck Chile and the amount of damage found across the country was unmeasurable. The scope of this research is the analysis of a precast reinforced concrete building, located at 314 km from the earthquake's epicenter, that was damaged during the Maule earthquake. In a previous research, this structure was modeled and assessed throughout the Chilean code prescriptions. In contrast, this research aims to assess the vulnerability of this structure introducing a horizontal combination of the seismic components which was exempted by the outdated version of the Chilean code at that moment, as well, the division of the structural model into two due to the presence of an expansion joint; these features were excluded in the previous work. In order to capture the vulnerability of the structure, two numerical models representing the two parts of the structure are built. Furthermore, linear and nonlinear procedures are employed to assess the structural elements and compare the results with the damages found. The results of the linear analysis showed the failure of some columns after applying the horizontal combination. These columns match with those found damaged by the Maule earthquake, underlying that the exclusion of a horizontal combination of the seismic components underestimates the excitation of the structure. Whereas, for the nonlinear procedures, the type of analysis selected is the nonlinear dynamic direct-integration analysis followed by a verification throughout pushover analysis using fiber hinges as a plasticity model to capture the post-elastic behavior. Suitable accelerograms of the Maule earthquake are used as loading. Damages found by non-linear analyses agree with those obtained from linear analysis.

Keywords: Maule earthquake, Precast concrete structure, Linear analysis, Nonlinear analysis, Nonlinear Dynamic Direct-integration, Nonlinear static analysis, Post-elastic response.

ABSTRACT IN ITALIAN

Il terremoto Maule è il più grande evento sismico avvenuto in Cile e l'ammontare dei danni percepiti in tutto il territorio sono inestimabili. La presente ricerca ha l'obiettivo di analizzare una struttura in cemento armato prefabbricato situata a 314 km dall'epicentro del sisma e danneggiata dallo stesso. Quest'ultima è già stata modellata e valutata in una precedente ricerca facente riferimento alla normativa cilena. la presente ricerca è volta a stimare la vulnerabilità della struttura introducendo una combinazione orizzontale di componenti sismiche, non considerata nella versione datata della normativa cilena, così come la presenza di giunti di espansione che porta a considerare il modello strutturale come diviso in due parti. Perciò, sono stati costruiti due modelli numerici rappresentanti due parti della struttura con il fine di cogliere la vulnerabilità della struttura stessa. Sono state sviluppate una procedura lineare e una procedura non lineare con l'obiettivo di valutare gli elementi strutturali e paragonare i risultati ottenuti con i danni percepiti. I risultati ottenuti dall'analisi lineare mostrano il danneggiamento di alcune colonne dopo la sollecitazione di combinazioni orizzontali, che corrispondono alle colonne danneggiate dal terremoto Maule. In particolare, l'esclusione della combinazione orizzontale delle componenti sismiche sottostima l'eccitazione della struttura. L'analisi non lineare utilizza l'integrazione dinamica diretta seguita da una verifica usando l'analisi pushover, utilizzando le cerniere in fibra come modello plastico per percepire il comportamento post elastico. Nell'analisi dinamica non lineare sono stati utilizzati accelerogrammi registrati durante il terremoto Maule opportunamente ruotati. I danni riscontrati dalle analisi non lineari concordano con quelli ottenuti dall'analisi lineare.

Parole chiave: Terremoto Maule, struttura in calcestruzzo prefabbricato, Analisi lineare, Analisi non lineare, Integrazione dinamica diretta non lineare, Analisi statica non lineare ,Risposta post elastica.

Acknowledgments

En honor a Maria Felicia Hernandez de Sotillo, descansa en paz.

Contents

List of Figures

List of Tables

1   Introduction.

On February 27, 2010, Chile was struck by an earthquake of M_w 8.8. The main shock of the earthquake was recorded by at least 15 strong motion instruments in the area, in which the accelerometers' maximum 1g range was exceeded. The total duration of the motion was 160 s, in which the shaking higher than 0.05g lasted only 60 s. Additionally, processing the earthquake's accelerograms, the elastic response spectra of several records were higher than elastic demands from the Chilean seismic design code NCh433.

The earthquake shaking caused extensive damage to many non-engineered and engineered buildings throughout the affected area. One of them is the example of an industrial one-story structure built in precast concrete which was studied in [1]. Its performance was assessed by looking at the prescriptions of the Chilean design code NCh2369-2003 and adopting it to the Maule earthquake's records. This structure is located around 341 km from the epicenter of the earthquake and some damages were observed.

The damages found include the failure of the connection of some perimetral cladding panels, damages ranging from heavily to none at the beam-column wet-joint connection, and cyclic damage at the bases of the columns.

The purpose of the aforementioned example [1] was to capture the response of the structure using two types of analysis (Linear and Nonlinear). In the code prescriptions for linear analysis procedures, one of the key points is the horizontal combination of earthquake components that is not mandatory from the code perspective, and it was excluded in the previous work. The reason is that the code only prescribes the combination in the particular situations of noticeably torsional irregularities and building having frame systems in two non-parallel directions.

Therefore, in this work, the structure is studied to assess its vulnerability considering the combination of horizontal components of the Maule earthquake. This is done to highlight the actual seismic load that the structure withstood and how the code might be underestimating the possible consequences with the hypothesis of no combination of horizontal components.

Furthermore, the numerical model employed in the previous work [1] lacks of a proper structural representation of the case of study, since the presence of an expansion joint was excluded, leading to a numerical model that was not able to capture the real response structure. Therefore, in this work, the response of the structure is more accurately represented by two separated models.

For this research, linear procedures are employed at first stage, using as references the code ACI 318-14, since the Chilean code is American based thinking school, as well, Chileans used the ACI standards as a reference for design. Afterward, nonlinear dynamic integration is applied to accurately capture the damage of the structure followed by nonlinear pushover analyses to verify the results found.

The main challenge to face is the modeling of the cladding panels and of their mechanism of failure, which will be described in the following. Furthermore, the description of the structure (dimension, material, loads, and spatial distribution) and the damages observed are restricted to the information given in the previous work and the technical drawings of the structure. Hence, this might be a drawback when building the numerical model since it will try to capture the actual response of the existing structure and it may be far from the real response.

1.1   Literature review.

A description of such an event as it is the Maule earthquake is of utmost relevance when trying to comprehend its magnitude. The investigation lead in [2] gives a comprehensive view of the seismic event that took place on February 27 of 2010 in Chile. The research described the effects of the Chilean earthquake from the tectonic setting and geologic aspects to the damages found in buildings. The authors stated that the mainshock exceeded the accelerometer's maximum 1g range and the elastic response spectra of several records are higher than the elastic design demands from the Chilean code. Furthermore, the authors remark that some records show an important contribution of the total signal energy from periods higher than 1 s. This behavior could be related to local soil conditions, nevertheless, soil conditions on several stations are known only for the first 10 m, so further studies are required.

The construction of a numerical model for the case of the study is of utmost importance to capture the response closest to the real one during the Maule earthquake. Hence, a closer look is taken to the work done in [1], where the authors built a structural model under the prescriptions of the NCh2369-2003 standard using the structural analysis software SAP2000. This previous work aims to reproduce the behavior of the structure under the aforementioned standard and to study the causes of the damage by employing both linear and nonlinear procedures. The authors concluded that precast elements were properly designed but the wet joint connection between them lacks a proper reinforcement layout to be considered suitable to withstand the Maule earthquake's excitation.

Furthermore, the Maule earthquake has attracted considerable academic attention when it comes to the response of the buildings designed to withstand seismic forces. One of the most recent is the work of [3], where the authors analyzed buildings that withstood the earthquake with no observable damage even though they were affected by ground accelerations significantly larger than those prescribed by the Chilean code. The authors discussed the suitability of linear concrete material models to assess the response of the apparently undamaged RC shear wall structures subjected to strong seismic demands since the nominal procedures were not consistent with the observed lack of damage. Further, by employing nonlinear response history analysis, the inconsistencies of results were overcome when foundation uplift was accounted for, underlying the importance of account the foundation modeling.

Subsequently, [4] investigated the correlation between a suite of global structural parameters and corresponding earthquake responses of 43 RC buildings. The authors employed a series of ordinal logistic regression models that showed the most significant variables that correlate with the building damage level are the region where the building was located and the soil foundation type. They observed that the damage concentrated in the first two stories and first basement, and in the vicinity of vertical irregularities in the resisting planes.

The selection of a suitable plasticity model to capture the post-elastic response using nonlinear dynamic analysis is needed, where a fair comparison between a lumped plasticity model and spread plasticity models is performed in [5]. The authors evaluated the performance of three numerical models with varying computational demand levels, including two nonlinear models with different complexities and one linear model with a concentrated plasticity approach. A total of 126 dynamic analyses were performed to derive fragility curves and the responses were assessed using the experimental results. The authors concluded that the spread plasticity model calculated significantly more accurate structural responses than the more-commonly used lumped plastic hinge model.

1.2   General objective.

- Assess the vulnerability of an industrial reinforced concrete structure damaged during the Maule earthquake, under the prescriptions of the Chilean standards and complementary ones.

1.2.1   Specific objectives.

- Build two numerical models capable to capture the structural response of the building.
- Apply linear analysis procedures to assess the structural components.
- Apply nonlinear procedures to capture the damages that the building withstood during the Maule earthquake.

1.3   Outline.

In the following, it is shown the research outline:

1. Introduction: The research purpose is described, along with the objectives and the literature background.

2. Maule earthquake description: A brief description of the Maule earthquake event and its accelerograms components are shown.

3. Structure description: Complete description of the structure's characteristics, such as: location, geometry, materials, and NCh2369-2003 prescriptions.

4. Seismic damages: Summary of the damages found on the structure due to the Maule earthquake event.

5. Modeling of structure: It is shown the procedures and hypotheses employed to build the two numerical models of the structure under study.

6. Linear procedure: Complete description of the linear procedures prescribed by the Chilean standards plus complementary ones.

7. Structural components verification: Complete description on the verification process of the structural elements.

8. Beam plasticity model: Complete description of the plasticity model employed.

9. Nonlinear analyses: Description of the dynamic direct-integration analyses along with the verification through Pushover analyses.

10. Conclusion: Discussion on the results and objectives achieved is given.

2   Maule Earthquake description.

On Saturday, February 27, 2010, at 03:34 a.m. local time (06:34:14 UTC), an M_w 8.8 earthquake struck the central-south region of Chile. The location of the main shock and aftershocks relative to major cities [2] is shown in Figure 2-1.

Note: The superimposed rectangle has dimensions 600 km by 200 km.
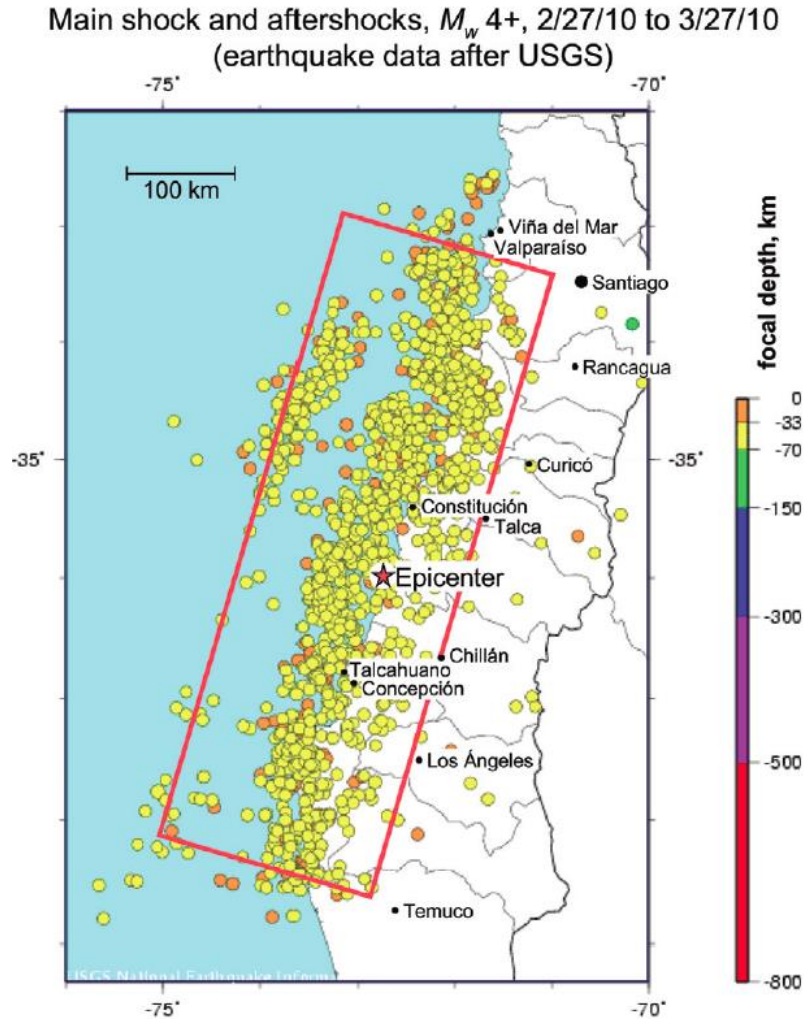
Figure 2-1: Main shock and aftershocks of M_w 4+, and larger between 2/27/2010 and 3/26/2010 (USGS) [2].

According to the United States Geological Survey (USGS), the earthquake epicenter was in a zone where the Nazca plate is being subducted downward and eastward beneath the South American plate. The earthquake occurred as a thrust faulting on the interface between the two plates, with an epicenter at 35.909 °S 72.733°W, and a focal depth of 35 km. The estimated dimensions of the rupture zone were 500km long by 100km wide. The earthquake struck in an area that had been identified as a seismic gap, with projected worst-case potential to produce an earthquake Mw-8.0-8.5 as reported by [2].

The main shock of the earthquake was recorded by at least 15 strong motion instruments in the area bounded by the cities of Santiago, Viña del Mar, Angol, and Concepcion. At the station nearest to the epicenter, in Cauquenes city, the accelerometer maximum 1.00 g range was exceeded. The recorded maximum accelerations from the Maule earthquake are shown in Table # 2-1.

Table # 2-1: Processed Records Maximum Accelerations [2].

Station	Maximum horizontal acceleration [g]	Maximum vertical acceleration [g]
Santiago Universidad de Chile	0.17	0.14
Santiago Elevated Train Station Mirador	0.24	0.13
Santiago CRS MAIPU	0.56	0.24
Santiago Hosp. Tisne	0.3	0.28
Santiago Hosp. Sotero de Rio	0.27	0.13
Santiago Cerro Calan	0.23	0.11
Santiago Campus Antumapu	0.27	0.17
El Roble hill	0.19	0.11
Viña del mar (Marga Marga)	0.35	0.26
Viña del mar (downtown)	0.33	0.19
Curico Hospital	0.47	0.20
Concepcion colegio san Pedro	0.65	0.58
Valdivia hospital	0.14	0.05

The Elastic response spectra of several records are higher than elastic design demands from the Chilean seismic design code NCh433 [6]. However, displacement spectra demands are in general lower than those required in the national base isolation building code NCh2745.

From the work of [1], after a comparison of the stations located in the Santiago chile city. the most suitable station to obtain the accelerogram data of the Maule earthquake is the Maipu station. This station has a moderate dense soil, that is classified by the Chilean standard a soil type III and coincides with the structure under study. The selection of this station was based on the soil type, since the structure to assess is located around 341 km from the epicenter of the earthquake as shown in Figure 2-2.
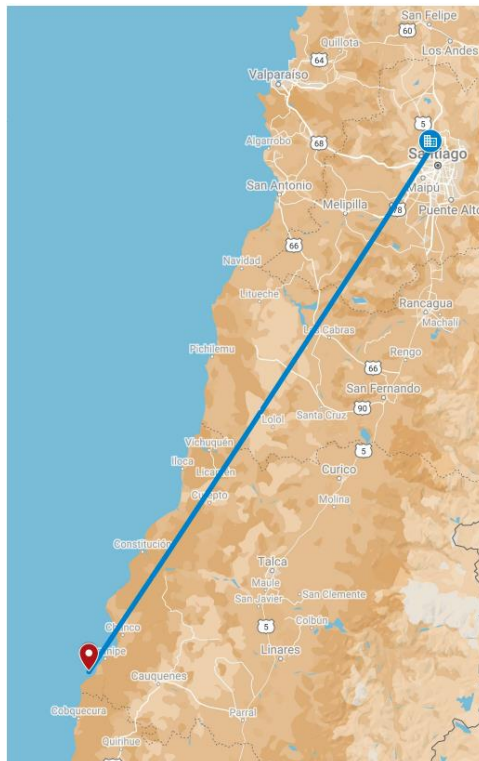
Figure 2-2: Relative distance of the Epicenter to the structure under study.

From the Maipu station and based on the work from [7], it is possible to obtain the three components necessary to assess the structure. The components recorded by the Maule earthquake are shown throughout Figure 2-3 to Figure 2-5.
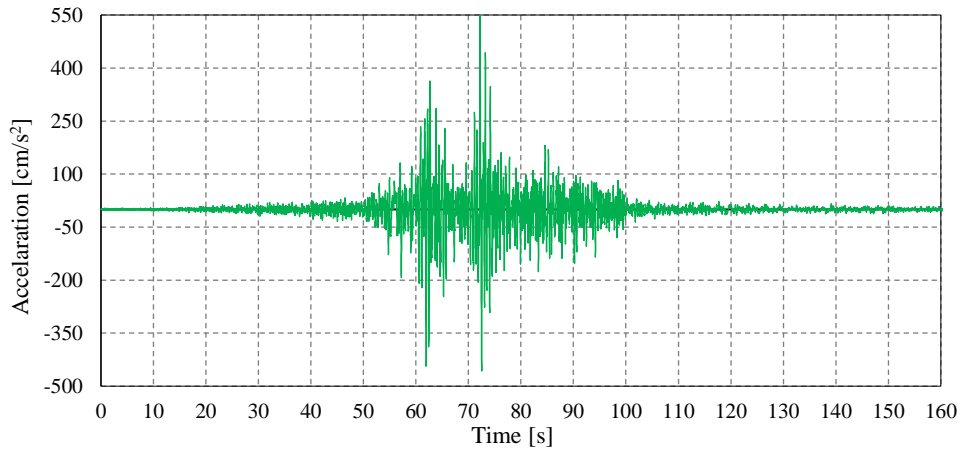
Figure 2-3: Maule Earthquake N-S component from Maipu Station.
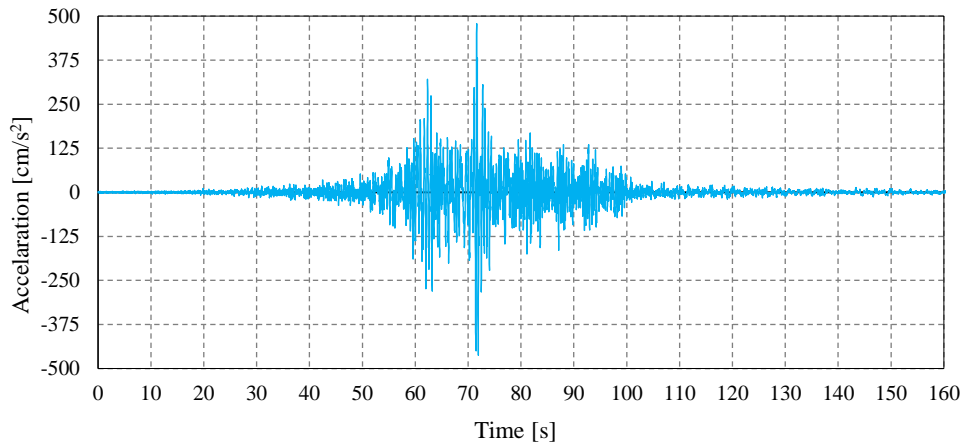
Figure 2-4: Maule Earthquake E-W component from Maipu Station.
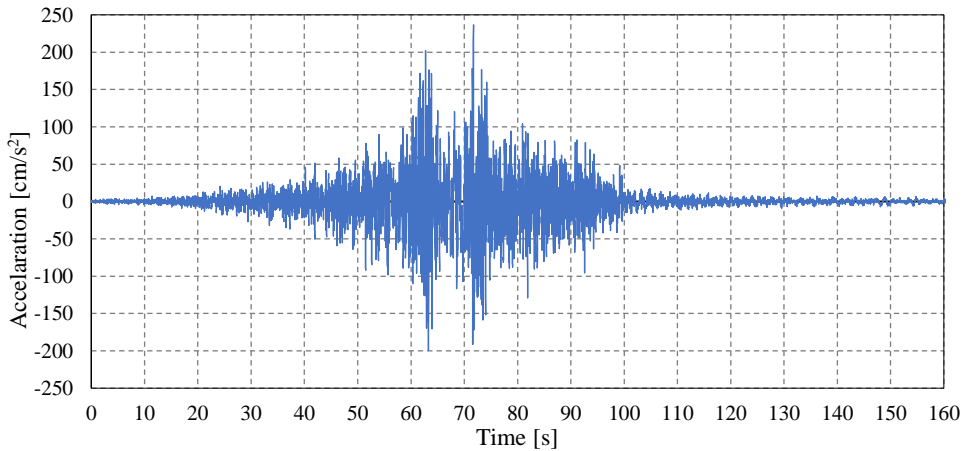
Figure 2-5: Maule Earthquake Vertical component from Maipu Station.

6

3 Description of the structure under evaluation.

The structure corresponds to a distribution center of a retail store that distributes products around Santiago de Chile City. It was built in 1996 and is located in Quilicura, a municipality at the northwestern edge of Santiago de Chile city as shown in Figure 3-1. Figure 3-2 presents a satellite view of the building under study.

The exact localization of the building in coordinates is N 33°19'41.1" S and E 70°42'49.0" W, and around 485 meters over the sea level.
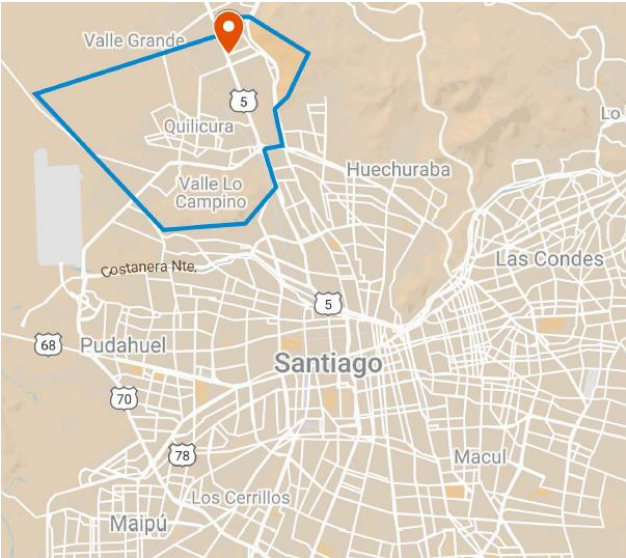
Figure 3-1: Johnson center location at Quilicura commune.

Figure 3-2: Satellite view of Johnson center.

3.1   NCh2369-2003 prescriptions.

To assess the structure the description of this under the scope of the Chilean code is needed. The standard to be used as a reference is the NCh2369-2003 "*Diseño sismico de estructuras e instalaciones industriales*" [8],

Special mention is made to the work of [1] since this previous study presents an additional description of the building under study, that is complementary to the one coming from the standard.

This structure classifies as Category C2 which means "*Normal Buildings, which may have minor damages that can be quickly repaired, which do not cause prolonged stoppages or significant production losses and which cannot endanger other buildings in category C1*". Related to this classification an importance factor *I* is assigned and equal to 1.00.

Based on the work of [1], the foundation soil in which the structure lays corresponds to the soil type III according to the code, which establishes certain parameters for the seismic hazard description given by [8] that's related to the structure under study.

The structural system changes its classification depending on the lateral-force resisting system. For the building under study two lateral force resisting system can be described below:

- In one direction the structure classifies as "*Precast structures with wet joints connections, with non-structural components included in the model*",

- In the orthogonal direction, it classifies as "*Precast structures with inverted pendulum*".

These classifications are directly related to the overall expected ductility for each lateral force resisting system and its inherent damping.

3.1.1   Special provision for concrete structures.

Relevant special provision for concrete precast structures are provided by NCh2369-2003 in *section 9* and they are listed below:

- The minimum base shear must be greater or equal to the one specified in [8] on its *section 5.4.5*.

- To consider a rigid diaphragm by precast slabs, it must have an upper slab that complies with the disposition ACI 318-99 (21.7.2/21.7.3/21.7.4/21.7.5), which in the case of study it doesn't possess such a slab.

- The confinement length of the columns should be greater or equal to twice the largest cross-sectional dimension.

- The slenderness of the column shall not surpass the following limit:

$$\lambda = \frac{kl}{r} \leq 100 \tag{3-1}$$

Where λ = is the slenderness ratio, k = is the effective length factor, l = is the clear length of the column, r = is the radius of gyration.

3.2   Materials.

The materials used in design are listed in Table # 3-1 The material properties are prescribed by Chilean standards NCh430-2007 *"Hormigon armado- Requisitos de diseño y calculo"* [9] and NCh204-2006 *"Acero – Barras laminadas en caliente para hormigon armado"* [10] for concrete and rebar reinforcement, respectively.

The prescriptions of the material properties of the prestressing cables are given by ASTM-A416-85 for steel wires of 270G and 250G.

Table # 3-1: Materials prescribed for design.

Element	Material	Designation
Beams and roof slabs		H35
Foundations	Concrete	H25
Columns and cladding panels		H30
Wet joint connections		
Reinforcement rebar		A63-42H
Prestressing cables	Steel	G270
		G250

Further description of the material properties for the stress-strain relationship is to be described in 5.2.

3.3   General Geometry.

The structure consists of a precast concrete frames structure industrial building, whose main lateral load resisting system is placed in one direction only and its additional function is to support the precast roof slabs, while on the orthogonal direction it works as an inverted pendulum [8].

The total surface area of the building is equal to 18480 m^2 (168x110 m). The roof is made out of prestressed pi-shape slabs simply supported on the precast frames and the building is surrounded by cladding panels on the perimeter.

The X direction corresponds to the direction of the frame system. Whereas, the Y Direction corresponds to the orthogonal direction, which includes columns in cantilever. The reference system of the building has been selected by looking at each direction that has a classified lateral-resisting system.

A general plan view of the building is shown in Figure 3-5, where the elements marked with *C* correspond to the columns that support elements *B*, that correspond to the prestressed precast concrete beams. Each frame system in the X direction corresponds to the axes shown from B to M, while in the orthogonal direction the distribution of the axes goes from 4-11.

The building is divided into two separate structures due to the presence of an expansion joint along axis 8 to avoid large thermal effects. A picture of the expansion joint in situ is shown in Figure 3-3 and a simple detail to exemplify the geometry of the joint is shown in Figure 3-4.

Figure 3-3: Expansion joint.
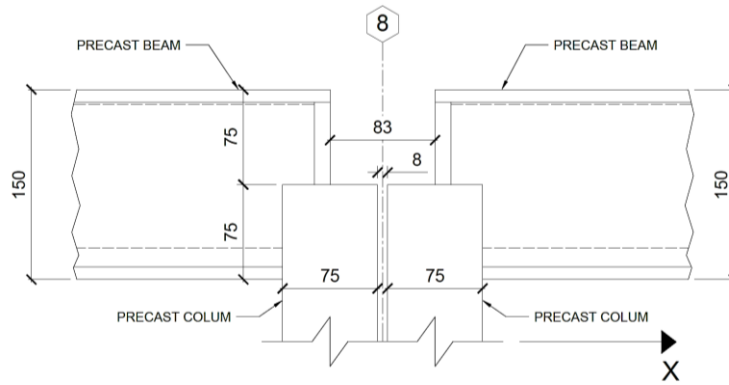
Figure 3-4: Expansion joint geometrical detail (units in cm).
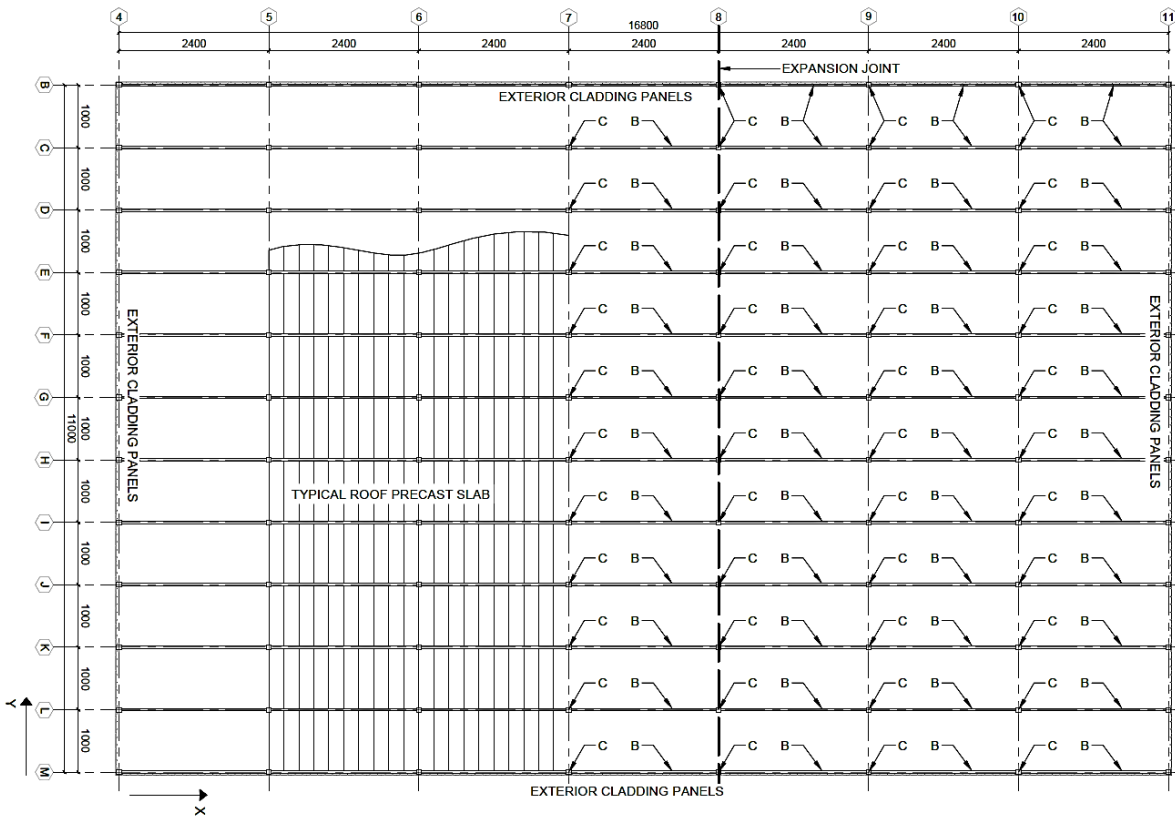
Figure 3-5: Building Plan view (units in cm).

The Elevation of the typical span frame is shown in Figure 3-6. Where it can be appreciated that the concrete precast beams are supported by columns joined by a wet joint connection, as indicated previously these frames are oriented in the X direction in each axis from B to M.
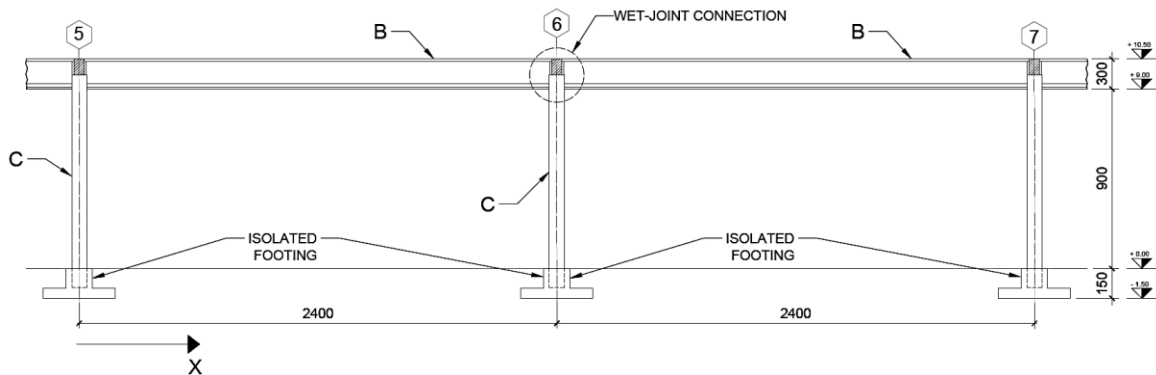
Figure 3-6: Frame geometry description (units in cm).

For the Y direction, the elevation of the precast slabs simply supported on the beams is shown in Figure 3-7.
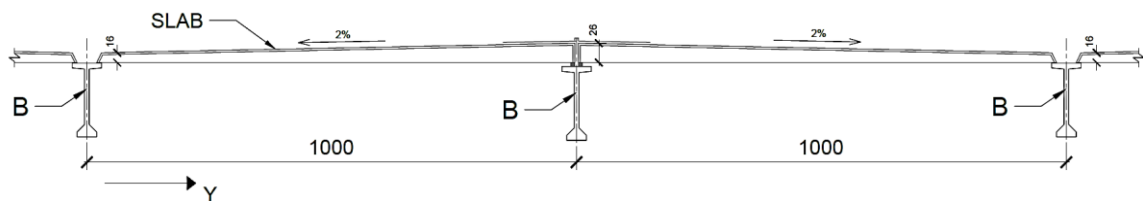
Figure 3-7: Slabs support elevation (units in cm).

3.4   Structural and non-structural elements description.

3.4.1   Precast roof slabs.

The roof slabs correspond to a prestressed precast concrete element, they possess a slab with a thickness equal to 4 cm and two joists per unit that vary in height from 16 to 26 cm along their length.

Furthermore, two prestressing cables are embedded in each joist, such cables have diameters of ½" and ¼". The cross-section and the connection detail are shown in Figure 3-8 and Figure 3-9, respectively.
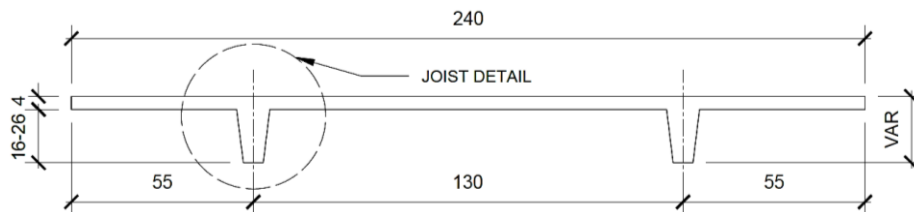
Figure 3-8: Unit slab geometry description (units in cm).
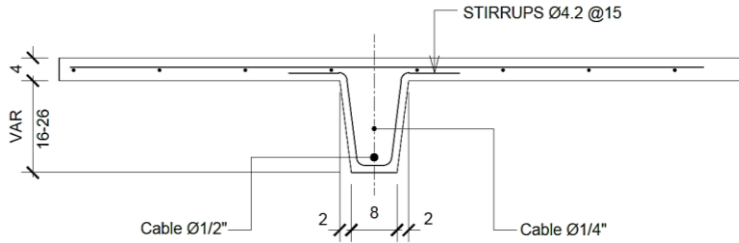
Figure 3-9: Joist cross-section description and reinforcement detail (units in cm).

In Figure 3-10 it can be appreciated that the slabs are not continuous, but simply supported on the beams' top flange.
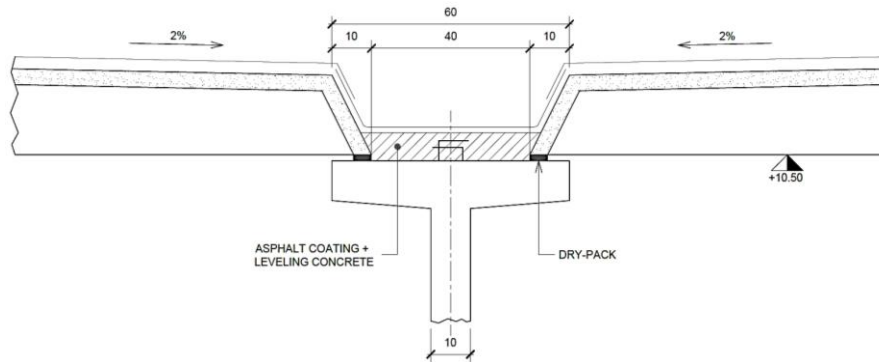
Figure 3-10: Support scheme for the slabs on the beams (units in cm).

3.4.2 Precast beams.

The precast concrete beams have dimensions of 150x60 cm, they are prestressed and connected to the columns by wet joints. All the beams have the same geometry and are 24 m long, they differ only in the amount of prestressing cables.

The interior beams between axes C to L have 12 prestressing cables at the bottom flange, whereas the exterior beams placed in axes B and M have 8 prestressing cables. In both cases, the prestressing cables have a diameter of ½ in. The cross-section details and the distribution of the prestressing cables are shown in Figure 3-11 and Figure 3-12, respectively.
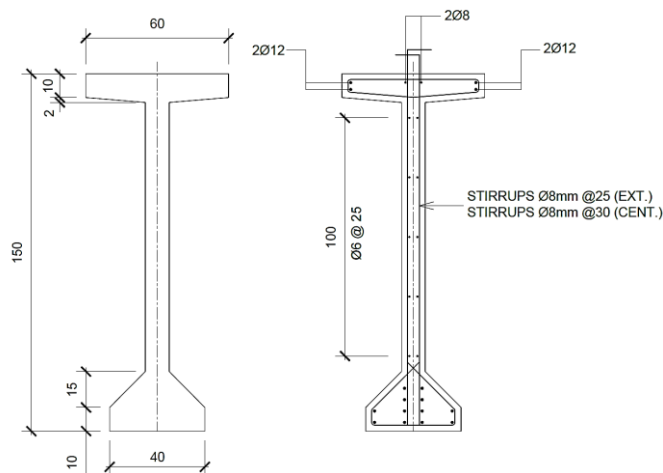
Figure 3-11: Geometry and Reinforcement detail of the prestressed beams (units in cm).
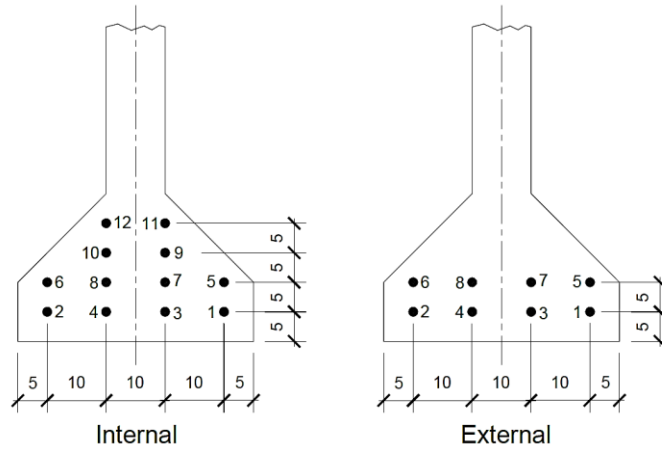
Figure 3-12: Prestressing cables distribution for internal and external beams (units in cm).

For the transversal reinforcement, the beams count with a stirrups distribution as shown in Figure 3-13, where near the supports it has stirrups of 8 mm diameter spacing each 25 cm, while elsewhere they have a spacing of 30 cm. This transversal reinforcement is the same for both internal and external beams.
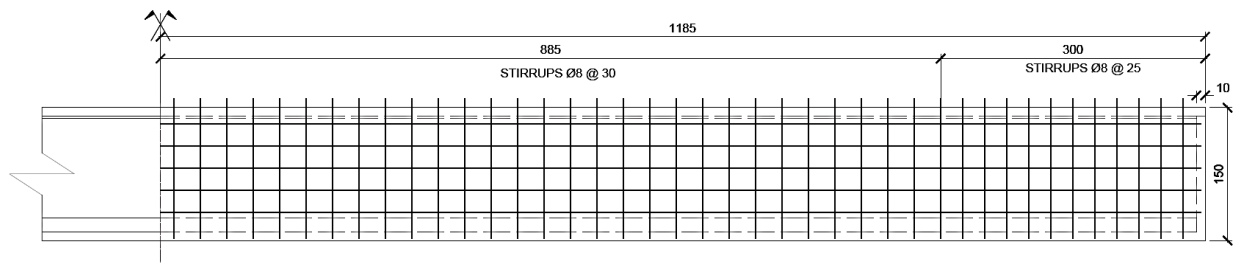
Figure 3-13: Elevation of the precast beam for transversal reinforcement layout (units in cm).

3.4.3 Precast columns.

The columns are composed of precast concrete elements, with a hollow square section of 75x75x14 cm. The cross-section geometry of the column and the layout of the reinforcement are shown in Figure 3-14 and Figure 3-15, respectively.
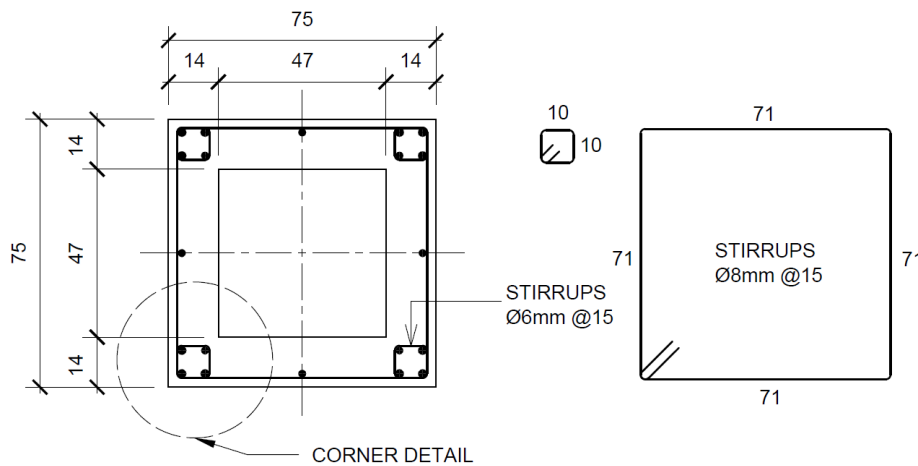
Figure 3-14: Column cross-section detail and reinforcement layout (units in cm).

13
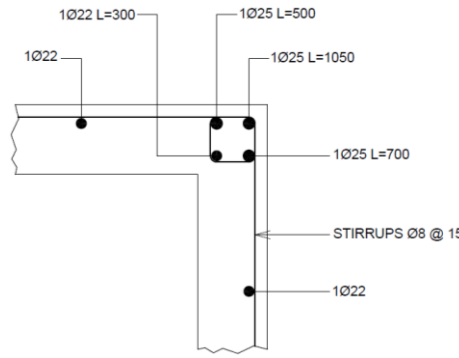
Figure 3-15: Corner column detail (units in cm).

The columns possess a confinement zone of 3.00 m measured from the columns' base. As shown in Figure 3-16 there is a larger stirrup of 8mm which holds the entire section, whereas the stirrups of 6mm confine the corner bars as previously shown in Figure 3-15.
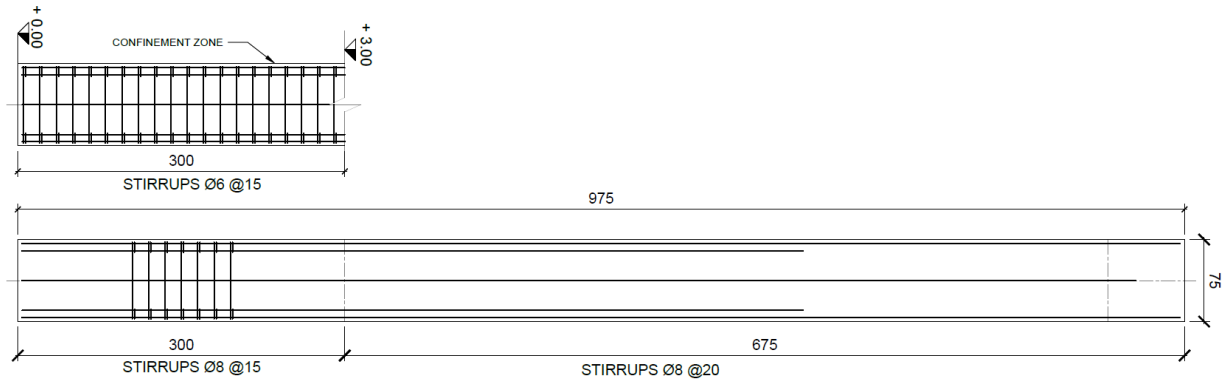
Figure 3-16: Elevation of column stirrups distribution (units in cm).

3.4.4 Wet joint Connection.

The wet-joint connection is detailed in Figure 3-17, the beam is supported by a gap in the column where a mortar placed in situ fills such gap until mid-height of the beam. The gap does not have any reinforcement.
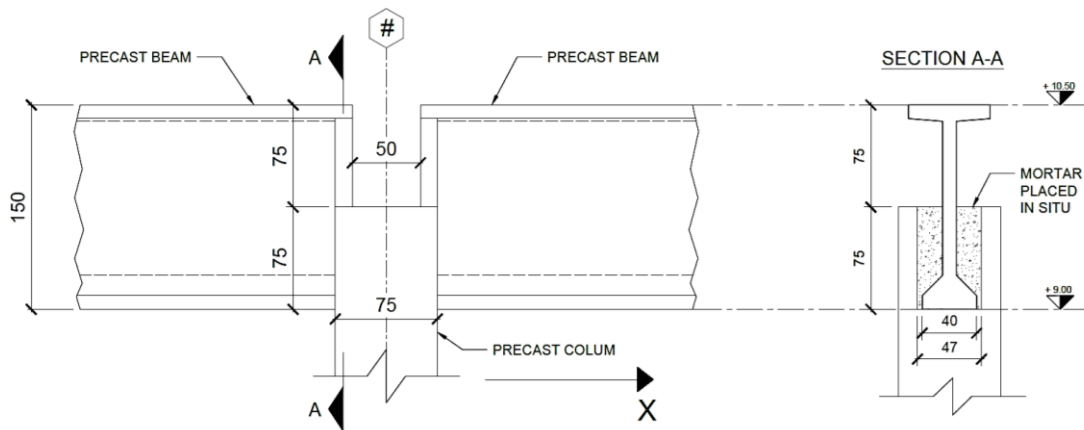
Figure 3-17: Wet joint detail for columns between the extreme axis (units in cm).

14

For the wet joint connection at the façade axis, the beams are practically embedded until the mid-with of the columns as shown in Figure 3-18.
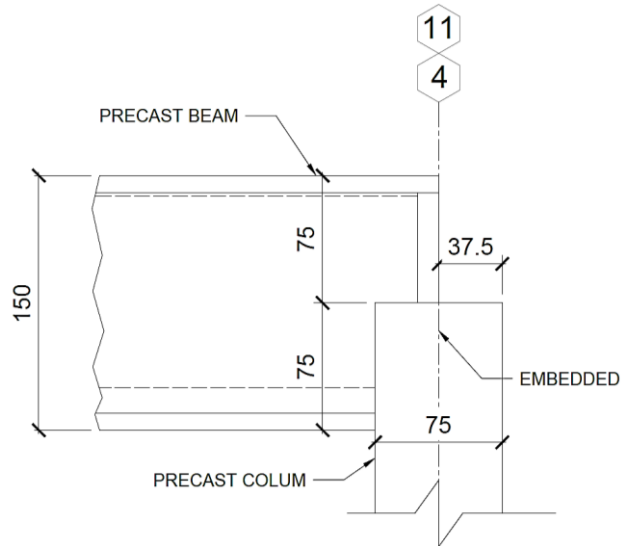
Figure 3-18: Wet joint detail at the façade axis (units in cm).

3.4.5   Precast cladding panels.

The exterior cladding panels are made of precast reinforced concrete sections with two layers of steel grids on each side. They are placed all around the perimeter of the structure. The cross-section geometry of the cladding panels and the layout of the reinforcement are shown in Figure 3-19 and Figure 3-20, respectively.

For the cladding panels placed along the M axis in the X direction, they are supported by a secondary structure that is separated from the main structure. The cladding panels placed along axes 4, 11, and B rest directly on the soil.
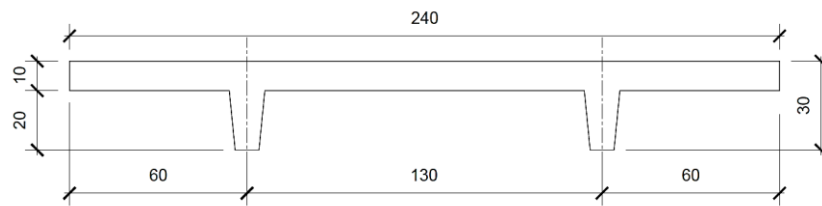
Figure 3-19: Unit Cladding panel geometry description (units in cm).
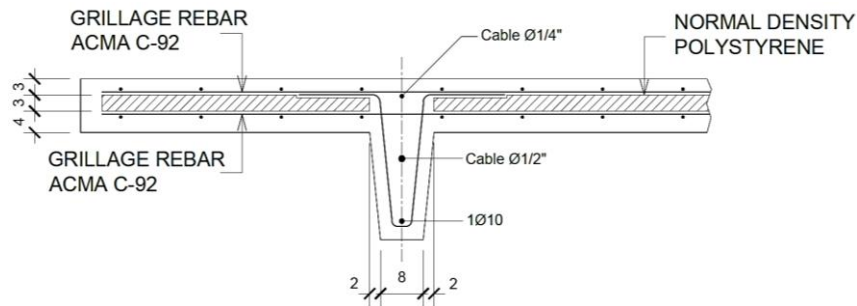
Figure 3-20: Cross-section and reinforcement layout of the cladding panel (units in cm).

15

3.4.6 Connection of cladding panels.

The connection of the cladding panels to the structure is made by an embedded bar of 12 mm under a concrete cover over the top of the beam's flange, as shown in Figure 3-21.

Figure 3-21: Cladding panel connection to the beams detail (units in cm).

3.4.7 Substructure for cladding panels.

The cladding panels placed along axis M are supported by this structure, as shown in Figure 3-22. The structure's function is to serve as a landing for the unloading and loading zone for the trucks arriving at the retail center and support the cladding panels.

The substructure consists of a simple superficial foundation as appreciated in Figure 3-23-(a), above it has a series of exterior columns of 150x20 cm connected by a secondary beam as shown in Figure 3-23-(b).

Figure 3-22: Elevation detail of the substructure and cladding panels on-axis M (units in cm).

Figure 3-23: (a) Section B-B: Geometry and layout of the foundation system. (b) Section A-A: Geometry and layout of the secondary beam (units in cm).

4   Seismic damage description.

After the seismic event occurred, a survey was performed to evaluate and document the damage suffered by the building during the earthquake. This section indicates and describes the different damages found during the inspection and it can be listed as follows:

- The Collapse of the exterior cladding panels on the X direction along with axis M from axes 5 to 9.
- The Collapse of the exterior cladding panels on the Y direction along with axis 4 from axes K to L.
- Lightly damage of the beam-column connection on the central portion of the building.
- The Beam-column connection is heavily damaged and the base of the column with spalling of the concrete.

Furthermore, a plan view indicating the location of the various damages is shown in Figure 4-1.
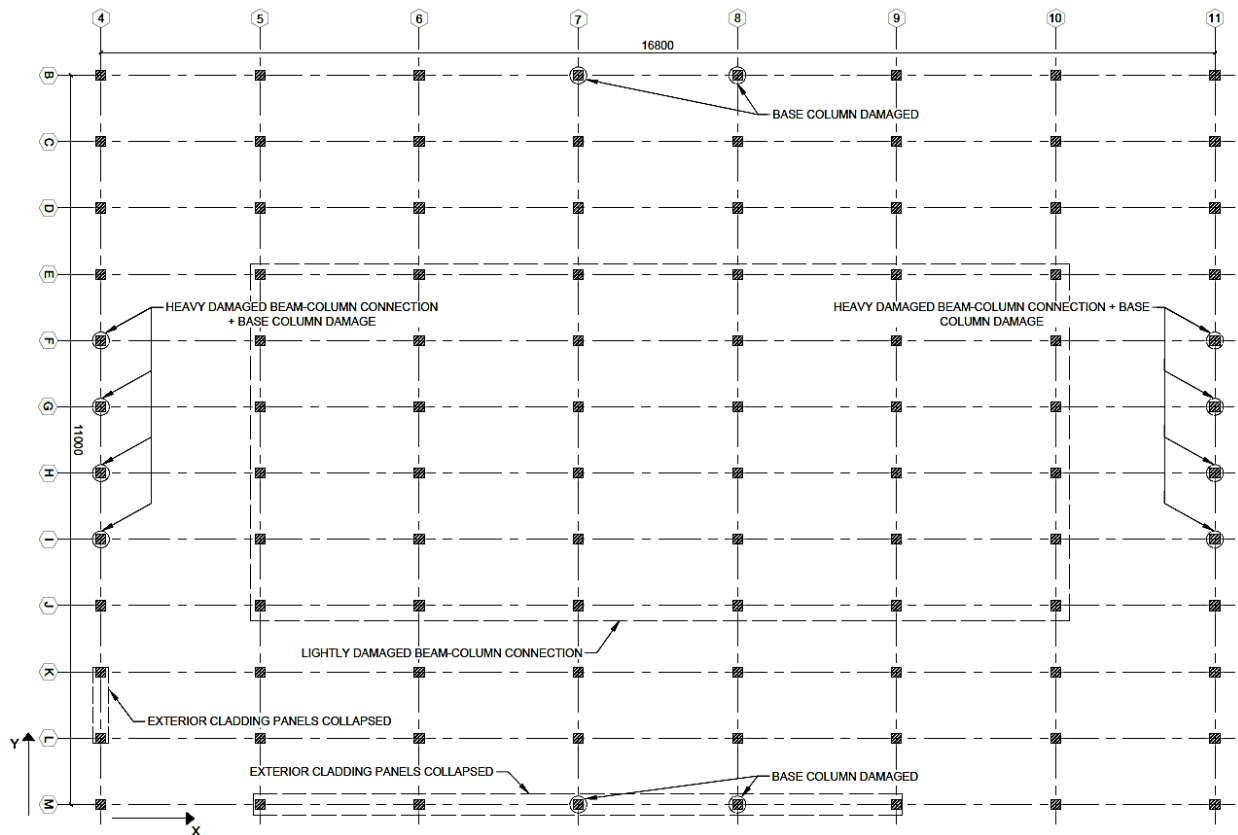
Figure 4-1: Plan view of the damaged (units in cm).

4.1   Exterior cladding panels on X direction.

This is the most noticeable damage suffered by the building during the earthquake, the motion of the building provoked the failure of the connection at the top of the cladding panels. The cladding panels fell from the substructure and broke after impacting either over the trucks or the pavement as shown in Figure 4-2.

18

As stated previously the cladding panels and the substructure were not joined together by any means, therefore, the only constraint during the motion in the lateral direction was the connection of each panel to the top of the beam, which wasn't able to withstand the internal forces.

Figure 4-2: Cladding panels collapsed in axis M picture 1.

As shown in Figure 4-2 and Figure 4-3 the cladding panels collapsed by falling over the pavement and impacting some trucks that were parked in the unloading and loading zone. The cladding panels that collapsed were the ones placed from axis 5 to axis 9 along axis M.

Figure 4-3: Cladding panels collapsed in axis M picture 2.

4.2 Exterior cladding panels on Y direction.

In direction Y, the only exterior cladding panels that overturned and fell on the ground were 5 between axis K and axis L along the Façade at axis 4 as shown in Figure 4-4. Caused basically by either debonding of the bar or tearing of the connection from the top of the cladding panel as shown in Figure 4-5.

Figure 4-4: Overturning of cladding panels in direction Y

Figure 4-5: Indication of the mechanism of failure on the cladding panel connection.

4.3   Columns' base.

Several columns suffered damage at the base during the earthquake motion, the location of these damages was shown previously in Figure 4-1 for a total of 12 bases damaged. In Figure 4-6 it can be appreciated an example of one base where the concrete cracked completely exposing the reinforcement; this happens during the formation of the plastic hinge, the section reached a curvature in which concrete cover spalled approximately within a length equal to the width of the column. It is noticeable that the buckling of the longitudinal bars did not take place.

Further investigation to find which state of damage reached the columns' base will be discussed later.

Figure 4-6: Detail of damage at the columns' base.

20

4.4 Beam-column connection.

The damage suffered by the connections is localized either at the central portion of the building as shown previously. These have slight damage with cracking and spalling of the concrete cover as shown in Figure 4-7. It is shown the cracking at the mortar and column portion belonging to the connection with no appreciable damage on the beam. This is due to the short length support that beams have on the connection to transmit the vertical force to the columns.

(a)   (b)
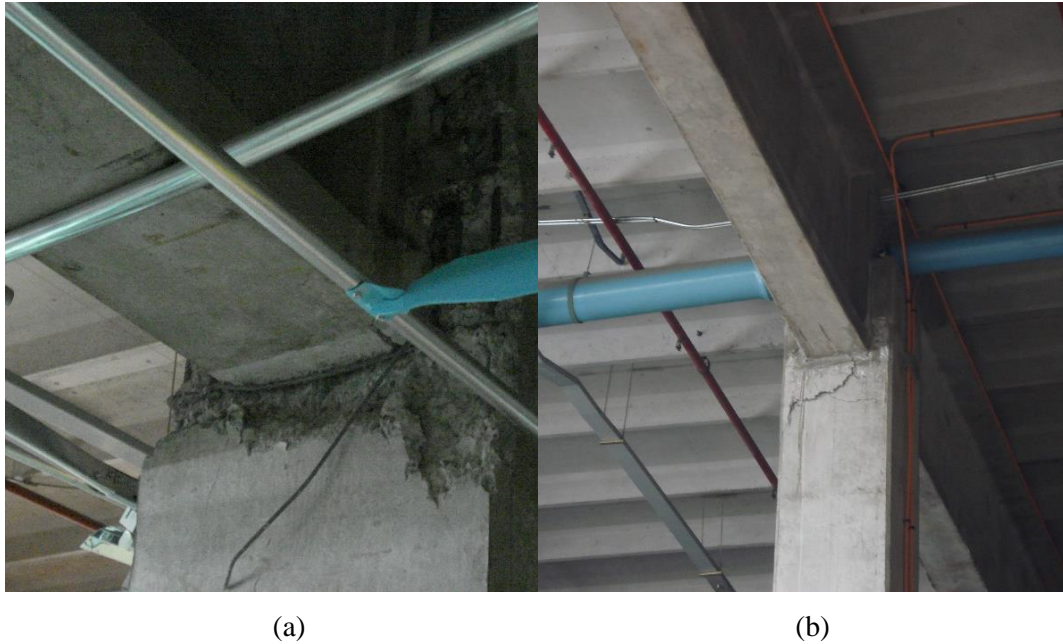
Figure 4-7: (a)-(b) Lightly damaged beam-column connection.

Whereas between axis I and F along the façade in axis 4 and 11, it was found that the connections were severely damaged as shown in Figure 4-8. Nevertheless, no beam collapsed though some of them suffered a high amount of damage on the web and bottom flange.

(a)   (b)
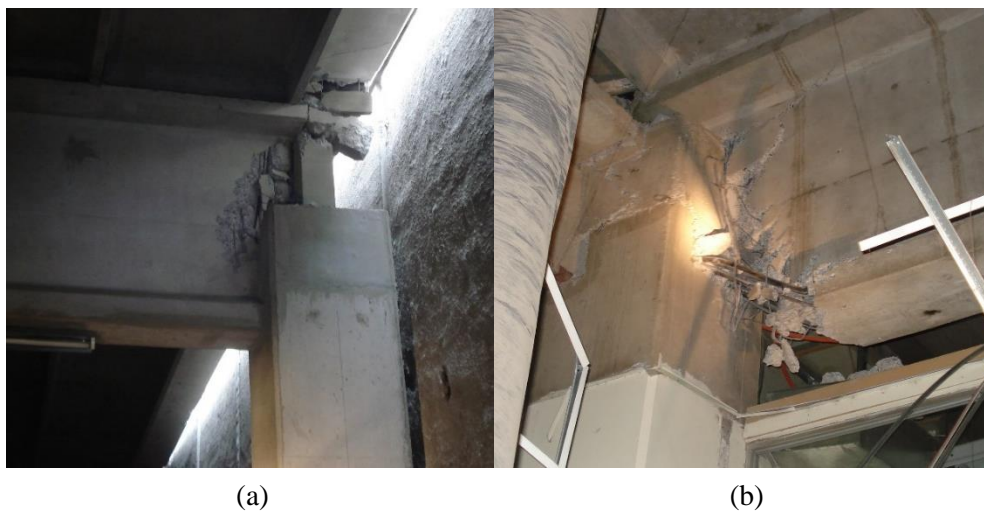
Figure 4-8: (a)-(b) Heavily damaged beam-column connection.

4.5   Slab collapse.

Additionally, a roof slab collapse was observed during the survey, the hypothesis based on the work from [1] regarding the collapse might be due to a poor assemblage of the connection. A picture of the collapsed slab is shown in Figure 4-9.

Figure 4-9: Collapsed of one roof slab.

5   Modeling of the structure.

For the structure under study, the structural analysis software SAP2000 is used to build a numerical model from the geometry and material of the real structure. The following section describes the modeling process and aims to detail the most important aspects as cross-section modeling, materials, restraints, and connection between elements.

The model is calibrated to represent the real structure to capture the mechanisms of failure or damages suffered by the structural elements by looking at the local and global behavior.

Due to the presence of an expansion joint, the numerical model of the building is split into two models called Building A and Building B, as shown in Figure 5-1. Building A is defined between axes 4 and 8, whereas Building B is defined from axis 8 to 11.
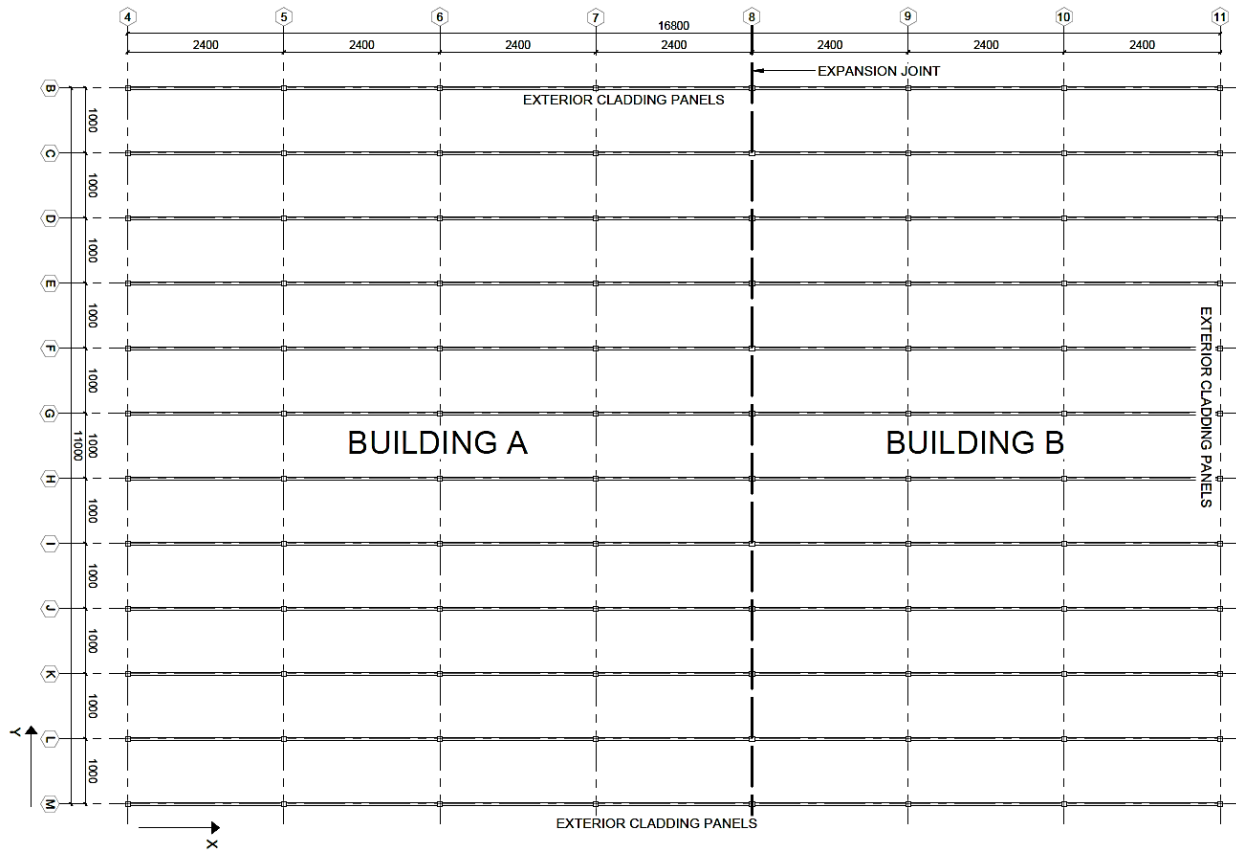
Figure 5-1: Modelling scheme of the two parts of the structure (units in cm).

Finally, The numerical model for the two structures, Building A and Building B are shown in Figure 5-2 (a)-(b), respectively.

<div align="center">(a)   (b)</div>
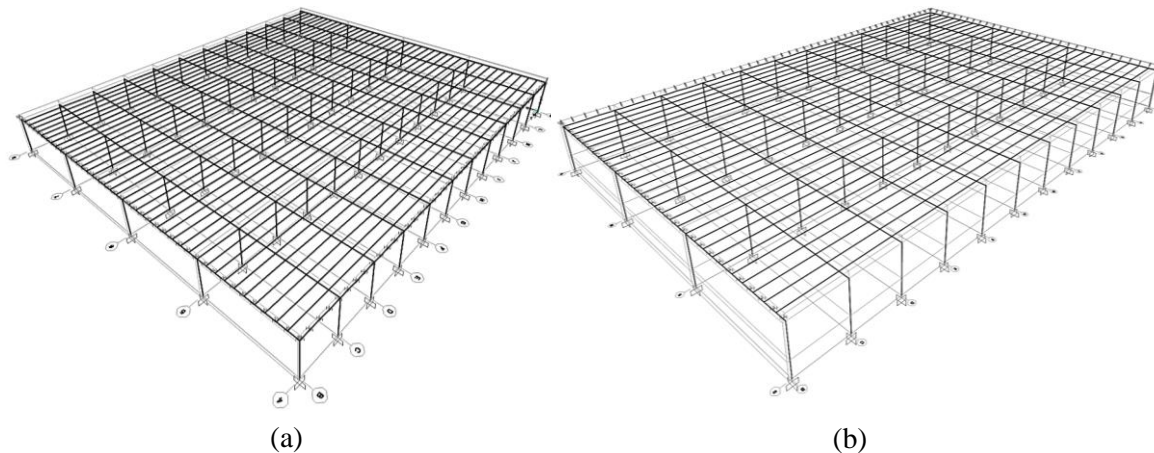
Figure 5-2: (a) Building A model in SAP2000. (b) Building B model in SAP2000.

5.1 General hypothesis.

For the modeling of the building some general hypotheses were defined, these are listed below:

- All columns are fixed to the base at the ground level.

- All structural elements are represented by beam-type elements.

- The masses are automatically computed by SAP2000. Such masses are based on the geometry and material properties of the finite element (FE), and these masses are checked by hand afterwards.

5.2 Material.

The analysis required to obtain a realistic picture of the behavior of the structure includes both linear and non-linear procedures looking to its static and dynamic parts. Therefore, a complete description of the material mechanical properties like stress-strain relationships and hysteric behavior is needed and shown in this section.

5.2.1 Reinforced concrete.

The mechanical properties for concrete H30 and H35 are described in the Chilean standard NCh430 [9]. This Chilean standard introduces some modifications and adjustments from the state of art at Chile into the American standard ACI 318-95. Nevertheless, the specifications used to define the concrete properties are taken from the American standard ACI 318-14 [11].

Furthermore, to have a complete assessment of the structure as recommended in [12], the nominal compressive strength of the concrete in place for more than a year should be increased, giving the so-called Expected strength of concrete. The increase factor recommended by the manual *"LRFD Seismic Analysis and design of Bridges reference"* [12] is set equal to 1.30. Additionally, the parameter related to the strain at which the spalling of the concrete cover occurs for unconfined concrete are recommended in [12] and is set as 0.005. This is the predefined value by SAP2000 for unconfined concrete.

The values for the mechanical properties for both concretes are given in Table # 5-1. The Mander model [13] description given by SAP2000 is shown in Figure 5-3.

Table # 5-1: Mechanical properties for concrete H30 and H35.

Concrete quality	H30	H35
Concrete compressive strength f'_c [MPa] [9]	30.00	35.00
Poisson ratio [-]	0.20	
Specific weight [kN/m³]	25.00	
Young modulus (Eq. 19.2.2.1.b) [MPa] [11]	25743	27806
ε_c Concrete strain at f'_c [%]	0.200%	0.200%
ε_{sp} Spalling strain of the concrete [%] [12]	0.500%	0.500%
Concrete tensile strength (Eq. 19.2.3.1) [MPa] [11]	3.87	4.18
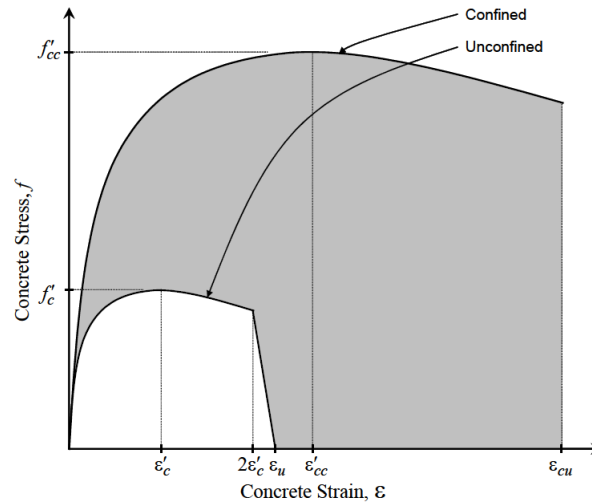
Figure 5-3: Mander confined and unconfined stress-strain curves [13].

For the reinforced concrete, SAP2000 permits to build the strain-stress relationship based on the Mander model for unconfined and confined concrete [14]. This has a set of rules to build a stress-strain relationship for both concretes. The stress-strain curves are plotted for exemplification and shown in Figure 5-4 and Figure 5-5. More detailed instructions can be found on the documentation from SAP2000, *"Technical note: Material stress-strain curves"* [13].
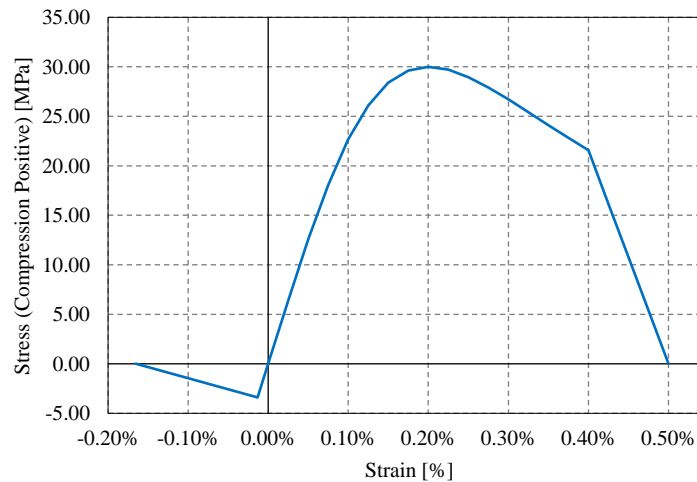
Figure 5-4: Stress-strain curve for unconfined H30 concrete based on [13].

25
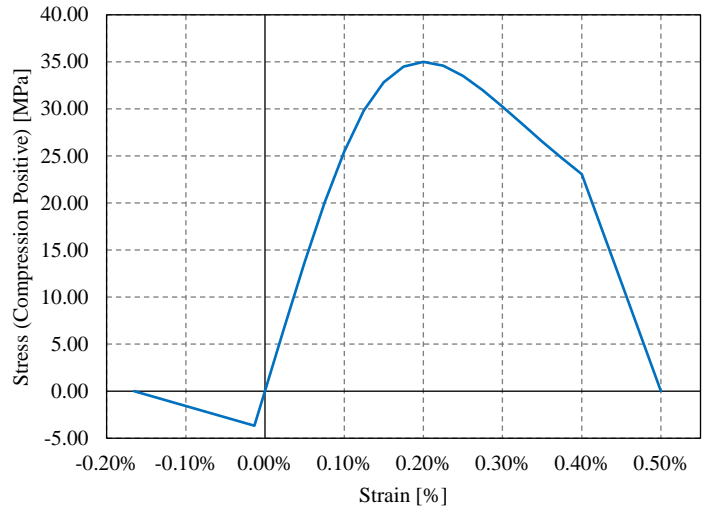
Figure 5-5: Stress-strain curve for unconfined H35 concrete based on [13].

For a confined concrete model the description of the geometry and layout reinforcement of each section is necessary. It will be introduced in 5.3 for each cross-section description.

SAP2000 includes a suitable model for the hysteretic behavior of the reinforced concrete based on the Takeda model [15]. It is similar to the kinematic model but uses a degrading hysteretic loop. This model was developed to handle cyclic loading-unloading behavior of reinforced concrete subjected to strong earthquake motion.

It works by setting a list of rules to follow during the cyclic loading-unloading behavior. An example of the hysteretic curve included in SAP2000 is shown in Figure 5-6. Further information related to the set of rules can be found in [15] and [16].
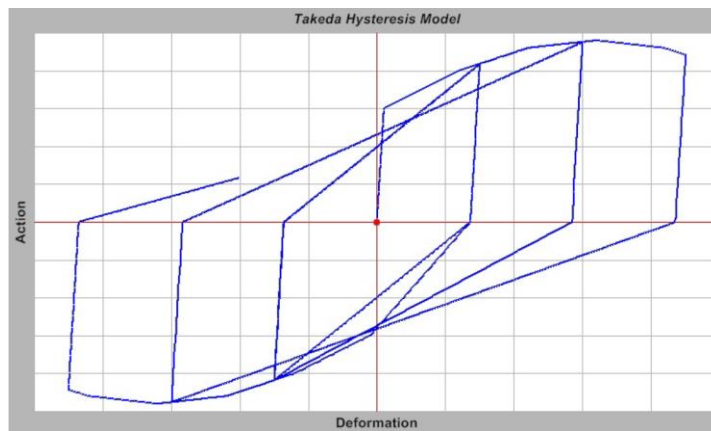
Figure 5-6: Takeda hysteresis model under increasing cyclic load [16].

5.2.2 Reinforcing steel.

The design values and the mechanical properties of the reinforcement steel A42-63H are taken from Chilean standard NCh204 [10] which refers to the ASTM-A615 [17].

The parameters related to the stress-strain relationship of the reinforcing steel are shown in Table # 5-2. The value of the ultimate strain capacity is given in [10] computed through Eq.*(5-1)*. Conservatively just

from all diameters of rebar included in the model, the lowest ultimate strain capacity was used to define the stress-strain relationship.

$$\varepsilon_u = \frac{7000}{f_u} - k \tag{5-1}$$

Where f_u: is the Rupture strength [MPa]; ε_u: Ultimate strain capacity; k: is a parameter dependent on the diameter of the rebar, which is given in [10].

Table # 5-2: A63-42H Reinforcing steel mechanical properties.

Yielding strength f_y [MPa]	420
Rupture strength f_u [MPa]	630
Yielding strength f_{yE} [MPa]	480
Rupture strength f_{uE} [MPa]	730
Young Modulus E [MPa]	199947
ε_y Yield strain [%]	0.210%
ε_{sh} Onset of strain hardening [%]	0.800%
ε_u Ultimate strain capacity [%]	9.100%

Furthermore, the stress-strain curve that SAP2000 employs to build the relationship is shown in Figure 5-7; for the onset of strain hardening a selected value of 0.008 recommended by [18] is used. Finally, the complete curve is shown in Figure 5-8.
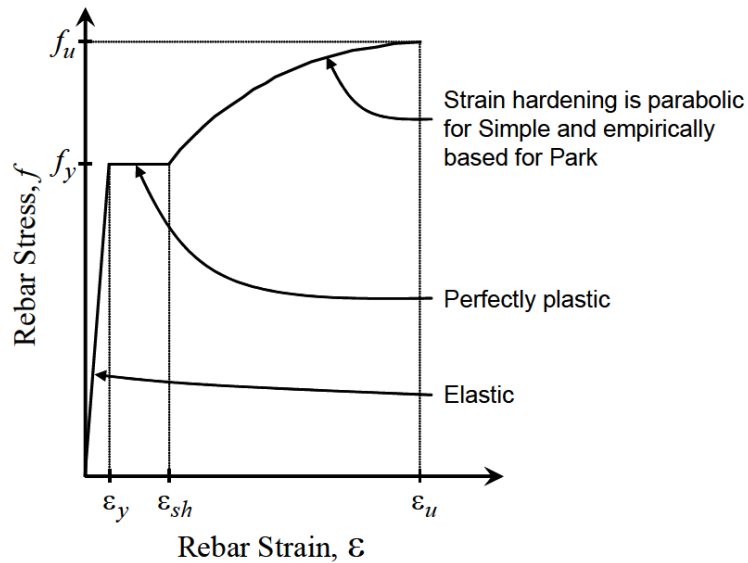
Figure 5-7: Rebar parametric stress-strain curve [13].
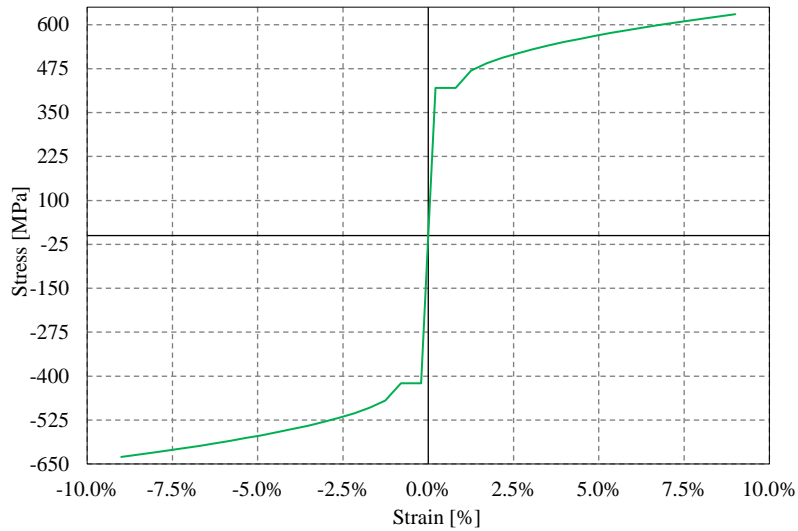
Figure 5-8: Stress-strain curve for reinforcing steel A63-42H.

For the hysteretic behavior of the reinforcing steel SAP2000 has a suitable model based on the kinematic hysteresis model [16]. This model is commonly observed in metals; it dissipates a significant amount of energy and is appropriate for ductile materials like reinforcing steel. An example of the loop cycle is shown in Figure 5-9.
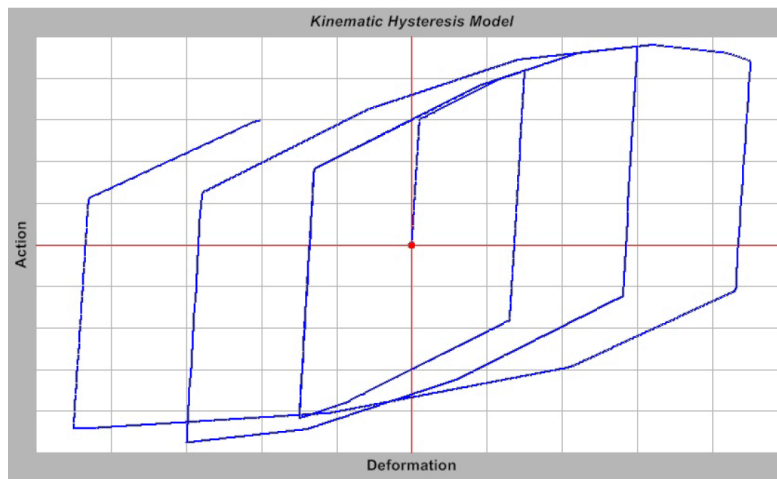
Figure 5-9: Kinematic hysteresis model under increasing cyclic load [16].

5.2.3   Prestressing steel.

The prestressing cable to be modeled is the 270G. This steel grade 270G is reported in ASTM-A416 [19], it is a low relaxation 7-wire strand with a minimum ultimate strength of 270 ksi /1860 MPa. SAP2000 includes already a description of this kind of prestressing steel in its selection of materials [13]. A stress-strain curve scheme is shown in Figure 5-10.

The mechanical properties of the prestressing steel to be implemented are shown in Table # 5-3 and the stress-strain curve's final representation is shown in Figure 5-11.

Table # 5-3: 270G prestressing steel mechanical properties.

Yielding strength f_y [MPa]	1689
Rupture strength f_u [MPa]	1862
Young Modulus E [MPa]	196501
Young Modulus E [Ksi]	28500
Yield strain ε_y [%]	0.8599%
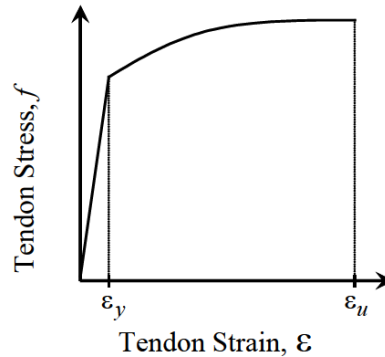
Figure 5-10: Tendon 270G Stress-strain curve [13].
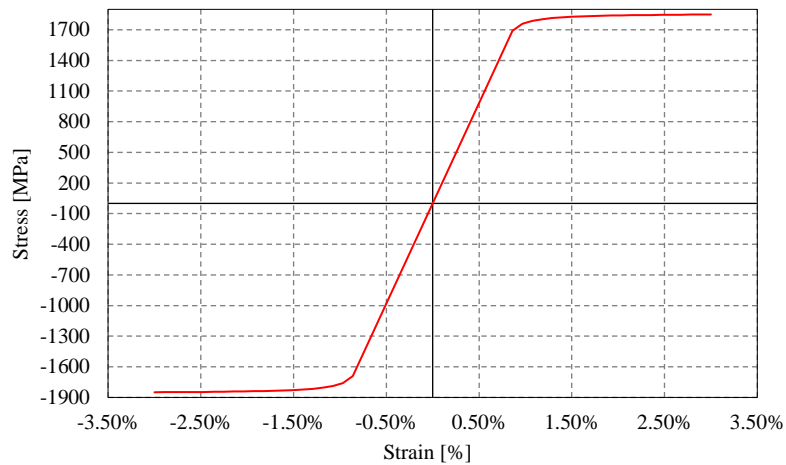
Figure 5-11: Stress-strain- curve for prestressing steel 270G.

5.3   Modeling of the structural elements.

All the elements representing the structure are modeled using the Frame element feature by SAP2000 [16]. This uses a general three-dimensional beam/column formulation which includes the effects of biaxial bending, torsion, axial, and biaxial shear deformations with six degrees of freedom (DoFs) at each node for a total of 12 DoFs. The local axes for the joints composing each frame element with each degree of freedom are shown in Figure 5-12.
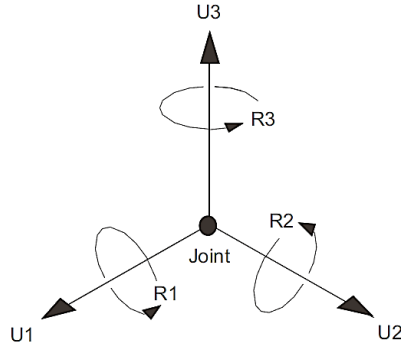
Figure 5-12: The six displacement degrees of freedom in the joint local coordinate system [16].

SAP2000 allows to represent these elements as a straight line connecting two points called joints, as shown in Figure 5-13. Local axes go from 1 to 3 to define the section properties, loads, and for interpreting the output. Element internal forces are produced at the ends of each element and at a user-specified number of equally spaced output stations along the length of the element.
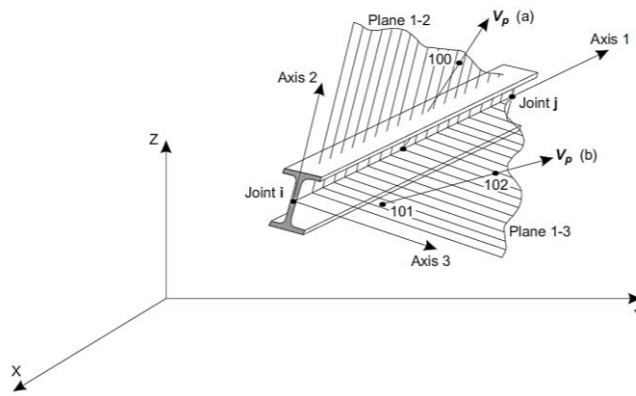
Figure 5-13: Frame SAP2000 representation scheme [16].

Usually, the arrangement of the local axis of the frame element is in numbers from 1 to 3, where Local axis 1 is aligned with the longitudinal direction which connects joint *i* with joint *j* as previously shown in Figure 5-13. Furthermore, Local axis 3 is aligned with the major axis and Local axis 2 the minor one, as shown in Figure 5-14 some examples of sections extracted from [16]. The aforementioned axes represent the directions of maximum and minimum inertia moment.
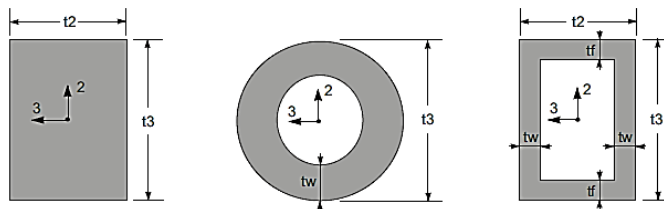
Figure 5-14: Sections example for the in-plane section local axes [16].

5.3.1 Column section.

To represent the properties of the column elements, the section designer module (SD) from SAP2000 has been used, which can compute the elastic properties to be used during linear analysis and describe non-linear behavior by using the material properties, geometry and reinforcement layout described previously.

30

The column's section implemented in SAP2000 is shown in Figure 5-15, and is used for both linear and non-linear analysis.
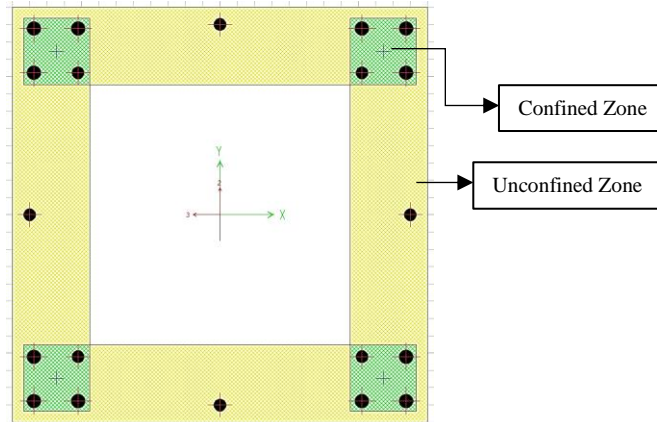
Figure 5-15: Section designer column section on SAP2000.

The concrete confined zone, as previously shown in Figure 5-15, has a stress-strain relationship that is based on the work of Mander [14] and is shown in Figure 5-16. SAP2000 includes an interface to insert the necessary parameters. The parameters to insert in order to build the Stress-strain relationship are related to the longitudinal and transversal reinforcement described in 3.4.3.
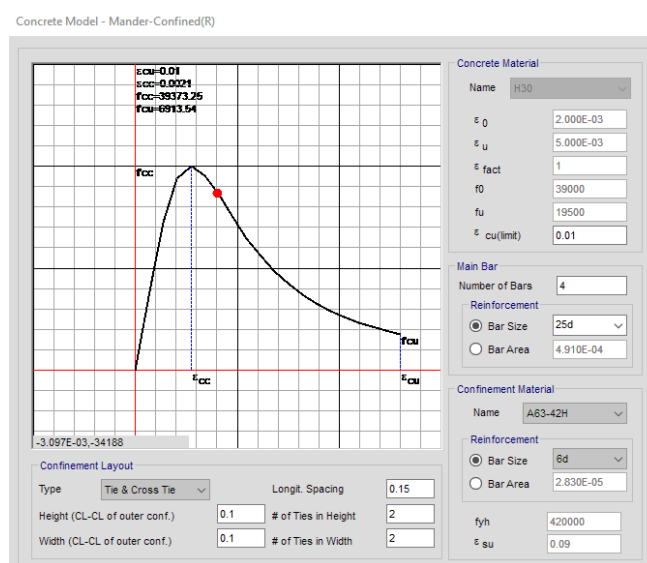
Figure 5-16: SAP2000 interface for stress-strain relationship for Mander concrete confined model [14].

5.3.2   Beam section.

As previously described for columns, beams are drawn on the section designer (SD) module, to compute both elastic properties and non-linear behavior parameters. The geometry and layout of reinforcement are based on the descriptions given in 3.4.2. Both beam sections to be implemented are shown in Figure 5-17(a)-(b).

(a)　　　　　　　(b)
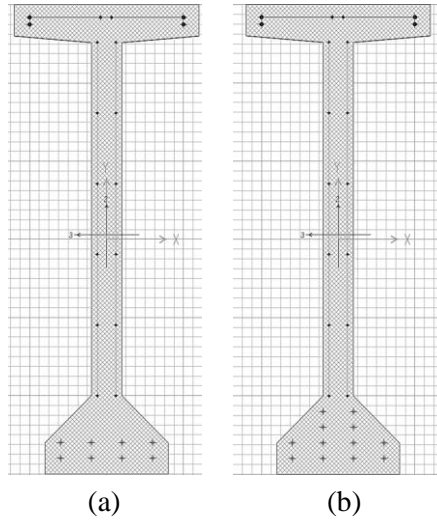
Figure 5-17: (a) SD External beam section. (b) SD Internal beam section.

5.3.3　Slab section.

For the roof slab section, only the elastic properties are needed, therefore a representation of the exact geometry is done on SD as shown in Figure 5-18 and Figure 5-19. Both slab sections are built and joined together by using the Non-prismatic section definition since they vary along their length. The roof slabs have a varying cross-section over a span of 10 meters. The interface to make use of Non-prismatic sections is shown in Figure 5-20. Further information about the modification can be found in [16].
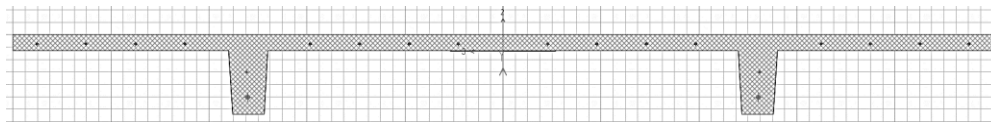
Figure 5-18: Section designer 16 cm joist roof slab section.
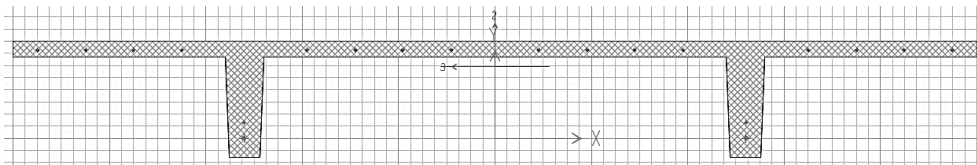
Figure 5-19: Section designer 26 cm joist roof slab section.
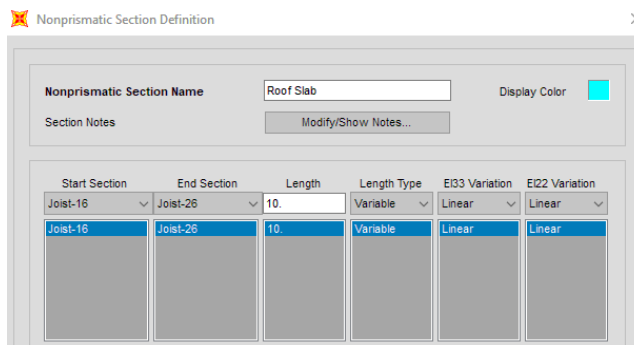
Figure 5-20: Non-prismatic section definition for the roof slab [16].

5.3.4 Assembling of the elements.

The assembling scheme of both buildings is described in this subsection. The purpose is to exemplify the connection and assembling of the different structural and non-structural components included in the model.

In the X direction, the frame elements are arranged following the centroidal axis of the structural elements that are placed in situ. An example of the structural scheme for the beam-column assemblage is shown in Figure 5-21 and the SAP2000 modeled frame is shown in Figure 5-22.
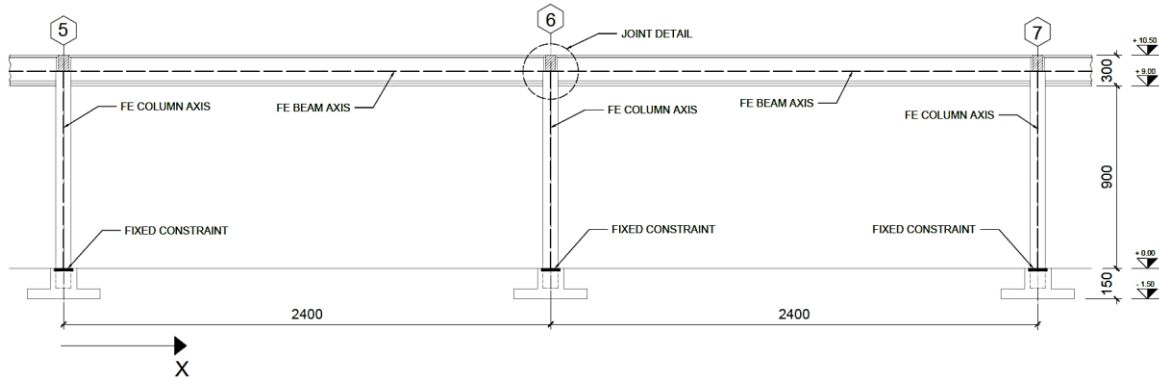
Figure 5-21: Frame modeling scheme in the X direction (units in cm).
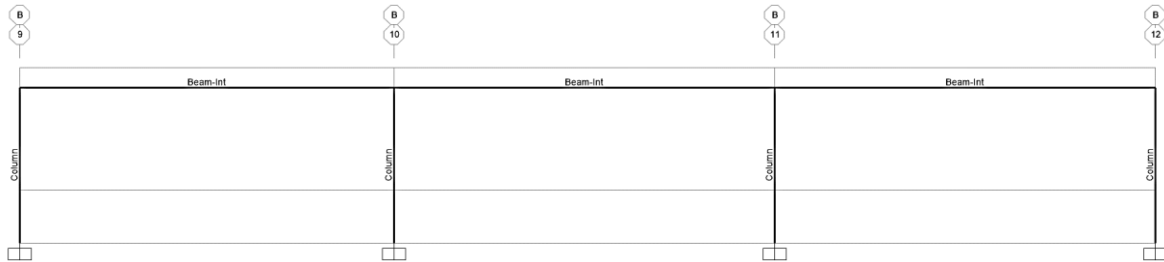
Figure 5-22: SAP2000 frame elevation in the X direction.

As shown in Figure 5-21, the beams that arrive at the joint with the column are not continuous and there is a gap partially filled with mortar. Thus, the beams are modeled by allowing them to rotate relatively to the joint by releasing the 3 DoFs related to rotation, as shown in Figure 5-23.

This is to simulate the incapability of the wet-joint connection to transmit any kind of bending moment and torsion. In further sections, it will be considered clamped to evaluate both situations.
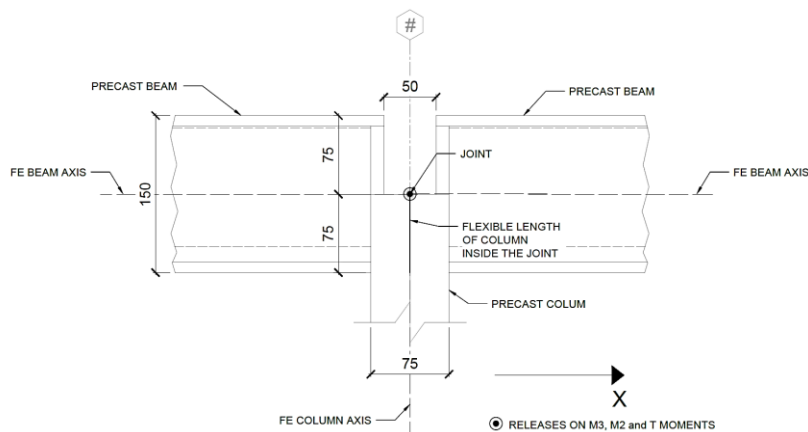
Figure 5-23: Beam-column Joint modeling scheme (units in cm).

The beam-column joints at the façades (axis 4 and 11) have the beams embedded until the mid-width of the column. After the damage observed on the beams-columns connection and considering the beams' support length, it will be modeled clamped. A portion of the beam is considered rigid at mid-span of the support given by the column as shown in Figure 5-24.
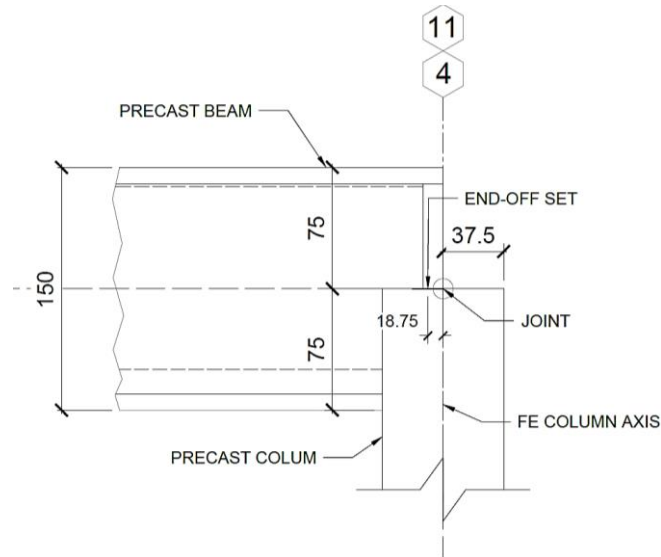
Figure 5-24: Façade wet joint connection modeling (units in cm).

The frame elements representing the precast roof slabs are arranged over 10 meters spans. They are set by joining them to the frame elements representing the beams in common joints as shown in Figure 5-25.

To consider the fact the roof slabs are supported by the beams' top flange, a rigid off-set is implemented as an eccentricity equal to half-height of the beam (0.75 meters).
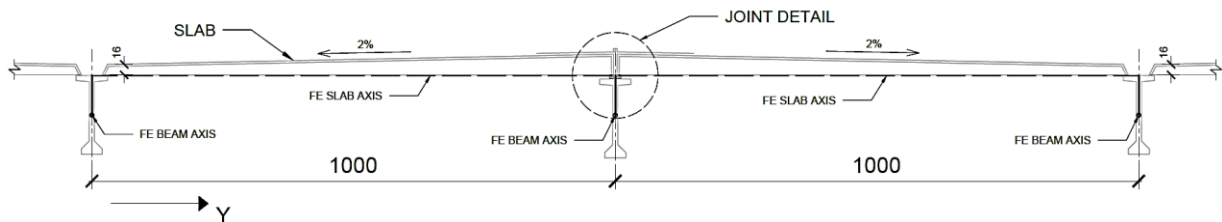
Figure 5-25: Slab supporting modeling scheme (units in cm).

More explicit detail of the connection of the slabs with the beam is shown in Figure 5-26, where the rigid offset is shown; the discontinuity of the slabs is taken into account by releasing the transferring of bending moments.
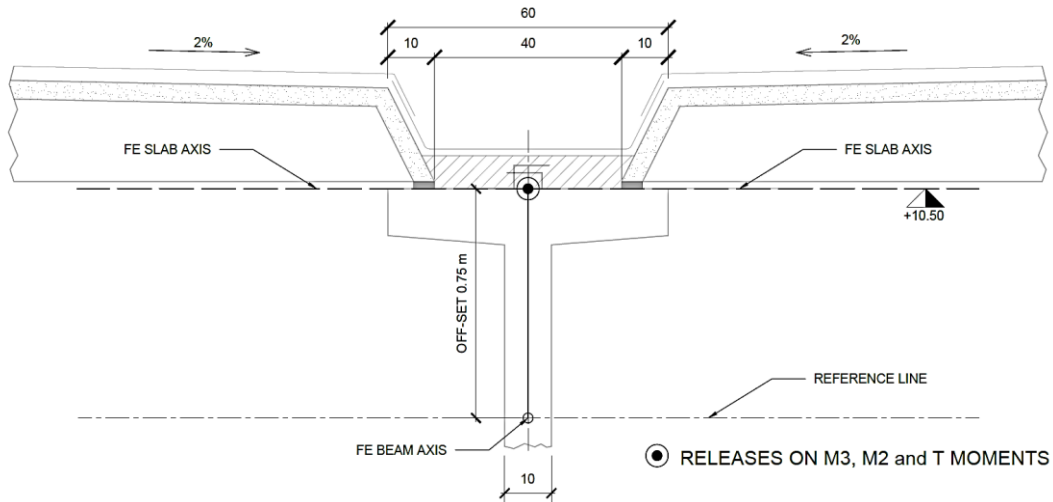
Figure 5-26: Beam to slab connection modeling scheme (units in cm).

The contribution of the cladding panels is simulated by including a portion of their mass and an equivalent stiffness provided by their connection. This is done by modeling an equivalent spring for the stiffness and considering the effective mass to be excited attached at the end of the spring.

The effective mass corresponds to the upper half of the cladding panel. A representation of the scheme modeling is shown in Figure 5-27 and Figure 5-28 for both directions X and Y, respectively. For the Y direction, it can be noticed that the slab axis and the joints inserted to attach the springs coincide.
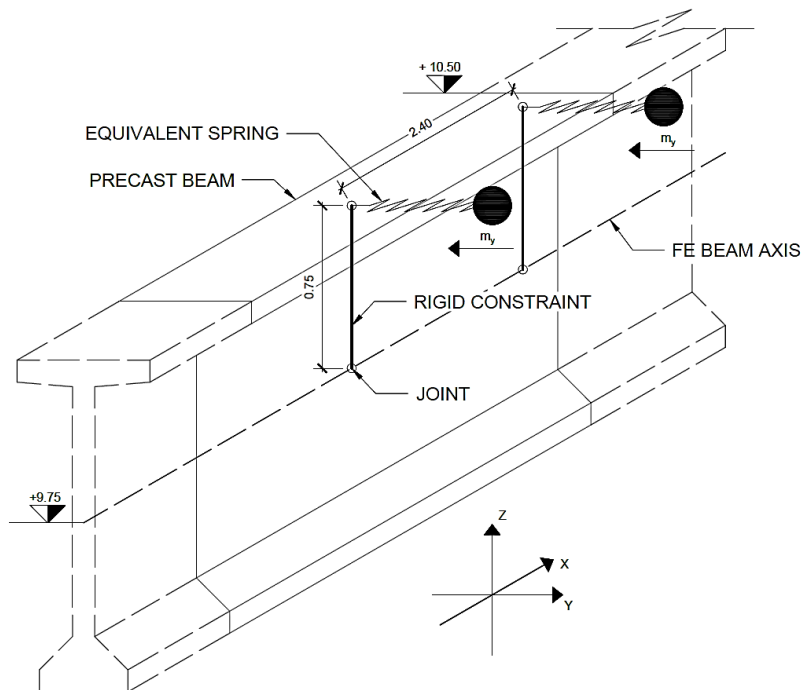
Figure 5-27: Modelling of cladding panel in the X direction (units in m).
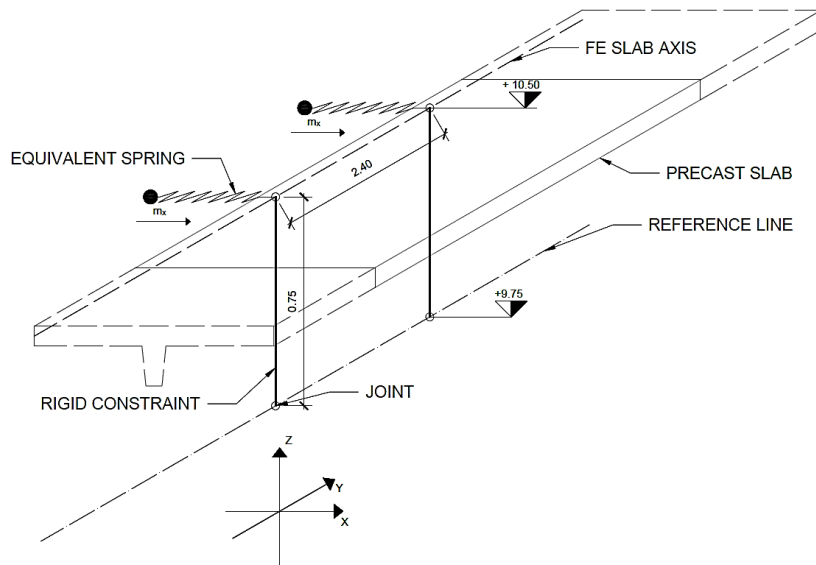
Figure 5-28: Modeling of cladding panel in direction Y (units in m).

The equivalent spring is jointed to a rigid constraint to the joints on the beam frame elements; these constraints are placed to simulate the fact of the connection being at the top of the beam at 0.75 m.

The equivalent stiffness is taken equal to the axial rigidity of the two bars placed in each cladding panel as shown in Figure 5-29. The computation of the equivalent stiffness is performed below:

$$k = \frac{2*EA}{l} = \frac{2*(199947\ MPa)(113.10mm^2)}{400mm} = 113070\ \frac{kN}{m}$$
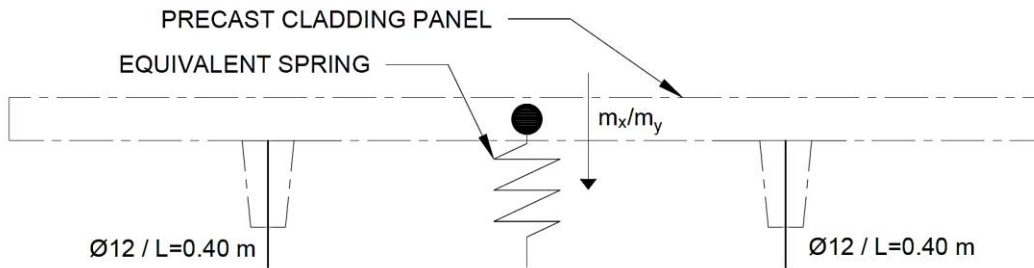
Figure 5-29: Modelling scheme of the cladding panel in X/Y direction.

5.4   Masses

The masses to be used to assess the modal data of both buildings are the ones related to the self-weight of each element included. These are automatically computed by SAP2000 and afterward checked by hand to control their assembling.

As stated [16] the element mass values computed by SAP2000 are equal for each of the three translational degrees of freedom and uncoupled. No mass moments of inertia are produced for the rotational degrees of freedom. Nevertheless, if necessary, rotational inertia can be added or any other additional mass can be implemented. The mass matrix for an element is shown in Figure 5-30 as well the inertia forces generated by SAP2000.

36

$$\begin{Bmatrix} F_1 \\ F_2 \\ F_3 \\ M_1 \\ M_2 \\ M_3 \end{Bmatrix} = - \begin{bmatrix} u1 & 0 & 0 & 0 & 0 & 0 \\ & u2 & 0 & 0 & 0 & 0 \\ & & u3 & 0 & 0 & 0 \\ & & & r1 & 0 & 0 \\ & \text{sym.} & & & r2 & 0 \\ & & & & & r3 \end{bmatrix} \begin{Bmatrix} \ddot{u}_1 \\ \ddot{u}_2 \\ \ddot{u}_3 \\ \ddot{r}_1 \\ \ddot{r}_2 \\ \ddot{r}_3 \end{Bmatrix}$$

Figure 5-30: Joint inertial force matrix example [16].

The masses belonging to each structure element's contribution to the principal directions are in Table # 5-4.

Table # 5-4: Modeled mass in each principal direction.

Structural element.	Building A			Building B		
	Mass X	Mass Y	Mass Z	Mass X	Mass Y	Mass Z
	[Ton]	[Ton]	[Ton]	[Ton]	[Ton]	[Ton]
Columns	509	509	509	408	408	408
Roof slabs	1526	1526	1526	1140	1140	1140
Beams	756	756	756	561	561	561
Cladding panels (X) on axis M	0	93	0	0	70	0
Cladding panels (X) on axis B	0	131	0	0	99	0
Cladding panels (Y)	144	0	0	144	0	0
Total mass	2936	3016	2792	2253	2278	2109

5.5   Model assessment.

To have further information about the influence of the stiffness given by the cladding panels modeled, two situations are set to study and they are listed below:

1. In both building models, the total contribution of the cladding panels is included, and they are named situations A and B for both buildings, respectively.

2. In both building models the cladding panels that collapsed after the events of the Maule earthquake are taken out, and they are named situation Collapse A and Collapse B for both buildings, respectively.

Therefore, with these analyses, the most suitable model to assess the global performance of the structure will be selected. The modal data extracted from the modal analyses are shown in Table # 5-5.

Table # 5-5: Modal data for Building A and Building B.

	Situation A					Situation B				
Mode	Period	Frequency	U_x	U_y	R_z	Period	Frequency	U_x	U_y	R_z
[#]	[s]	[Hz]	[%]	[%]	[%]	[s]	[Hz]	[%]	[%]	[%]
1	1.0384	0.9630	0.00%	99.15%	0.00%	1.0053	0.9947	0.00%	100.00%	0.00%
2	0.8093	1.2356	0.01%	0.00%	91.12%	0.7360	1.3587	0.00%	0.00%	93.00%
3	0.7800	1.2821	96.74%	0.00%	0.01%	0.7334	1.3635	95.00%	0.00%	0.00%
	Situation A Collapse					Situation B Collapse				
Mode	Period	Frequency	U_x	U_y	R_z	Period	Frequency	U_x	U_y	R_z
[#]	[s]	[Hz]	[%]	[%]	[%]	[s]	[Hz]	[%]	[%]	[%]
1	1.0216	0.9789	0.00%	99.00%	0.00%	0.9985	1.0015	0.00%	100.00%	0.00%
2	0.8014	1.2479	0.00%	0.00%	92.00%	0.7334	1.3634	95.00%	0.00%	0.00%
3	0.7781	1.2852	97.00%	0.00%	0.00%	0.7319	1.3664	0.00%	0.00%	93.00%

As it can be noticed, in both situations for the buildings, the first three modes are enough to consider the more than 90% excitation of masses in each principal direction.

Furthermore, Figure 5-31 shows the comparison of the periods for both buildings showing the first 3 modal periods. The variation between periods is significantly low, being the largest difference 1.65% of the first mode for Building A.

Nevertheless, for building B when passing from one situation to another (taking out the cladding panels that collapsed) the modes are inverted from having a second mode in torsion to a mode in the X direction. The modal frequencies are very close, around 0.30% of relative difference meaning it becomes more flexible in the X direction than torsional.

In conclusion, the exclusion of the collapsed cladding panels in the model does not introduce a significant change in the dynamic behavior of the buildings. It just reduces slightly the mass to be excited in one specific direction as shown in Figure 5-32. Being said this, the model considering all the claddings as lumped masses connected to the frame elements is more than suitable to consider their contribution to the dynamic behavior of the structure.
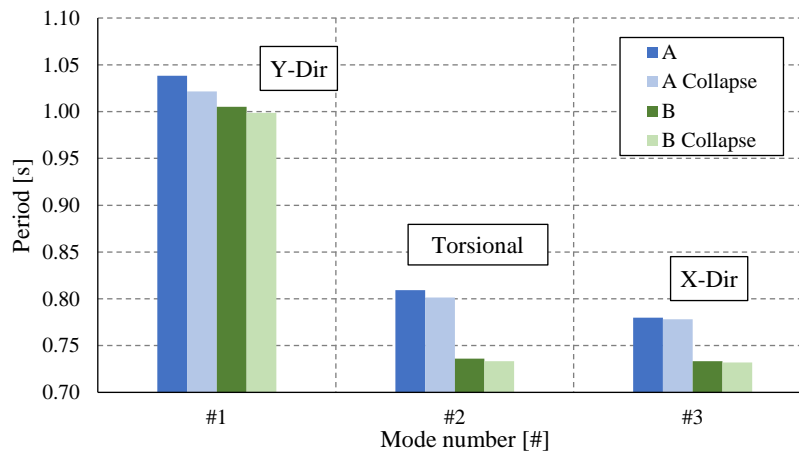
Figure 5-31: Modal periods comparison for Building A and Building B.
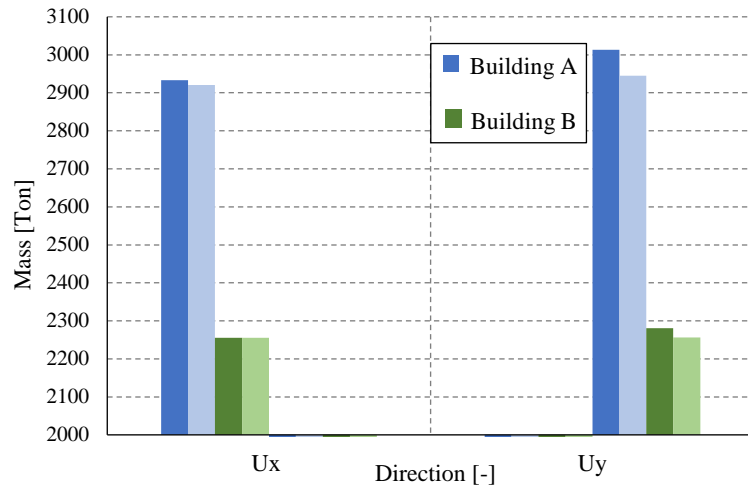
Figure 5-32: Effective mass comparison for Building A and Building B.

6   Linear procedures for structural assessment.

For this section, the structural components of both buildings are checked by using linear procedures describe by the Chilean standards [8] and recommendations of other standards that are meant to be described later. The purpose of this section is to compare the existing structure with the prescriptions of the Chilean code, and the seismic situation of the Maule earthquake. This is to underline the possible reasons for the amount of damage suffered by the structural components from the linear procedures' point of view.

The hypotheses taken to check the structural components are listed below:

- To evaluate the contribution of the wet-joint connection, 2 situations are set; one with beams hinged to the columns and the other one completely clamped. By analyzing both extremes, the average situation can be used as a reference to check the level of stress on the columns.

- To evaluate the beams, both situations described above are taken as a reference to check end-sections and compared it with the damage observed.

As a reference for the structural check, recommendations, and procedures for the analysis are taken from a set of codes that have been preselected and are listed below:

  A. Chilean Standards.

     1. NCh2369-2003 "*Diseño sísmico de estructuras e instalaciones industriales*"

     2. NCh433-1996 "*Diseño sísmico de edificios*"

     3. NCh430- "*Hormigon Armado Diseño*"

     4. NCh1537-2009 "*Diseño estructural – Cargas permanentes y cargas de uso.*"

     5. NCh431-2010 "*Diseño estructural – Cargas de nieve.*"

     6. NCh3171-2010 "*Diseño estructural –Disposiciones generals y combinaciones de carga.*"

  B. United States Standards.

     1. ACI 318-14 "*Building Code Requirements for structural concrete and commentary*".

The methodology to arrive at a conclusion using linear procedures is shown in Figure 6-1. This flowchart is used to exemplify the procedure taken to evaluate the structural elements and each sub-step necessary.
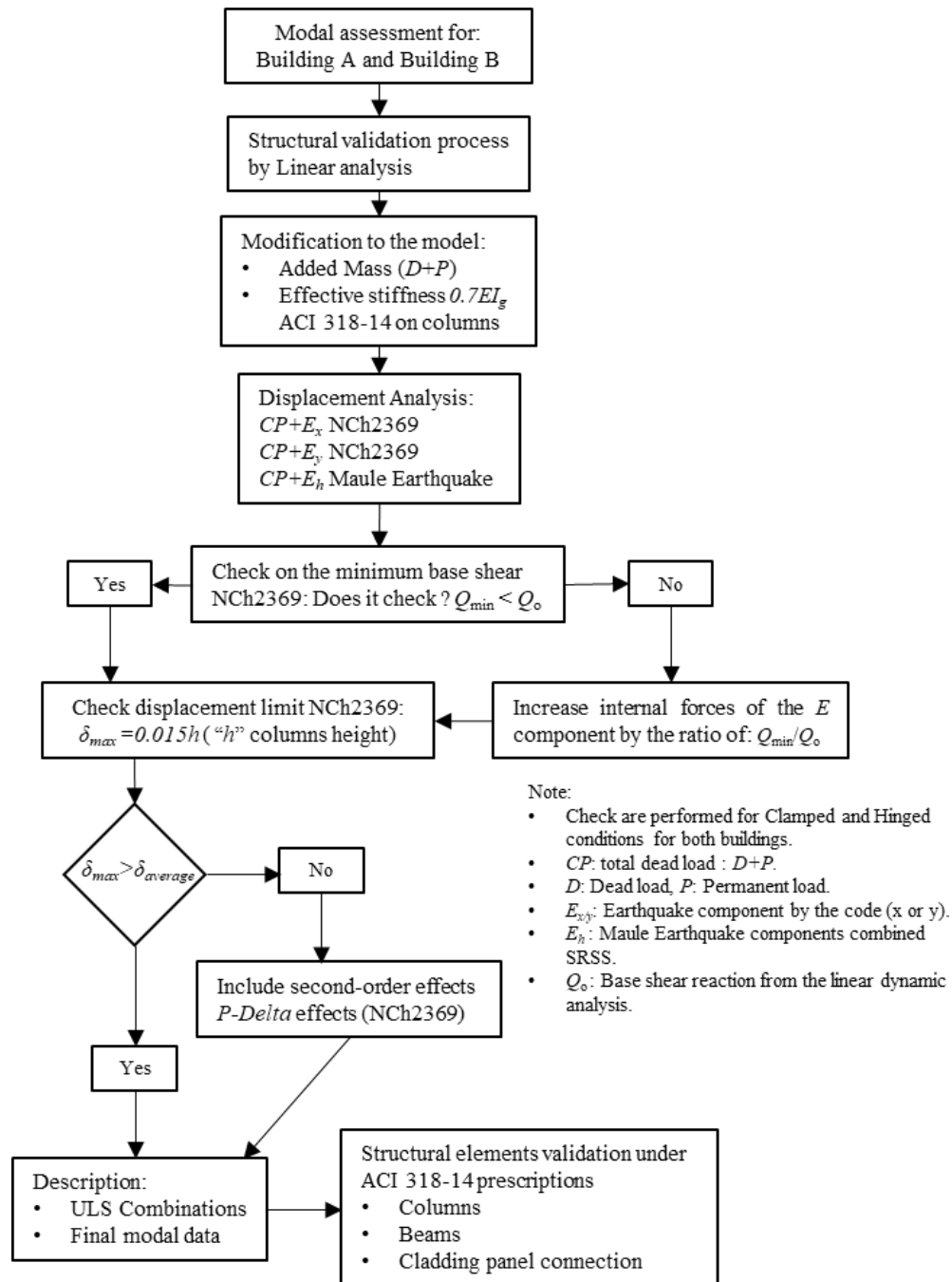
Figure 6-1: Linear procedure scheme flowchart.

6.1   Actions.

In this section, the loads to be used in the analysis are described. These are based on the previous list of standards, details of non-structural elements, and Seismic input of the Maule earthquake.

6.1.1   Code action prescriptions.

The actions prescribed by the Chilean standard are taken from the codes NCh1537-2009 and NCh431-2010. These give information of the roof live load and snow load respectively, whereas the seismic input is given by NCh2369-2003.

6.1.1.1 Dead load (*D*).

The dead load corresponds to the self-weight of the structural elements included in the model. This is automatically computed by SAP2000 and is based on the geometry and material properties of each element, as described in 3.4.

6.1.1.2 Permanent load (*P*).

The permanent load is based on the roof components that are supported by the slabs which essentially are for isolation and sealing, as shown in Figure 6-2.

The load is composed by:

- Logs of treated pines with rectangular sections. These are spanning one meter each and have a specific self-weight of 4.20 kN/m^3 [20].

- Over the slabs lays a ZICALUM smooth sheet which represents a distributed load of 0.04 kN/m^2.

- Under the smooth sheet is an AISLAPOL thermal isolation plate that weighs around 0.3 kN/m^3.
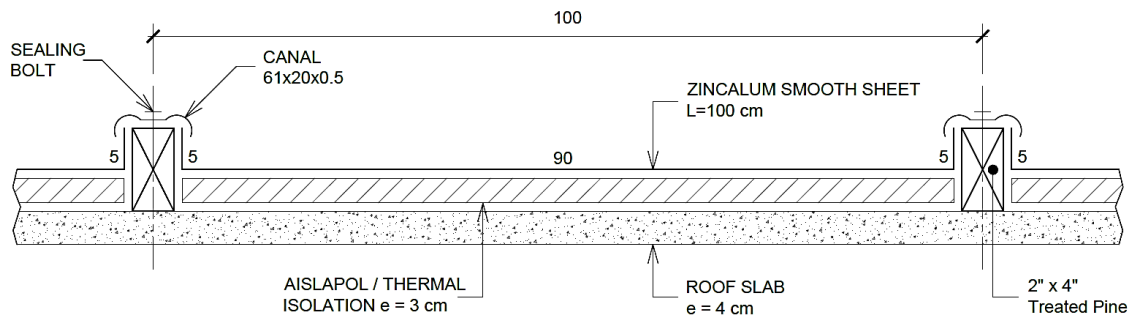
Figure 6-2: Roof thermal isolation and finish detail elevation (units in cm).

With this previous information, a permanent load of 0.07 kN/m^2 is computed and uniformly distributed in the models with an area element capable of transferring these loads to the frame elements.

6.1.1.3 Live load roof (*L_r*).

The roof live load is given by [20] and is equal to 1.00 kN/m^2 for roofs that are only visited for maintenance.

This load shall be reduced by a reduction factor [14] depending on the tribute area of the structural elements and the roof's slope. In this case, the roof's slope is nearly zero and the tributary area of the columns is 240 m^2. Based on this data, from Table 3 in [14] the reduction factor is obtained as 0.60, giving a live roof load of 0.60 kN/m^2.

6.1.1.4 Snow load (*S*).

The snow load is given by the coordinates of the building and its position with respect to the sea level. The coordinates are N 33°19'41.1" S and E 70°42'49.0" W, and the position with respect to the sea level is around 485 m. With these parameters, the snow load is set equal to 0.25 kN/m^2.

Nevertheless, this load is discarded since the live roof load is greater, meaning that it leads the combinations at the Ultimate limit states.

6.1.1.5   Seismic load (*E*).

To build the Horizontal response spectrum given by the Chilean code, a selection of parameters must be made based on the building characteristics, soil condition, and location of the structure. A discussion of this seismic input that is given by the Chilean code is shown in [1].

Some of the characteristics related to the seismic hazard input given by the code for the structure under study are listed below:

- The code gives 3 zones of seismic hazard that are described in [8]. The structure under study belongs to Zone 2 at the Metropolitan zone at Santiago de Chile city, as shown in Figure 6-3.

- The type of soil on which the structure is founded belongs to the category of soil type III.

- The lateral-force resisting system as described by the code gives the ductility demand and damping to be employed. In this case, for both directions, the behavior factor *R* is equal to 3, and the modal damping is equal to 0.05.

The horizontal response spectrum to be used in the analysis by modal superposition is computed throughout Eq.(6-1) and shown in Figure 6-4.

$$S_a = 2.75 * \frac{A_o I}{R} \left(\frac{T'}{T}\right)^n * \left(\frac{0.05}{\xi}\right) \leq IC_{max} \tag{6-1}$$

S_a [g] = is the Pseudo-spectral acceleration component of the design, A_o [g] = effective ground acceleration related to the seismic zone, R = is the ductility factor related to the structural system, ξ = modal damping ratio, T'/n = parameters dependent of the foundation soil.

The pseudo-spectral acceleration must not be greater than the product of the importance factor *I* and the maximum seismic coefficient (C_{max}) given in *Table 5.7* on [8].

A summary of the parameters related to the Seismic input is shown in Table # 6-1.

Table # 6-1: NCh2369-2003 Seismic Input parameters.

Seismic zone	2
A_o [g]	0.30
Soil type	III
T' [s]	0.62
n [-]	1.80
ξ [-]	0.05
R [-]	3
I [-]	1
C_{max} [g]	0.21
P Building A [kN]	28274
P Building B [kN]	21447
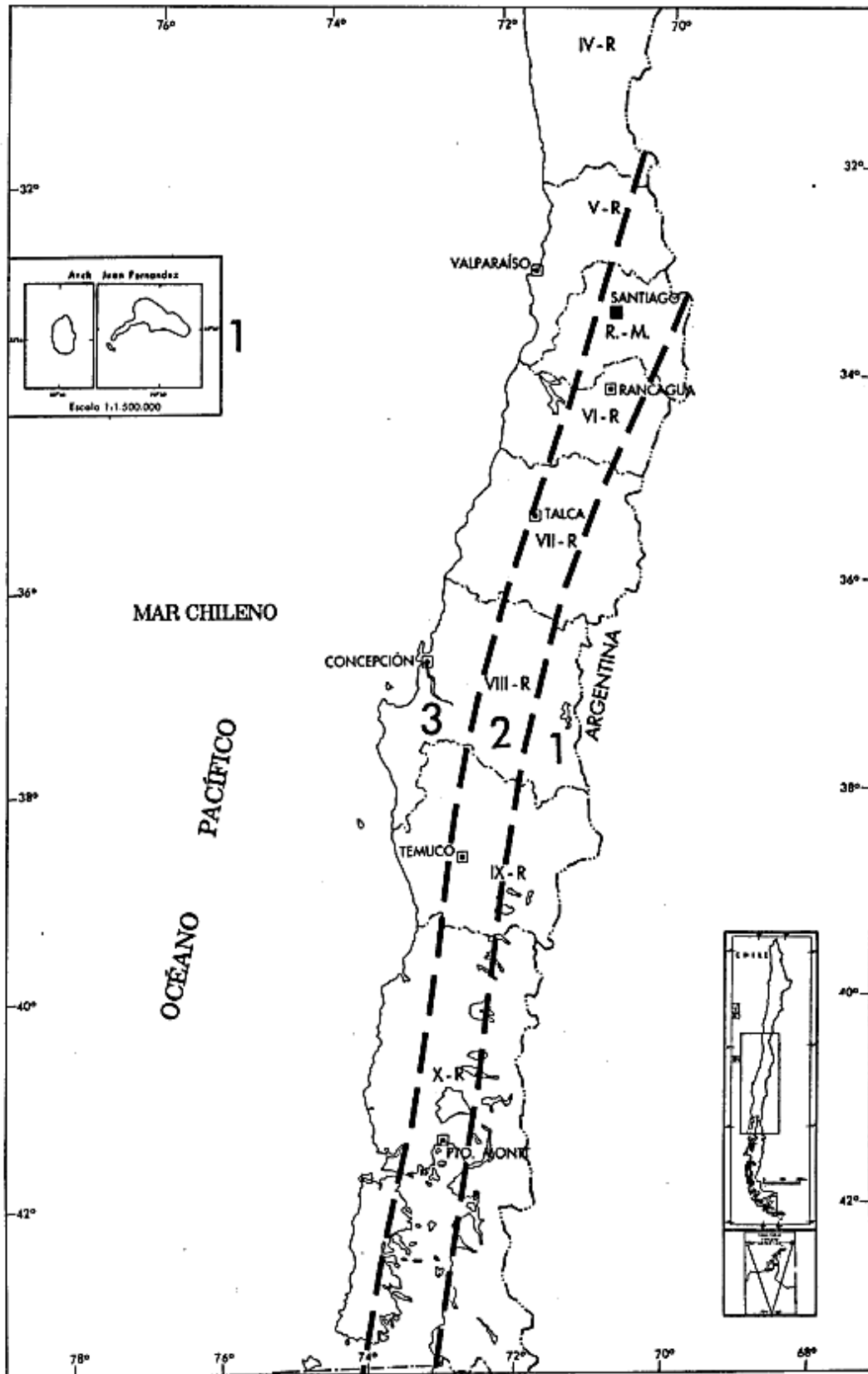
Figure 6-3: Seismic hazard zonification [8].
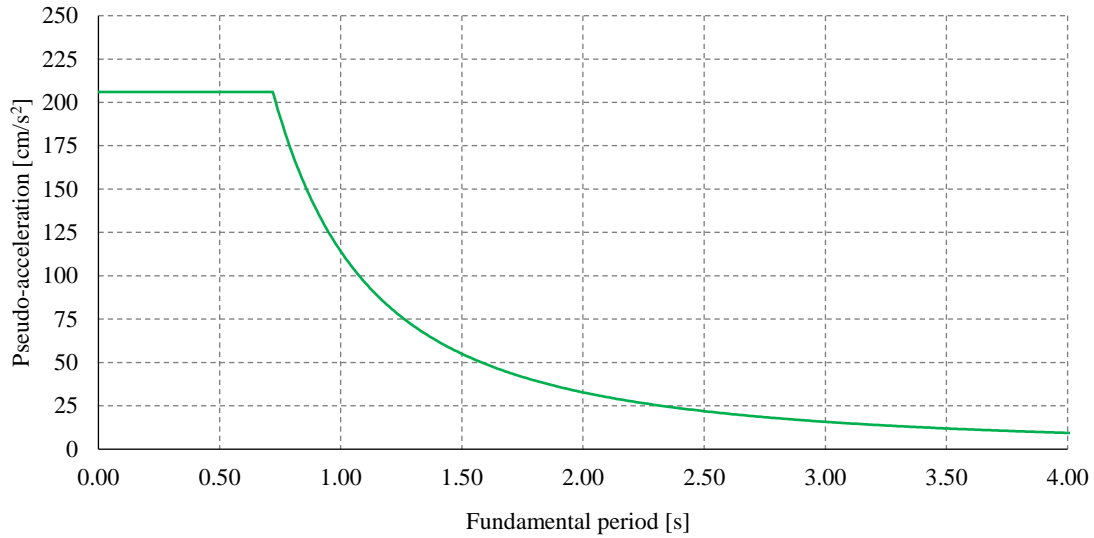
Figure 6-4: Horizontal component of seismic hazard from [8].

Furthermore, the code prescribes a vertical component to include only when the structural elements are prestressed, as it is for the case of study which has the precast prestressed beams. The vertical response spectrum component is computed through Eq.(6-1), but with a structural damping ratio equal to 0.03 and a behavior factor R equal to 3.

The limit value of the pseudo-spectral acceleration for this case changes and it is shown in Eq.(6-2).

$$S_a \leq IA_o \tag{6-2}$$

The vertical component of the seismic hazard prescribed by the Chilean code is shown in Figure 6-5.
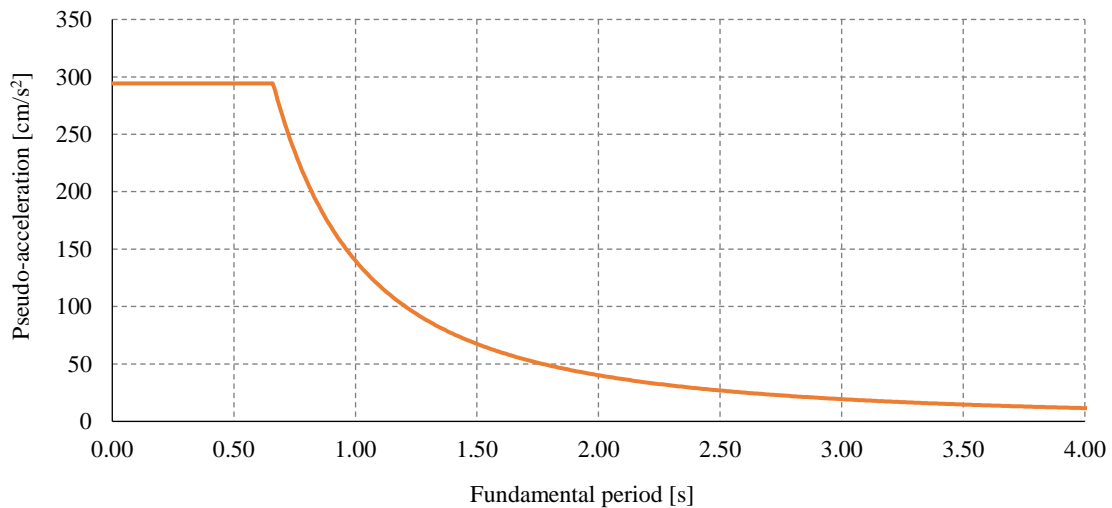
Figure 6-5: Vertical component of seismic hazard from [8].

6.1.2 Seismic loading Maule Earthquake (E).

Using the recorded accelerograms described in Section 2, it is possible to compute the corresponding inelastic response spectrums to assess the structure. As shown in Figure 6-6, the given horizontal components do not coincide with the principal reference system of the building, which is inclined 20° respect to the East in a counterclockwise sense.
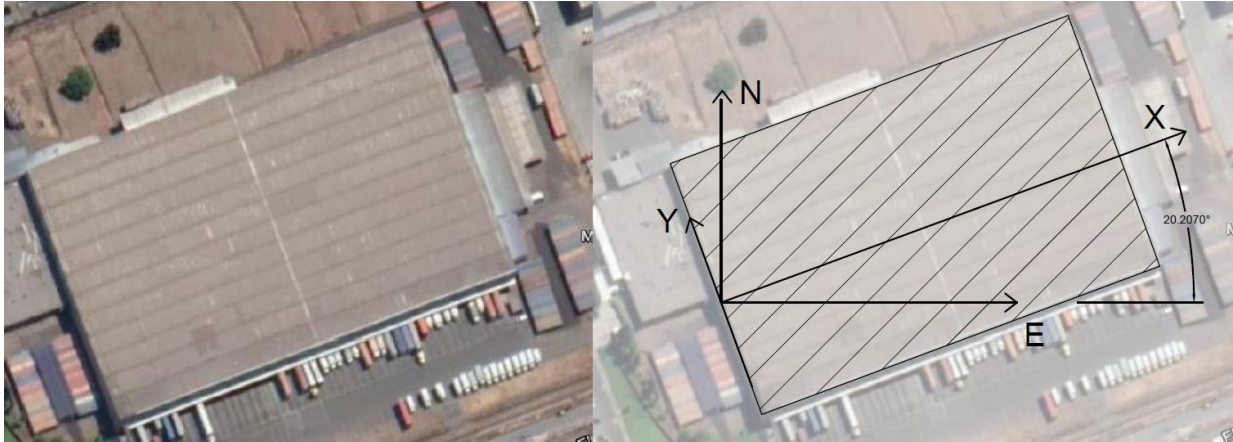
Figure 6-6: Building inclination with respect to the cardinal points.

The global ductility of the building in each direction is prescribed by the Chilean code and is related to the type of lateral-force resisting system. Thus, is necessary to perform a rotation of the horizontal components of the Maule Earthquake to make them coincide with the reference system of the building.

By using the software DEGTRA is possible to make the accelerogram rotation. This is done by giving an angle measured from the North axis in a clockwise sense and two orthogonal horizontal accelerograms. In this case, the angle is 69.793° and the new rotated components can be computed throughout Eq.(6-3) & Eq.(6-4).

$$X = cos(\theta) * N + sen(\theta) * E \tag{6-3}$$

$$Y = cos(\theta) * E - sen(\theta) * N \tag{6-4}$$

Where $N =$ is the earthquake component in the North-South direction, $E =$ is the earthquake component in the East-West direction. $\theta =$ is the angle measured from the North.

Afterward, the accelerograms are ready to be used to compute the inelastic response spectrum. the X, Y, and Vertical Maule Earthquake components, where accelerograms are shown in Figure 6-7, Figure 6-8, and Figure 6-9, respectively.
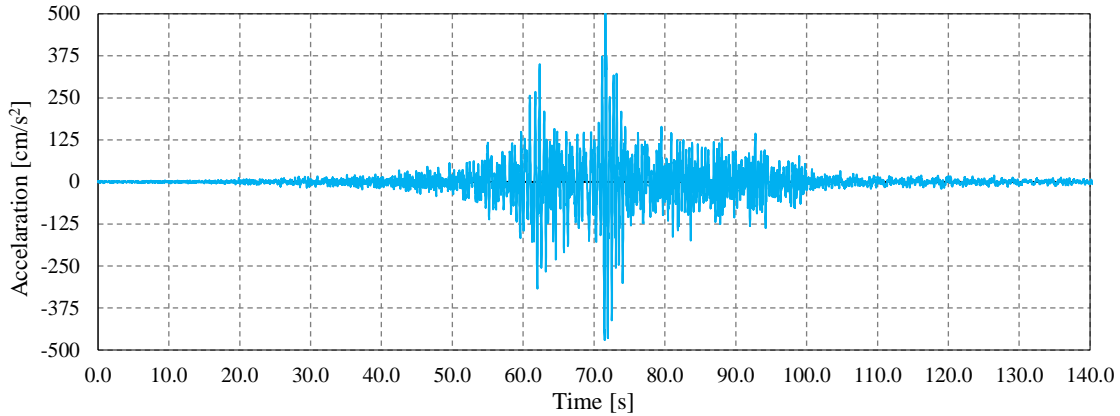
Figure 6-7: X direction Maule Earthquake component.
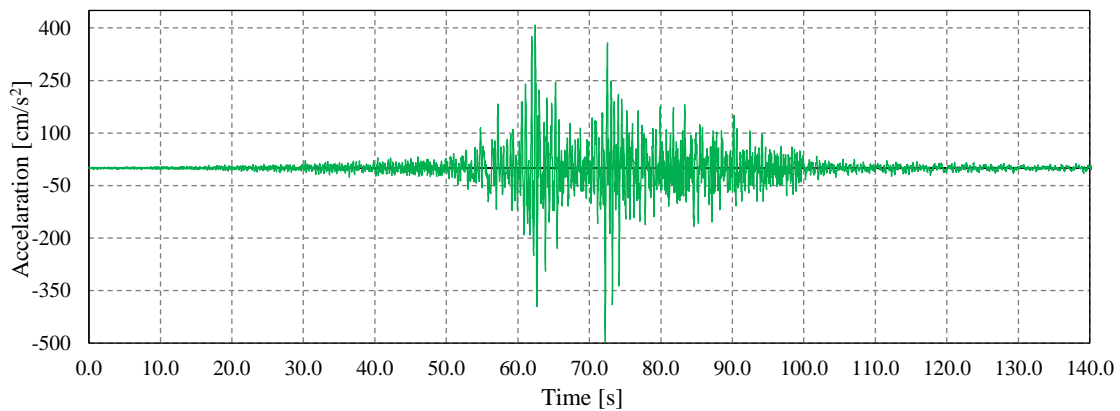
Figure 6-8: Direction Y Maule Earthquake component.
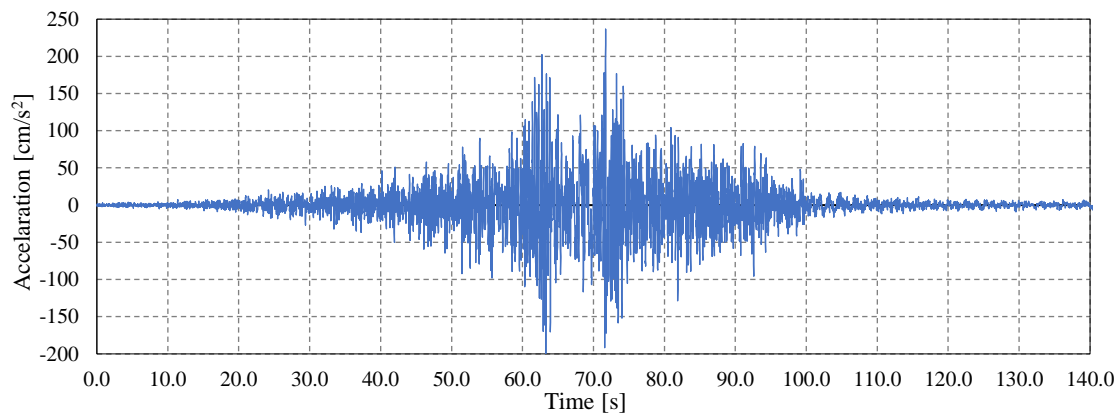
Figure 6-9: Vertical Maule Earthquake component.

The software DEGTRA is used for the computation of the inelastic response spectrums by looking at the response of a single degree of freedom subjected to a selected accelerogram.

The program computes the response spectrum for a chosen hysteretic model and constant ductility. The constant ductility is shown in Table # 6-1 and it refers to the behavior factor of each lateral-force resisting system of the building. The hysteretic model is based on the work [21] which makes a modification to the Takeda hysteretic model taking into account pinching, stiffness degradation, and strength reduction proper of R/C structures subjected to strong earthquake motions.

The response spectrums for the three components to be used in the analysis are shown in Figure 6-10.

47
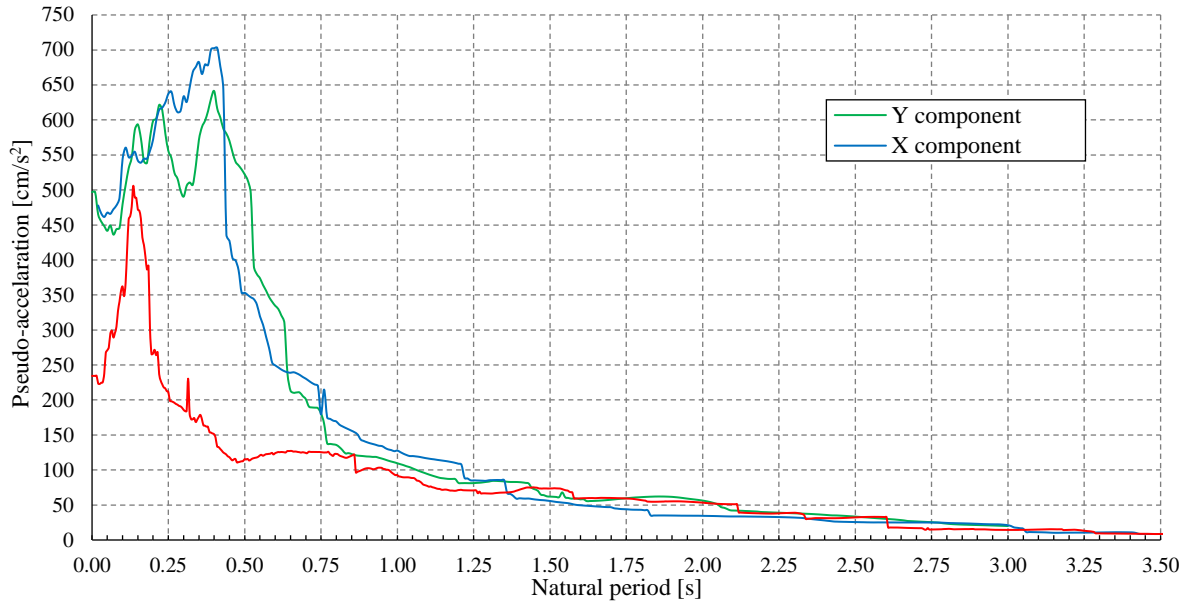
Figure 6-10: Inelastic response spectrum from the Maule Earthquake based on [21].

6.2 Model modifications.

The modifications are performed to the models that were used to study the cladding panel modeling. They are necessary to assess the structure at the Ultimate limit state in an implicit way by using linear analysis.

The first one is related to the mass coming from the permanent load (P) described in 6.1.1.2. This weight is added as a uniform spread load that is automatically distributed by SAP2000 using an Area Element as shown in Figure 6-11.
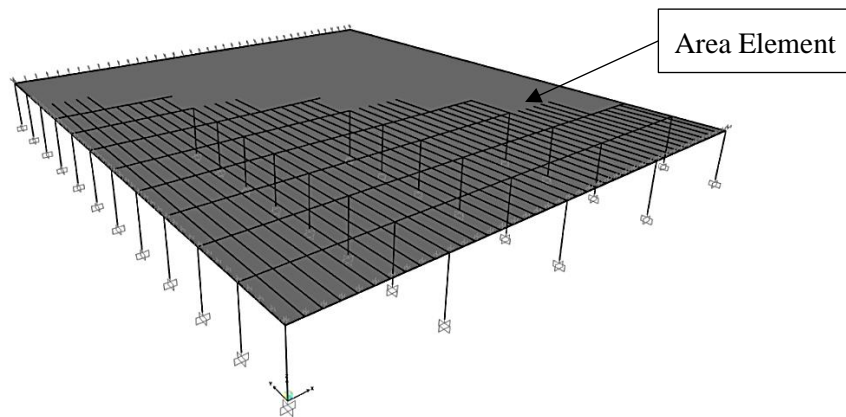
Area Element

Figure 6-11: SAP2000 3D view of Area element example.

Furthermore, the Chilean code [8] prescribes in its *Section 5.1.3* that to compute the inertia forces coming from the seismic input a percentage of the mass coming from the live load must be considered. For a warehouse, the factor to multiply the live load is the following:

- Roof, platforms, and industrial walkway the factor is 0.

48

- For Storage rooms, the factor is 0.5.

Therefore, since the only live load is on the roof, it is not included in the seismic mass to compute the inertia forces. The new values of masses to be used on analysis are shown in Table # 6-2.

Table # 6-2: Modelled mass in each principal direction adding the Permanent Load.

Structural element.	Building A			Building B		
	Mass X [Ton]	Mass Y [Ton]	Mass Z [Ton]	Mass X [Ton]	Mass Y [Ton]	Mass Z [Ton]
Columns	509	509	509	408	408	408
Roof slabs	1526	1526	1526	1140	1140	1140
Beams	756	756	756	561	561	561
Cladding panels X Dir. on axis M	0	93	0	0	70	0
Cladding panels X Dir. on axis B	0	131	0	0	99	0
Cladding panels in Y Dir.	144	0	0	144	0	0
Permanent load *P*	75	75	75	56	56	56
Total mass	3011	3091	2867	2309	2334	2165

The second modification is related to the effective stiffness recommend for the columns. This reduction comes from [11] by implementing a reduction of 30% of the bending stiffness of the columns.

6.3 Displacement analysis.

A displacement analysis is performed to evaluate whether the *P-Delta* effects should be included. The analysis and check of the displacement limits are prescribed by the Chilean code.

The prescribed limit is set equal to 0.015 times *h*, where *h* is the height of the columns that in this case is 9.75 m. The limit is set equal to 15.00 cm that represents both the maximum lateral displacement allowed by the code and threshold to include the *P-Delta* effects.

Furthermore, the code prescribes an equation to compute the lateral displacement coming from the analysis, and it is shown in Eq.(6-5). Further description can be found in section *6.2 & 6.4* in [8].

$$d = d_0 + S_0 * R_1 * d_d \tag{6-5}$$

Where d = is the seismic displacement, d_0 = is the displacement due to services loads non-seismic, R_1 = is the factor that comes from multiplying the behavior factor R by the ratio of Q_o/Q_{min} only if $Q_o/Q_{min} \leq 1$, if not R_1 should be taken equal to R, d_d = is the displacement coming from the seismic input reduced by R, S_0 = Amplification factor for industrial building with columns in cantilever depending on the soil type, in this case, it is set equal to 1.5.

For the displacement analysis, the following combination of loads are used:

- *CP+E*$_{x/y}$ is the combination using the NCh2369-2003 Horizontal response spectrum components in X and Y separately.

- *CP+E*$_h$ is the combination using the Maule Earthquake Horizontal response spectrum components acting simultaneously using the Square Root of Sums of the Square (SRSS) Rule.

After performing the analysis, the base shear reaction (Q_o) obtained by the horizontal components using a dynamic analysis must not be less than the minimum base shear computed throughout Eq.(6-6). If this condition is not fulfilled, all internal forces must be increased by the ratio of Q_{min}/Q_o.

$$Q_{min} = 0.25 * \frac{IA_o}{g}P \leq Q_o \qquad (6\text{-}6)$$

Where Q_{min} = is the minimum base shear [kN], P = is the seismic weight of the structure [kN].

The minimum base shear reaction for both buildings is shown in Table # 6-3

Table # 6-3: Minimum base shear values.

Building	A [kN]	B [kN]
Q_{min}	2120	1608

The checks on the minimum base shear requested by the Chilean code, previously stated in 6.1.1.5, are shown in Table # 6-4 and Table # 6-5.

Table # 6-4: Base shear verification for Building A.

Seismic Action	Q_{ox} [kN]	Q_{oy} [kN]	Q_{min}/Q_o
Clamped			
E_h	6541	2292	0.31
E_x	5631	2	0.38
E_y	1	2208	0.96
Hinged			
E_h	3743	2290	0.48
E_x	3654	1	0.58
E_y	1	2173	0.98

Table # 6-5: Base shear verification for Building B.

Seismic Action	Q_{ox} [kN]	Q_{oy} [kN]	Q_{min}/Q_o
Clamped			
E_h	5029	1773	0.30
E_x	4310	0	0.37
E_y	0	1758	0.91
Hinged			
E_h	3216	1731	0.44
E_x	3136	0	0.51
E_y	0	1737	0.93

As shown in the previous tables, none of the base shear reactions fall below the minimum required. Hence, the adjustment of the internal forces is skipped.

The models do not include a rigid diaphragm due to the specification given in 3.1.1. Therefore, as a measurement of displacement, the average displacement at the roof level from the joints belonging to the columns is used to make a comparison with the limit set. The comparisons are presented in Table # 6-6 and Table # 6-7.

Table # 6-6: Average displacement for Building A.

Connection model	$CP+E_h$ [m]	$CP+E_x$ [m]	$CP+E_y$ [m]
Hinged	0.18	0.12	0.13
Clamped	0.17	0.10	0.13

Table # 6-7: Average displacement for Building B.

Connection model	$CP+E_h$ [m]	$CP+E_x$ [m]	$CP+E_y$ [m]
Hinged	0.18	0.12	0.13
Clamped	0.17	0.09	0.13

As can be seen in Table # 6-6 and Table # 6-7, The displacements coming from the code's combinations comply with the established limits, whereas the Maule earthquake combination surpasses the threshold by 20%.

Thus, *P-Delta* effects must be included as part of the analysis for the verifications of the structural elements.

6.3.1   Second-order elastic analysis (*P-Delta* effects).

After applying the displacement analysis in each building, the need was found to include the *P-Delta* effects as required by the code. SAP2000 [16] is capable of considering the geometric nonlinearity in the form of *P-Delta* effects.

The *P-Delta*/*Large-stress* effect occurs when large stresses (forces or moments) are present within a structure. Thus, Equilibrium equations writing for the original and the deformed geometries may differ significantly, even if the deformations are very small.

This is effect is usually known as the second-order geometric effects, and it may be analyzed together with other non-linearities. An example is shown in Figure 6-12.
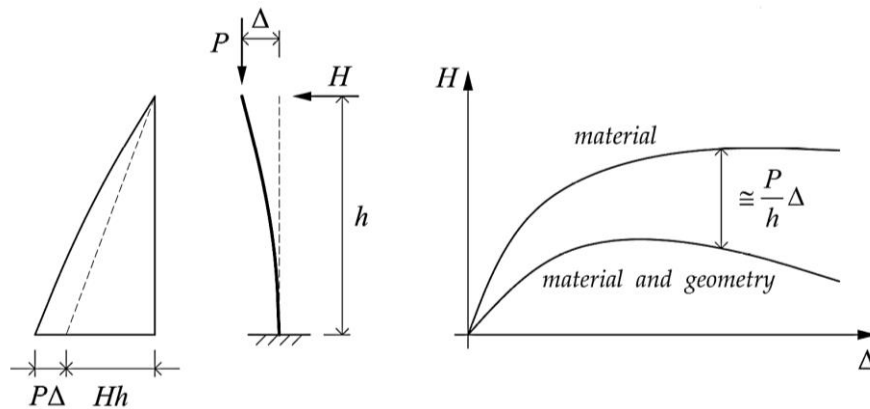
Figure 6-12: *P-Delta* effects on a cantilever frame.

In SAP2000 the equilibrium equations can take into account the *P-Delta*/*Large-stress* effect. The way to implement it is to define a nonlinear static case that takes into account these effects. Once a nonlinear static analysis has been performed, its final stiffness matrix can be used for subsequent linear analysis.

The exact *P-Delta* effects of the axial load upon the transverse deflection and stiffness is a rather complicated function of the ratio of the axial force to the buckling load P_{cr}. The true deflected shape of the frame element and the effect upon the moment diagram is described by specific functions depending on the axial load condition (zero loads, tension, or compression).

SAP2000 integrates along the length of each frame element the *P-Delta* effects, considering the deflection within the element. For this purpose, the transverse deflected shape is assumed to be cubic for bending and linear for shear between the joints of the element. The assumed cubic shape is usually a good approximation to these shapes except under a compressive P-force near the buckling load with certain end restraints. The geometric matrix can be computed throughout Eq.(6-7).

$$K_G = \int_0^l N(x)G^T(x)G(x)dx \qquad (6-7)$$

Where K_G = is the geometric matrix, $N(x)$ = is the *P-Delta* axial force, $G(x)$ = is the shape functions describing the deflected shape assumed.

The *P-Delta* effect of most concern occurs in the columns due to gravity load, including Dead load and live load. The column axial forces are compressive, making the structure more flexible against lateral loads, therefore building codes like ACI recognize two types of *P-Delta* effects:

- The first is due to the overall sway of the structure, which usually is significant, and it can be accounted accurately by considering the total vertical load, as well called *P-Δ*.

- The second is due to the deformation of the member between its ends. This is significant only in very slender columns or columns bent in single curvature, as well called *P-δ*.

SAP2000 does a good job considering the overall sway of the structure (*P-Δ)*, whereas the local effect of the single columns (*P- δ)* is better accounted for by the amplification factors that codes like ACI describe. For analysis, the load combination to be used to account for the *P-Delta* effects is shown in Eq.(6-8):

$$1.2D + 1.2P + 0.5L_r \qquad (6-8)$$

From this load combination, the stiffness matrix is used for subsequent linear analysis for each combination of the loads described previously and combined in section 7.1.

Furthermore, the moment capacity demand for the columns is computed using Eq.(6-9). It takes into account the *P-Delta* effects in separated parts as described before, and then summed them up with the linear combination of this effect as shown in Figure 6-13.

$$M_{CAP} = aM_{nt} + bM_{lt} \qquad (6-9)$$

Where M_{CAP} = is the flexural design capacity required, M_{nt} = Required flexural capacity of the member assuming there is no joint translation of the frame associated with δ, M_{lt} = Required flexural capacity of the member as a result of the lateral translation of the frame only Δ, a = Unitless factor computed by SAP2000 when checking the frame element, b = Unitless factor assumed equal to 1 by SAP2000, thus *P-Delta* effects must be considered to computed M_{lt}.
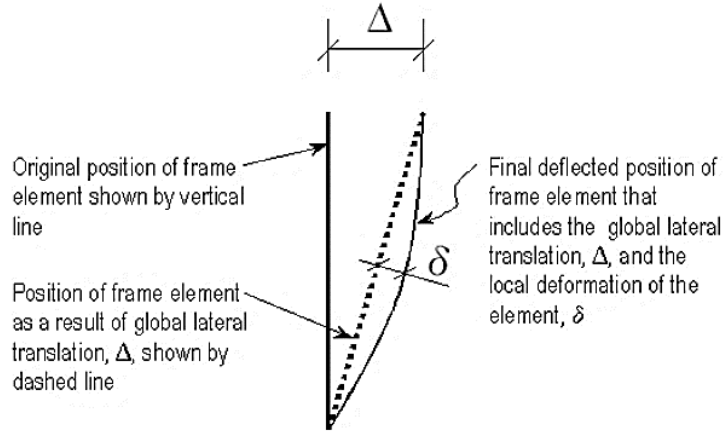
Figure 6-13: Total second-order *P-Delta* effects on a frame element caused by both $\varDelta$ and δ [22] .

6.4   Modal information.

The modal information is extracted after the modifications to the models described in 6.2 were included, and is shown in Table # 6-8 and Table # 6-9. This data is used to perform the response spectrum analysis by modal superposition.

Table # 6-8: Building A modal Data information.

Clamped				
Mode	T	U_x	U_y	R_z
[#]	[s]	[%]	[%]	[%]
1	1.240	0.00%	92.06%	0.01%
2	0.798	0.00%	0.00%	75.89%
7	0.641	93.46%	0.00%	0.00%
Hinged				
1	1.285	0.00%	99.30%	0.01%
2	0.974	0.01%	0.01%	94.23%
3	0.927	97.92%	0.00%	0.01%

Table # 6-9: Building B modal Data information.

Clamped				
Mode	T	U_x	U_y	R_z
[#]	[s]	[%]	[%]	[%]
1	1.205	0.00%	92.00%	0.00%
2	0.696	0.00%	0.00%	82.00%
3	0.631	93.00%	0.00%	0.00%
Hinged				
1	1.213	0.00%	92.00%	0.00%
2	0.848	0.00%	0.00%	87.00%
3	0.845	90.00%	0.00%	0.00%

53

The first three modes of Building A and their pseudo-spectral acceleration comparison are shown in Figure 6-14. It can be appreciated that the first mode that excites the masses in direction Y is not influenced by changing the condition of the wet-joint.

Nevertheless, the modal period in the X direction is greatly influenced by the model of the beam-column connection. The spectral coordinate is increased twice its value from the hinged condition to clamped (1.37 m/s² to 2.50 m/s²). The same goes for the torsional mode that increases its spectral ordinated around 38% with respect to hinged condition to clamped.

The modal data comparison with the response spectrum for the modes belonging to Building B is shown in Figure 6-15. Once again for Direction Y, there is no influence on the spectral ordinates by changing the condition of the wet-joint. Instead, for modal periods in the X direction and Torsional, there is an increase in the spectral ordinate by 100 % and 45% respectively from the hinged condition to clamped.
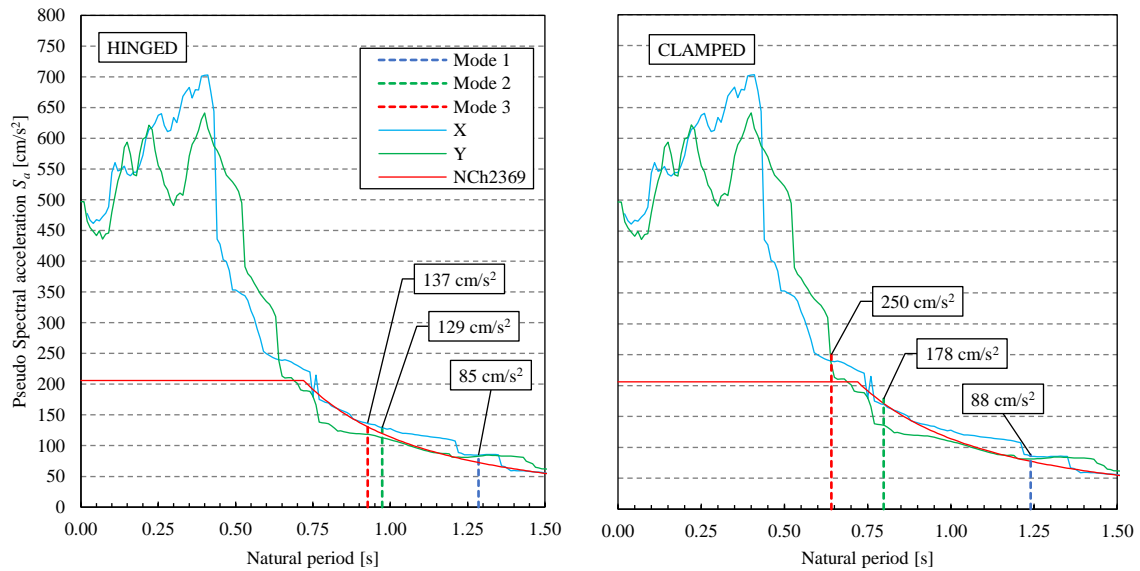
Figure 6-14: Modal data comparison with the response spectrum for Building A.
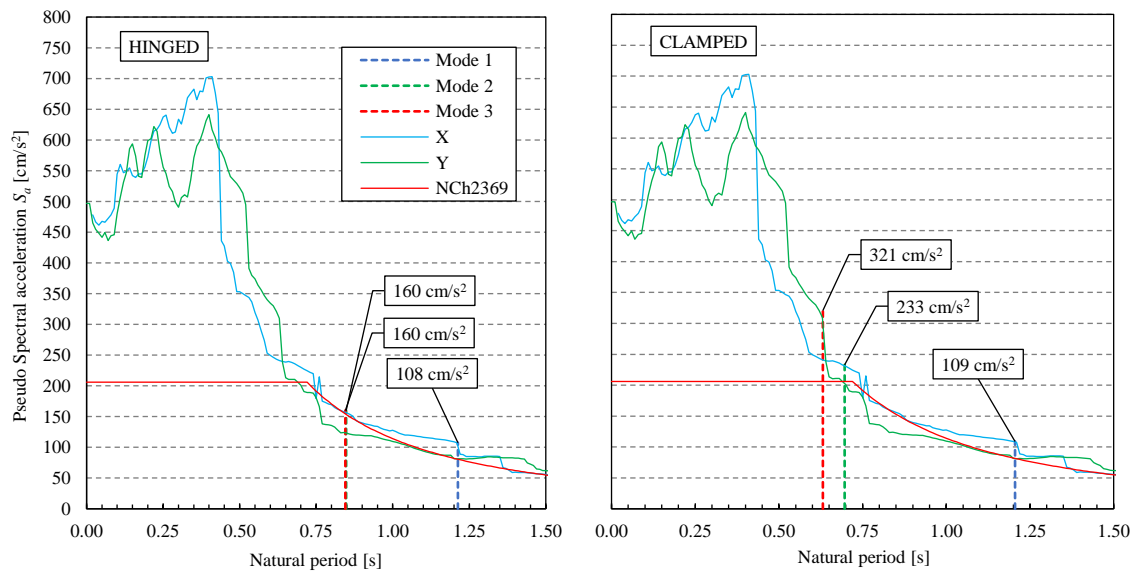
Figure 6-15: Modal data comparison with the response spectrum for Building B.

54

It worth to mention, that for a period equal or larger than 0.71 s, the spectral ordinates of the Maule earthquake components and those related to the Chilean code match, as can be appreciated in Figure 6-14 and Figure 6-15. Thus, the exclusion of a horizontal combination of the components using the Chilean code respond spectrum during the design of the structure might underestimate the excitation of the structure subjected to an earthquake motion.

7   Structural components verification.

The structural elements' verifications are to be described and performed in the following section. The structural verifications are carried out using the specification prescribed by the NCh2369 [8] and ACI 318-14 [11] standards.

7.1   Code Combinations.

To check the structural elements, a set of combinations to verify their strength at the ultimate limit state (ULS) is prescribed by NCh2369 [8] and NCh3171 [23].

    The combinations prescribed by the code include the response spectrum given by [8], in which the seismic action is taken independently in each direction, or better to say, no combination rule of the horizontal components is used.

$$1.4CP$$

$$1.2CP + 1.6\,L_r$$

$$0.9\,CP \pm 1.4E_x \pm 0.3E_v$$

$$1.2CP \pm 1.4E_x \pm 1.4E_v$$

$$0.9\,CP \pm 1.4E_y \pm 0.3E_v$$

$$1.2CP \pm 1.4E_y \pm 1.4E_v$$

    Where CP = is the sums of the Dead load (D) plus the Permanent load (P), E_x = is the horizontal component in the X direction prescribed by the code, E_y = is the horizontal component in direction Y prescribed by the code, E_v = is the vertical component prescribed by the code.

    On the other hand, the following combinations include the response spectrum coming from the Maule Earthquake. In this case, the bidirectional combination of the horizontal seismic components is considered by using the combination rule of SSRS.

$$0.9\,CP \pm 1.4E_h \pm 0.3E_v$$

$$1.2CP \pm 1.4E_h \pm 1.4E_v$$

E_h = are the horizontal components of the Maule earthquake combined using the SRSS.

    In total, the number of combinations to be used to verify the structural elements is 26.

7.2   Demand-Capacity ratio.

For the structural checks is used the so-called Demand-Capacity ratio (D/C). Which in short is the force/moment demand coming from the ULS combination compared against the cross-section strength related to the specific action. A structural element is considered to be safe when the inequality shown in Eq.(7-1) is satisfied.

$$\frac{Demand}{Capacity} = \frac{D}{C} \leq 1.00 \tag{7-1}$$

7.2.1   Strength reduction factors.

To compute the cross-sectional resistance of the structural elements, SAP2000 uses a based design algorithm on the American code ACI 318-14 [11]. Depending on the kind of action to check, a factor Φ is

given, whose values can be found in *Table 21.2.1* on [11]. For summary, the reduction factors to be used are shown in Table # 7-1.

Table # 7-1: Reduction factors for specific actions.

Action on the cross-section	Reduction Factor Φ
Moment, axial force, or combined moment and axial force	0.65 to 0.90
Shear	0.75
Anchors in concrete elements	0.70

For the bending moment, axial force, or combined moment and axial force (P-M-M) the effect of the strength reduction factor Φ varies from compression controlled to tension controlled. The selection of the reduction factor is based on the maximum tensile strain in the reinforcing steel at the extreme edge of the cross-section ε_t.

A cross-section is considered compression controlled when the tensile strain in the extreme tension steel is equal to or less than the compression-controlled strain limit. The compression-controlled strain limit is set equal to the yielding strain of the reinforcing steel.

Sections are tension controlled when the tensile strain in the extreme tension steel is equal to or greater than 0.005. Nevertheless, in the situation in which the tensile strain falls between these two limits, SAP2000 performs an interpolation as shown in Eq.(7-2).

$$\Phi = \begin{cases} \Phi_c & if\ \varepsilon_t \leq \ \varepsilon_y \\ \Phi_t - (\Phi_t - \Phi_c)(\dfrac{0.005 - \varepsilon_t}{0.005 - \varepsilon_y}) & if\ \varepsilon_y \leq \varepsilon_t \leq \ 0.005 \\ \Phi_t & \varepsilon_t \geq 0.005 \end{cases} \tag{7-2}$$

Where Φ_c = is the reduction factor for compression-controlled sections; in this case for transversal ties reinforcement is equal to 0.65. Φ_t = is the reduction factor for tension-controlled sections, set equal to 0.90. ε_t = is the maximum tensile strain in the reinforcing at the extreme edge.

7.2.2   Precast Columns.

Information based on the geometry and reinforcement layout described in 3.4.3 is used to compute the cross-section strength of the columns. These checks are performed for the PMM interaction and the shear strength using the prescriptions of [11], with references to the computations using the SAP2000 recommendations [22].

A summary of the cross-sectional properties and reinforcement detail to be used on the computations is shown in Table # 7-2, And this information corresponds to the details shown in Figure 3-14, Figure 3-15, and Figure 3-16.

Table # 7-2: Columns cross-section characteristics.

Cross-sectional properties	
Clear height h [m]	9.75
Cross section area A_g [m]	0.3416
Second-order moment of Area I_g [m]	0.0223
Reinforcement Details	
Longitudinal reinforcement	
Bars [#]	$12\phi25 + 8\phi22$
Total Rebar area A_l [cm^2]	89
Reinforcement ratio ρ_l [%]	2.61%
Shear reinforcement at first 3.00 m from the base	
legs in X & Y of $\phi8$ [#]	2
Reinforcement Spacing S [cm]	15.00
Total shear area A_v [cm^2]	1.005
A_v /S [cm^2/cm]	0.067

7.2.2.1 PMM interaction

To check the capacity of the columns is necessary to generate axial force-biaxial moment interaction surface as shown in Figure 7-1. This depends on the spatial distribution of the steel reinforcement, geometry of the section, and material properties. SAP2000 allows the user to generate a three-dimensional interaction failure surface to check the capacity of the columns.
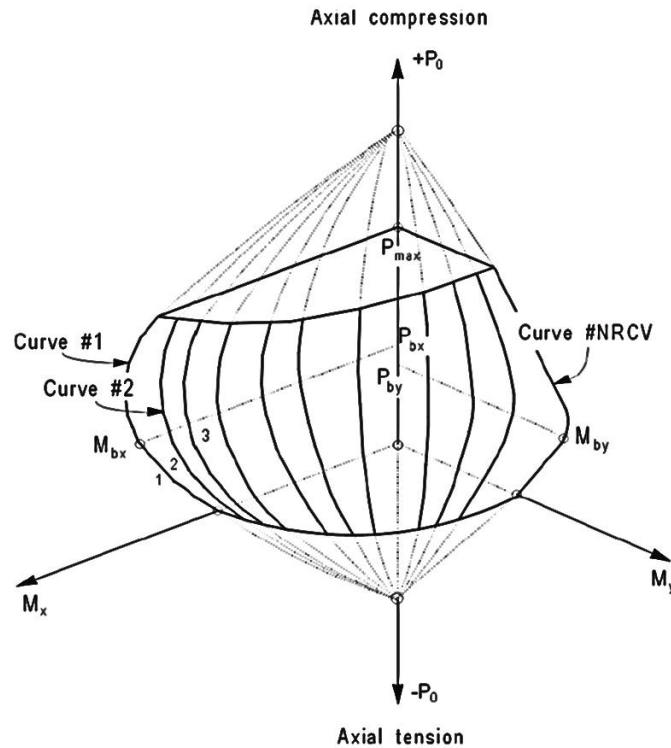
Figure 7-1 : Typical column interaction surface [22].

As shown in Figure 7-2, the coordinates of the points representing the surface are determined by rotating a plane of linear strains in three-dimensions over the section of the column. The linear strain diagram limits the maximum concrete strain ε_c up to 0.003 as prescribed by ACI 318-14 [11], consistently with the general principles of ultimate limit strength design.
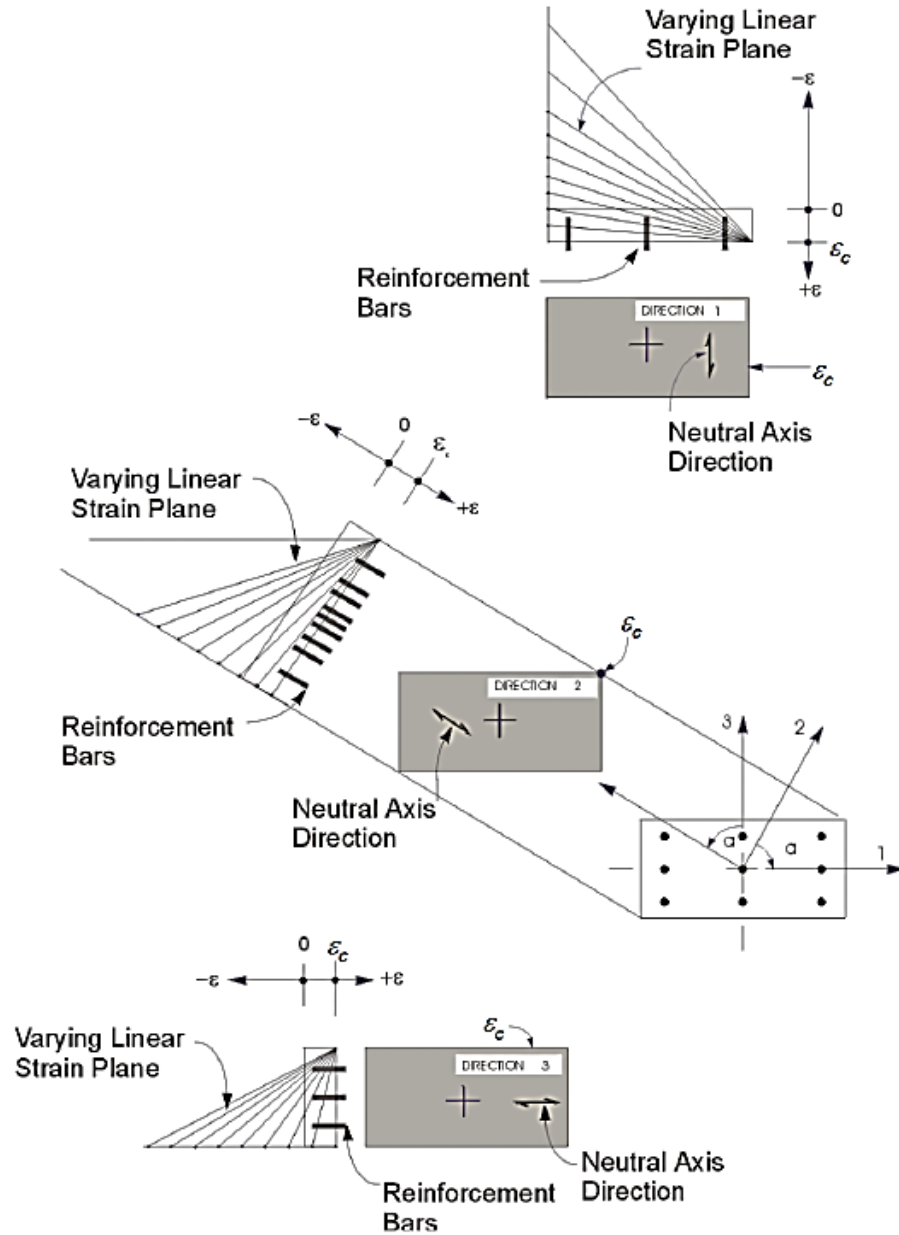
Figure 7-2: Interaction surface scheme computation [22].

The concrete compression stress is given by an equivalent rectangular stress block. The stress is given by $0.85f'_c$ as shown in Figure 7-3. The depth of the equivalent rectangular block is computed as shown in Eq.(7-3).

$$a = \beta_1 c \tag{7-3}$$

Where β_1 = is a factor depending on the range of the compressive strength of the concrete, that in this case is set equal to 0.85, and c= is the depth of the neutral axis measured from the compressive extreme fiber on the section.

Concrete Section   **Strain Diagram**   **Stress Diagram**
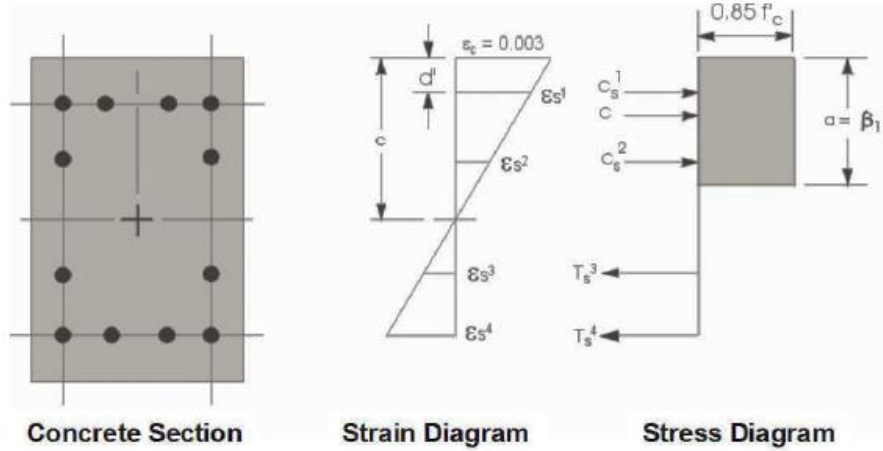
Figure 7-3: Idealization of stress and strain distribution in a column section [22].

ACI 318-14 defines that the maximum compressive axial load must be limited to $P_{n,max}$, that can be computed throughout Eq.(7-4).

$$\phi P_{n,max} = 0.80\phi P_o \tag{7-4}$$

Where Φ = compression controlled reduction factor, that in this case is equal to 0.65.

The expression to compute P_o is shown in Eq.(7-5).

$$P_o = 0.85 f_c'\left(A_g - A_l\right) + f_y A_l \tag{7-5}$$

Where A_g = is the cross-section gross area, A_l = is the longitudinal reinforcement in the section. f'_c = is the compressive stress strength of the concrete, f_y = is the yielding strength of the longitudinal rebar.

Furthermore, the maximum tensile strength that the column can sustain can be computed throughout Eq.(7-6), by considering the concrete contribution being null on tension.

$$\phi P_{nt,max} = \phi f_y A_l \tag{7-6}$$

A summary of these values is shown in Table # 7-3, whereas the interaction diagram is shown in Figure 7-4, which is plotted in the principal axis of the columns section.

Table # 7-3: ACI 318-14 Nominal strength to build the interaction surface.

Compressive strength P_o [kN] [11] (*22.4.2.2*)	12234
Nominal Compressive strength $\phi P_{n,max}$ [kN]	6362
Tension strength P_t [11] [kN] (*22.4.3.1*)	3751
Nominal Tension strength $\phi P_{nt,max}$ [kN]	3376
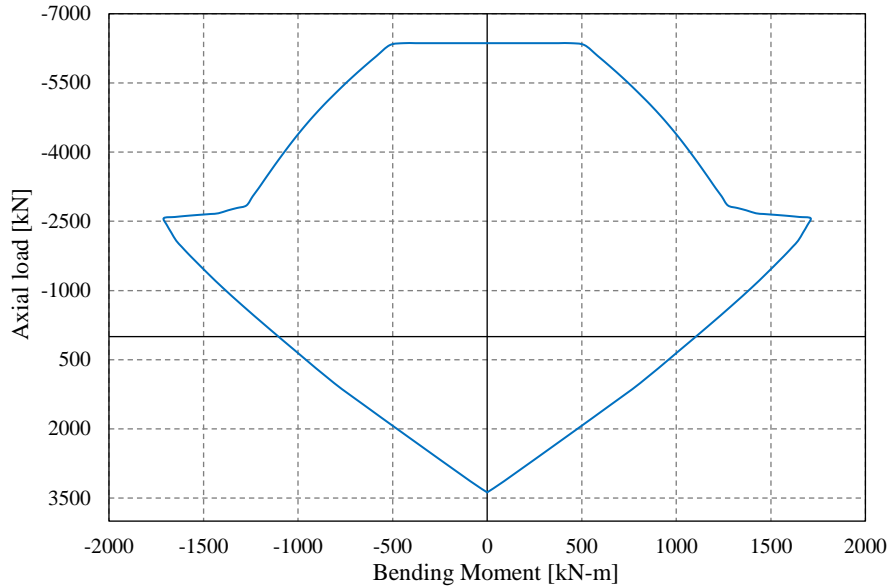
Figure 7-4: Interaction diagram of the column section in the Principal plane axis.

The ULS actions coming from the analysis with the *P-Delta* effects shall be increased using a magnification factor for the moments to consider the *P-δ* for local effects. This magnification factor is computed by the prescriptions given in [11] depending on the columns' slenderness in each direction.

The threshold value to consider further amplification of moments due to the columns' slenderness is shown in Eq.(7-7).

$$\frac{kl}{r} \leq 22 \tag{7-7}$$

Where k = effective length factor, r = radius of gyration in the buckling direction, l = clear length of the columns.

The effective length factor in direction Y for the columns is set equal to 2. As shown in Figure 7-5, the columns do not have any kind of bracing or restraint to reduce the buckling length. Thus, the most probably deformed shape shall be the one related to a cantilever beam, whose effective factor k is equal to 2.00.

Figure 7-5: Buckling length for the columns in the Y direction.

61

For the X direction, the effective factor is computed using the Jackson and Moreland Alignment Charts [11] that provide a graphical determination of k. A summary of the slenderness parameters to consider in the magnification factor's computation is shown in Table # 7-4.

<div align="center">Table # 7-4: Slenderness ratio for the columns.</div>

Free Length l [m]	9.75
Effective length in Direction Y factor k	2.00
Effective length in the X direction factor k	1.10
Radius of gyration r [m]	0.255
Column slenderness the X direction λ [-]	42
Column slenderness the Y direction λ [-]	76

As shown in Eq.(6-9), the M_{CAP} is the moment in one direction to be used for design. To compute the capacity ratio of the columns this moment shall be increased by a factor δ_{ns} to consider the individual column stability effect.

The final moment to be used to compute the capacity ratio is shown in Eq.(7-8):

$$M_U = \delta_{ns}M_{CAP} \tag{7-8}$$

Where δ_{ns} = the non-sway moment magnification factor.

The magnification factor can be computed throughout Eq.(7-9) and Eq.(7-10)

$$\delta_{ns} = \frac{C_m}{1 - \frac{P_u}{0.75P_c}} \tag{7-9}$$

Where C_m = transversal load factor, P_u = is the axial load related to the specific combination considered, P_c = is the Elastic Eulerian critical load.

$$C_m = \begin{cases} 0.6 + 0.4\left(\frac{M_a}{M_b}\right) & \textit{Without transverse load} \\ 1.0 & \textit{With transverse load} \end{cases} \tag{7-10}$$

Where M_a/M_b = is the ratio between the end moments of the columns to consider possible bending in double curvature.

After performing the analysis for each ULS combination, the checks on the columns for P-M-M interaction are automatically done by SAP2000. The combinations having the seismic hazard input coming from the Chilean code [8] can be checked independently in each direction as shown in Figure 7-6 and Figure 7-7.

The fact that the horizontal components are not combined, makes it easier to evaluate the capacity ratio of the columns in each independent direction. This is done by just looking at the P-M plane instead of at the whole surface.
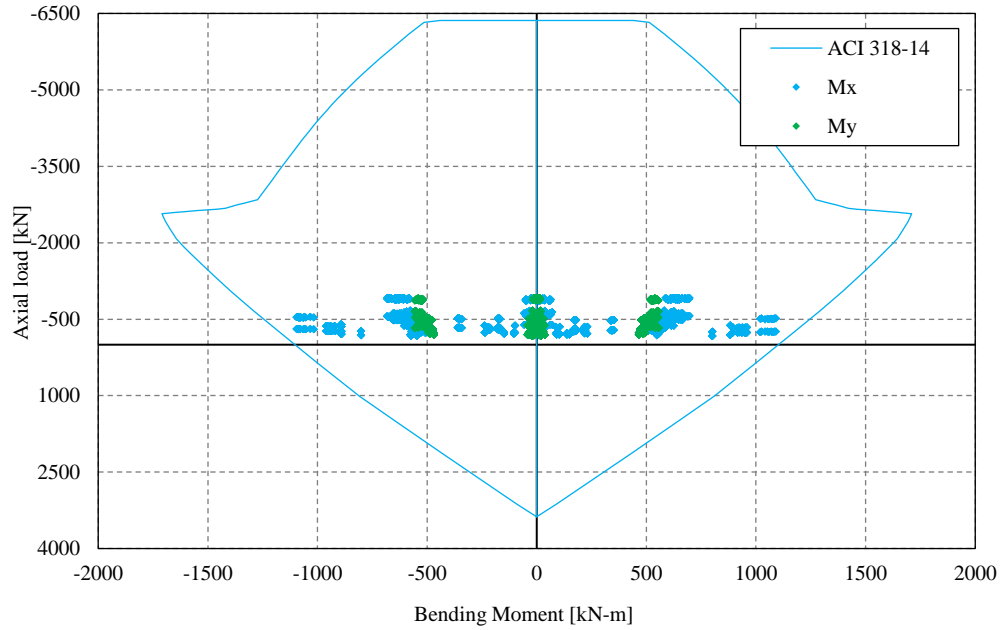
Figure 7-6: PMM interaction diagram for the typical column of Building A with NCh2369-2300 Actions.
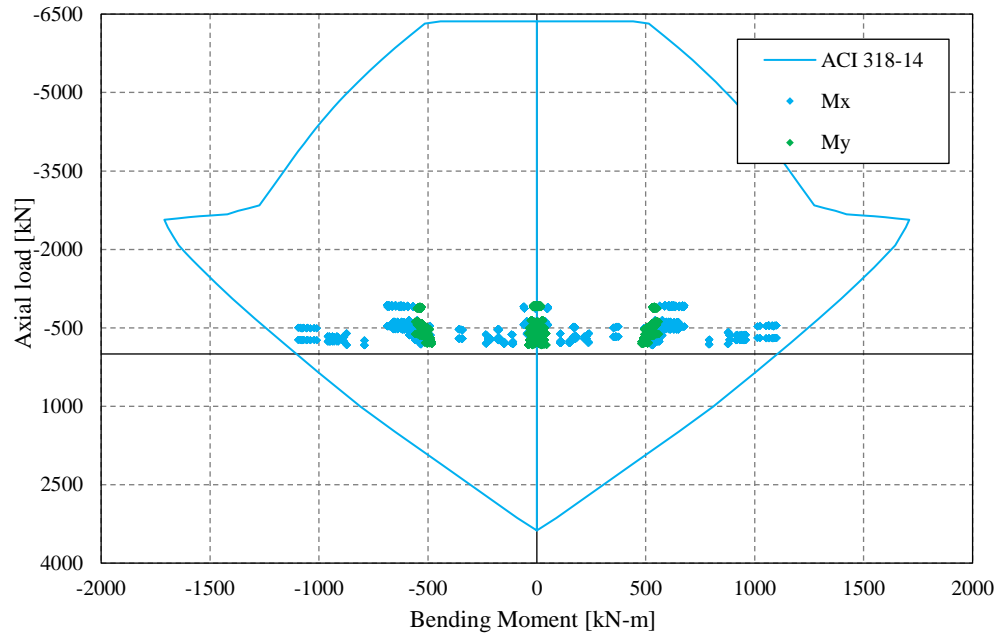
Figure 7-7: PMM interaction diagram for the typical column of Building B with NCh2369-2300 Actions.

As shown previously in Figure 7-6 and Figure 7-7, for both buildings no column becomes unsafe, since all actions coming from the combination code (M_u & P_u) remain inside the P-M interaction curve.

Due to the bidirectional combination of the horizontal components of the Maule Earthquake, the bending moment demand on both directions acting simultaneously on the same column section becomes large. Thus, the check on the capacity ratio becomes complex to evaluate.

63

The geometric interpretation of SAP2000 to intersect the P-M-M surface is shown in Figure 7-8, where the distance of the "Demand point" L from "Capacity point" C is shown.

The capacity ratio is given by the ratio of the distance OL over OC following the rules listed below:

- If OL = OC (capacity ratio equal to 1), the point lies on the interaction surface and the column is stressed to its capacity.

- If OL < OC, (capacity ratio lower than 1), the point lies within the interaction volume and the column capacity is adequate.

- If OL > OC (capacity ratio greater than 1), the point lies outside the interaction volume and the column is overstressed.
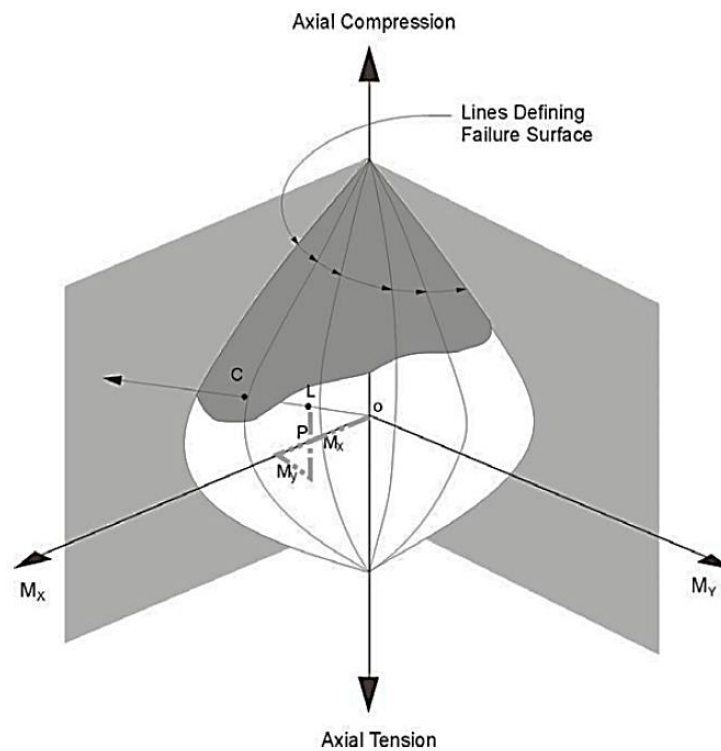
Figure 7-8: Geometric representation of column capacity ratio [22].

A plan view of both buildings is shown in Figure 7-9, showing in each column the capacity ratio of the column for the most severe combination. In this case, this is the combination $1.2CP + 1.4E_h + 1.4E_v$.

Furthermore, having the spatial distribution of the capacity ratio, is possible to divide the building plan into zones, one related to the columns that have the adequate capacity (Safe Zone) and the other in which they are overstressed (Unsafe zone).
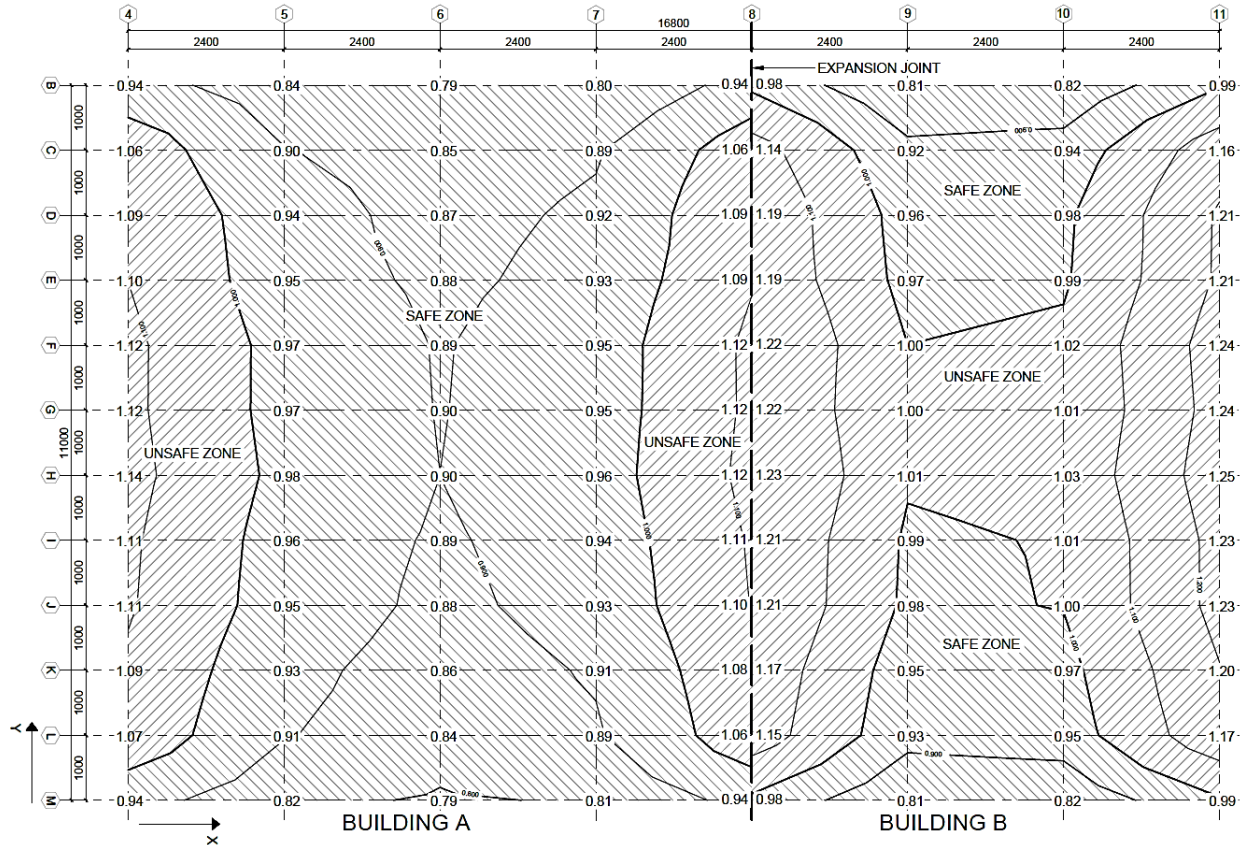
Figure 7-9: Spatial distribution of Capacity ratios for the column under ULS combination with Maule Earthquake (units in cm).

Comparing Figure 7-9 with Figure 4-1, it can be appreciated that the linear analysis was able to capture the failure of the columns' bases that suffered damage at axis 4 and 11. Nevertheless, it seems that it overestimates the demand at the columns located at the expansion joint. During the survey, it came out that no damage was found at the base of those columns.

7.2.2.2 Shear strength.

The shear strength of the column can be computed throughout Eq.(7-11).

$$V_n = V_c + V_s \tag{7-11}$$

Where V_n = nominal total shear strength of the cross-section, V_c = shear strength contribution from concrete, V_s = shear strength contribution from transversal reinforcement.

The shear resistance of the cross-section comes out from the sum of two contributions given by the concrete and by the transversal reinforcement. The concrete shear resistance can be computed throughout Eq.(7-12).

$$V_c = 0.17 * \left(1 + \frac{P_u}{14A_g}\right)\sqrt{f_c'}\,b_w d \tag{7-12}$$

Where P_u = Axial force coming from the same combination of the shear force acting, A_g = gross area of the cross-section, b_w = width of the resistance cross-section, d = Effective depth.

Whereas the contribution coming from the transversal reinforcement can be computed throughout Eq.(7-13).

65

$$V_s = \frac{f_y A_v d}{S} \tag{7-13}$$

A_v = Total transversal reinforcement area. f_y = Yielding strength of the transversal reinforcement. S = transversal reinforcement spacing.

For every ULS combination, the nominal shear strength of the cross-section must satisfy the inequality shown in Eq.(7-14).

$$V_u \leq \phi V_n \tag{7-14}$$

Where V_u = is the shear demand coming from the ULS combination, ϕ= is the shear reduction factor set equal to 0.75.

The most loaded columns and their D/C ratios are shown in Table # 7-5 and Table # 7-6. They were selected by looking separately at the two possible models of the beam-column connection. Regardless of the connection's model, every column complies with Eq.(7-14).

Table # 7-5: Most loaded columns in Shear for Building A.

Column	Combination	Connection Model	P_u [kN]	V_{ux} [kN]	V_{uy} [kN]	N_u/A_g [MPa]	V_c [kN]	V_s [kN]	ϕV_n [kN]	D/C_x [-]	D/C_y [-]
H-8	NCh *1.2CP-1.4E_x-1.4E_v*	Hinged	-295	280	-1	0.9	194	197	293	0.95	0.003
	1.2CP-1.4E_h-1.4E_v	Clamped	-217	241	-60	0.6	191	197	291	0.83	0.210

Table # 7-6: Most loaded columns in Shear for Building B.

Column	Combination	Connection Model	P_u [kN]	V_{ux} [kN]	V_{uy} [kN]	N_u/A_g [MPa]	V_c [kN]	V_s [kN]	ϕV_n [kN]	D/C_x [-]	D/C_y [-]
H-11	NCh *1.2CP-1.4E_x-1.4E_v*	Hinged	-337	289	-1	1.0	195	197	294	0.983	0.003
H-8	*1.2CP-1.4E_h-1.4E_v*	Clamped	-242	-228	-53	0.7	192	197	292	0.782	0.180

7.2.3 Precast Prestressed beams.

The checks that are carried out correspond to the bending and shear strength of the cross-section. By using the information given on the geometry and reinforcement layout described in 3.4.2 it is possible to compute the cross-section strength of the beams. These checks are performed using the prescriptions of [11], with references to the computations using the SAP2000 recommendations [22].

A summary of the cross-sectional properties and reinforcement detail to be used on the computations is shown in Table # 7-2, corresponding to the details shown in Figure 3-11, Figure 3-12, and Figure 3-13.

Table # 7-7: Beams cross-section characteristics.

Parameters	Internal beams	External beams
Top reinforcement [cm^2]	5.53	5.53
Total prestressing area A_p [cm^2]	15.20	10.13
Prestress centroid measured from the bottom [cm]	10.83	7.50
Web width b_w [cm]	10	10
Effective depth to prestressing centroid. d_p [cm]	139	143
Longitudinal reinforcement Ratio ρ_p [%]	0.590%	0.394%

7.2.3.1 Bending strength

The bending strength computation is based on the same assumptions used for the computation of bending strength on the columns, as previously shown in Figure 7-3.

To estimate the positive bending strength is necessary to compute the effective tendon strength given in [11], that can be computed through Eq.(7-23). For the case of negative bending strength, the normal rebar on the top flange is used.

$$f_{ps} = f_{pu}\left\{1 - \frac{\gamma_p}{\beta}\left[\rho_p \frac{f_{pu}}{f_c'}\right]\right\} \tag{7-15}$$

f_{ps} = is the effective tendon strength, f_{pu} = is the rupture tendon strength, γ_p = is the factor depending on the ratio of f_y/f_{pu}. In this case is set equal to 0.28.

For a cross-section to be considered safe, the inequality shown in Eq.(7-16) shall be satisfied.

$$M_u \leq \emptyset M_n \tag{7-16}$$

A summary of the bending strength for both beams is shown in Table # 7-8.

Table # 7-8: Bending strength for the beam.

Parameters	Internal beams	External beams
Effective Strength of tendons f_{ps} [MPa]	1669.	1734
Total tension force $A_p * f_{ps}$ [N]	2537642	1756834
Stress block depth a [mm]	366	98
Positive Bending strength $+M_n$ [kN-m]	2978	2175
Negative Bending strength $-M_n$ [kN-m]	300	300

To check the resistance of the beams in bending, the comparison of their resistance is made against the ULS actions for both seismic inputs. The most loaded beams in positive bending considering both clamped and hinged situations of the wet joint for building A are shown in Table # 7-9 to Table # 7-10.

Table # 7-9: Positive bending demand for combinations of the NCh2369 in Building A.

Beam	Output case	Connection Model	M_u [kN-m]	D/C [-]
D-5-6	NCh 1.2CP-1.4E_{hx}-1.4E_v	Hinged	2660	0.89
D-4-5	NCh 1.2CP-1.4E_{hx}-1.4E_v	Clamped	1402	0.47

Table # 7-10: Positive bending demand for combinations of the Maule Earthquake in Building A.

Beam	Output case	Connection Model	M_u [kN-m]	D/C [-]
D-4-5	1.2CP+1.4E_h+1.4E_v	Hinged	2402	0.81
D-4-5	1.2CP+1.4E_h+1.4E_v	Clamped	1426	0.48

It can be seen in the Tables above, that for the ULS combinations in either clamped or hinged situation the bending positive demand on the beams is successfully satisfied.

Furthermore, when it comes to the negative bending moment actions, only the clamped situation is used for comparison. The most loaded beams in negative bending for Building A are listed in Table # 7-11. It can be appreciated that the demand is almost 8 times the bending resistance. Therefore, this would explain the fact that the beams in the façade (like axis 4) suffered a huge amount of damage.

Hence, to properly capture the real degree of restraint at the connection an explicit model of the connection should be used.

Table # 7-11: Negative bending demand in Building A.

Beam	Output case	M_u [kN-m]	D/C [-]
H-4-5	$1.2CP+1.4E_h\text{-}1.4E_v$	-2331	7.77
H-4-5	NCh $1.2CP\text{-}1.4E_{hx}\text{-}1.4E_v$	-2241	7.47

The most loaded beams in positive bending considering both clamped and hinged situations of the wet joint for Building B are shown in Table # 7-12 to Table # 7-13.

Table # 7-12: Positive bending demand for combinations of the NCh2369 in Building B.

Beam	Output case	Connection Model	M_u [kN-m]	D/C [-]
D-9-10	NCh $1.2CP\text{-}1.4E_{hx}\text{-}1.4E_v$	Hinged	2670	0.90
H-10-11	NCh $1.2CP\text{-}1.4E_{hx}\text{-}1.4E_v$	Clamped	1437	0.48

Table # 7-13: Positive bending demand for combinations of the Maule Earthquake in Building B.

Beam	Output case	Connection Model	M_u [kN-m]	D/C [-]
D-10-11	$1.2CP\text{-}1.4E_h\text{-}1.4E_v$	Hinged	2421	0.81
H-10-11	$1.2CP\text{-}1.4E_h\text{-}1.4E_v$	Clamped	1441	0.48

The most loaded beams in negative bending for building B are shown in Table # 7-14, and it can be appreciated that the demand is almost 8 times the bending resistance. Therefore, this would explain the fact that the beams in the façade (like axis 11) suffered a huge amount of damage.

Table # 7-14: Negative bending demand in Building B.

Beam	Output case	M_u [kN-m]	D/C [-]
H-10-11	$1.2CP\text{-}1.4E_h\text{-}1.4E_v$	-2392	7.97
H-10-11	NCh $1.2CP\text{-}1.4E_{hx}\text{-}1.4E_v$	-2360	7.87

7.2.3.2   Shear strength.

The shear strength of the beams can be computed through Eq.(7-25).

$$V_n = V_c + V_s \tag{7-17}$$

Where $V_n =$ is the nominal total shear strength of the cross-section, $V_c =$ is the shear strength contribution from concrete, $V_s =$ is the shear strength contribution from transversal reinforcement.

For every ULS combination, the nominal shear strength of the cross-section must satisfy the inequality previously shown in Eq.(7-14).

This shear strength of the cross-section comes out from the sum of two contributions given by the concrete and by the transversal reinforcement. The concrete shear resistance shall be the least between Eq.(7-18), Eq.(7-19), and Eq.(7-20) but not less than Eq.(7-21).

$$\left(0.05\sqrt{f_c'} + 4.8 * \frac{V_u d_p}{M_u}\right) b_w d \tag{7-18}$$

$$\left(0.05\sqrt{f_c'} + 4.8\right) b_w d \tag{7-19}$$

$$0.42\sqrt{f_c'} b_w d \tag{7-20}$$

V_u = is the shear demand coming from the ULS combination, M_u = is the bending demand coming from the ULS combination, b_w = width of the resistance cross-section, d = Effective depth, d_p = Effective depth to prestressing centroid. M_u and V_u act simultaneously in the same section.

$$0.17\sqrt{f_c'} b_w d \tag{7-21}$$

The contribution coming from the transversal reinforcement can be computed through Eq.(7-22).

$$V_s = \frac{f_y A_v d}{S} \tag{7-22}$$

A_v = Total transversal reinforcement area. f_y = Yielding strength of the transversal reinforcement. S = transversal reinforcement spacing.

The values corresponding to the computation of the shear strength contribution coming from the concrete are shown in Table # 7-15.

Table # 7-15: Parameters for concrete shear strength contribution.

Parameters	Internal beams	External beams
Effective depth d	145	145
Shear area $A_w = b_w d$ [mm^2]	145000	145000
$V_{c,min}$ Eq.(7-21) [kN]	146	146
V_c Eq.(7-20) [kN]	739	739
V_c Eq.(7-19) [kN]	360	360

The value of Eq.(7-18) is not shown in Table # 7-15 since it depends on the acting shear and bending moment (V_u & M_u) on the specific section under evaluation. The values corresponding to the computation of the shear strength contribution coming from the reinforcing steel are shown in Table # 7-16.

Table # 7-16: Parameters for reinforcing steel shear strength contribution.

Parameters	Internal beams	External beams
Shear area on the web A_v [cm^2]	1.01	1.01
Spacing S [cm]	25	25
Shear steel strength V_s [kN]	245	245

After performing the analysis with the ULS combination, the shear demands are extracted and compared with the shear strength of the beams' cross-section. Since the models of the structure include two ways of modeling the wet joint connection to assess both possible extremes (Hinged and Clamped). It is found that

in the clamped situation every beam's end-section for both buildings (A and B) does not satisfy the inequality shown in Eq.(7-14).

Hence, these results might be a possible statement that the actual rigidity of the connection is closer to the hinged situation. The most loaded beams for the clamped connection are shown in Table # 7-17 and Table # 7-18.

Table # 7-17: Shear demand for Clamped connection in Building A.

Beam	Output case	V_u [kN]	M_u [kN-m]	V_c [kN]	ΦV_n [kN]	D/C [-]
D-7-8	$1.2CP+1.4E_h-1.4E_v$	-445	-2278	233	358	1.240
F-7-8	$1.2CP+1.4E_h-1.4E_v$	-444	-2294	231	357	1.244
H-7-8	$1.2CP+1.4E_h-1.4E_v$	-444	-2298	231	357	1.244
J-7-8	$1.2CP+1.4E_h-1.4E_v$	-443	-2280	232	358	1.238
H-7-8	NCh $1.2CP-1.4E_{hx}-1.4E_v$	-437	-2220	235	360	1.220

Table # 7-18: Shear demand for Clamped connection in Building B.

Beam	Output case	V_u [kN]	M_u [kN-m]	V_c [kN]	ΦV_n [kN]	D/C [-]
H-10-11	$1.2CP-1.4E_h-1.4E_v$	-455	-2392	228	355	1.282
F-10-11	NCh $1.2CP-1.4E_{hx}-1.4E_v$	-454	-2356	231	357	1.272
H-10-11	NCh $1.2CP+1.4E_{hx}-1.4E_v$	-454	-2360	230	356	1.273

Furthermore, the most loaded beams for the hinged situation in both buildings are shown in Table # 7-19 and Table # 7-20. It can be appreciated that for these conditions every beam's end-section for both buildings (A and B) satisfies the inequality shown in Eq.(7-14).

Table # 7-19: Shear demand for Hinged connection in Building A.

Beam	Output case	V_u [kN]	M_u [kN-m]	V_c [kN]	ΦV_n [kN]	D/C [-]
J-4-5	NCh $1.2CP-1.4E_{hx}-1.4E_v$	-437	-1368	354	449	0.972
L-7-8	$1.2CP+1.4E_h-1.4E_v$	438	176	360	454	0.965

Table # 7-20: Shear demand for Hinged connection in Building B.

Beam	Output case	V_u [kN]	M_u [kN-m]	V_c [kN]	ΦV_n [kN]	D/C [-]
D-10-11	NCh $1.2CP-1.4E_{hx}-1.4E_v$	444	212	360	454	0.979
D-10-11	$1.2CP-1.4E_h-1.4E_v$	443	144	360	454	0.975

7.2.4 Connection of the cladding panel.

For the ULS verification of the cladding panels' connection according to [11], the force developed inside the equivalent spring connection will be taken as the ULS action to be compared with the nominal strength of the connection. The nominal strength bond shall satisfy the inequality shown in Eq.(7-23).

$$N_u \leq \Phi N_a \qquad (7\text{-}23)$$

$N_u =$ is the tension force developed in the spring for the ULS combinations, $N_a =$ the nominal bond strength in tension for a single adhesive anchor.

The nominal bond strength in tension for a single adhesive anchor shall be computed through Eq.(7-24).

$$N_a = \frac{A_{Na}}{A_{Nao}} \Psi_{ed,Na} \Psi_{cp,Na} N_{ba} \qquad (7\text{-}24)$$

Where $A_{Na} =$ is the projected influence area of a single adhesive anchor that shall be approximated as a rectilinear area that projects outward a distance C_{Na}, $A_{Nao} =$ is the projected influence area of a single adhesive anchor with an edge distance equal to or greater than C_{Na}. $\Psi_{ed,Na} =$ The modification factor for edge effects, $\Psi_{cp,Na} =$ is the modification factor for adhesive anchors designed for uncracked concrete, in this case, is set 1.00.

C_{Na} can be computed using the following Eq.(7-25).

$$C_{Na} = 10 d_a \sqrt{\frac{\tau_{cr}}{7.6}} \qquad (7\text{-}25)$$

$\tau_{cr} =$ is the characteristic bond stress taken for *Table 17.4.5.2* on [11] set equal to 1.4 MPa. $d_a =$ is the diameter bar.
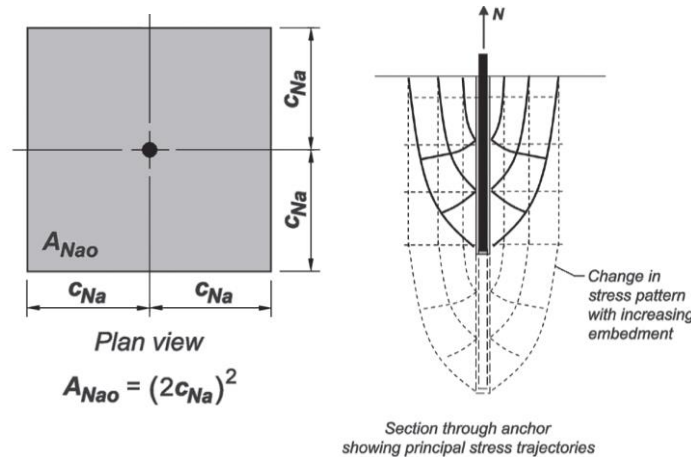
Figure 7-10: Influence area A_{Nao} of a single anchor [11].

The basic bond strength N_{ba} of a single adhesive anchor in tension in cracked concrete shall not exceed Eq.(7-26).

$$N_{ba} = \lambda_a \tau_{cr} \pi d_a h_{ef} \qquad (7\text{-}26)$$

$h_{ef} =$ is the Effective embedded length. $\lambda_a =$ is a reduction factor related to the type of concrete, in this case, is set to 1.00.

The calculation of the parameters related to the basic bond strength and its reduction factor is based on Figure 3-21. The effective length embedded in the concrete is equal to 300 mm and the influence area is

computed assuming a thickness of concrete equal to 10 cm. A summary of the parameters to compute the nominal bond strengths of the cladding panels connection is shown in Table # 7-21.

Table # 7-21: Cladding panels connection resistance parameters.

Strength Reduction Condition B on tension ϕ	0.70
Bonding Stress τ_{cr} [MPa]	1.40
Diameter Bar d_a [mm]	12
Effective length h_{ef} [mm]	300
The basic bond Strength N_{ba} [kN]	13
C_{Na} [mm]	52
Full Strength develop area A_{Nao} [mm^2]	10611
Real influence area A_{Na} [mm^2]	8241
Edge effect factor $\psi_{ed,Na}$ [-]	0.93
The Nominal bond strength N_a [kN]	8.03

The D/C ratios of the cladding panel connections for the three perimeter axes (M, B, and 4) in Building A are shown in Figure 7-11 to Figure 7-13. The D/C ratios showed are those coming from the most severe ULS combinations, which are the combination $1.2CP+1.4E_h-1.4E_v$ from Maule Earthquake and NCh $1.2CP-1.4E_{hy}-1.4E_v$.
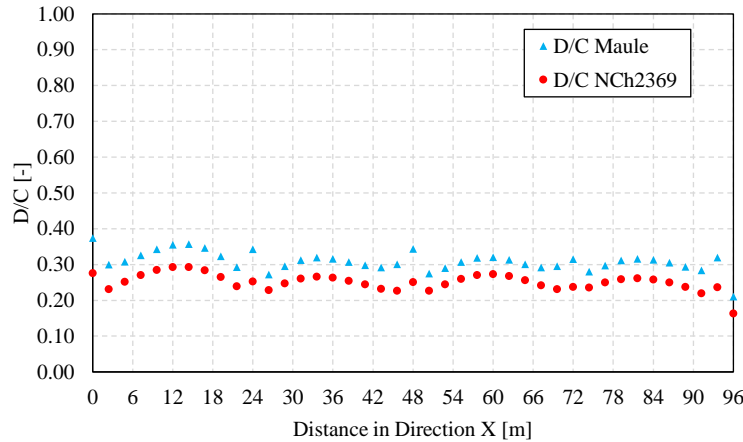
Figure 7-11: D/C for the cladding panel connections on axis M for Building A.
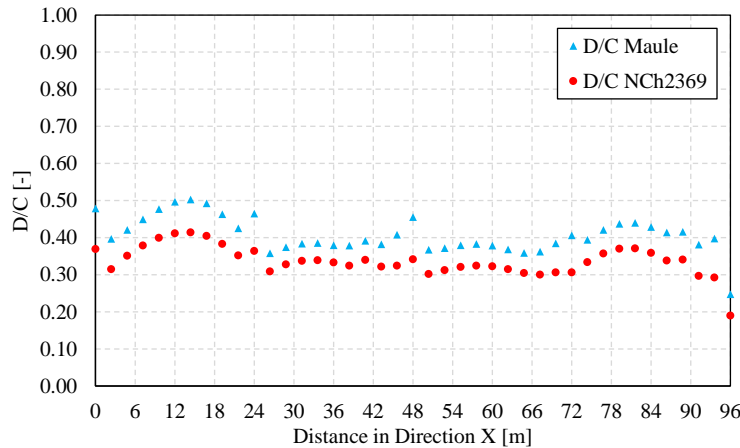
Figure 7-12: D/C for the cladding panel connections on axis B for Building A.
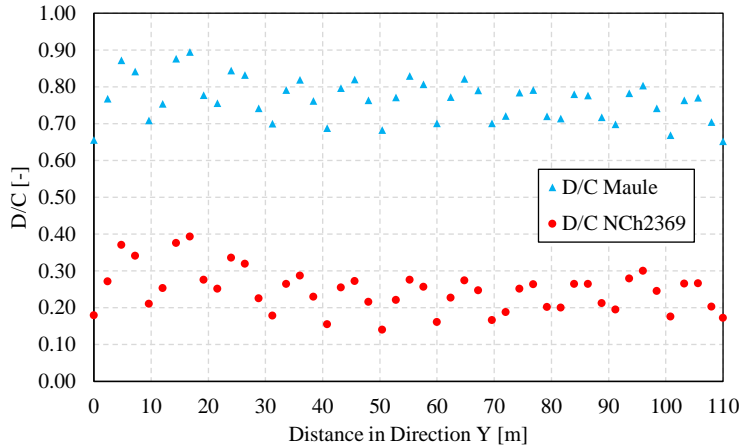
Figure 7-13: D/C for the cladding panel connections on axis 4 for Building A.

It can be appreciated, no cladding panel connection fails for any of the ULS combinations. Furthermore, for those axes aligned in the X direction, the difference between the D/C ratios of the two seismic inputs is small. Whereas, when looking at axis 4, the D/C ratios of the combination coming from the Maule earthquake are three times larger than those coming from NCh2369. The range of the D/C ratios around the perimeter of Building A is shown in Figure 7-14.
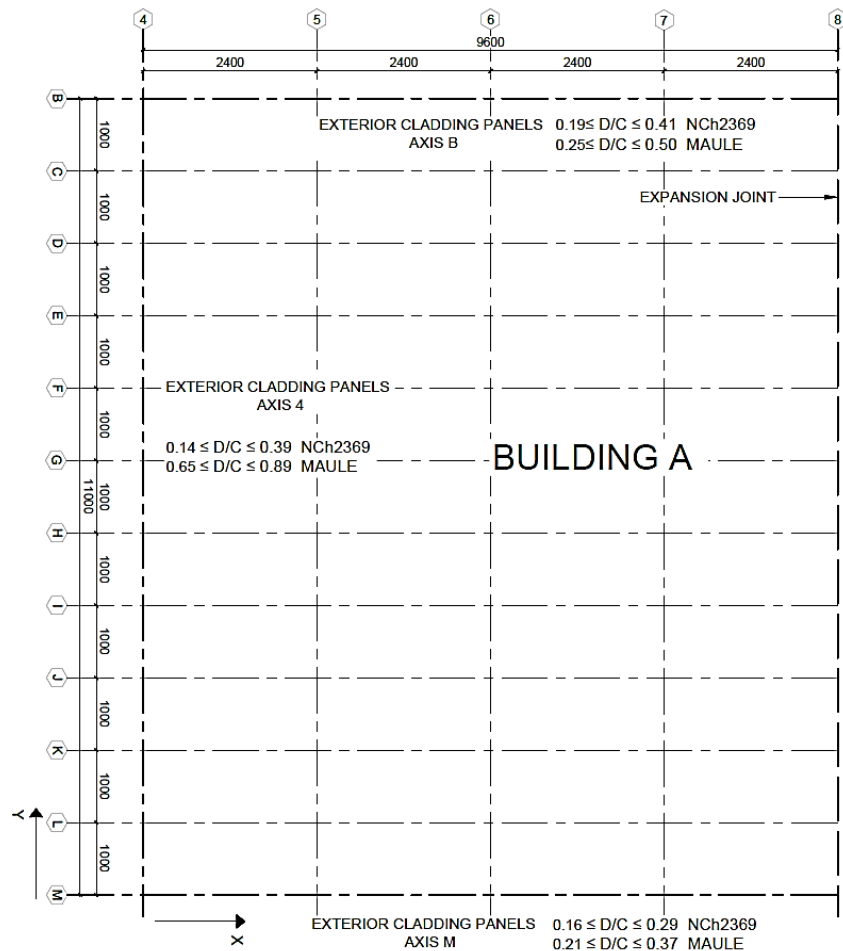
Figure 7-14: D/C Range for the connection of the cladding panels for Building A (units in cm).

73

The D/C ratios of the cladding panel connections for the three perimeter axes (M, B, and 11) in Building B are shown in Figure 7-15, Figure 7-16, and Figure 7-17. The D/C ratios showed are those coming from the most severe ULS combinations, which are the combination $1.2CP+1.4E_h-1.4E_v$ from Maule Earthquake and NCh $1.2CP-1.4E_{hy}-1.4E_v$.
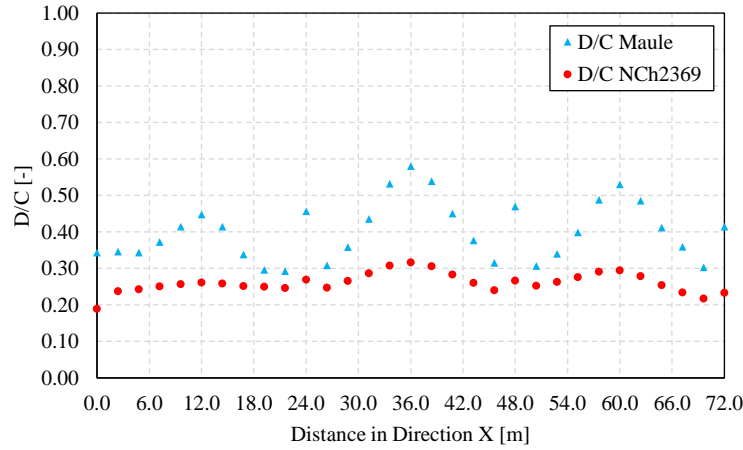
Figure 7-15: D/C for the cladding panel connections on axis M for Building B.
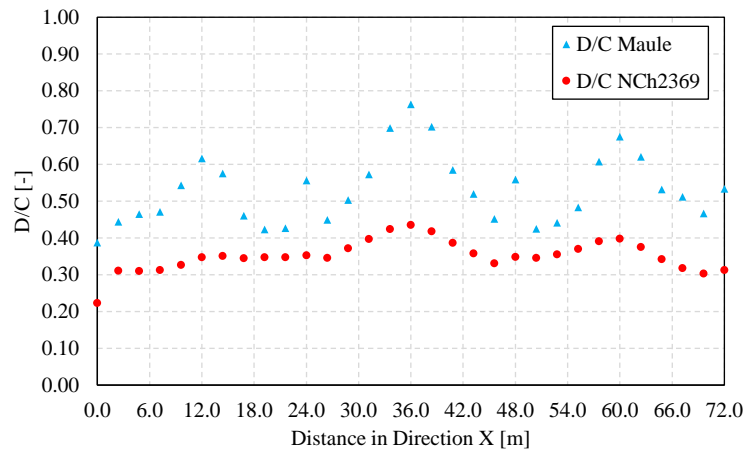
Figure 7-16: D/C for the cladding panel connections on axis B for Building B.
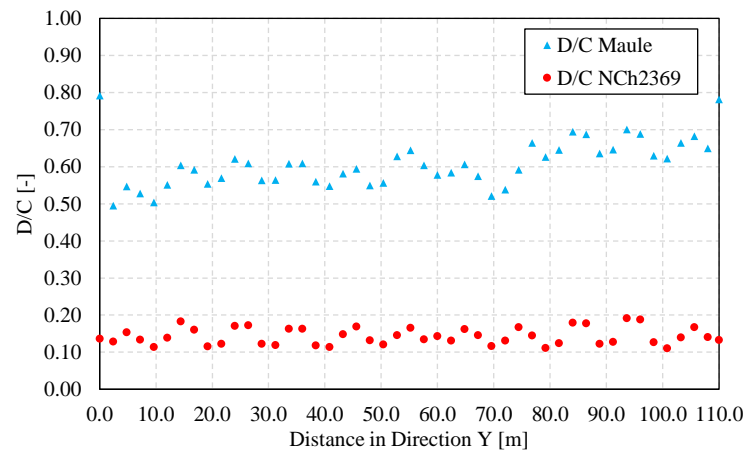
Figure 7-17: D/C for the cladding panel connections on axis 11 for Building B.

As mentioned before for Building A, no cladding panel connection failure is detected for any of the ULS combinations. Furthermore, for those axes aligned in the X direction, the difference between the D/C ratios of the two seismic inputs is small. Whereas when looking at axis 11, the D/C ratios of the combination coming from the Maule earthquake are three times larger than those coming from NCh2369. The range of the D/C ratios around the perimeter of Building B is shown in Figure 7-18.
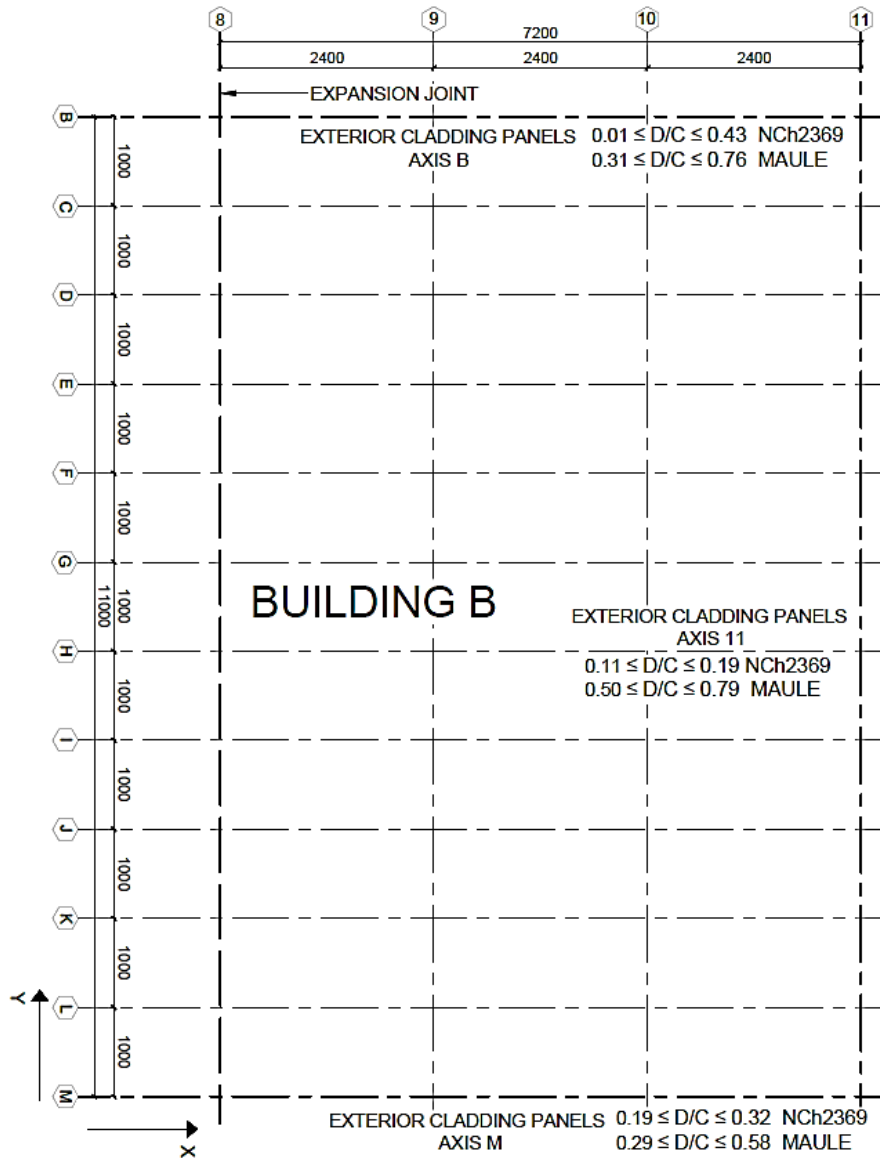
Figure 7-18: D/C Range for the connection of the cladding panels for Building B (units in cm).

8 Plasticity model implementation.

The extension of the analyses into the nonlinear range must be performed properly to capture the damage suffered by the building during the Maule Earthquake. Preliminary to the description of the analyses performed and their results, a sensitivity analysis of the plasticity model included in SAP2000 takes place to understand better its implementation.

8.1 Plasticity model.

For the nonlinear analysis procedures, a plasticity model shall be included to capture yielding and post yielding behavior.

The post-elastic behavior can be employed in SAP2000 by using Fiber hinges with PMM interaction. These are a collection of material points over the cross-section, in which each point represents a tributary area and has its own stress-strain curve. An example of a fiber hinge is shown in Figure 8-1, which is developed to track the plastic properties of every fiber's uniaxial stress-strain relationship in the cross-sections.
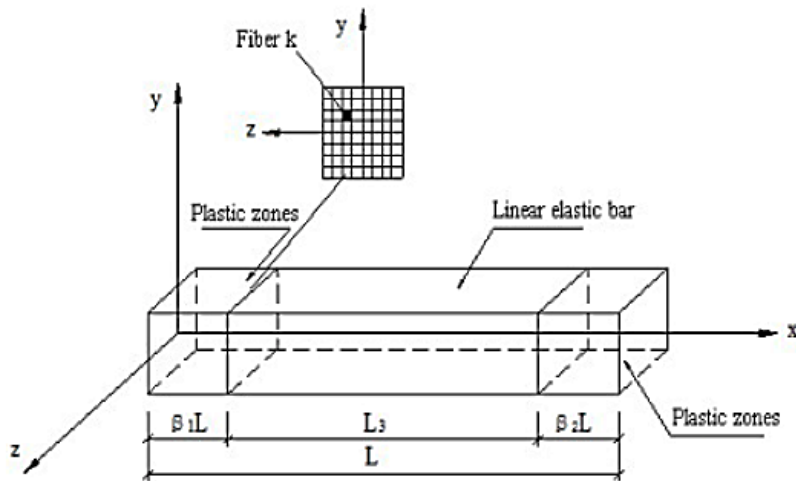
Figure 8-1: A frame element with fiber hinges inside [24].

An additional hypothesis is that plane sections are assumed to remain planar, which ties together the behavior of the material points. Fiber hinges are often more realistic since are based on the actual distribution of materials over the cross-section. Nevertheless, they are more computationally intensive with respect to other plasticity models (lumped plasticity).

Three aspects require attention in applying the fiber hinge models. These include the material constitutive relations given in 5.2, the cross-section division, and the fiber hinge length.

The main reason for using the previously described type of plasticity model is due to the geometrical characteristics and reinforcement layout of the columns. When it comes to the use of lumped plasticity models, these directly describe a force-deformation relation to assess the post-elastic behavior of the structural elements. Many standards like ASCE give acceptance criteria based on experimental results for common column shapes and reinforcement detailing, that for the case of study is not suitable.

8.2   Fiber hinge implementation on SAP2000.

In this section, a summary of how the fiber hinge is implemented in SAP2000 is described. Furthermore, a more detailed description of key aspects like the cross-section division into fibers, and the fiber hinge length is given.

To implement a Hinge property in SAP2000, one shall click on the upper menu on the program interface as follows: Define → Section properties → Hinge properties. Then it is possible to create a new hinge property. For the Fiber hinges type the following steps shall be taken as list below:

- Select the hinge type "*Deformation controlled (ductile)*" and from the drop-list menu choose "*Fiber P-M2-M3*" as shown in Figure 8-2.

- From the new window "*Frame hinge property data for Fiber P-M2-M3*" it is possible to select the fiber hinge length (specified as Relative or Absolute distance), and the fiber layout. The latter one shall be specified as user-defined or default from the frame's cross-section. An example is shown in Figure 8-3.
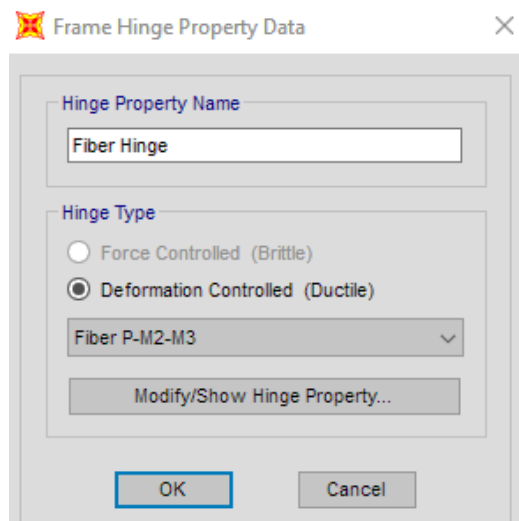
Figure 8-2: Frame Hinge property data window.
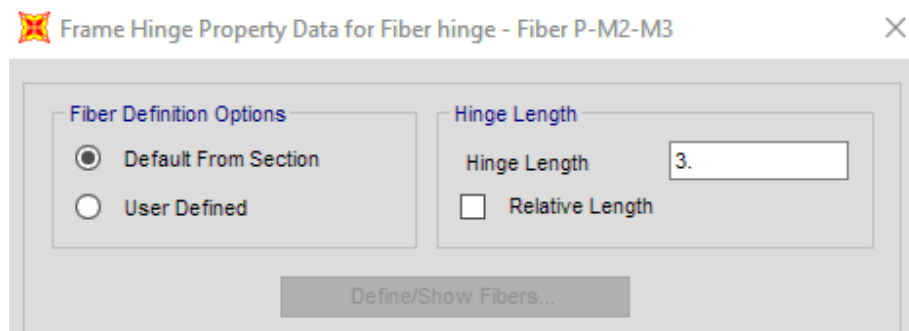
Figure 8-3: Frame hinge property data for Fiber P-M2-M3 window.

To assign a hinge property to a frame element the only information needed is the relative distance along the frame element's length. As shown in Figure 8-4, one must insert the relative distance in which the hinge shall be placed and this distance is always measured from the *end-i* as shown in Figure 8-5. At the location where the hinge is placed the program will evaluate the internal forces and deformations.
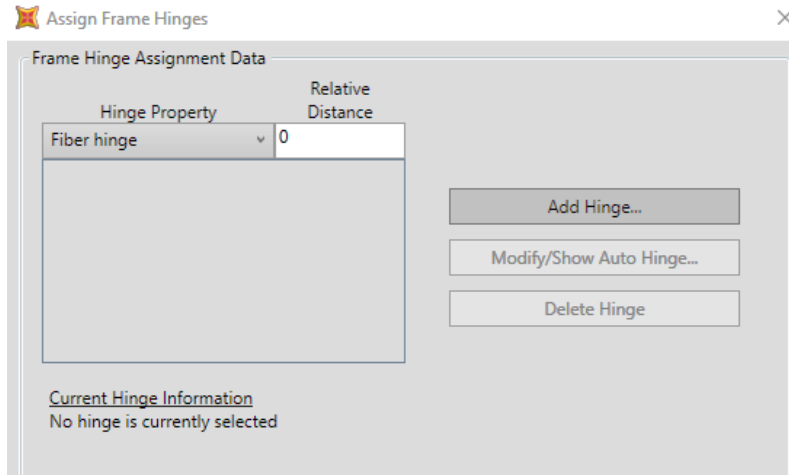
Figure 8-4: Assign Frame hinges window.

A graphical representation of a fiber hinged assigned to a frame element is shown in Figure 8-5.
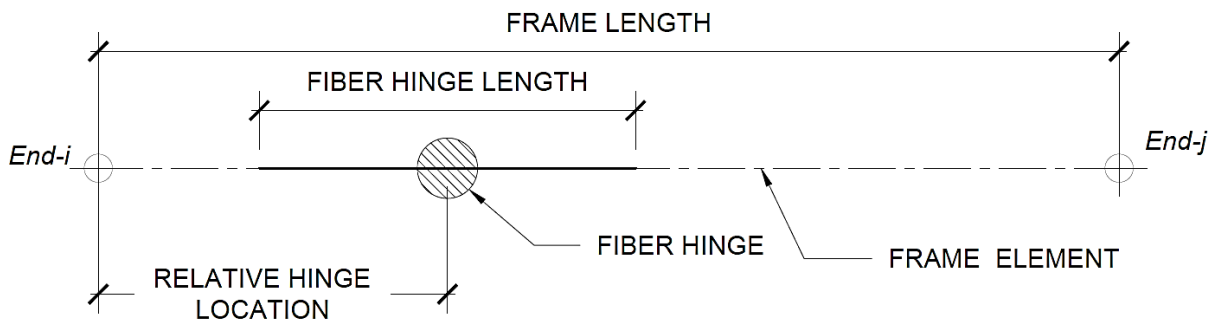
Figure 8-5: Fiber hinge assigning to a frame element.

8.2.1 Moment-Curvature analysis for the columns' sections.

The fiber hinge response at the cross-section level directly depends on the fiber layout. The number of fibers shall be selected to have an accurate description of the moment-curvature response of the columns' cross-section.

Therefore, three fiber layouts of the column's cross-section are presented in Figure 8-6. These are selected to capture the moment-curvature diagram and choose a suitable mesh to balance accuracy and computational efficiency. SAP2000 allows to create a fiber mesh and extract the moment-curvature diagram. This is done by the Section designer module.
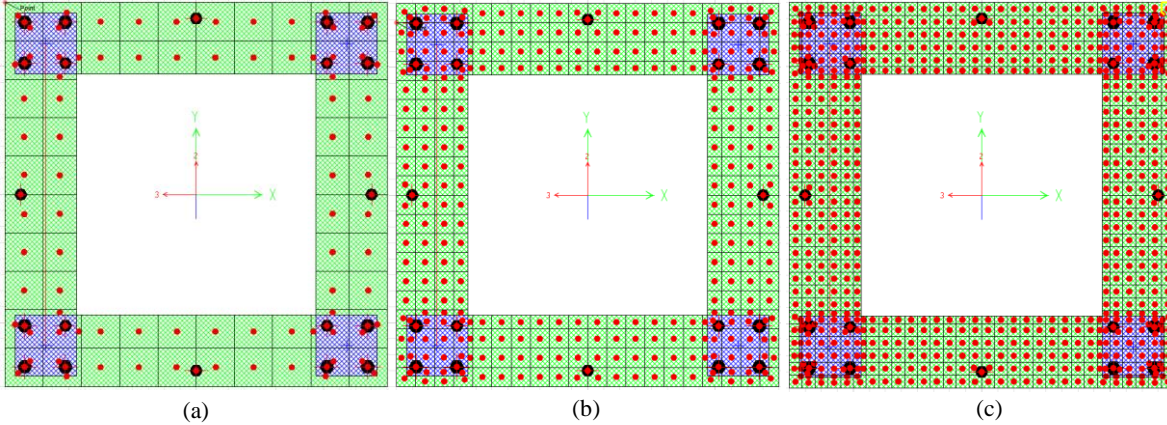
Figure 8-6: (a) Fiber layout mesh of 10x10. (b) Fiber layout mesh of 20x20. (c) Fiber layout mesh of 30x30.

As shown in Figure 8-7, the comparison for the different fiber layouts is presented. It can be appreciated that a mesh 10x10 is too coarse since it overestimates the bending moment strength of the cross-section. The 20x20 mesh and 30x30 mesh's diagrams match perfectly. Thus, for computational efficiency reasons the 20x20 mesh is sufficient to have an accurate moment-curvature response of the cross-section.
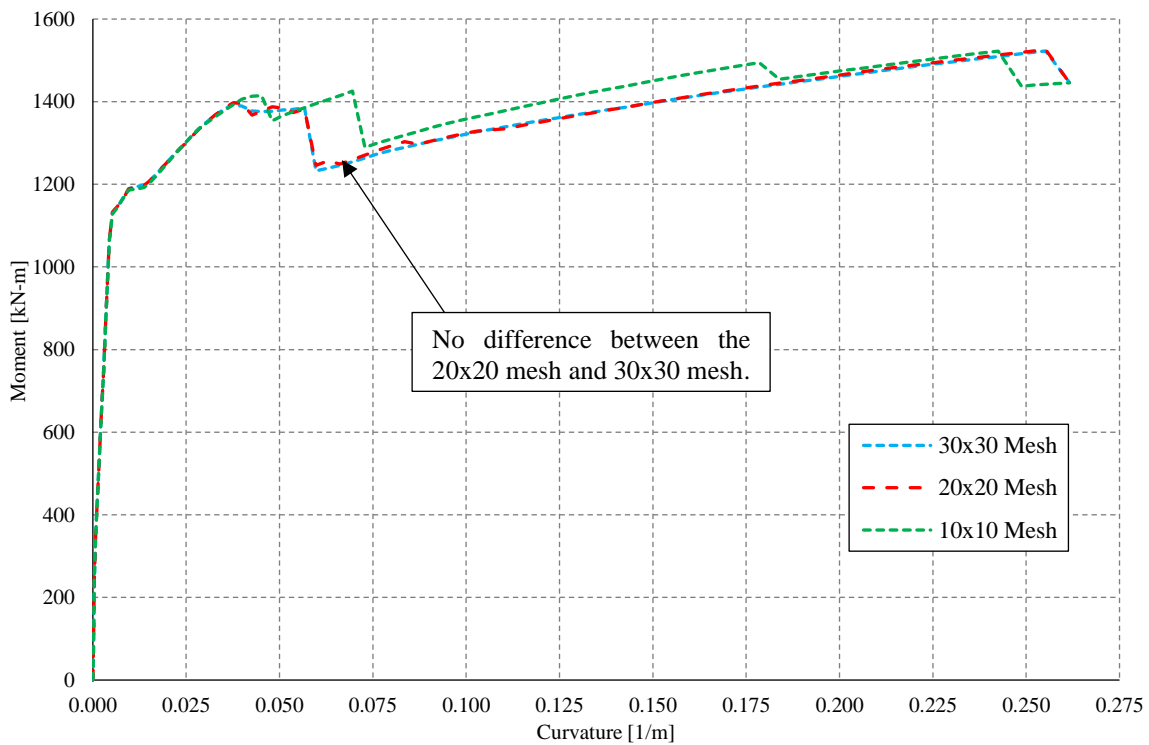
Figure 8-7: Moment-curvature comparison for different fiber layouts.

8.2.2   Elastic behavior of the fiber hinge.

It is worth to mention that in SAP2000 assigning a Fiber hinge to a frame element will affect its elastic flexibility. The elastic behavior along the fiber hinge length is determined from the hinge material stress-strain curves, and the elastic properties of the Frame element are ignored within the hinge length. For this reason, the hinge length should not exceed the length of the frame element [16]. As well the part element containing the fiber hinge will tend to be stiffer.

79

Regardless of the type of analysis (linear/nonlinear), SAP2000 will divide the frame element into two parts, one corresponding to the frame element and one to the hinge length portion. Joints are automatically added by SAP2000 at the ends of the hinge length, separating the frame element from the fiber hinge. An example is shown in Figure 8-8.
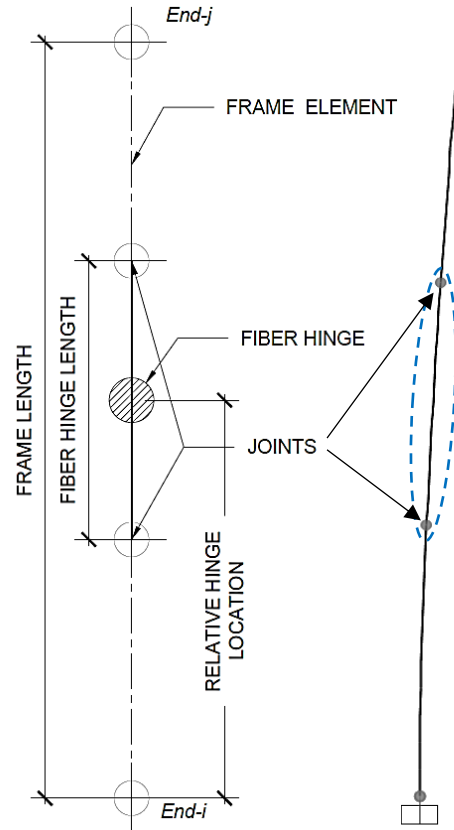
Figure 8-8: Frame element division from the hinge length and SAP2000 example.

Furthermore, by the configuration of the software, when a hinge is assigned in a point where it cannot extend half of its tributary length to each side (for example for hinges at the ends of the member), the program will shift the tributary hinge lengths as necessary so that they do not overlap the ends of the member or end offsets. However, the bending behavior of fiber hinges works best when the hinge is located at the center of its tributary hinge length (axial behavior is not affected significantly by location), reason for which attention should always be paid to the fiber hinges assignment.

To exemplify the influence of the hinge location with respect to the center of its tributary length, a simplified problem is proposed. A cantilever frame element with no distributed mass, clamped on the bottom, and having a lumped mass equal to 20 tons on its free end is used to study the hinge location influence.

The comparison is made against a hand-computation of the period of the structure. The period's value is computed throughout Eq.(8-1).

$$T = 2\pi \sqrt{\frac{m}{\frac{3EI}{L^3}}} \tag{8-1}$$

The parameters used to compute the period are shown in Table # 8-1.

Table # 8-1: Hand-computation parameters.

Elastic young modulus E [MPa]	25743
Cross-section inertia I [m⁴]	0.0223
Clear length L [m]	9.75
Lumped mass m [Ton]	20
Stiffness $3EI/L^3$ [kN/m]	1858
Period T [s]	0.652

Two cases for comparison are presented in Figure 8-9 and are listed below:

- Case 1 has a fiber hinge located at the end of the frame element, where its hinge length is shifted by the program.

- Case 2 has a fiber hinge located at the center of its tributary length.
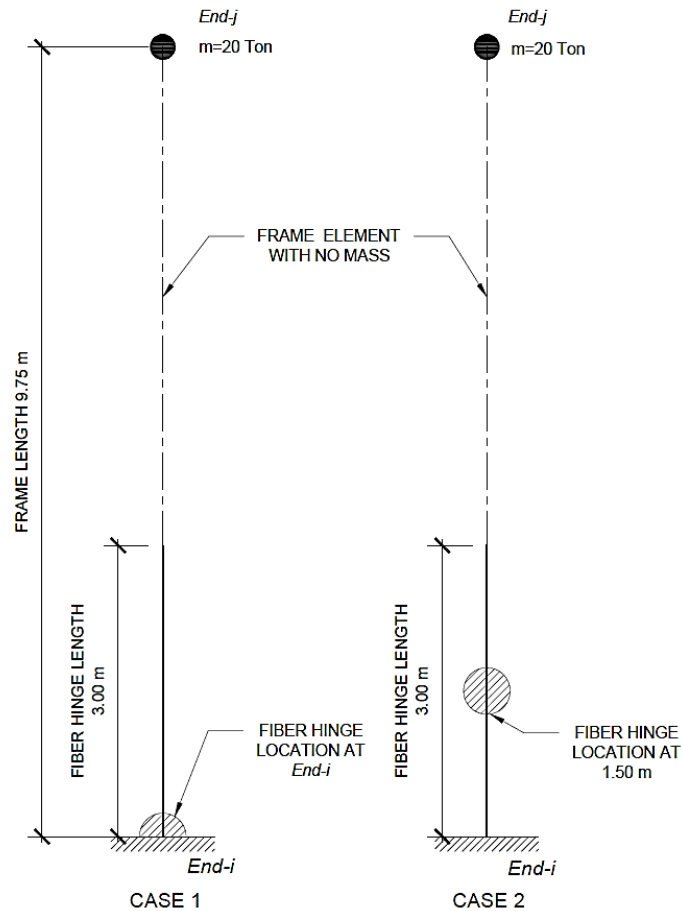
Figure 8-9: Benchmark problem for Hinge's location influence.

The analysis used to extract the information for both cases is a common eigenvalue analysis performed by SAP2000. Additionally, a Frame element without a fiber hinge case is included to check the hand-computation values.

The results of the comparison for both cases are shown in Table # 8-2. As it can be seen for Case 1, the assigned hinge is not centered at its tributary hinge length and this makes the frame more flexible, which is not expected from a fiber hinge. Conversely, by assigning the hinge at the center of its tributary hinge length, as it is for Case 2, this will make the frame stiffer.

Table # 8-2: Hinge location comparison.

Case	Tributary Length [m]	Hinges [#]	Absolute Hinge location [m]	Relative Hinge location [-]	**Period** [s]	Difference (*) [%]
Hand computation	-	-	-	-	**0.652**	-
Frame Elastic	-	-	-	-	**0.652**	-0.02%
Case 1	3.000	1	0.00	0	**0.722**	10.68%
Case 2	3.000	1	1.50	0.1538	**0.643**	-1.45%

Positive difference means that the case is more flexible with respect to the hand-computation value.

8.2.3   Frame discretization influence.

For hinge lengths that exceed the length of the element, adjacent elements will not be adjusted, and some double counting of elastic flexibility will remain in the model due to the adjacent elements. For this reason, it is not recommended to use objects or elements discretization that are smaller than the hinge lengths.

Thus, discretizing the frame element into shorter elements inside the hinge length will make the model more flexible. To exemplify this, three cases for comparison are presented in Figure 8-10 and they are listed below:

- Case 1 has a fiber hinge located at the center of its tributary length within a frame element that has a discretization of 2 finite elements (FE).

- Case 2 has a fiber hinge located at the center of its tributary length within a frame element that has a discretization of 10 FE.

- Case 3 has a fiber hinge located at the center of its tributary length within a frame element that has a discretization of 20 FE.

The analysis used to extract the information for the three cases is a common eigenvalue analysis performed by SAP2000. Additionally, a Frame element without a fiber hinge case is included to check the hand-computation values.

The results of the comparison for the three cases are shown in Table # 8-3. As can be seen for Case 1, the discretization of the frame element does not influence the behavior of the fiber hinge since the FE is still larger than the fiber hinge length. Thus, no double counting of elastic flexibility remains inside the model.

The other two cases (Case 2 and Case 3) which have smaller FE elements within the fiber hinge length, introduce considerable elastic flexibility to the model, having a deviation with respect to the theoretical period of the structure greater than 20%. In conclusion, no FE discretization that yields shorter FE within the fiber hinge length must be used.

Table # 8-3: FE discretization comparison.

Case	Tributary Length [m]	Hinges [#]	Absolute Hinge location [m]	Relative Hinge location [-]	FE Discretization [#]	Period [s]	Difference (*) [%]
Hand-computation	-	-	-	-	-	0.652	-
Completely elastic	-	-	-	-	-	0.652	-0.02%
Case 1	3.000	1	1.50	0.1538	2	0.643	-1.45%
Case 2	3.000	1	1.50	0.1538	10	0.778	19.26%
Case 3	3.000	1	1.50	0.1538	20	0.808	23.98%

Positive difference means that the case is more flexible with respect to the hand-computation value.
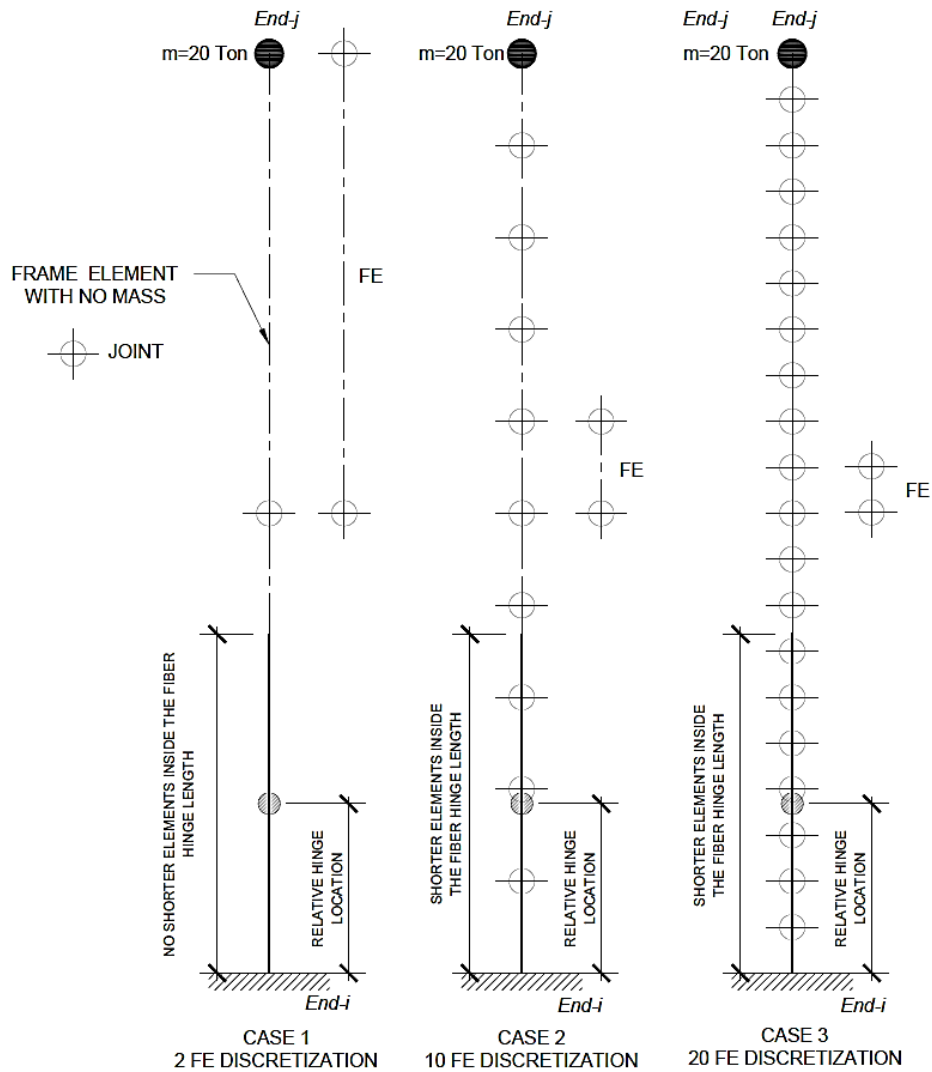
Figure 8-10: Benchmark problems for the frame element discretization influence.

8.2.4 Sensitivity analysis.

The post-elastic response of the fiber hinge is tested using four examples. These examples are used to study the influence of the total plastic length considered within the frame element, given a certain number of hinges. Additionally, the influence of placing more fiber hinges representing the same total plastic length is considered.

The total plastic length is equal to the region within the frame element in which the program can capture the post-elastic response, and it is represented by the number of hinges assigned and their length.

Four examples are shown in Figure 8-11, where the total plastic length is increased by adding a hinge with a tributary length of 0.75 m. These examples are listed below:

- Case 1 has a total plastic length equal to 0.75 m with 1 hinge.

- Case 2 has a total plastic length equal to 1.50 m with 2 hinges.

- Case 3 (a) has a total plastic length equal to 3.00 m with 4 hinges.

- Case 3 (b) has a total plastic length equal to 3.00 m, but within this region there are 12 hinges with a tributary length of 0.25 m each.
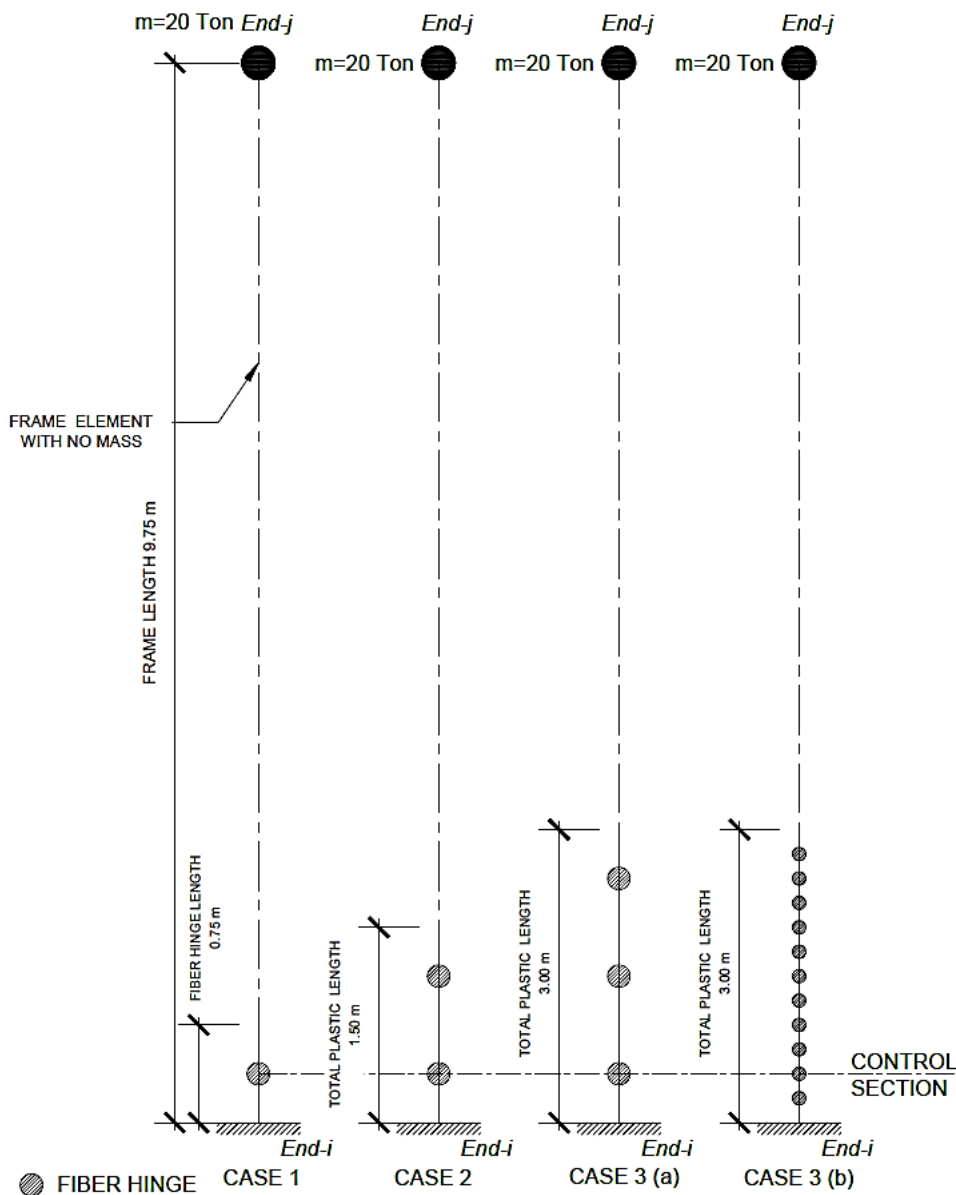
Figure 8-11: Examples' schemes for the post-elastic response.

As done previously, the analysis used to extract the information for the four cases is a common eigenvalue analysis performed by SAP2000. Additionally, a frame element without a fiber hinge case is included to check the hand-computation values.

The results of the four examples are shown in Table # 8-4. As expected, for every example the fiber hinges tend to make the frame a little stiffer with a maximum difference of -1.12%.

<p align="center">Table # 8-4: Modal data comparison for Fiber hinges.</p>

Case	Total plastic length [m]	Tributary Length [m]	Hinges [#]	Control Hinge Location [m]	Period [s]	Difference(*) [%]
Hand- computation	-	-	-	-	0.652	-
Completely elastic	-	-	-	-	0.652	-0.02%
Case 1	0.75	0.750	1	0.375	0.650	-0.37%
Case 2	1.50	0.750	2	0.375	0.648	-0.66%
Case 3 (a)	3.00	0.750	4	0.375	0.645	-1.12%
Case 3 (b)	3.00	0.250	12	0.375	0.645	-1.10%

Positive difference means that the case is more flexible with respect to the hand-computation value.

The post-elastic response of the fiber hinge is described and compared in global and local terms. From the local point of view, the response is given by looking at the control hinge section, as shown previously in Figure 8-11. This control hinge section is set at 0.375 m from the *end-i* for every case, as shown in Table # 8-4.

The comparison scenarios are listed below:

- Global response of fiber hinges using Pushover analysis.

- Local response of fiber hinges using Pushover analysis.

- Global response of fiber hinges using Time history Direct integration analysis

- Local response of fiber hinges using Time history Direct integration analysis.

8.2.4.1   Global response of fiber hinges using pushover analysis.

To capture the global response of the fiber hinges a pushover analysis is performed by imposing a monotonically increasing force at the top of the column until it reaches a displacement equal to 0.50 m. The analysis is done for the different cases specified in Table # 8-4 and the capacity curve diagrams are shown in Figure 8-12.

It can be appreciated in Figure 8-12, all curves comply with same the elastic branch up to a displacement of 20 mm. After this point, the curves follow independently a branch with a slope directly related to the total plastic length considered. This is because by adding more total plastic length the concrete fibers in tension fail. Hence, the stiffness is reduced.

In terms of final strength, all curves seem to agree with Case 1 giving an overstrength of 30kN. Case 3 (a) and Case 3 (b)'s capacity curves match perfectly, meaning that including more hinges along the length do not affect the global response of the column.
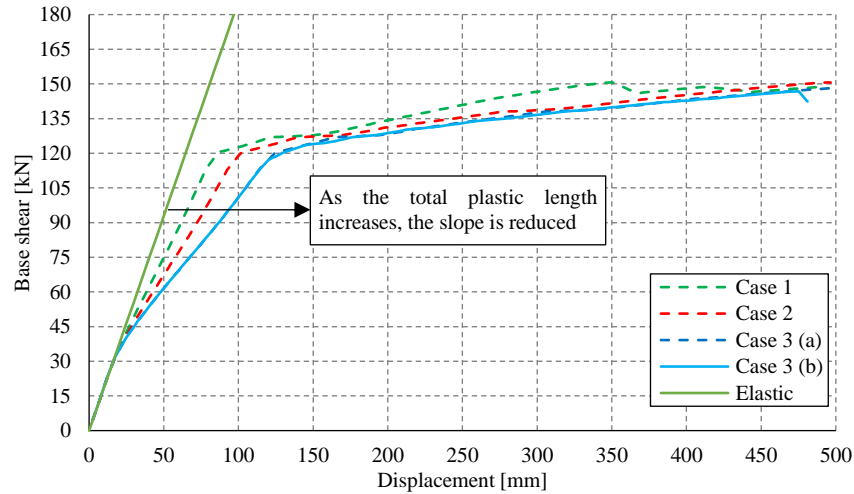
Figure 8-12: Benchmark Capacity curves.

8.2.4.2   Local response of the fiber hinges using pushover analysis.

The results of the control hinge in terms of moment-rotation (M-ϑ) are shown in Figure 8-13. All the hinges with the same tributary length match perfectly in their elastic and post-elastic branches, as it is for cases 1, 2, and 3 (a). When it comes to Case 3 (b), which includes a shorter tributary length (0.25 m), the rotation at the control hinge is lower.
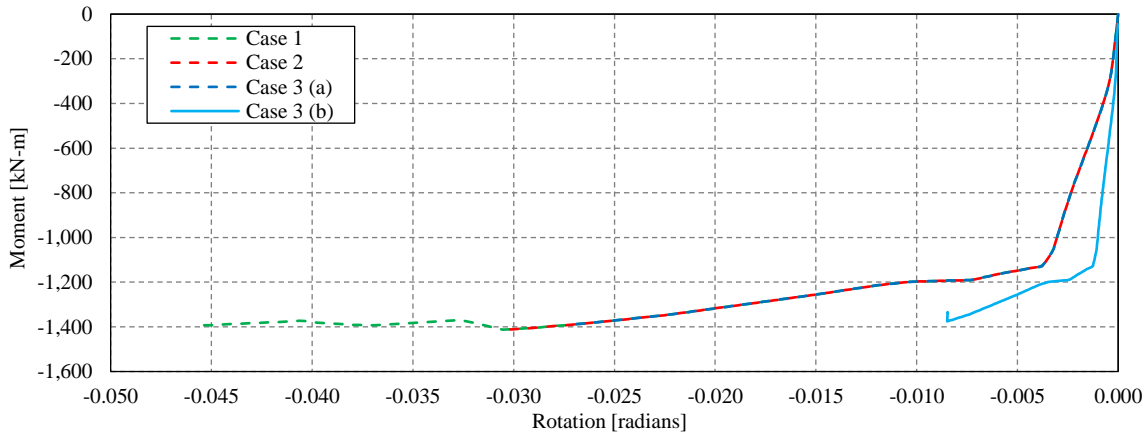
Figure 8-13: Moment-rotation diagram (M-ϑ) for the control hinge.

Nevertheless, as shown in Figure 8-14, the moment-curvature diagrams (M-χ) of Case 3 (a) and Case 3 (b) match perfectly in their elastic branch, post-elastic branch, and in the maximum curvature reached. Thus, by including more hinges along the same total plastic length do not affect the local response of the column.

A trend related to the maximum rotation reached versus the total plastic length considered can be commented on. With a lower total plastic length, the plasticity concentrates in a shorter zone of the frame element. A shorter length will experience more damage at the control hinge section when reaching the same displacement with respect to cases with larger total plastic length.

This trend is more noticeable in Figure 8-14, where the control hinge sections for the different total plastic lengths follow the same diagram but with different maximum curvature reached. The maximum

86

curvature reached values corresponding to each case of study are shown in Table # 8-5 and it is highlighted in Figure 8-14.

Table # 8-5: Maximum curvature reached for the cases of study.

Case	Total plastic length [m]	Maximum curvature χ [1/m]	Normalized ratio with respect to Case 3 (b) [-]
Case 1	0.75	-0.0611	1.800
Case 2	1.50	-0.0409	1.204
Case 3 (a)	3.00	-0.0364	1.071
Case 3 (b)	3.00	-0.0339	-

The moment-rotation diagram can be transformed into a moment-curvature diagram by using Eq.(8-2)

$$\theta = \chi L_t \tag{8-2}$$

Where ϑ = is the rotation in the control hinge location, χ = is the curvature at the control hinge location, L_t = is the tributary length of the fiber hinges.
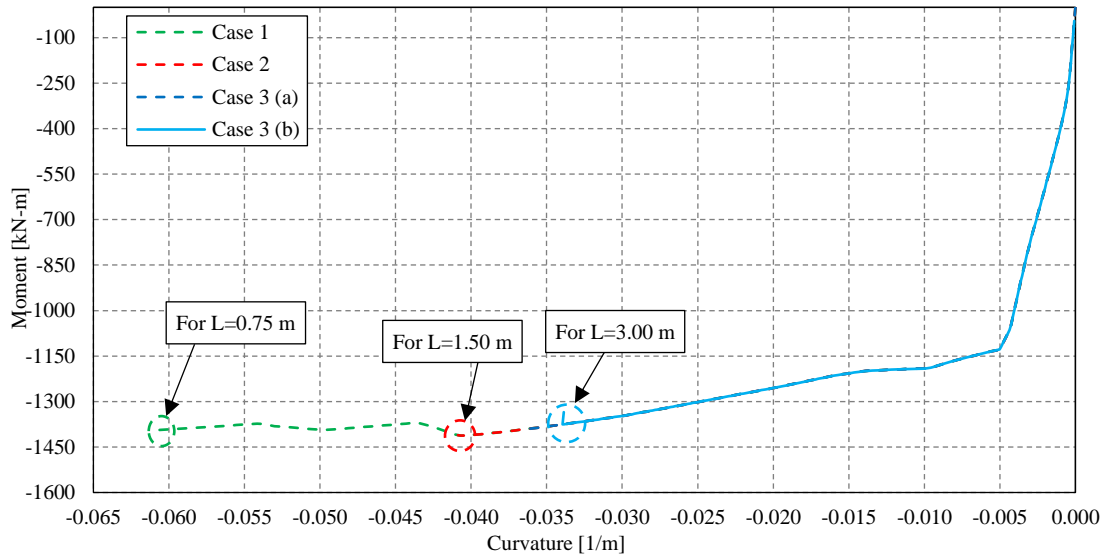
Figure 8-14: Moment-curvature diagram for the control hinge.

8.2.4.3   Global response of fiber hinges using Time history Direct integration analysis.

To capture the dynamic response of the fiber hinges, the examples presented in Table # 8-4 are subjected to ground-excitation equal to a sine function. The sine function is represented in Figure 8-15.
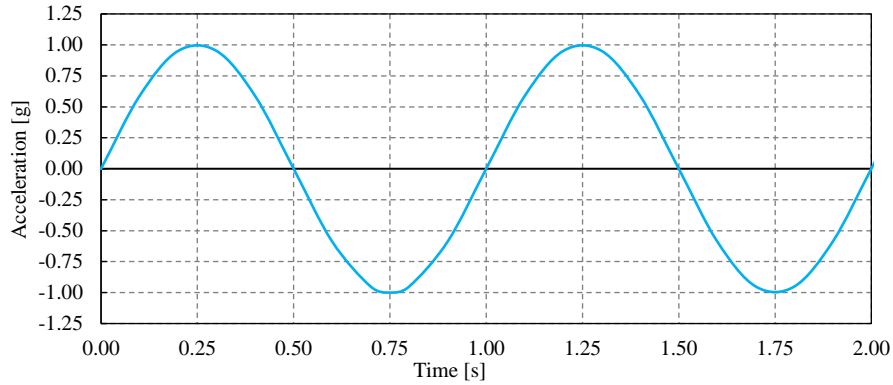
Figure 8-15:Ground function excitation

As shown in Figure 8-16, the global response of the examples is measured through the column's top displacement. As can be seen the Case 3 (a) and Case 3 (b)'s time history diagrams match, and they experience the largest displacement among the cases analyzed. Thus, when reducing the total plastic length, the displacement experienced at the top is reduced.
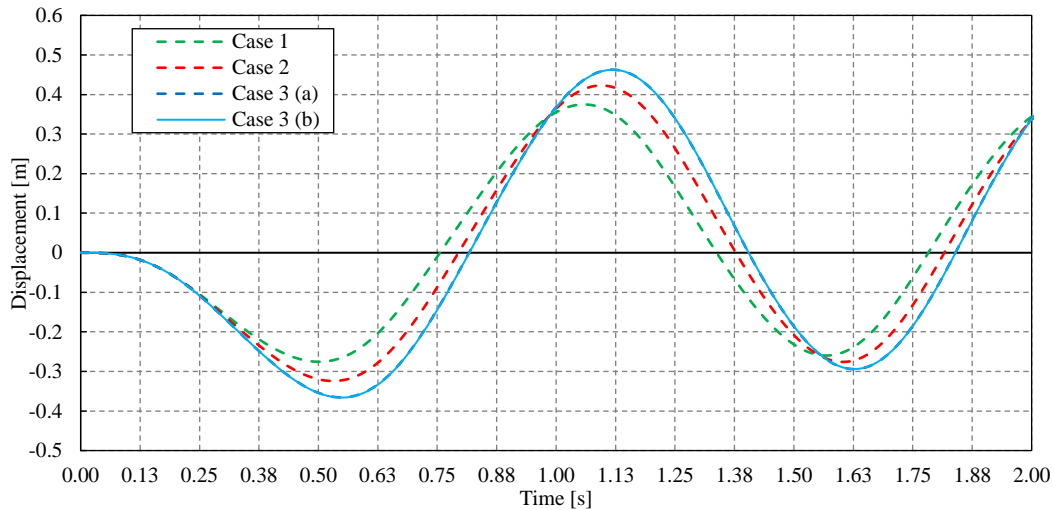
Figure 8-16: Top column's displacement.

This result seems to be in contrast with the results shown in Figure 8-13 and Figure 8-14. Nevertheless, it can be shown that this is not the case if the increment of displacement along the column's height is measured for every case and compared. The increment of displacements from joint to joint normalized with respect to their distance is shown in Figure 8-17. It can be appreciated that for a larger total plastic length the increments of displacement along the plastic zone are larger with respect to the ones at the zone in which the frame remains elastic. Contrary to the results shown in Figure 8-13 and Figure 8-14, all the cases had the same displacement, which means that for a shorter plastic length the hinge will need to rotate more (More damage) to have the same displacement.

88
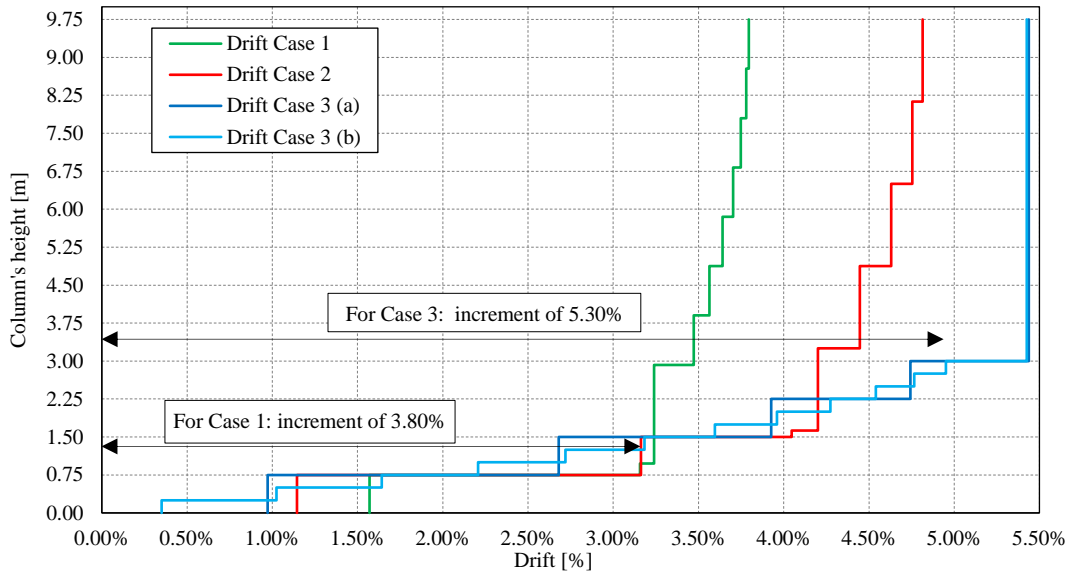
Figure 8-17: Displacement increments along the column's height.

8.2.4.4   Local response of fiber hinges using Time history Direct integration analysis.

The local response of the control hinges is shown in Figure 8-18. The hysteretic response for all the cases under study share the same loop's shape, but the loop's size in terms of curvature reached is lower as the total plastic length increases. With a lower total plastic length plasticity concentrates in a shorter zone of the frame element. A shorter length will experience more damage at the control hinge section in order to reach the dynamic equilibrium with respect to cases with larger total plastic length.
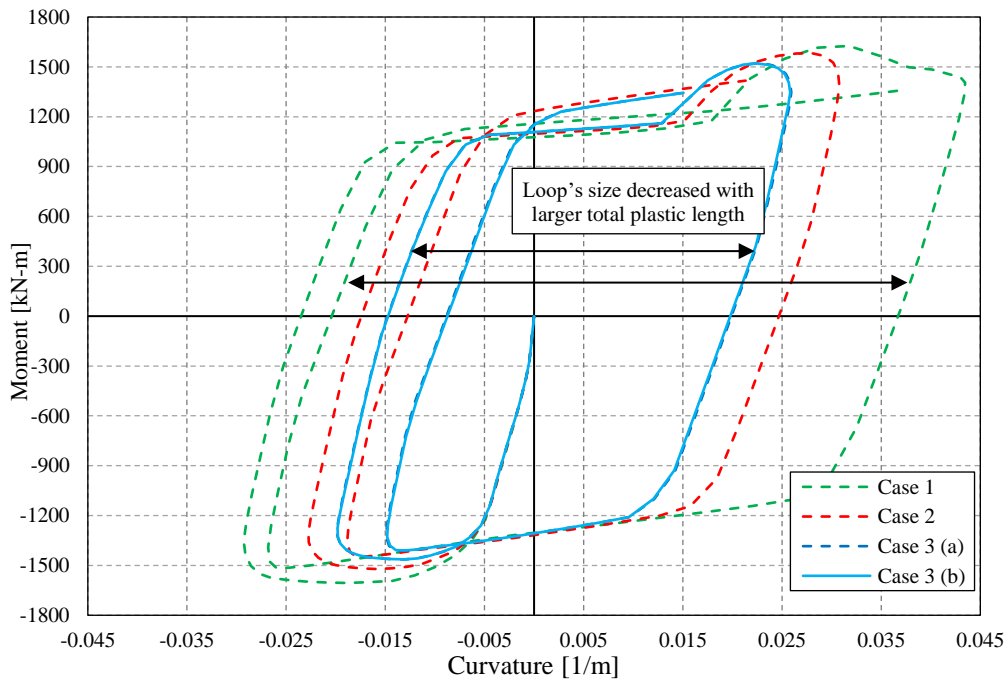
Figure 8-18: Hysteretic response of the control hinge.

From the analyses results, it can be concluded that the control hinge's response (either static or dynamic) is governed by the total plastic length considered. The question remains about which length should be considered to assess the structures under study.

8.2.5   Hinge length hypothesis.

After exemplifying the response of the fiber hinges, the next step is to choose a proper plastic length to assess the structures. From the analyses shown in the previous section, it can be shown that the damage at some columns concentrated at their base, particularly there was evidence of some cyclic damage. As shown in Figure 8-19, the cyclic damage extension is estimated as equal one time the size of the column cross-section, with the concentration of the damage at half of this length.

Taking as reference this value for the total plastic length can be a good approximation, since it is directly related to the damage suffered by the column during the seismic motion. Nevertheless, a comparison is made against empirical equations based on well-recorded experimental data.
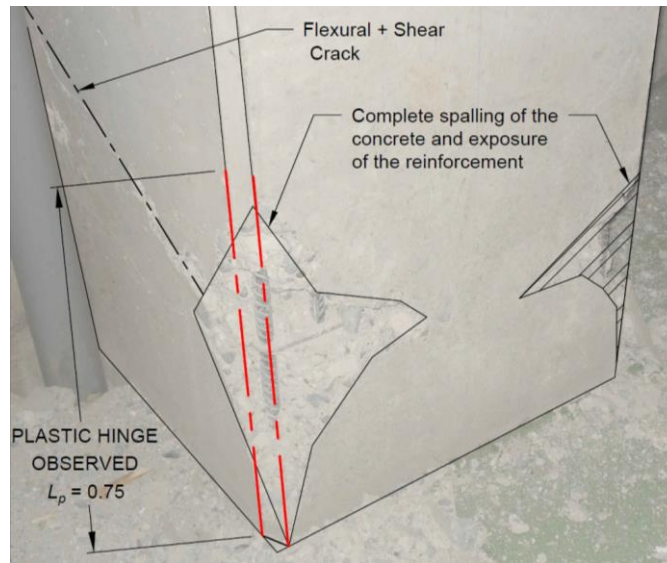
Figure 8-19: Plastic zone observed at the column's base.

From the discussion given in [25], a series of equations to estimate the plastic hinge length are given. These equations are the following:

$$\frac{L_p}{h} = \left[0.3\left(\frac{P}{P_o}\right) + 3\rho_l - 0.1\right]\left(\frac{L}{h}\right) + 0.25 \geq 0.25 \tag{8-3}$$

$$L_p = 0.05L + \frac{0.1f_y d_b}{\sqrt{f'c}} \tag{8-4}$$

$$\frac{L_p}{h} = 0.9\left[1 + 0.5\left(\frac{P}{P_o}\right)\right] k_1 \left(\frac{L}{h}\right)^{0.25} + 0.25 \tag{8-5}$$

$$L_p = 0.08L + 0.022f_y d_b \tag{8-6}$$

Where L_p = is the plastic hinge length. P_o = is the compressive strength of the cross-section computed as $A_g f'_c$.

The parameters used to compute the plastic hinge lengths are listed in Table # 8-6.

Table # 8-6: Parameters used to estimate the plastic hinge length.

Cross-section Height h [m]	0.75
Clear length L [m]	9.75
Reinforcement ratio ρ_l [-]	0.0261
Dimensionless axial force ratio (P/P_o)	0.08
Concrete compressive strength f'_c [MPa]	30.00
Steel yielding strength f_y [MPa]	420
Longitudinal bar diameter d_b [mm]	25.00
Factor k_1 [-]	0.67

As presented in Table # 8-7, the plastic hinge lengths estimated by Eq.(8-4) and Eq.(8-5) are quite close to the damage observed. Whereas Eq.(8-3) may underestimates the capacity of the column to dissipated energy with such a short length (0.19 m) and Eq.(8-6) is slightly above the observed damage.

Table # 8-7: Estimated plastic hinge length.

Proposed equation	L_p/h [-]	Plastic hinge length L_p [m]
Eq.(8-3)	0.25	0.19
Eq.(8-4)	0.91	0.68
Eq.(8-5)	1.18	0.89
Eq.(8-6)	1.35	1.01

The next step is to bound the response of the structure using the estimated hinge lengths from Eq.(8-4) and Eq.(8-5), being the lower limit and upper limit, respectively. Therefore, the response of the building for these computed hinge lengths will be compared against the hinge length saw during the survey and estimated in Figure 8-19.

For the sake of simplicity, the comparisons are done only in terms of global and local response of Building A throughout a Pushover analysis. The analyses are performed in the positive verse of X direction and Y direction using a modal distribution of forces.

The control node of displacement is made with references to the closest joint to the mass centers. The fact that the model does not possess a rigid diaphragm makes it quite complex to track the displacement of the actual mass center, that is why is used the closest joint representing a column's top. In the case study, the column H-6's top is used as a control node, as shown in Figure 8-20.
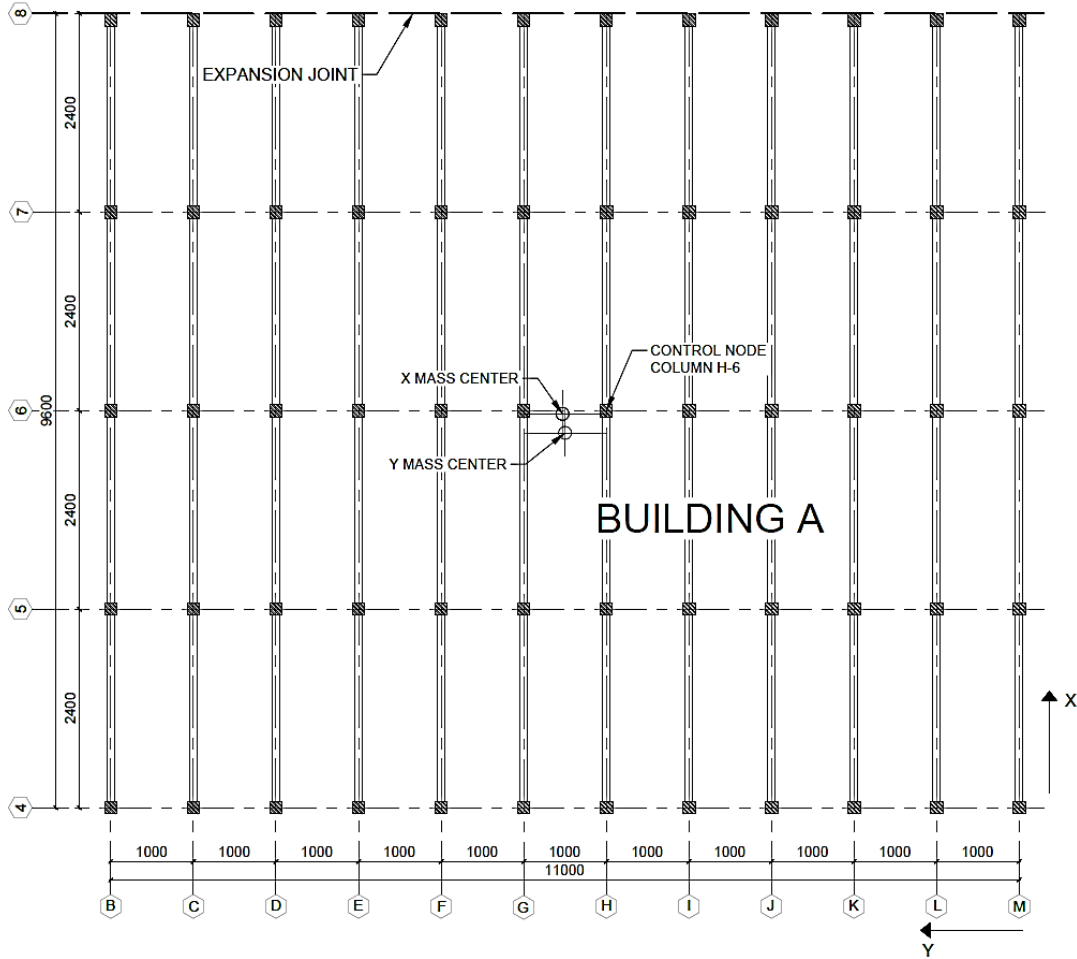
Figure 8-20: Mass centers in each direction for Building A (units in cm).

The coordinates of both mass centers and the coordinates of column H-6 are shown in Table # 8-8. It is worth mentioning that the fact of having different mass centers is related to the modeling of the cladding panels which possess masses to be excited in one direction only.

Table # 8-8: Mass centers coordinates for building A.

Mass center	X [m]	Y [m]
g_X	45.3	55.0
g_Y	47.6	55.7
Column H-6 joint	48.0	50.0

For the pushover analyses, the load combination used to account for the *P-Delta* effects is shown in Eq(8-7):

$$D + P \tag{8-7}$$

A comparison of the modal data with the fiber hinges length assigned is shown in Table # 8-9.

Table # 8-9: Modal data comparison.

Mode	Period	U_x	U_y	R_z
[#]	[s]	[%]	[%]	[%]
$L_p = 0.89$ m				
1	1.1892	0.00%	91.79%	0.01%
2	0.7741	0.00%	0.00%	73.58%
3	0.6174	93.18%	0.00%	0.00%
$L_p = 0.75$ m				
1	1.1967	0.00%	91.83%	0.01%
2	0.7776	0.00%	0.00%	73.92%
3	0.6207	93.22%	0.00%	0.00%
$L_p = 0.68$ m				
1	1.2005	0.00%	91.85%	0.01%
2	0.7793	0.00%	0.00%	74.09%
3	0.6224	93.24%	0.00%	0.00%

As shown in Table # 8-9, there is no significant variation in terms of modal data between the models having different plastic lengths.

The capacity curves and the hinge response for each plastic hinge length considered are shown in Figure 8-21 and Figure 8-22. The immediate result that can be appreciated is the perfect match of the capacity curves in both directions independently of the plastic length. The X direction has a slight difference between the curves after reaching 20 cm of displacement, whereas for the Y direction the curves remain overlapped during all the analysis.
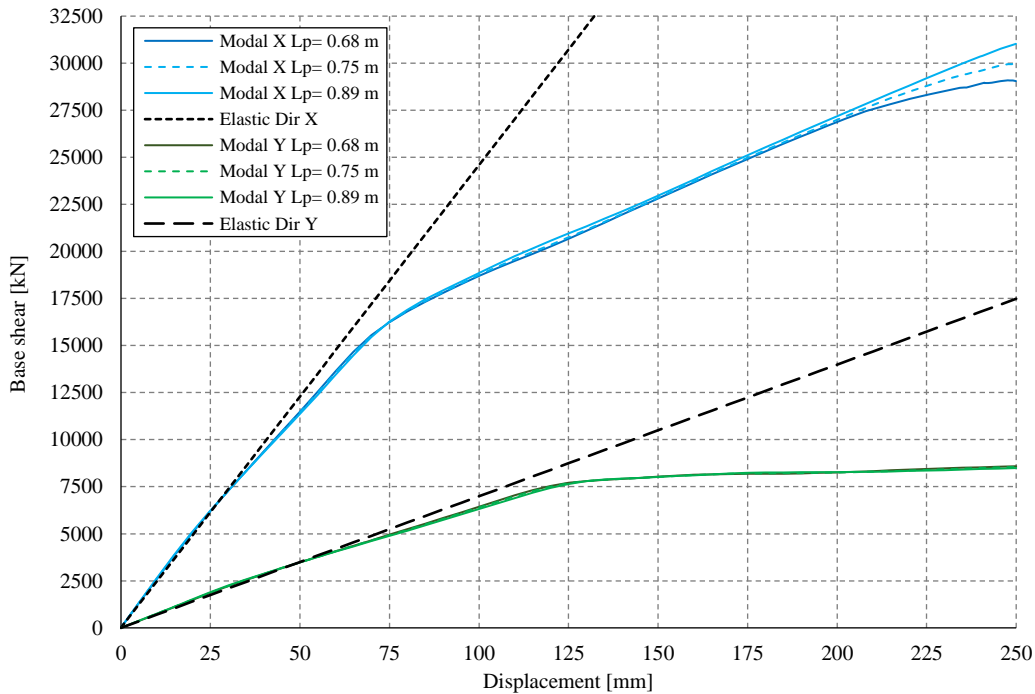
Figure 8-21: Capacity curves comparisons for building A.

For the local response of the fiber hinge, the column G-4 is chosen to exemplify the moment-rotation diagrams in the X direction. It can be noticed in Figure 8-22 that the difference of the response between the plastic lengths estimated and the one found during the Maule Earthquake is not significant.
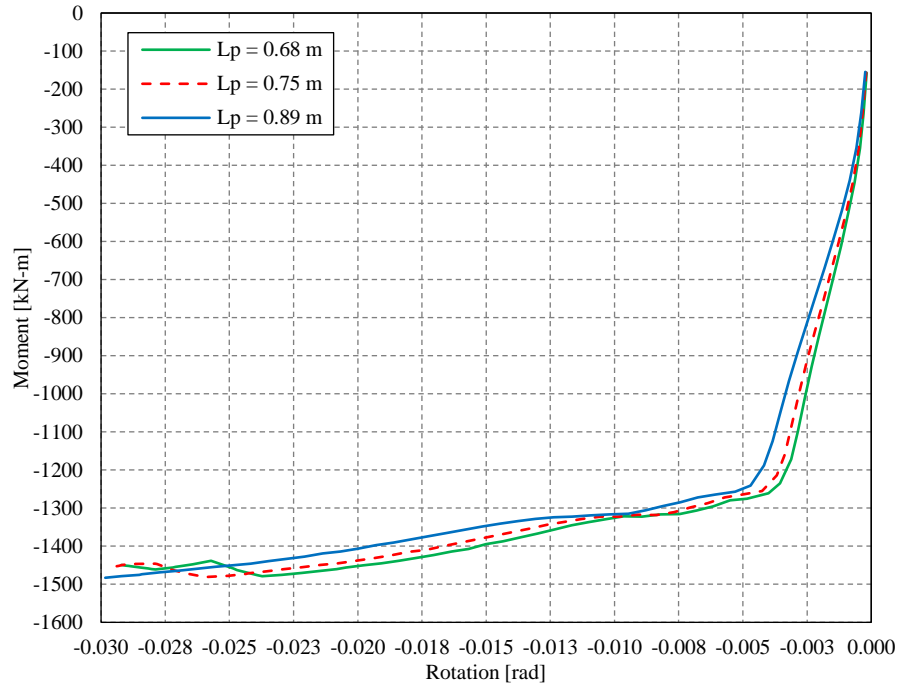
Figure 8-22: Local response of the fiber hinge of column G-4.

From this analysis is concluded that plastic hinge length observed after the earthquake at the column's base is suitable and backed up from empirical formulas. Now a description of the nonlinear procedures to evaluate the buildings is done.

9 Nonlinear analyses.

Nonlinear procedures used to assess the damage of the structural elements and the capacity of the structure are described in this section. The analyses correspond to the nonlinear dynamic analysis and pushover analysis.

9.1 Nonlinear dynamic procedure.

The nonlinear dynamic response of the structure subjected to earthquake motion of the Maule earthquake is studied using the direct-integration time-history analysis.

The time-history analysis is used to determine the dynamic response of a structure to an arbitrary loading by solving the dynamic equilibrium equations. The matrix form of these equations is shown in Eq.(9-1).

$$\boldsymbol{K}\boldsymbol{u}(t) + \boldsymbol{C}\dot{\boldsymbol{u}}(t) + \boldsymbol{M}\ddot{\boldsymbol{u}}(t) = \boldsymbol{r}(t) \tag{9-1}$$

Where $\boldsymbol{C}$ = is the viscous damping matrix, $\boldsymbol{M}$ = is the mass matrix, $\boldsymbol{K}$ = is the stiffness matrix. $\boldsymbol{u}, \dot{\boldsymbol{u}}$, and $\ddot{\boldsymbol{u}}$ = are the displacement, velocities, and acceleration vectors of the structure, $\boldsymbol{r}$ = is the applied load.

This equation is solved by a scheme of step-by-step type of analysis. Since this is a nonlinear analysis, the stiffness, damping, and load may all depend upon the displacements, velocities, and time. This requires an iterative solution to the equations of motion.

9.1.1 Additional nonlinearities.

Apart from including the nonlinear behavior from the materials, SAP2000 allows to continue the analysis from a previous nonlinear case. Hence, a nonlinear case is defined to impose gravitational loads upon the structure to consider the *P-delta effects*. The combination of load for gravity loads is shown in Eq.(8-7).

Furthermore, to increase the accuracy of the *P-delta effects* the columns are auto-subdivide by SAP2000 into shorter elements. The columns are subdivided into ten elements having a length equal to 0.975 m, as well, it must be remembered that this length is larger than the fiber hinges' length, so no elastic flexibility is included.

9.1.2 Time integration scheme.

For performing the integration of the equations of motion, a time integration scheme suitable for the problem shall be selected. SAP2000 has a collection of common methods for performing direct-integration time-history analysis. The integration scheme available on SAP2000 and their corresponding parameters are shown in Figure 9-1.
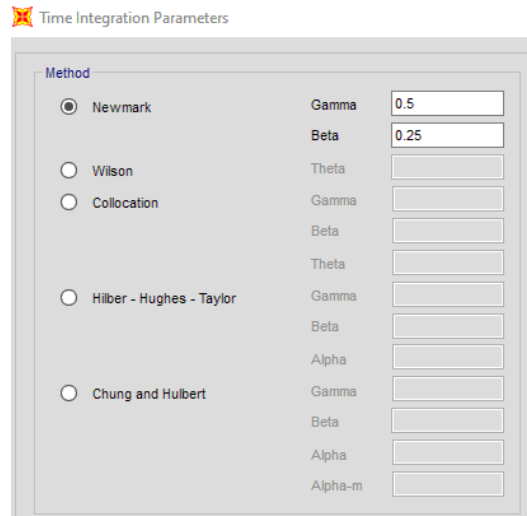
Figure 9-1: Time Integration schemes available on SAP2000.

From this collection of possible schemes, the Newmark method is chosen. In this analysis, the special case of the Average acceleration method corresponding to the values of $\gamma = \frac{1}{2}$ $\beta = 1/4$ is selected since it is unconditionally stable.

The nonlinear equations are solved using event-to-event stepping and equilibrium iteration in each time step. The analysis will stop and solve at every output time step and at every time step where one of the input history functions is defined. The integration parameters used for the analysis are shown in Figure 9-2.
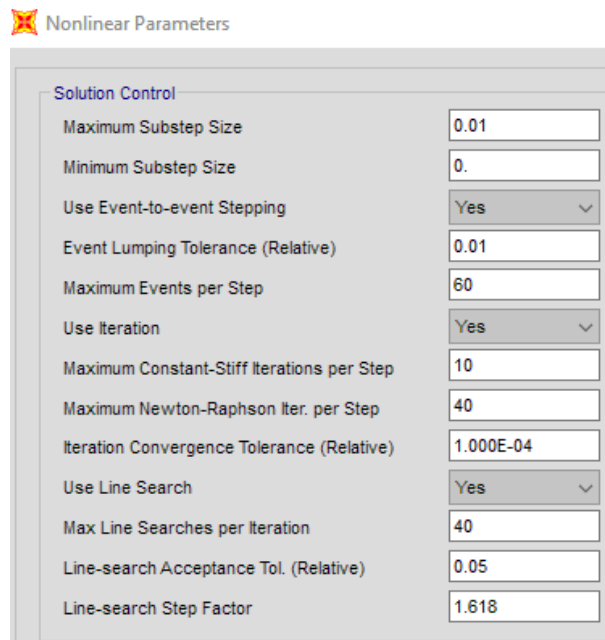
Figure 9-2: Solution control parameters for nonlinear direct integration.

The event-to-event stepping is a strategy in which an increment of the load is applied in each time step until one of the nonlinear elements experiences an "event" that causes a significant change in the stiffness of the structure. Therefore, the stiffness matrix is then re-formed, and another load increment is applied to reach the next event. This continues in a series of events steps until the entire load for that time step has been applied.

These "events" are recognized as first yield, unloading, strength loss, increasing stiffness, and other significant changes in behavior that depend on the type of element or material.

The iteration procedure is to ensure that equilibrium is achieved at each step of the analysis within a specified convergence tolerance. For each time step, constant-stiffness iteration is tried first. If it fails to converge, the Newton-Raphson iteration is tried next. If both fail, the step size is reduced, and the process is repeated.

9.1.3 Damping modeling.

The Rayleigh damping model is selected for the direct integration procedure. The viscous damping matrix is built by employing a linear combination of the stiffness matrix scaled by a coefficient β, and the mass matrix scaled by a second coefficient α. The linear combination is shown in Eq.(9-2).

$$\underline{C} = \alpha \underline{M} + \beta \underline{K} \tag{9-2}$$

Where β, α = are the linear combination coefficients.

The values of the linear combination coefficient can be obtained by imposing the damping factors of two modes. The relationship between the linear combination factors and the damping modal factor is shown in Eq.(9-3).

$$\xi_i = \frac{\alpha 1}{2\omega_i} + \frac{\beta \omega_i}{2} \tag{9-3}$$

Where ξ_i = is the damping modal factor for mode i, ω_i = is the circular modal frequency for mode i.

SAP2000 can employ this model to build the damping matrix by specifying damping modal factors at two different frequencies or periods. The modal data for both buildings and the parameters related to the computation of the viscous damping matrix are shown in Table # 9-1 and Table # 9-2.

Table # 9-1: Modal data for Building A and Building B.

Mode	Period	U_x	U_y	R_z
[#]	[s]	[%]	[%]	[%]
Building A				
1	1.1967	0%	92%	0%
2	0.7776	0%	0%	74%
3	0.6207	93%	0%	0%
Building B				
1	1.1416	0%	92%	0%
2	0.6686	0%	0%	0%
3	0.6027	93%	0%	0%

Table # 9-2: Damping parameter values for Building A and Building B.

Building	First period	Second period	Damping ratio ξ	α	β
	[s]	[s]	[-]	[1/s]	[s]
A	1.1967	0.6207	0.03	0.2074	3.903E-03
B	1.1416	0.6027	0.03	0.2161	3.767E-03

The SAP2000 implementation of the Rayleigh damping is shown in Figure 9-3 and Figure 9-4.
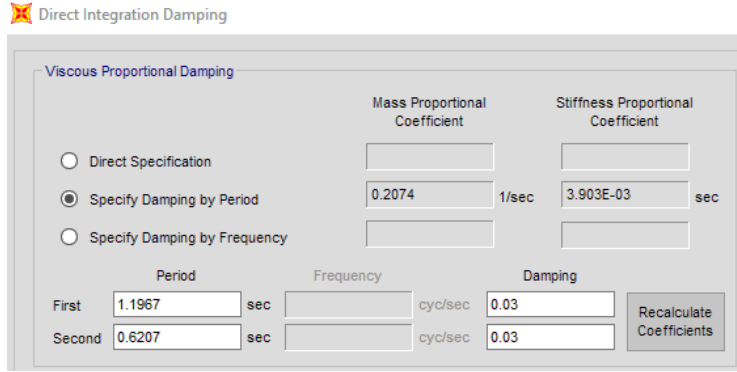
Figure 9-3: Direct integration damping modeling for Building A.
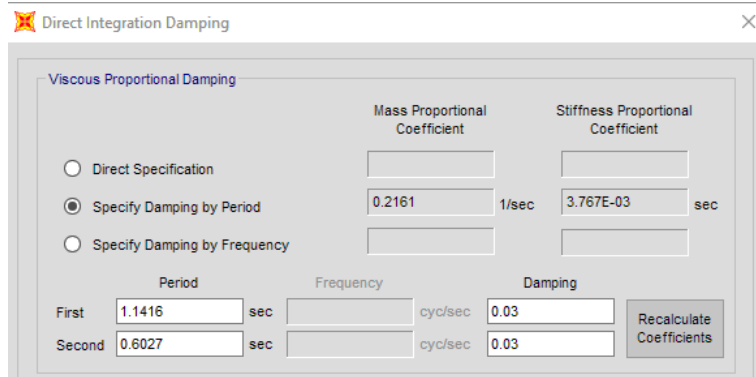
Figure 9-4: Direct integration damping modeling for Building B.

9.1.4   Loads.

The arbitrary loads used for the direct integration analysis are all the components of the accelerograms of the Maule earthquake. These accelerograms are shown in Figure 6-7 to Figure 6-9.

The Direct-integration load case in SAP2000 for both buildings is shown in Figure 9-5.

Figure 9-5: Load case definition in SAP2000 for direct-integration analysis.

The output time step set for the direct-integration analysis is equal to 0.05 s. Since the recordings are 160 s long, SAP2000 will store 3200 output time steps of information during the analysis.

9.1.5   Results for the direct-integration analysis.

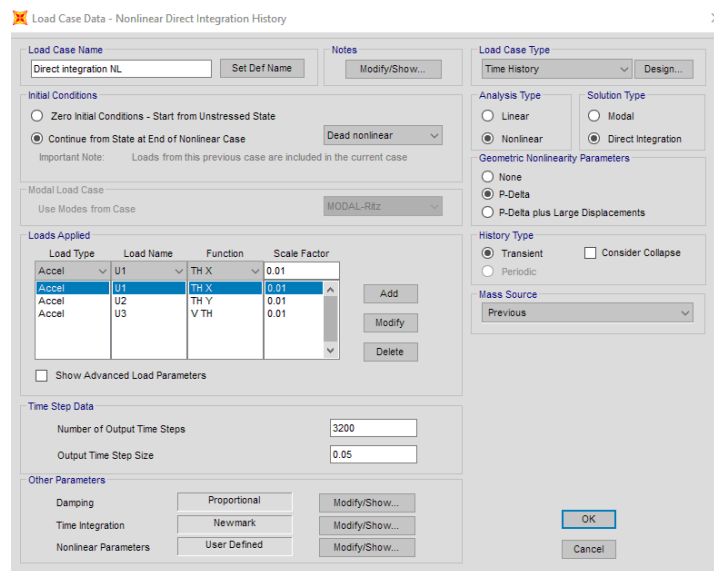In this section, the results from the direct integration analysis for both buildings subjected to the Maule Earthquake are presented. For the sake of simplicity, the explanation is given for Building A followed by a few comments related to building B. The results items that are commented on are the followings:

- Displacements comparison of the columns belonging to axes in the X direction.

- Displacements comparison of the columns belonging to axes in the Y direction.

- Comparison of linear versus nonlinear response.

- Cyclic damage observed at the base of the columns.

- Comparison of cyclic damage for the most damaged columns versus the less damaged.

The axes chosen for the comparison of displacements are shown in Figure 9-6. From the analysis, the axes in which columns experienced the largest displacements are taken here to exemplify the dynamic response of the building to the Maule earthquake excitation. Those axes correspond to Axes 6 and 4 parallel to Y direction and Axis M and G in parallel to the X direction.
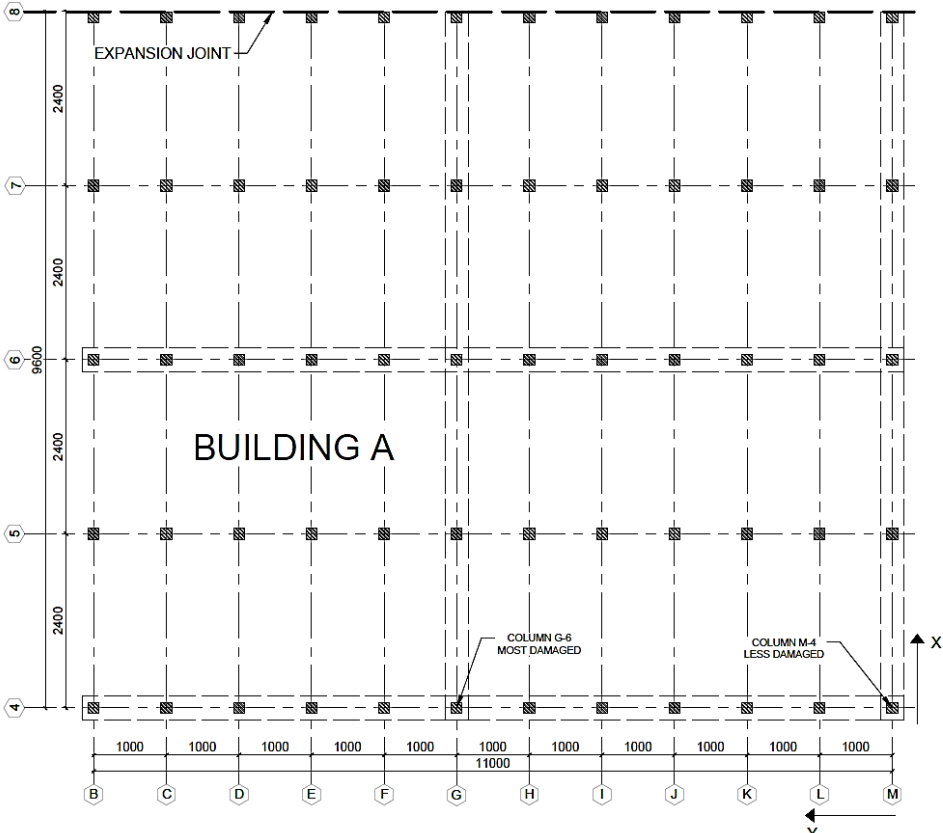

Figure 9-6: Plan view of Building A with the chosen axes for comparison (units in cm).

Furthermore, in the following pages a series of figures to be commented about Building A's response are shown. These figures represent the dynamic response of various columns on the same axis. First is shown the whole response for 160 s of dynamic excitation and after it is shown a selected time window of the most intense part of the response to see the difference in the displacements.

9.1.5.1   Displacements comparison of the columns belonging to axes in the X direction.

The dynamic response of the columns in axis G is shown in Figure 9-7 to Figure 9-10. As shown in Figure 9-8, all the displacements in the X direction match with no difference. This kind of response is related to the fact that the beams couple the columns in the same direction enforcing them to have the same displacement.

Contrarily, as shown in Figure 9-10, the displacements in the Y direction do not match all along the time history, and they are bounded between the displacement of columns G-6 and G-8, being G-6 the column that experiences the largest displacement in Y and G-8 the lowest. Nevertheless, the bounded region of displacement is small around 1 cm, which makes it practically negligible.

Figure 9-7: Displacement U_x at the column's top comparison for Axis G.

Figure 9-8: Displacement U_x at the column's top comparison for Axis G for the Intense time window.

By comparing Figure 9-7 and Figure 9-9, it can be seen that after the intense part of the earthquake, in the Y direction the columns still oscillate around considerable displacements (2 cm – 1 cm), whereas in the X direction, the displacements remain oscillating in a relatively small range (<0.5 cm).
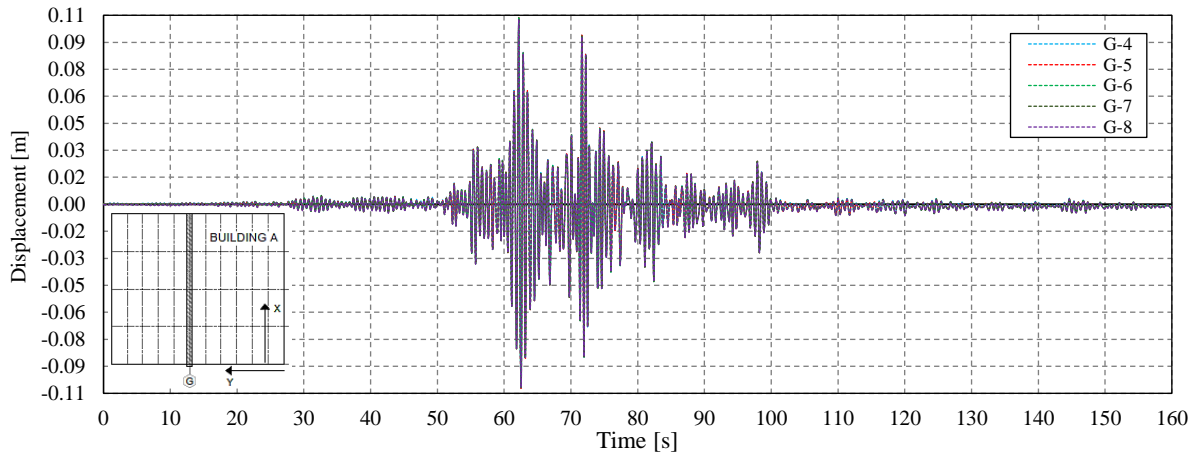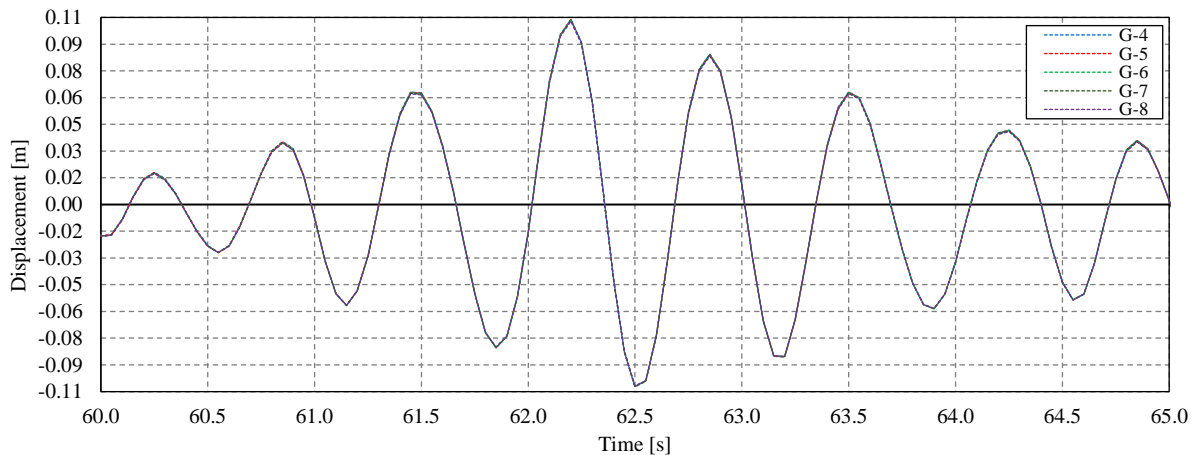
100

Figure 9-9: Displacement U_y at the column's top comparison for Axis G.
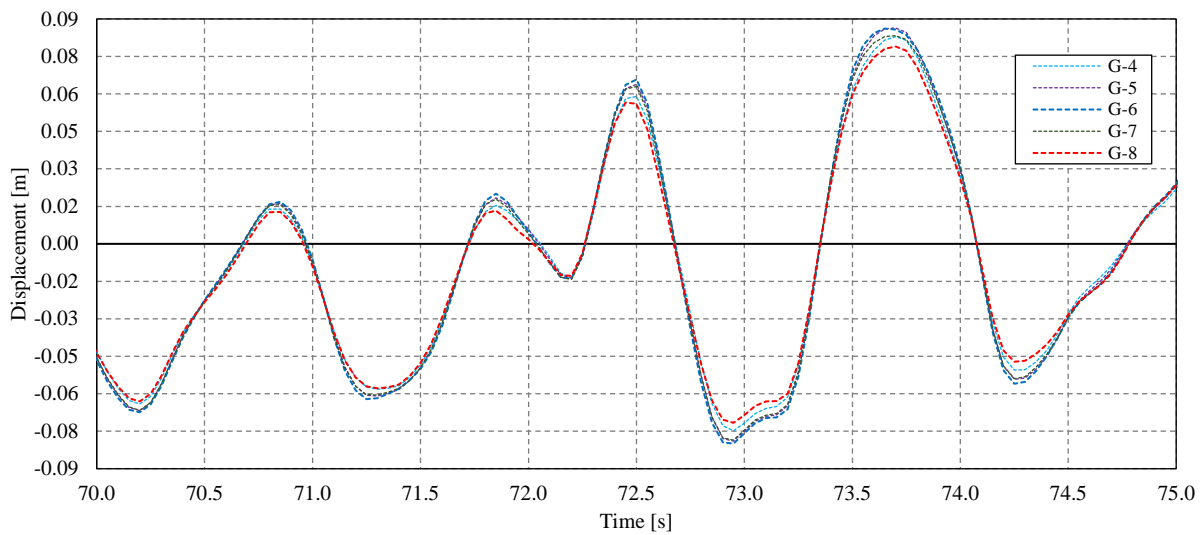
Figure 9-10: Displacement U_y at the column's top comparison for Axis G for the Intense time window.

For the sake of simplicity, the same comments on the dynamic response of axis G can be given to axis M, which yielded the same response as axis G. In conclusion, by studying an axis aligned with the X direction, the columns' response in this same direction will match. Whereas, in the Y direction the columns show some difference in the response. For axis M the response is shown from Figure 9-11 to Figure 9-14.

Figure 9-11: Displacement U_x at the column's top comparison for Axis M.

101

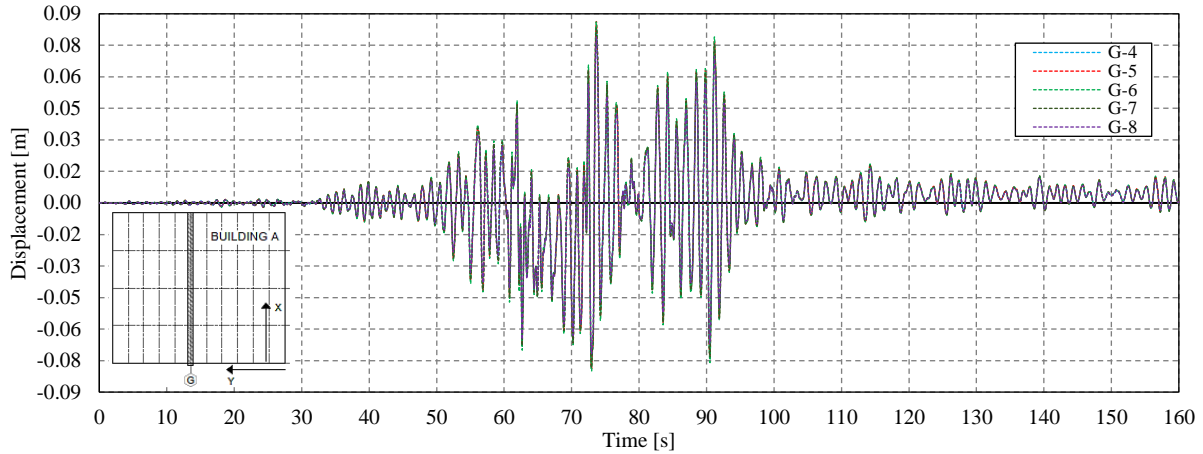Figure 9-12: Displacement U_x at the column's top comparison for Axis M for the Intense time window.

Figure 9-13: Displacement U_y at the column's top comparison for Axis M.

Figure 9-14: Displacement U_y at the column's top comparison for Axis M for the Intense time window.

9.1.5.2   Displacements comparison of the columns belonging to axes in the Y direction.

The dynamic response of the columns in axis 4 is shown in Figure 9-15 and Figure 9-18. As shown in Figure 9-16, the displacements in the X direction do not match all along the time history, and they are bounded between the displacement of columns G-4 and B-4. Being G-4 the column that experiences the largest displacement in X and B-4 the lowest.

Figure 9-15: Displacement U_x at the column's top comparison for Axis 4.
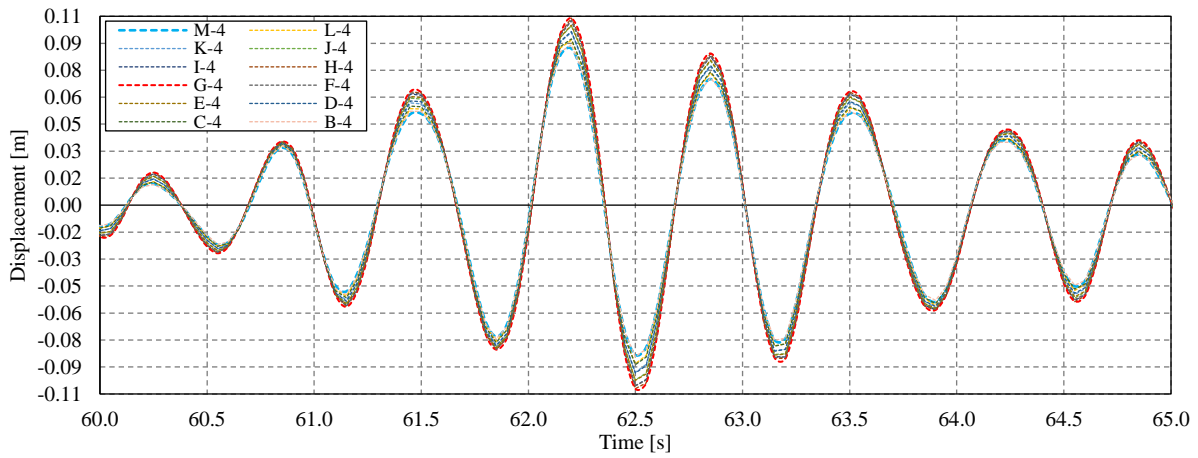
Figure 9-16: Displacement U_x at the column's top comparison for Axis 4 for the Intense time window.

For the response in the Y direction, it can be concluded that the corner columns B-4 and M-4, experience a lower displacement with respect to the columns in the middle of axis 4. This difference is between 3.0-2.0 cm at the peak response.

Furthermore, as shown in Figure 9-18, all the displacements in the Y direction match with no difference.
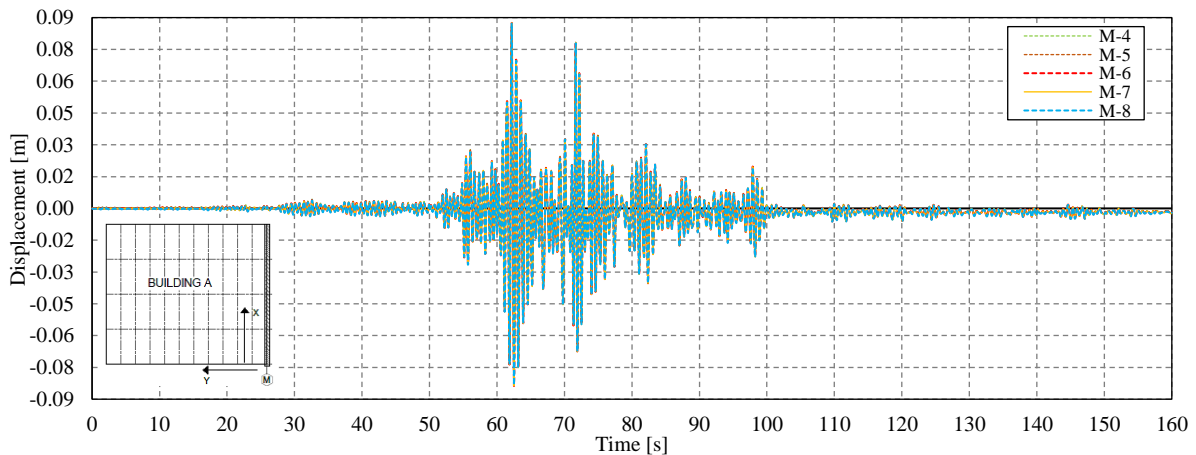

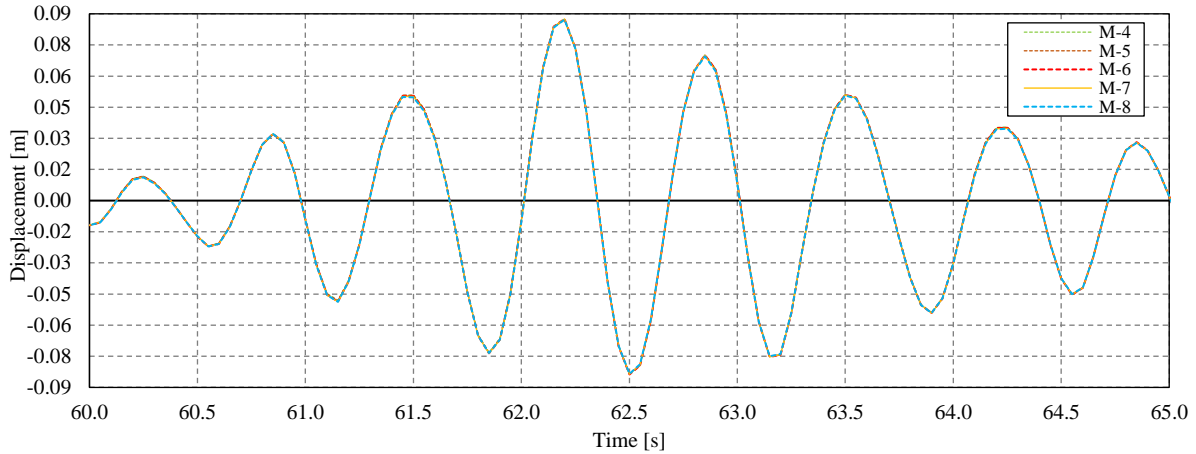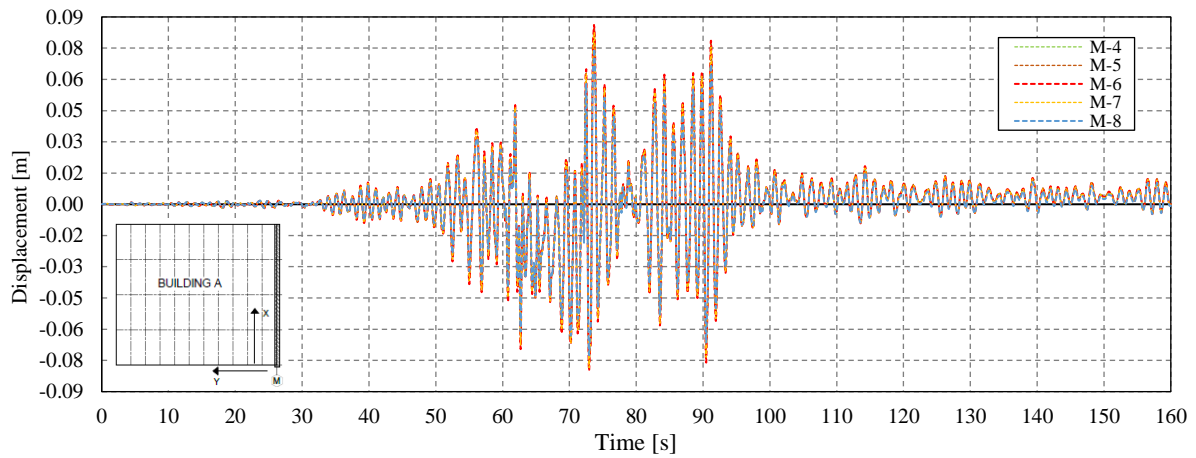Figure 9-17: Displacement U_y at the column's top comparison for Axis 4.

103
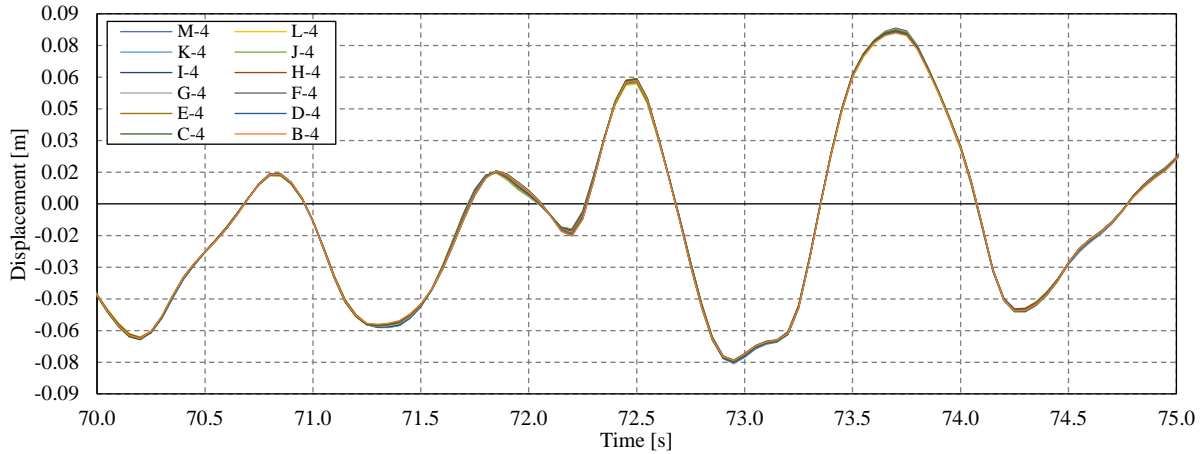
Figure 9-18: Displacement U_y at the column's top comparison for Axis 4 for the Intense time window.

For the sake of simplicity, the same comments on the dynamic response of axis 4 can be given to axis 6, which yielded the same response as axis 4. In conclusion, by studying an axis aligned with the Y direction, the columns' response in the same direction will match. Whereas, in the X direction the columns show a noticeable difference in the response when compared to an axis aligned with the Y direction. For axis 6 the response is shown from Figure 9-19 and Figure 9-22.

Figure 9-19: Displacement U_x at the column's top comparison for Axis 6.

Figure 9-20: Displacement U_x at the column's top comparison for Axis 6 for the Intense time window.

104

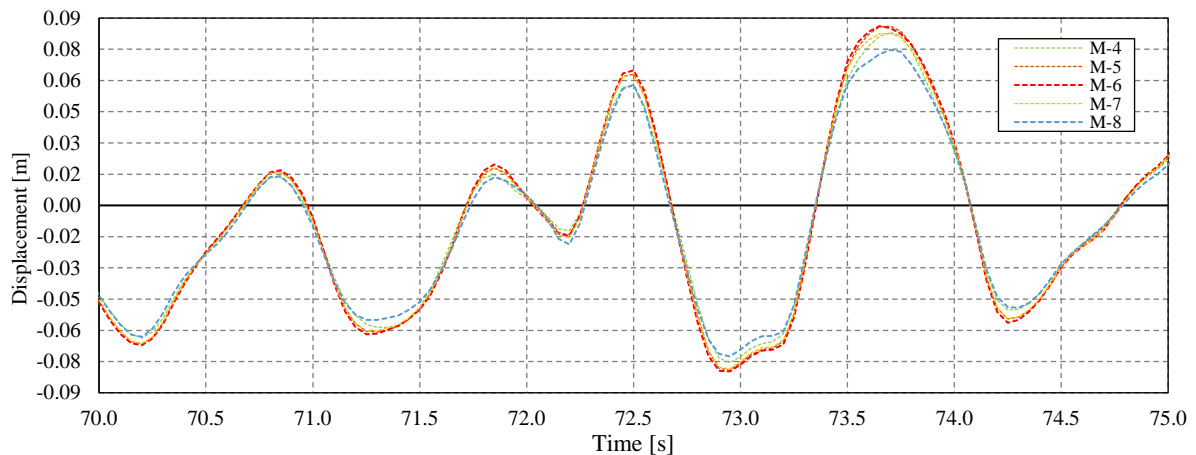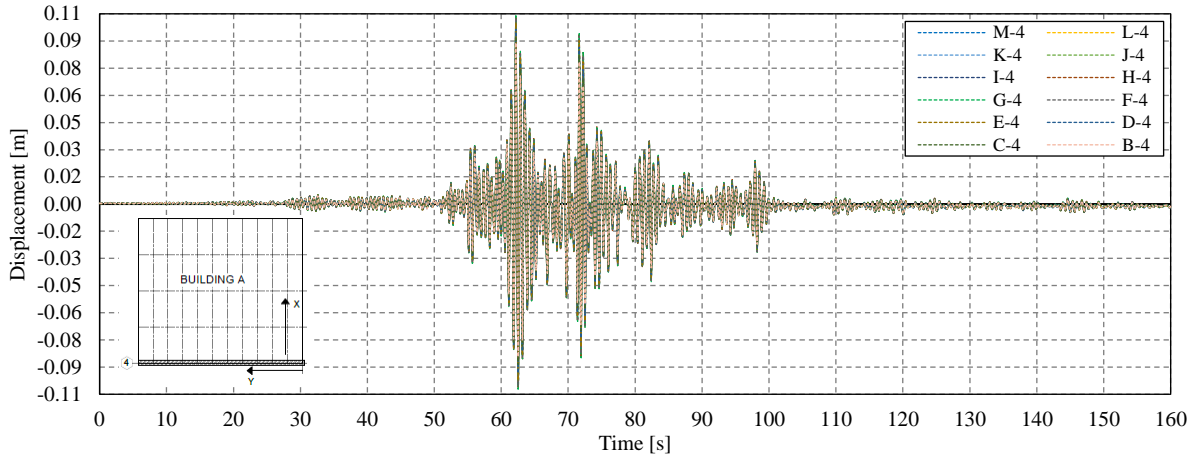Figure 9-21: Displacement U_y at the column's top comparison for Axis 6.
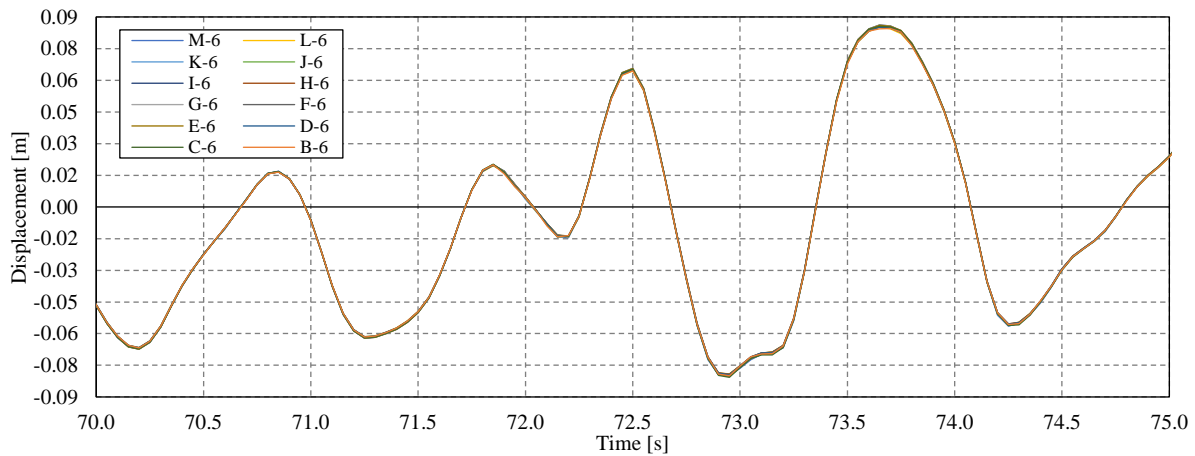
Figure 9-22: Displacement U_y at the column's top comparison for Axis 6 for the Intense time window.

9.1.5.3 Displacements comparison for the dynamic response of building B.

After showing the results for building A, the dynamic response of building B is only shown for Axis M and Axis 11, as represented in Figure 9-23. These axes are the equivalent to axes M and 4 in Building A respectively. This is related to the fact that the dynamic response found for the columns aligned in each direction is equal to the ones exemplified for Building A. Therefore, the next figures are for the sake of completeness.
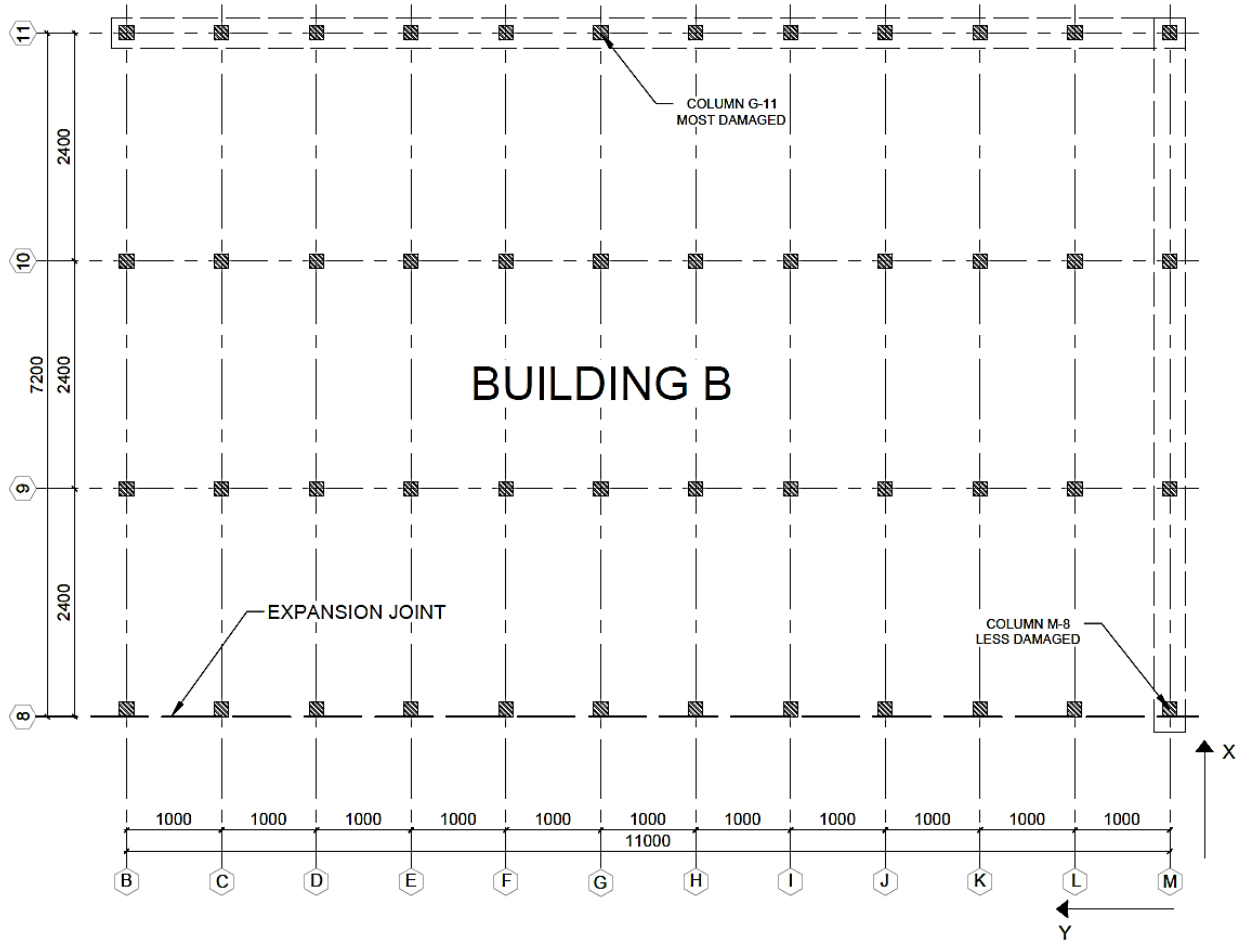
Figure 9-23: Plan view of Building B with the chosen axes for comparison (units in cm).
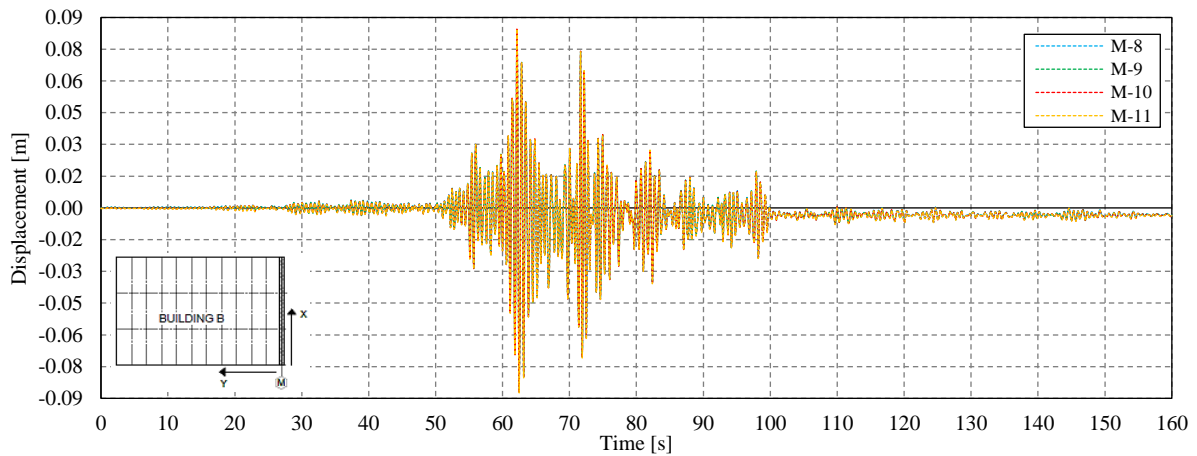
Figure 9-24: Displacement U_x at the column's top comparison for Axis M.
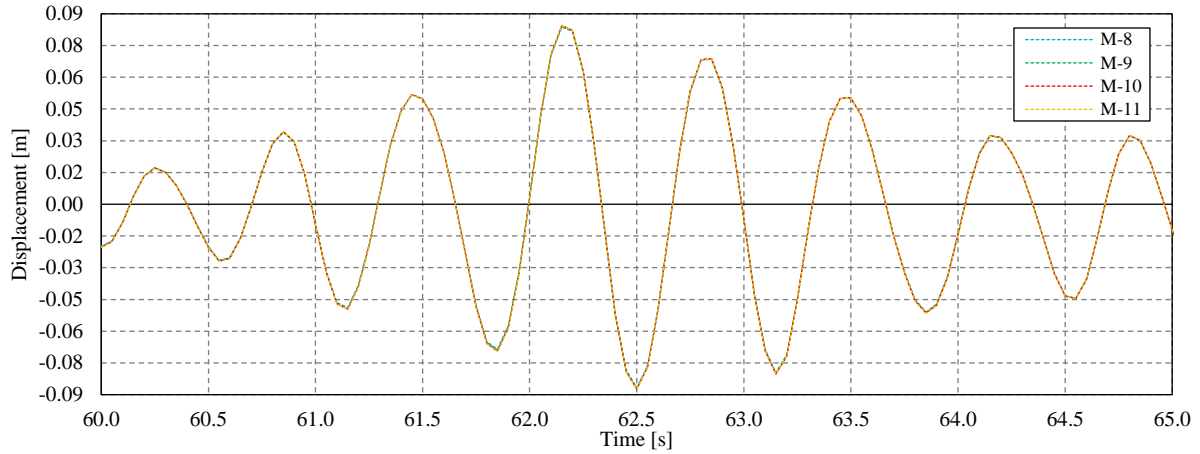
Figure 9-25: Displacement U_x at the column's top comparison for Axis M for the Intense time window.
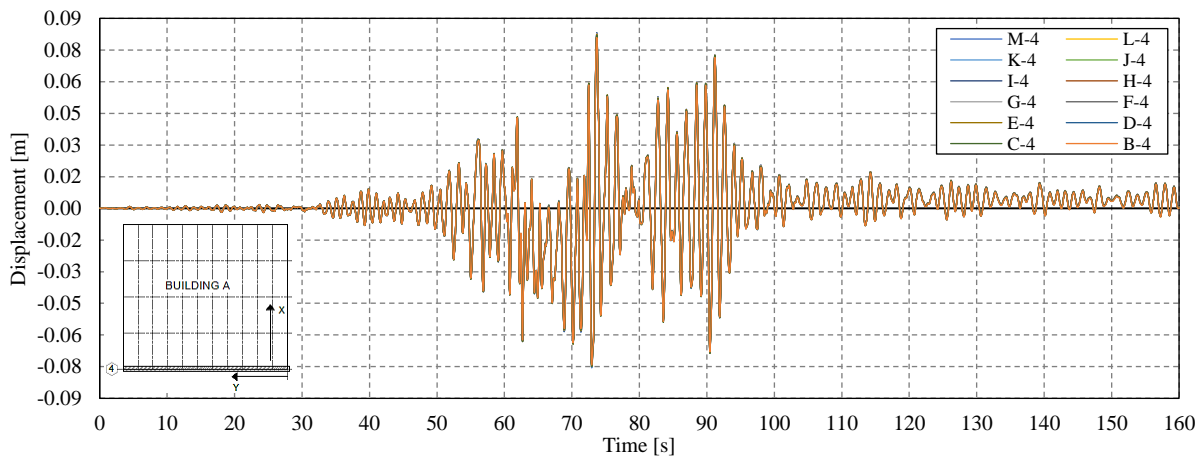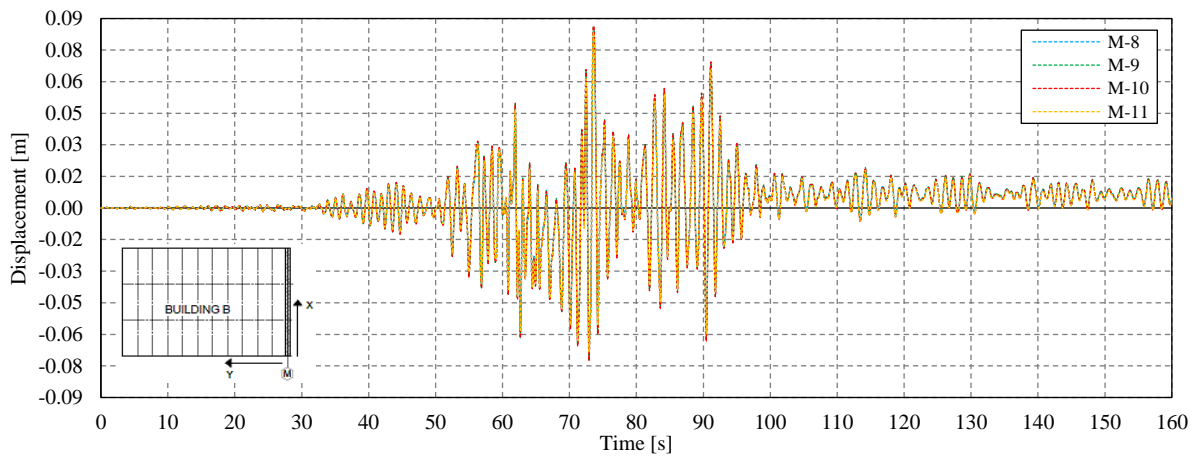

Figure 9-26: Displacement U_y at the column's top comparison for Axis M.
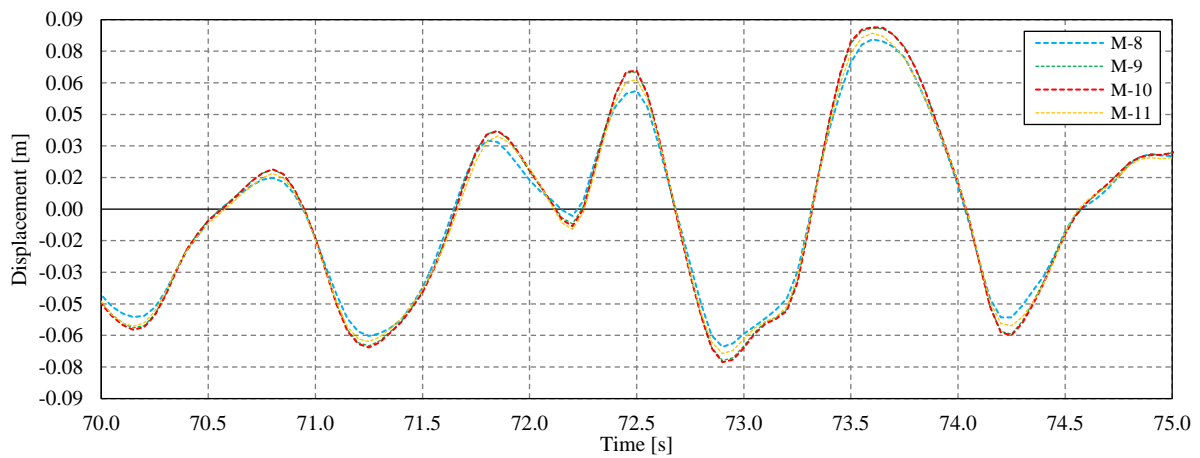
Figure 9-27: Displacement U_y at the column's top comparison for Axis M for the Intense time window.
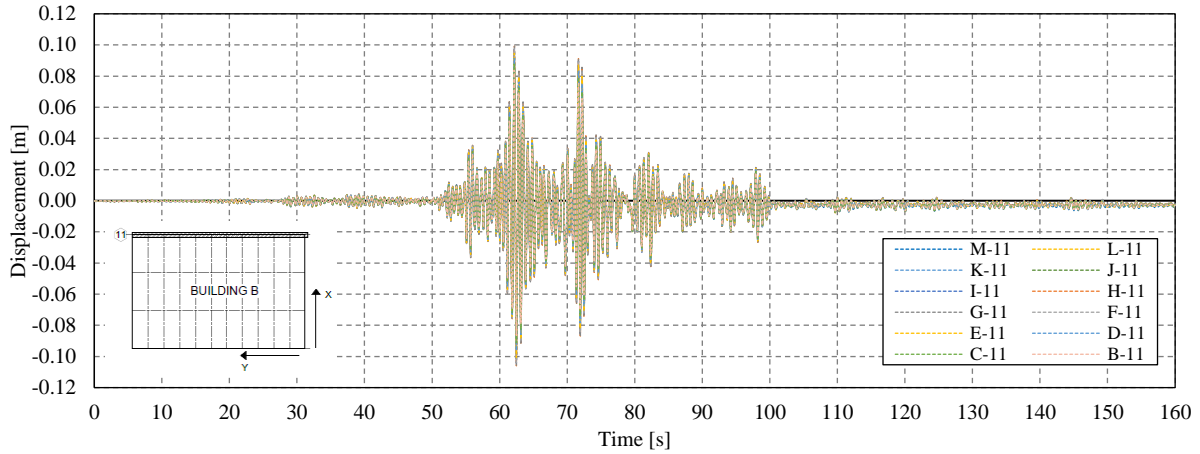
Figure 9-28: Displacement U_x at the column's top comparison for Axis 11.
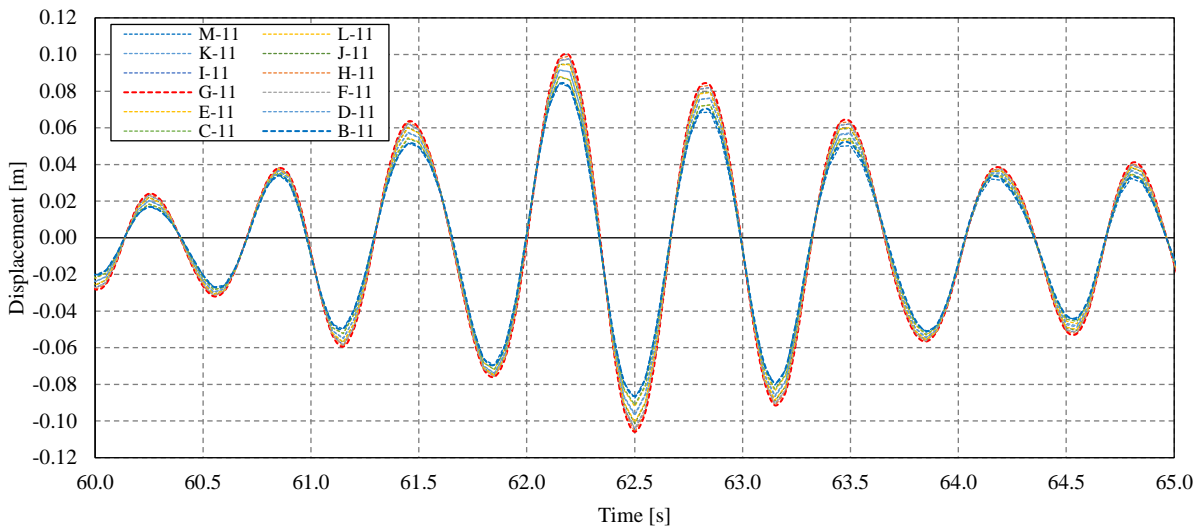
Figure 9-29: Displacement U_x at the column's top comparison for Axis 11 for the Intense time window.
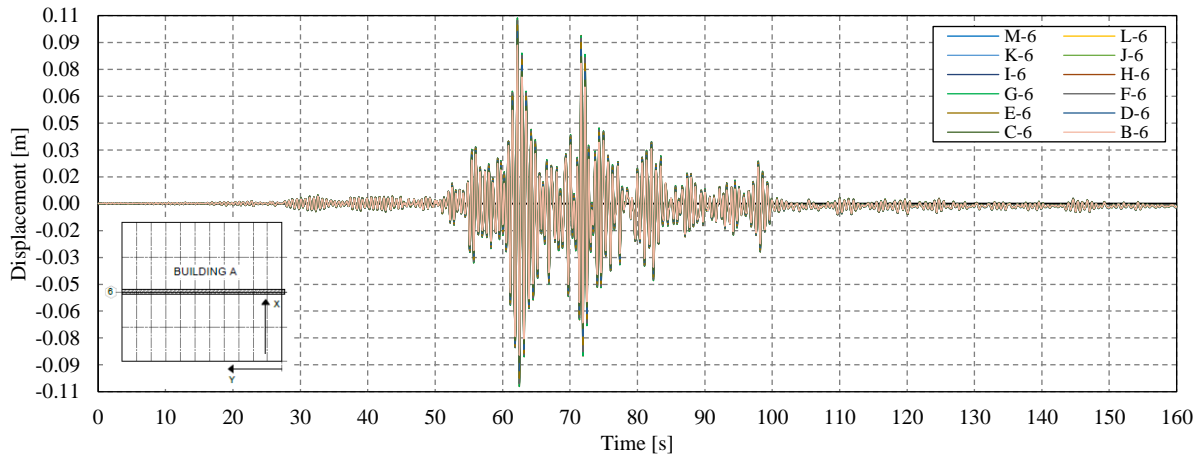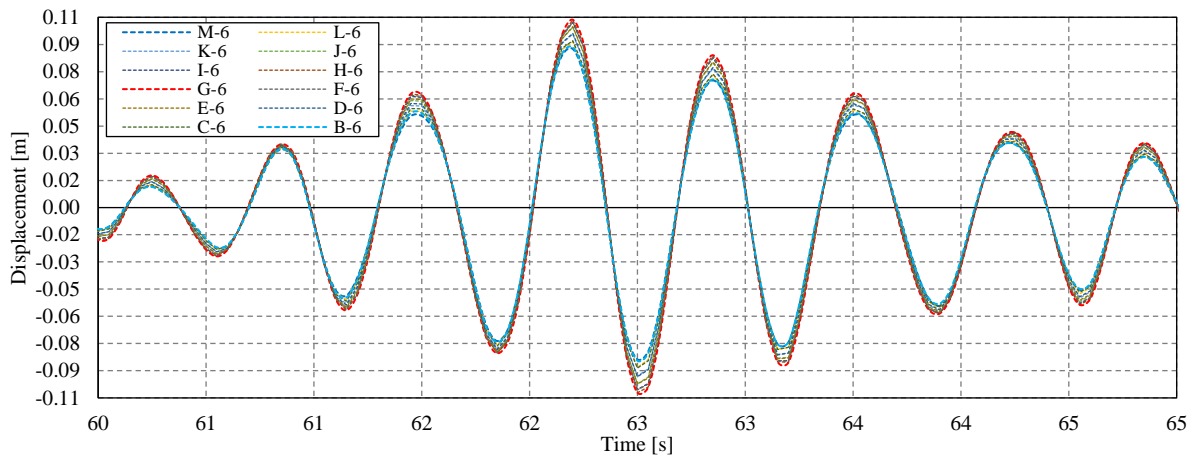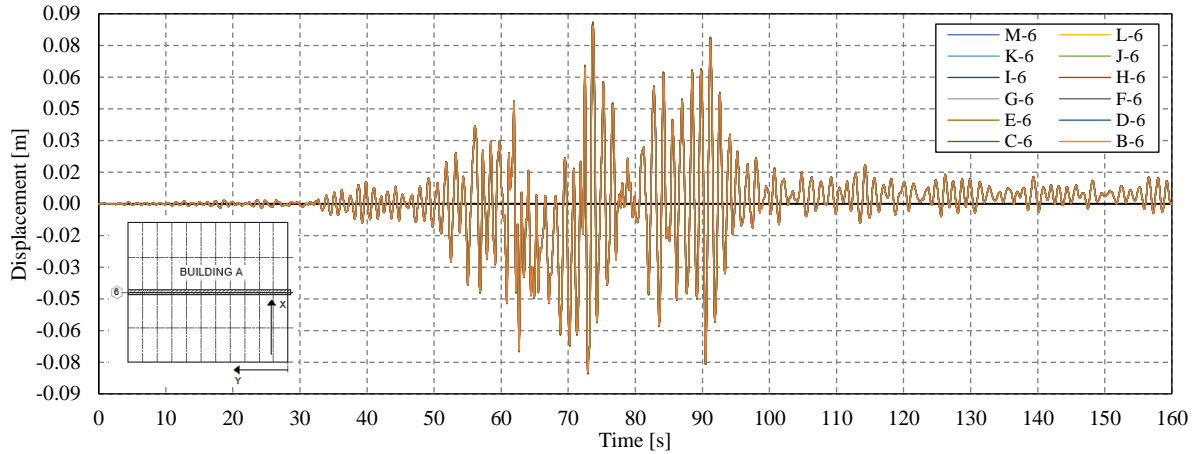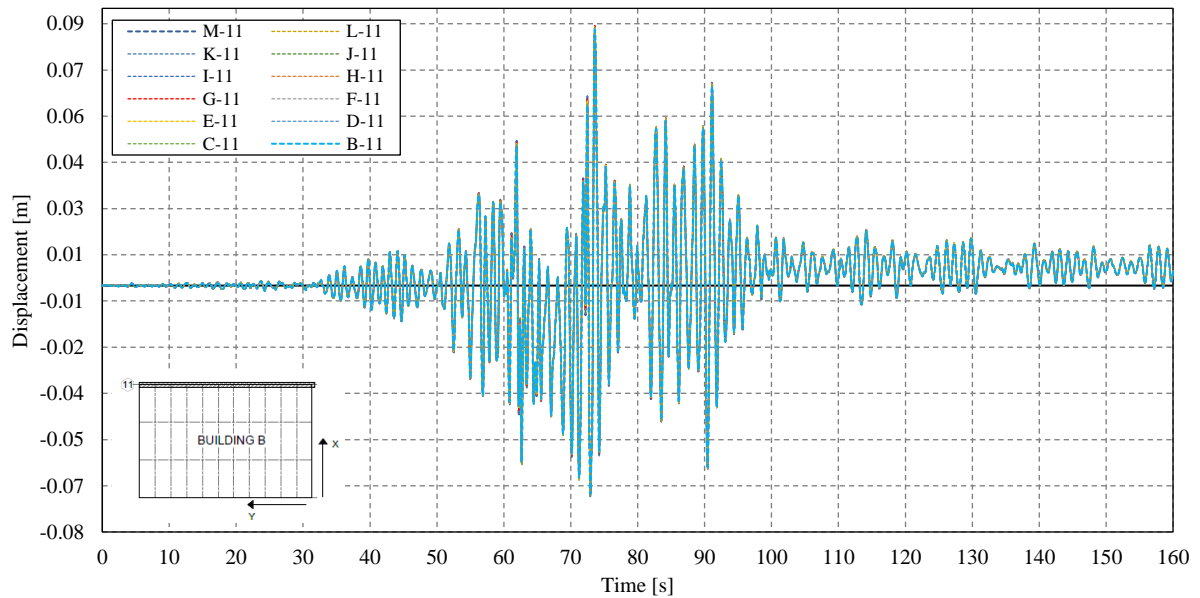

Figure 9-30: Displacement U_y at the column's top comparison for Axis 11.

108
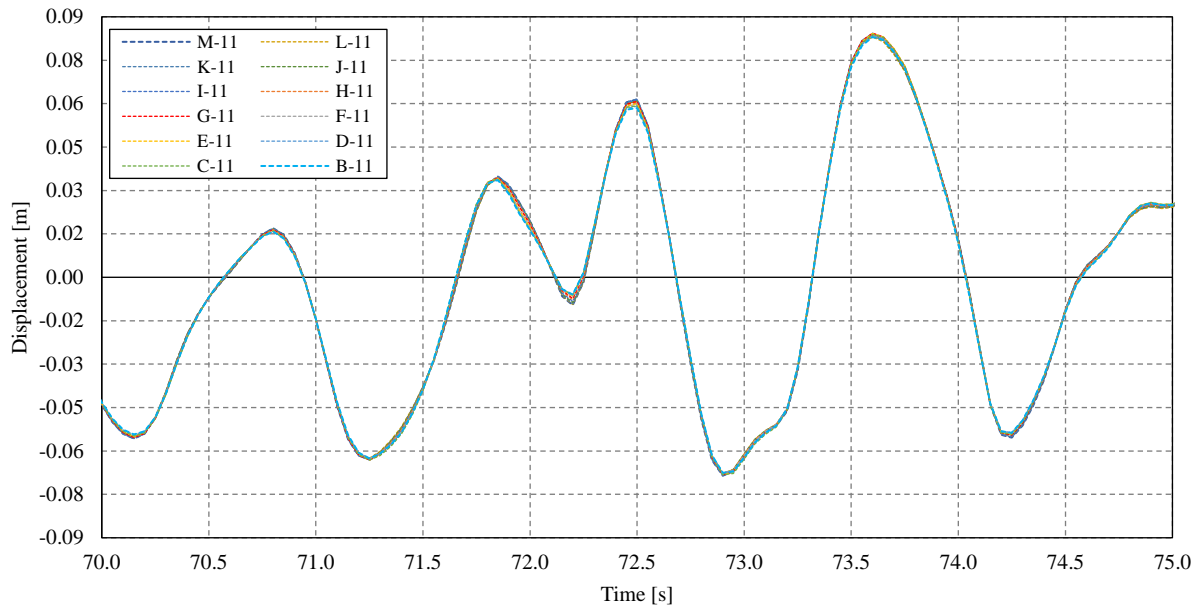
Figure 9-31: Displacement U_y at the column's top comparison for Axis 11 for the Intense time window.

9.1.5.4 Comparison of linear versus nonlinear response.

Now the comparison is made against the response in the linear range. For this purpose a linear time history analysis by modal superposition applying the loads as saw in 9.1.4 is performed. The columns displacement to be compared are G-4 for Building A and G-11 for Building B. These are the columns that experienced the largest displacement. The comparison is also made in both directions X and Y, to see the differences of the lateral forces system and how the columns sustained the damage.

The excitation of column G-4 in the X direction is shown in Figure 9-32 to Figure 9-33. For the intense time window of the earthquake, the time history of the nonlinear response is progressively departing from its linear counterpart. As shown in Figure 9-33, it can be noticed the period starts to elongate between second 61 to 62, which is directly related to the start of the damage at the base of the column.
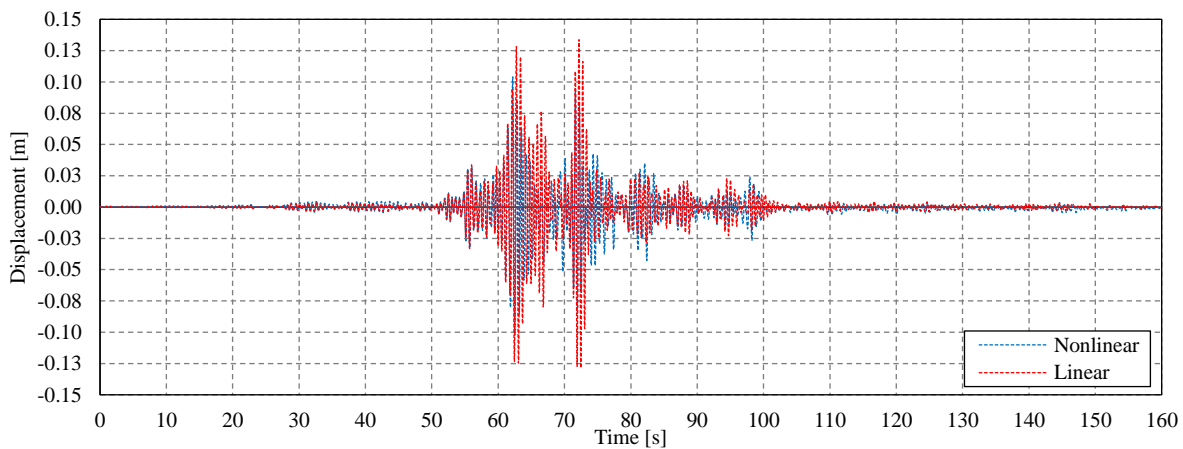
Figure 9-32: Displacement U_x for Column G-4.
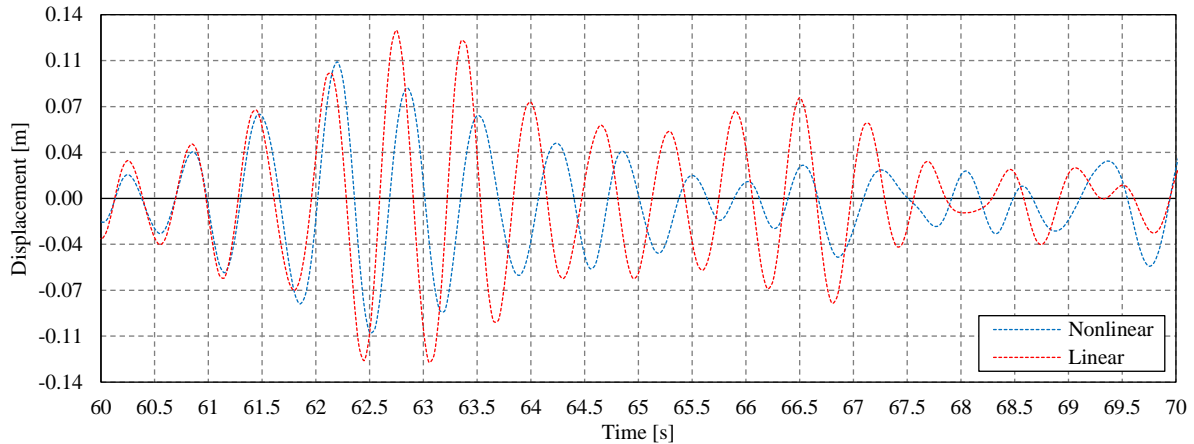
Figure 9-33: Displacement U_x for Column G-4 for the Intense part time window.

The excitation of column G-4 in the Y direction is shown in Figure 9-34 to Figure 9-35. By looking at the same intense part of the excitation shown in the X direction (around 61 to 62 seconds), the departure of the nonlinear time history from its linear counterpart is more pronounced.

As can be appreciated in Figure 9-35, a shift around -2.08 cm of the mean displacement appears between cycles from the second 62 to 72. Afterward, this shift goes back to the positive branch and remains practically stable for the rest of the analysis.
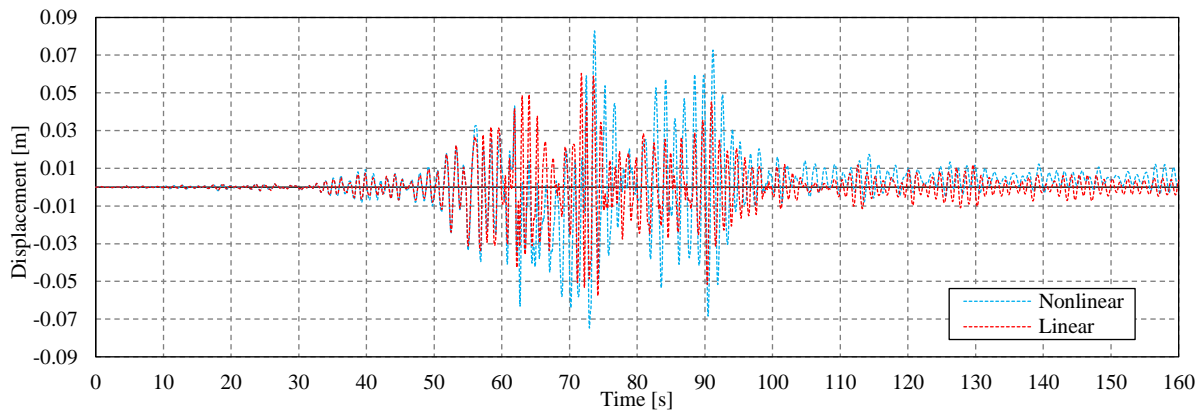
Figure 9-34: Displacement U_y for Column G-4.
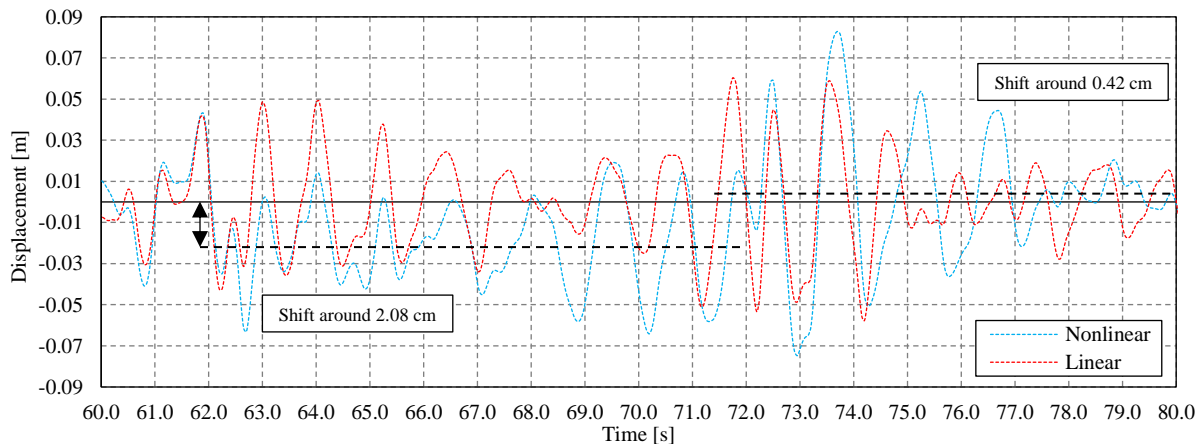
Figure 9-35: Displacement U_y for Column G-4 for the Intense part time window.

110

As commented for G-4, the same response is shown by the column G-11 from Figure 9-36 to Figure 9-39. The main difference is the shift in displacement Y, which in this case is equal to 1.64 cm in the same time window as column G-4.
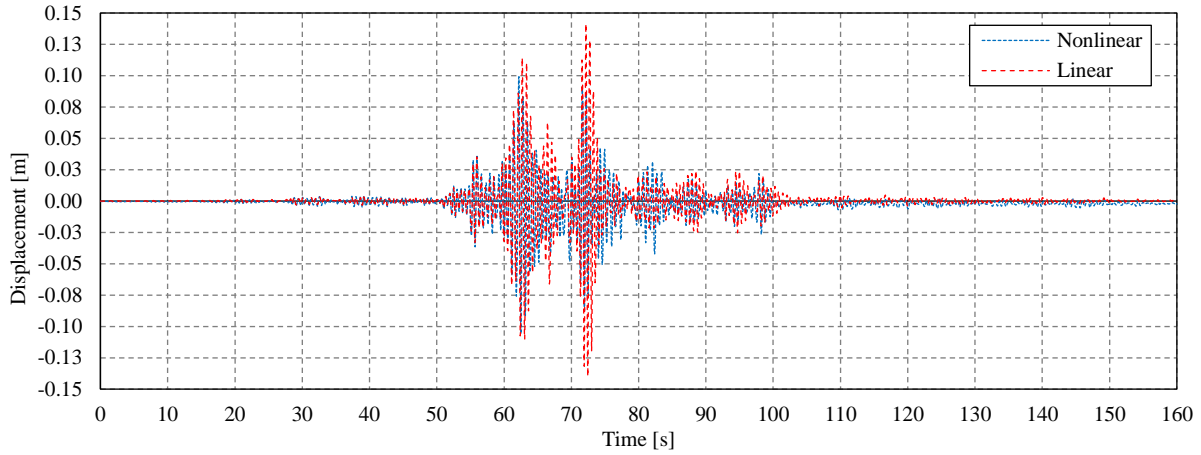
Figure 9-36: Displacement U_x for Column G-11.
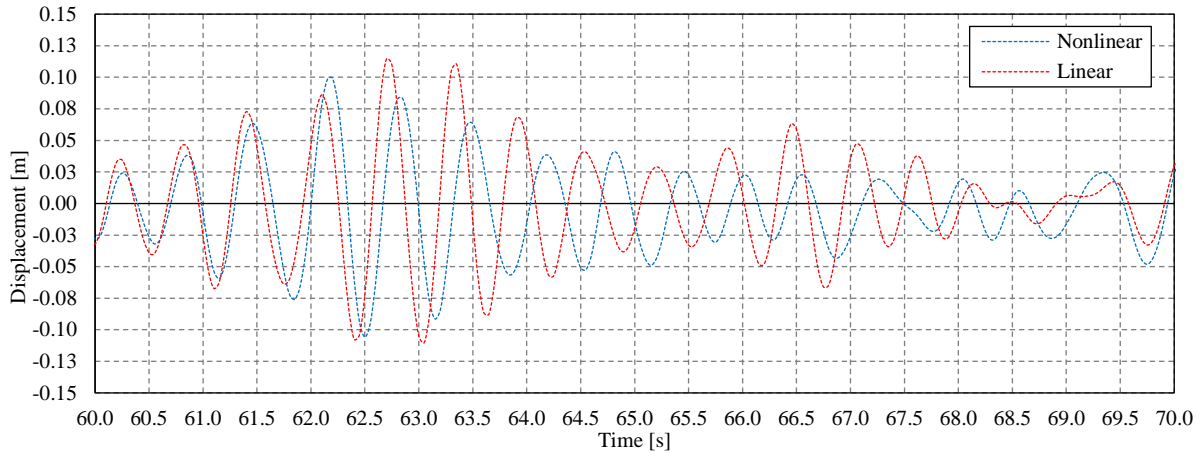
Figure 9-37: Displacement U_x for Column G-11 for the Intense part time window.
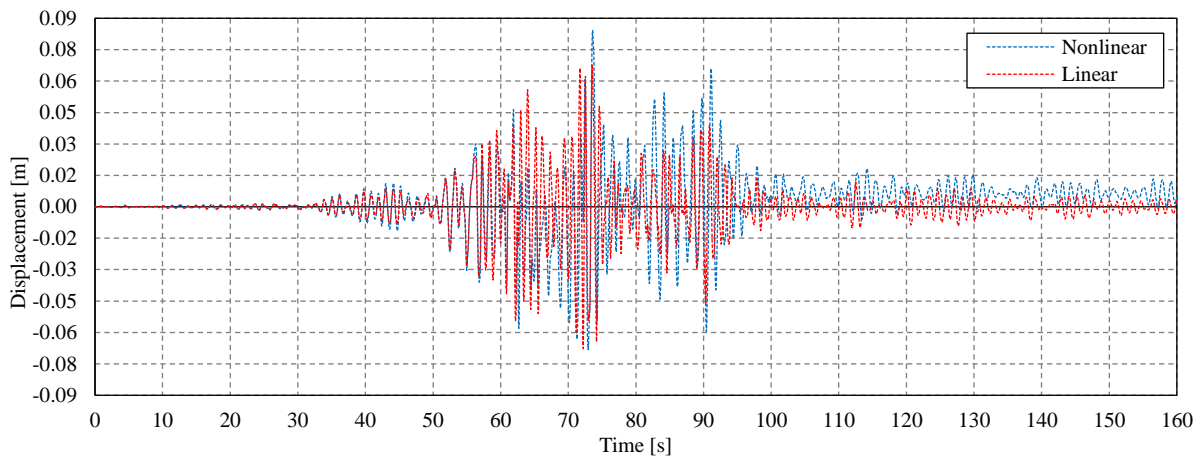
Figure 9-38: Displacement U_y for Column G-11.
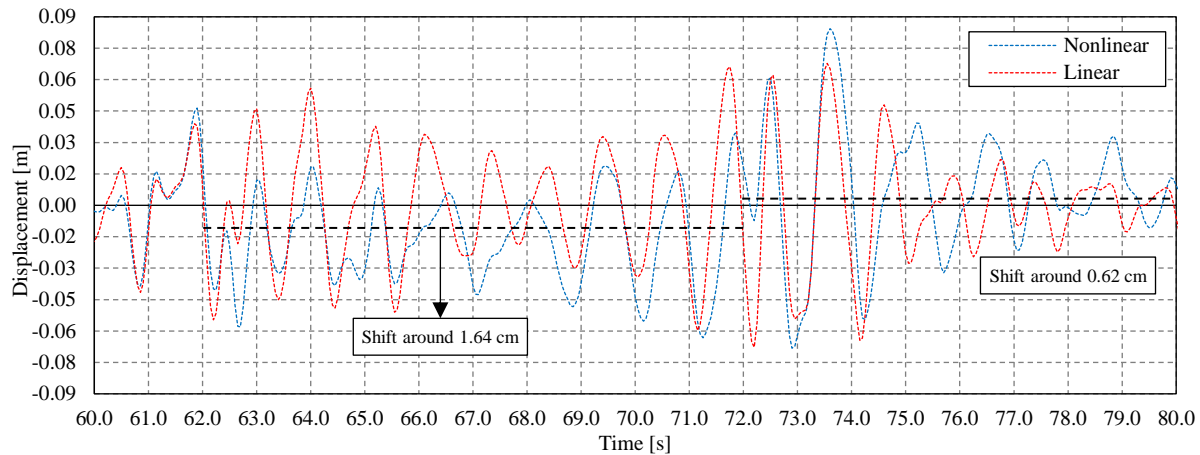
Figure 9-39: Displacement U_y for Column G-11 for the Intense part time window.

9.1.5.5 Cyclic damage observed at the base of the columns.

The fiber hinges responses in both directions are shown in Figure 9-40 to Figure 9-47. As shown previously, the responses to be presented are to exemplify the damage experienced by the columns, this is presented for the columns that suffered the largest cyclic damage. These columns are column G-4 for building A and column G-11 for building B.

The cyclic response of columns G-4 in each direction is shown in Figure 9-40 and Figure 9-41. Looking at the first figure, the cyclic response in the X direction shows stable cycles, with an estimated reduction of the stiffness around 62% with respect to the initial slope.

Instead, when looking at Figure 9-41, the cyclic response in the Y direction shows a more linear elastic behavior with small loops compared to the response in the X direction. Furthermore, a shift takes in the same time window as commented in 9.1.5.4, where the behavior remains elastic with a reduction of the stiffness. After the intense part of the earthquake ends, another shift occurs that remains closer to the axis with no reduction of the stiffness. The reduction of the stiffness is estimated to be around 72%.
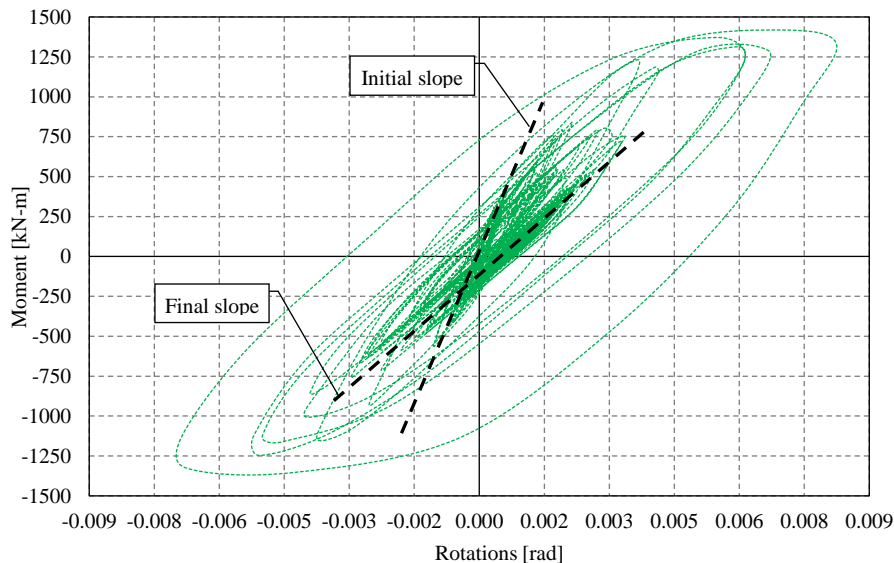
Figure 9-40: Cyclic behavior in the X direction for column G-4.

112
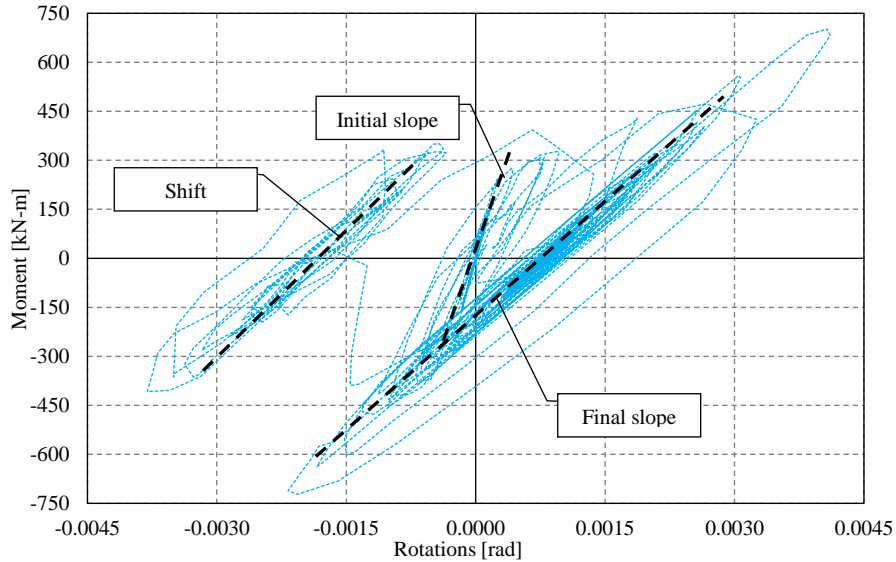
Figure 9-41: Cyclic behavior in the Y direction for column G-4.

The huge difference in the hysteretic behavior between the two orthogonal directions is connected to the lateral force system. While in the X direction the building has the frame system, whose initial period is almost half the period in the Y direction which only has the columns in cantilever. In short, the columns in the Y direction should exhibit a more linear behavior than the X direction, and the shift shown in the figures is directly related to the damage that the section suffered due to the excitation in the X direction.

For building B, column G-11 presented a similar response as G-4 as shown in Figure 9-42 and Figure 9-43. In this case, the stiffness reduction for both directions were 75% and 71%, for the X direction and Y direction, respectively.
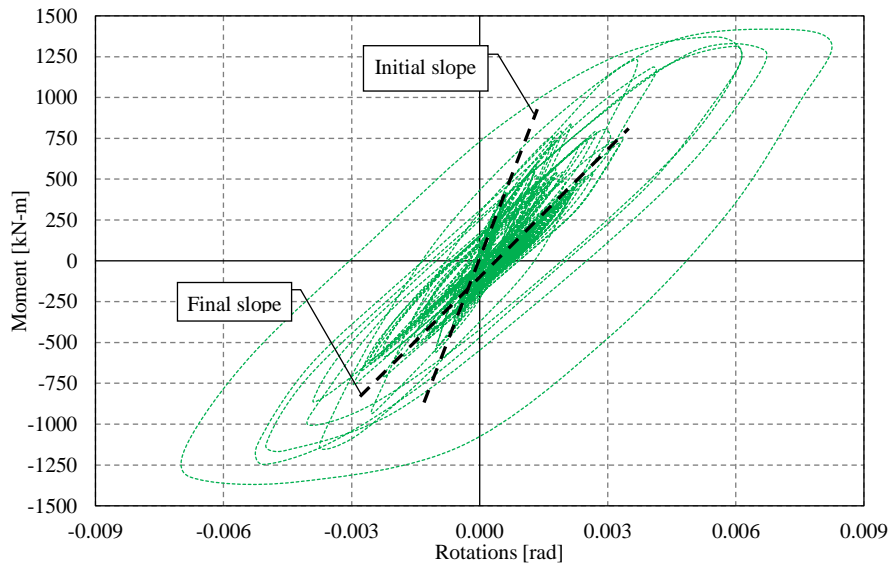
Figure 9-42: Cyclic behavior in the X direction for column G-11.
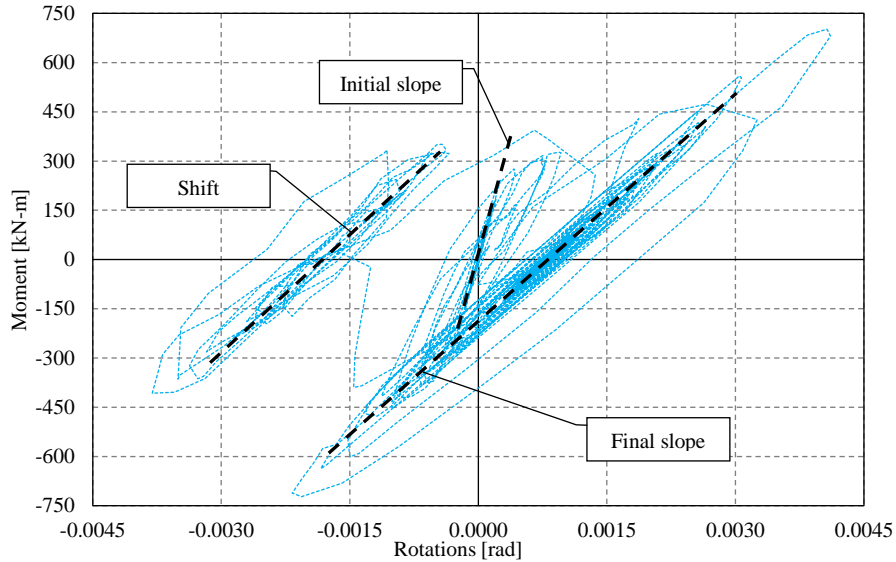
Figure 9-43: Cyclic behavior in the Y direction for column G-11.

9.1.5.6 Comparison of cyclic damage for the most damaged columns versus the less damaged.

Now, to evaluate the range of damage that the columns suffered, the extremes situation are compared. For building A, column G-4 and Column M-4 are compared; these are the most damaged and less damaged columns. For Building B, the columns selected for comparison are column G-11 and column M-8.

The responses in each direction for Building A's columns are shown in Figure 9-44 and Figure 9-45. It can be noticed in Figure 9-44 that the loops from G-4 completely envelop the smaller loops in M-4 because G-4 experienced larger bending moments. As well, this is in accordance with the displacements in the X direction that both columns experienced and showed in Figure 9-15 and Figure 9-16, since they represent the largest and the lowest displacement of all the columns in axis 4. In terms of stiffness reduction, both columns present a similar post-response slope with no significant difference.
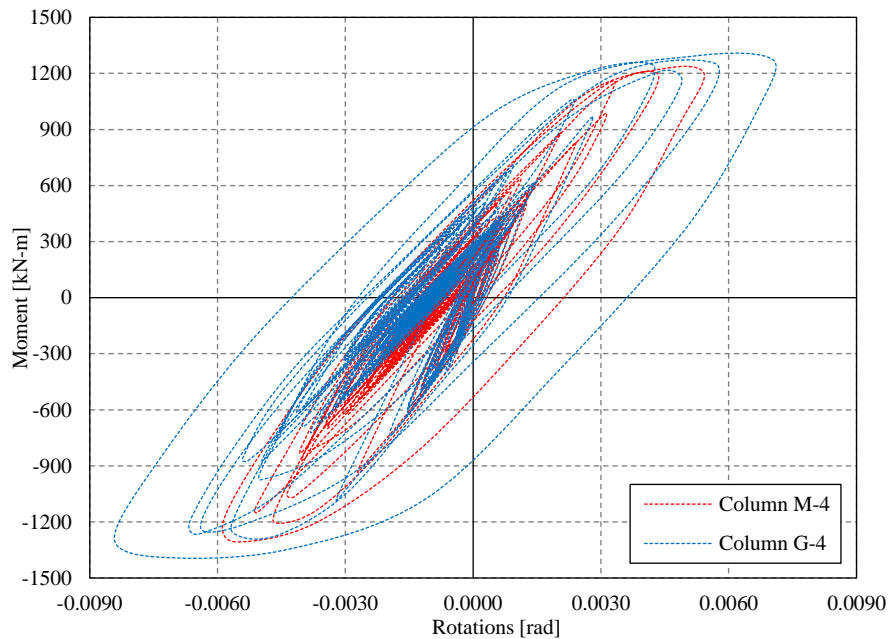
Figure 9-44: Cyclic response comparison in the X direction between column M-4 and G-4.

114

Furthermore, when looking at Figure 9-45, it can be noticed that the shift that took place in both columns match, having the same slope. Nevertheless, after this phase, the final residual rotation is larger for G-4, around 0.001 rad. The final slopes are very close.
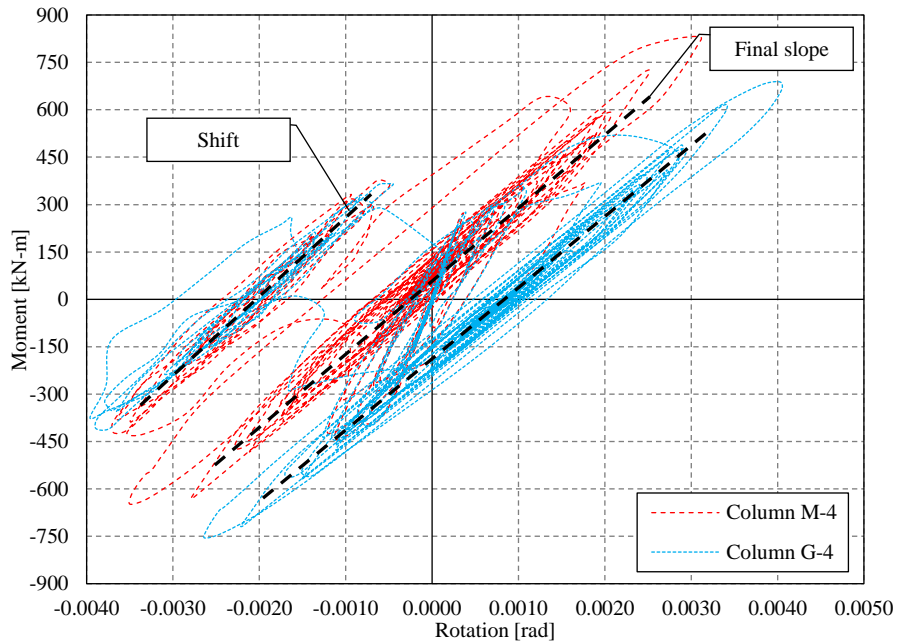
Figure 9-45: Cyclic response comparison in the Y direction between column M-4 and G-4.

For building B, the columns to be compared are Column G-11 and M-8. The responses in both directions are shown In Figure 9-46 to Figure 9-47. In this case, Column G-11 and M-8's responses yielded similar results in both directions as the columns shown for Building A. Thus, the comments that were given in the previous comparison apply to the responses of these columns.
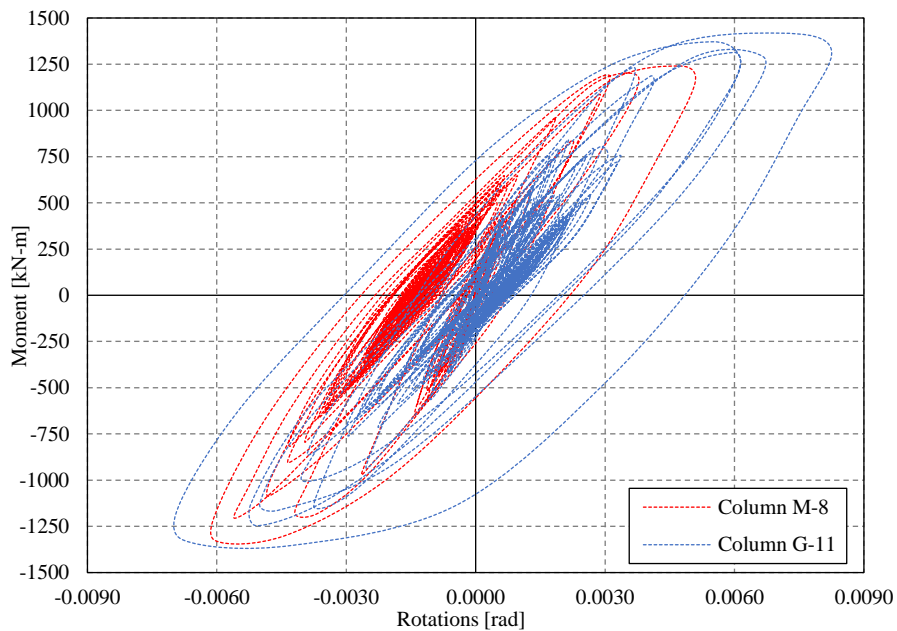
Figure 9-46: Cyclic response comparison in the X direction between column M-8 and G-11.

115
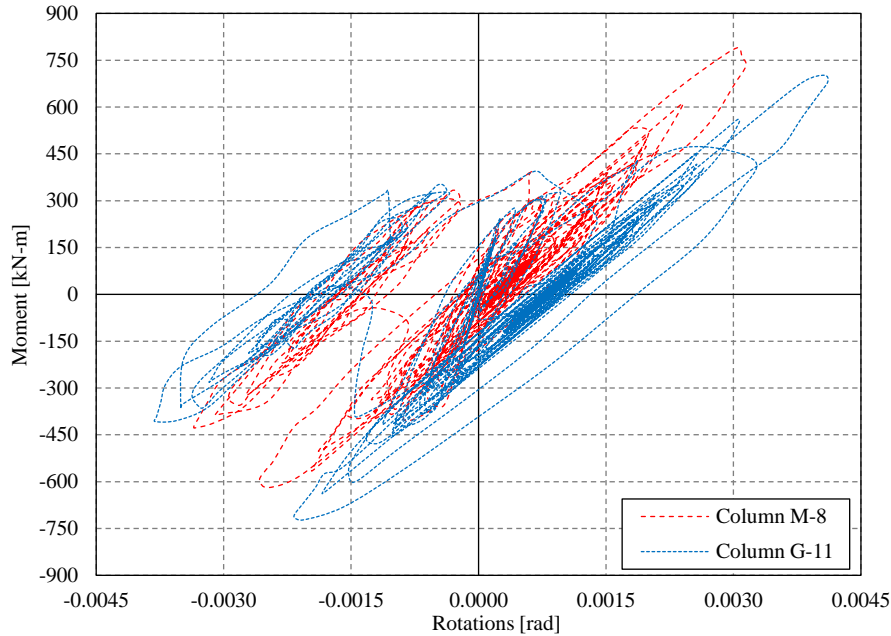
Figure 9-47: Cyclic response comparison in the Y direction between column M-8 and G-11.

9.2   Nonlinear static procedure.

In this section pushover analyses are described and carried out for both models, aiming to verify the results obtained through the nonlinear dynamic analysis and to apply the target displacement method prescribed by ASCE 41-17 [26] to assess the capacity curves obtained.

9.2.1   General hypotheses.

- Preliminary to the application of the lateral forces, the dead loads are imposed to take into account the effects of the axial load on the columns.

- The control node is selected as the joint nearest to the mass center.

- The distribution of lateral forces used to compute the capacity curves are the constant and the fundamental modal shape distribution.

9.2.2   Additional nonlinearities.

Apart from including the nonlinear behavior from the materials, SAP2000 allows to continue the analysis from a previous nonlinear case. Hence, a nonlinear case is defined to impose gravitational loads upon the structure to consider the *P-delta effects*. The combination of load for gravitational loads is shown in Eq.(8-7).

Furthermore, to increase the accuracy of the *P-delta effects* the columns are auto-subdivided by SAP2000 into shorter elements. The columns are subdivided into ten elements having a length equal to 0.975 m each. It is important to highlight that this elements' length is larger than the fiber hinges' length, so no elastic flexibility is included, as it was stated in section 8.2.3.

9.2.3 Lateral forces distribution.

Pushover analysis is carried out under conditions of constant gravity loads and monotonically increasing horizontal loads. These horizontal loads are distributed using a certain pattern, at each level of a structure where at least 2 distributions of horizontal forces are required.

- Modal pattern (F_1): where the mass proportional forces are consistent with the lateral force distribution in the direction under consideration. This is a pattern of forces on the joints that is proportional to the product of a specified mode shape times the mass on the joint.

- Uniform o constant pattern (F_2): where the mass proportional forces, regardless of the elevation. This pattern of forces only the depend on the mass on the joints.

An example of both patterns is shown in Figure 9-48.
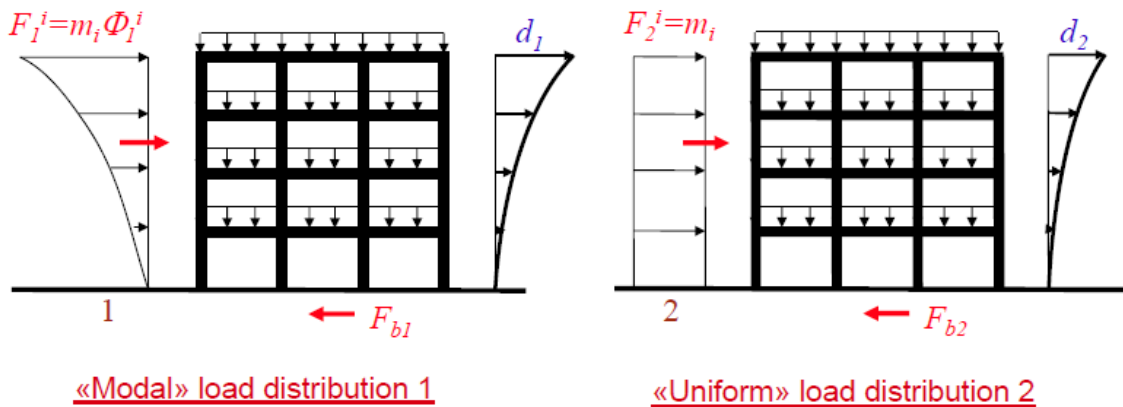
Figure 9-48: Modal and uniform lateral load distribution examples [27] .

9.2.4 Control node.

The control node to assess the displacement-force relationship of the structure must be equal to the mass center in the direction under consideration. Nevertheless, the lack of a rigid diaphragm hypothesis makes complex the evaluation of the displacement of the mass center. To overcome this problem, the nearest joint to the mass center representing a column's top is selected. This problem was already tackled in section 8.2.5 for Building A, where the location of the mass centers and the joint selected are shown in Figure 8-20, and their coordinates are shown in Table # 8-8.

For Building B the selected column's top joint is the H-10, where the coordinates are shown in Table # 9-3 and their location is shown in Figure 9-49.

Table # 9-3: Mass centers coordinates for Building B.

Mass center	X [m]	Y [m]
g_X	38.65	55.02
g_Y	36.41	55.68
Column H-10 joint	48.00	50.00
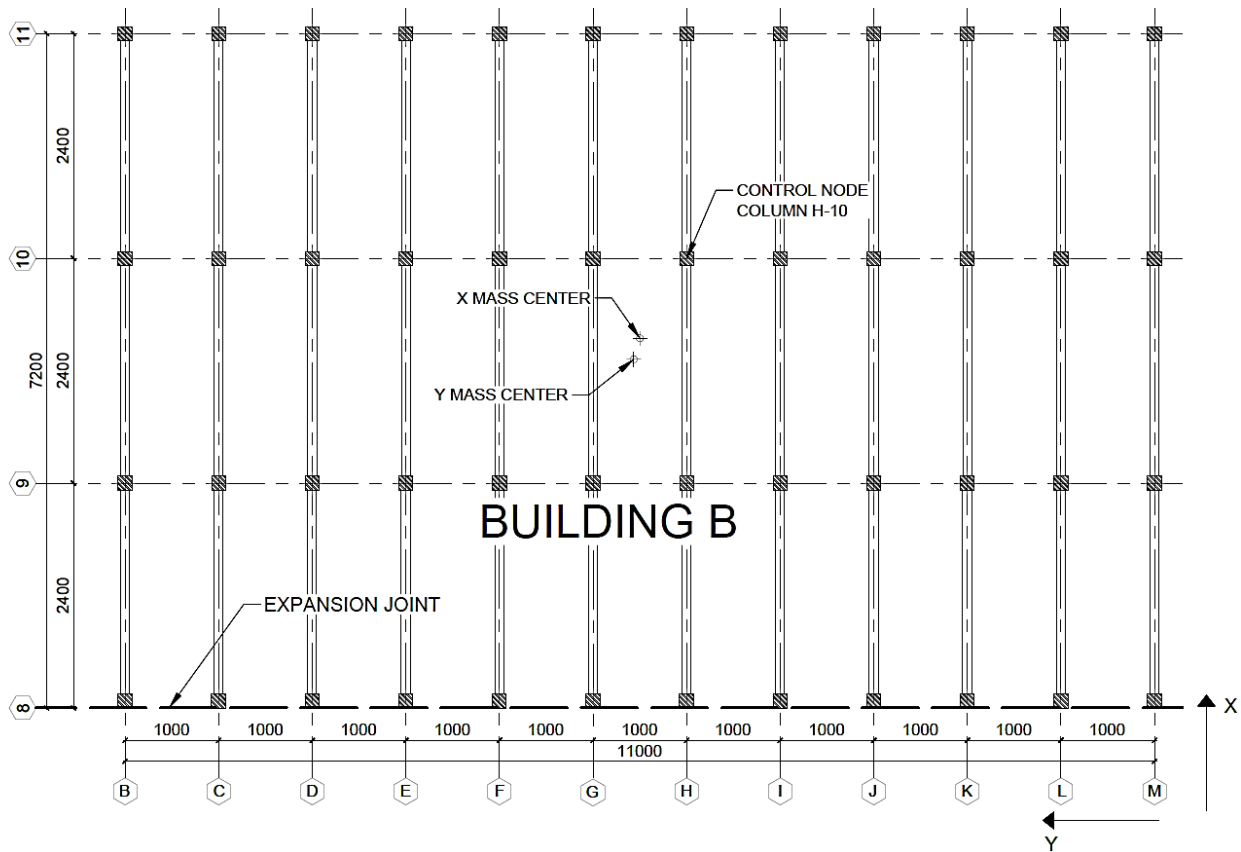
Figure 9-49: Mass centers in each direction for Building B (units in cm).

Once selected the control node, the pushover analyses should be carried out in the positive and negative verse for each direction (X and Y), by employing the aforementioned distributions of lateral forces. For consistency, each pushover analysis is set to reach a displacement of the control node equal to 0.35 m; the selection of displacement is due to the prescriptions of ASCE 41-17, since this standard suggests that the capacity curves shall be obtained for displacement ranging within 0 a 150% of the target displacement computed. Later on, it will be shown that the displacement set is sufficient to assess the results of the pushover analyses.

The capacity curves obtained for Building A are shown in Figure 9-50 to Figure 9-51 for direction X and Y, respectively. It can be appreciated immediately that independently of the verse in which the lateral forces are imposed (positive or negative) the curves are completely overlapped.
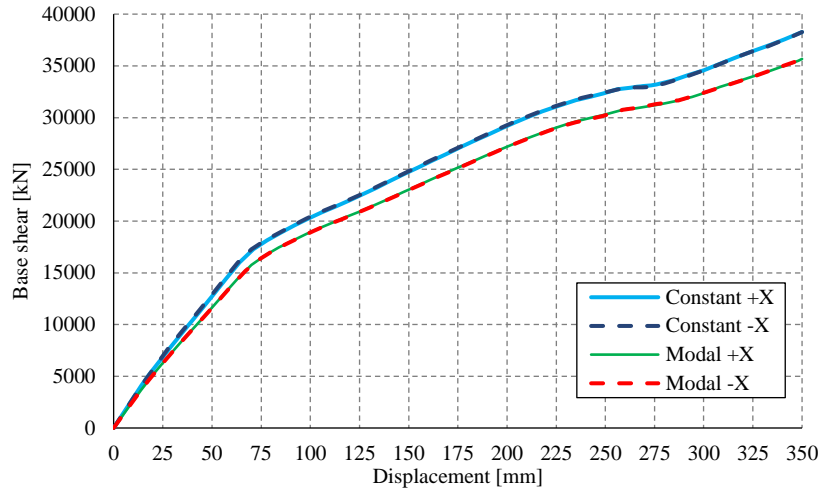
Figure 9-50: Capacity curves for Building A in the X direction.
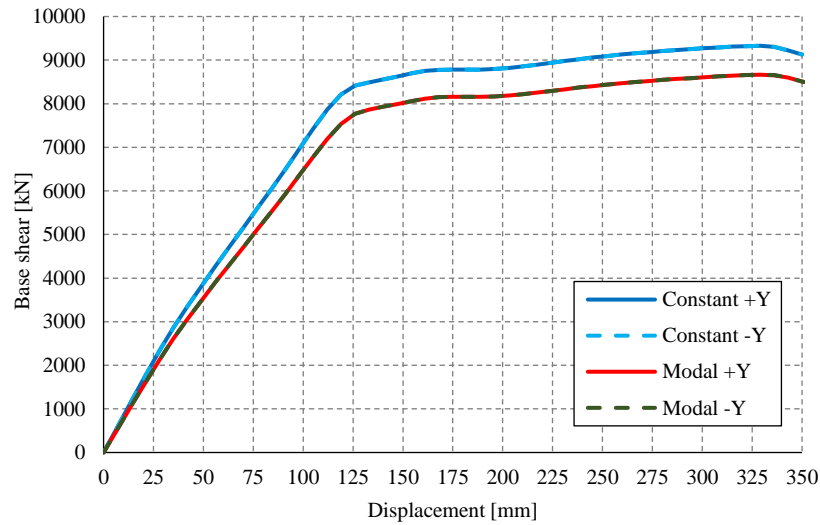
Figure 9-51: Capacity curves for Building A in the Y direction.

Furthermore, the difference in terms of base shear capacity between curves related to each lateral-force distribution is small. This might be related to the subdivision of the columns along the height as prescribed in section 9.2.2, even though almost all the mass is located at the roof, the subdivision of the frame elements along height changes the shape of the fundamental modes which affects the distribution of forces.

For the sake of completeness, the capacity curves for Building B are shown in Figure 9-52 and Figure 9-53. It is worth to mention that the same comments made for the capacity curves of Building A apply to the ones obtained for Building B.
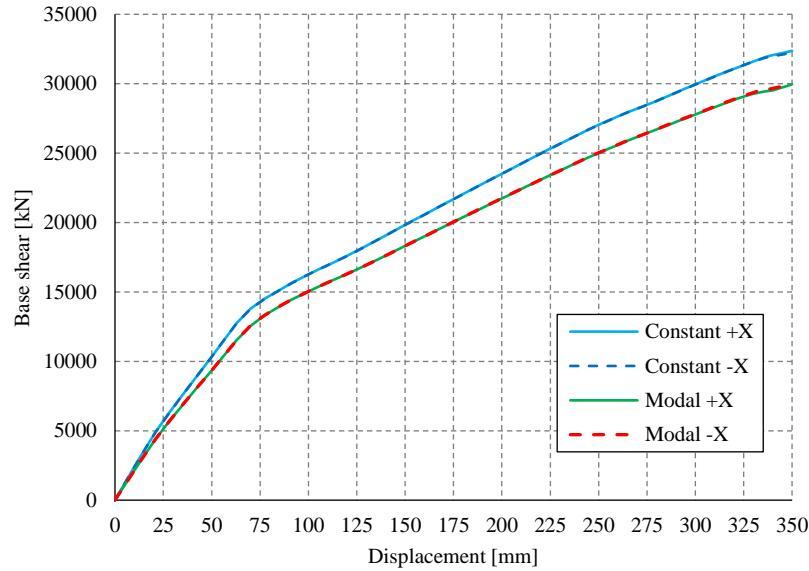
Figure 9-52: Capacity curves for Building B in the X direction.
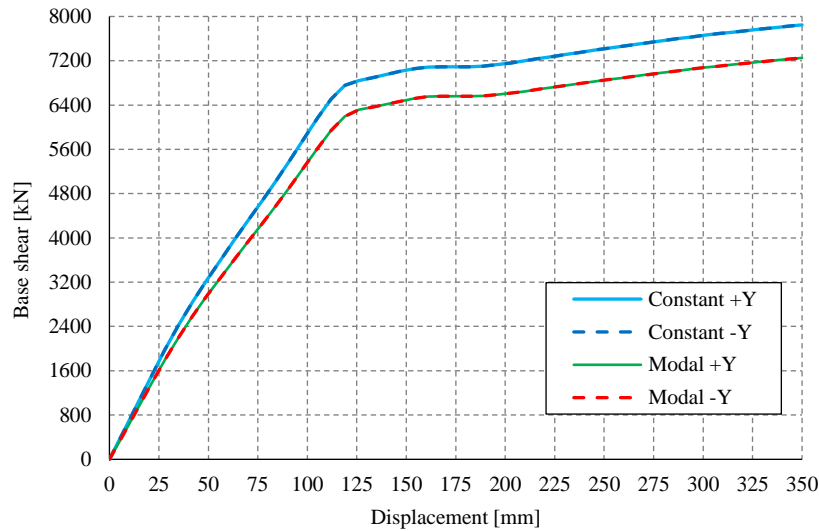
Figure 9-53: Capacity curves for Building B in the Y direction.

Now the next step is to evaluate the capacity curves through a prescribed method, in this case, the selected method is the "*target displacement method*" suggested by ASCE 41-17. For the sake of simplicity, the capacity curves evaluated throughout this method are the ones related to the positive verse for each lateral force distribution, since independently of the analysis verse the capacity curves match or have a negligible difference.

9.2.5   Target displacement method.

ASCE 41-17 prescribes a method to evaluate the capacity of the structure and the local response of the structural elements, this method is called the "*target displacement method*". It aims to build an idealized force-displacement curve, as shown in Figure 9-54, and compute a target displacement (δ_t) at which the overall response of the structure and the internal forces on the structural elements are evaluated.
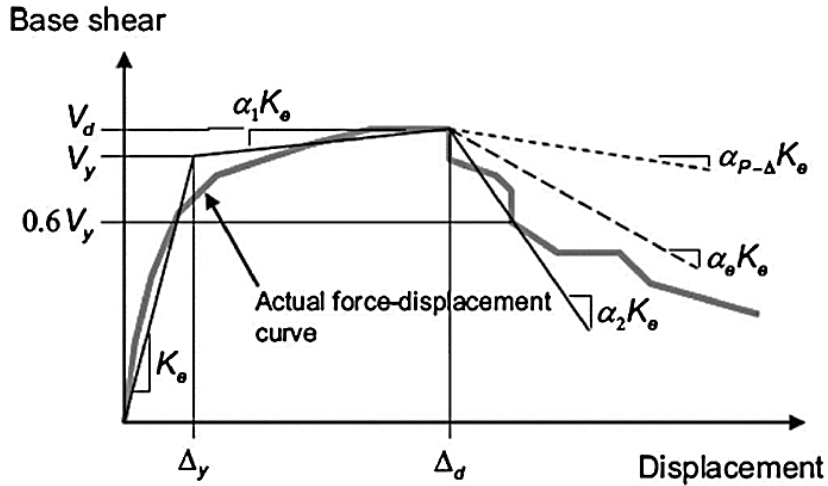
Figure 9-54: Idealized force-displacement curves [26].

The capacity curve of the multi-degree of freedom structure (MDoF) is replaced with an idealized relationship to calculate the effective lateral stiffness, K_e, and effective yield strength, V_y, of the building. The idealized curve can be divided into two parts and are listed below:

- The first-line segment shall begin at the origin and have a slope equal to K_e.

- The second line segment shall represent the positive post-yield slope ($\alpha_1 K_e$), determined by a point (V_d, Δ_d) and a point at the intersection with the first line such that the areas above and below the actual curve are approximately balanced.

Additionally, some parameters to build the idealized curve shall be defined and are listed below:

- The effective lateral stiffness (K_e) shall be taken as the secant stiffness calculated at a base shear force equal to 60% of V_y.

- The effective yield strength, V_y, shall not be taken greater than the maximum base shear force at any point along the force-displacement curve.

- (V_d, Δ_d) shall be a point on the capacity curve at the calculated target displacement, or at the displacement corresponding to the maximum base shear, whichever is less.

The Target displacement shall be computed through Eq.(9-4)

$$\delta_t = C_0 C_1 C_2 S_a \frac{T_e}{4\pi^2} g \tag{9-4}$$

The parameters related to the computation of the Target displacement are described and listed below:

C_0 is the modification factor to relate spectral displacement of an equivalent SDOF system to MDOF system and is computed by multiplying the first mode mass participation factor multiplied by the ordinate of the first mode shape at the control node.

T_e is the effective fundamental period (based on the idealized force-displacement curve) and is computed through Eq.(9-5).

121

$$T_e = T_i \sqrt{\frac{K_i}{K_e}} \qquad\qquad (9\text{-}5)$$

Where T_i = Elastic fundamental period (in seconds) in the direction under consideration, K_i = Elastic lateral stiffness of the building in the direction under consideration.

C_1 is the modification factor to relate the expected maximum inelastic displacements to displacements calculated for linear elastic response and is computed through Eq.(9-6). For periods greater than 1.0 s, C_1 shall be taken equal to 1.0.

$$C_1 = 1 + \frac{(\mu_{strength} - 1)}{aT_e^2} \qquad\qquad (9\text{-}6)$$

Where $\mu_{strength}$ = is the ratio of elastic strength demand to yield strength coefficient. (So-called R or q factor), a = is a parameter related to a class site, in this case, is set equal to 60 for a site class D (Equivalent to Soil type III).

C_2 is the modification factor to represent the effect of pinched hysteresis shape, cyclic stiffness degradation, and strength deterioration on the maximum displacement response and can be computed through Eq.(9-7). For periods greater than 0.7 s, C_2 shall be taken equal to 1.0.

$$C_2 = 1 + \frac{1}{800} \left(\frac{\mu_{strength} - 1}{T_e} \right)^2 \qquad\qquad (9\text{-}7)$$

$\mu_{strength}$ can be computed through Eq.*(9-8)*.

$$\mu_{strength} = \frac{S_a}{V_y/W} C_m \qquad\qquad (9\text{-}8)$$

Where C_m = is the effective mass factor, in this case, is set equal to 1.00 from *Table 7-4* [26], W = is the effective seismic weight.

S_a is the spectral acceleration at the effective fundamental period and damping ratio of the building in the direction under consideration and can be obtained from the elastic spectra related to the Maule earthquake, as shown in Figure 9-55.
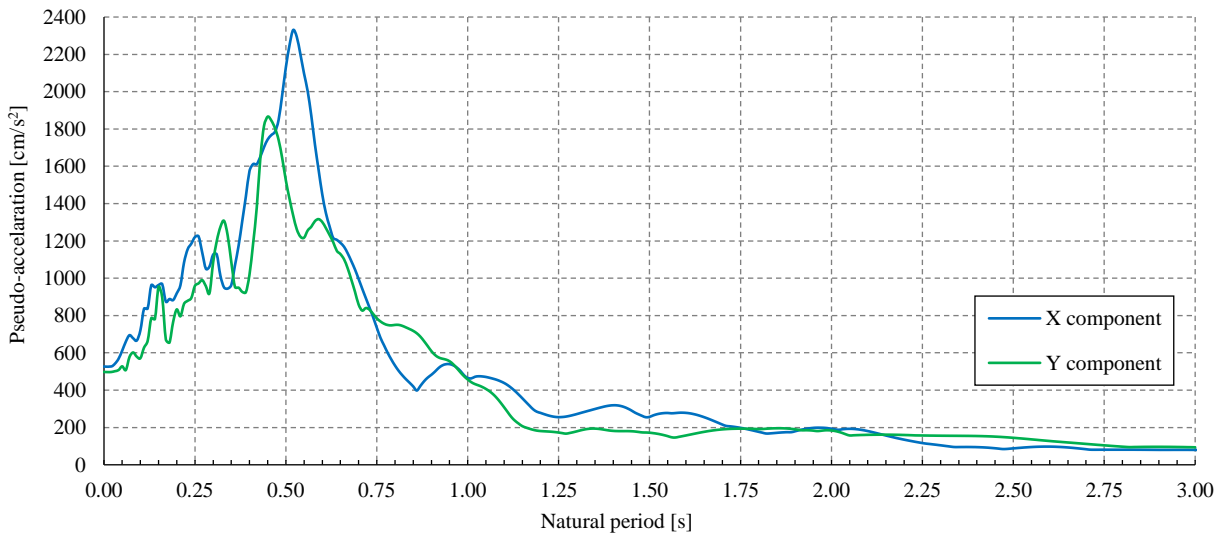
Figure 9-55: Elastic response spectrum for the Maule earthquake components.

9.2.5.1   Results for the Target displacement method.

After running the analyses, SAP2000 allows to compute the aforementioned parameters for the capacity curves obtained. For the sake of simplicity, the evaluation of the capacity curves is explained for Building A since comments given on the results obtained apply also for Building B.

The parameters corresponding to each pushover analysis for Building A are listed in Table # 9-4.

Table # 9-4: Target displacement parameters for Building A's capacity curves.

Pushover analysis	Constant +X	Modal +X	Constant +Y	Modal +Y
Modification factor C_0 [-]	1.049	1.069	1.024	1.028
Modification factor C_1 [-]	1.206	1.191	1.000	1.000
Modification factor C_2 [-]	1.000	1.000	1.000	1.000
Spectral acceleration S_a [g]	1.274	1.224	0.265	0.199
Effective fundamental period T_e [s]	0.63	0.66	1.12	1.17
Fundamental period T_i [s]	0.60	0.62	1.12	1.17
Effective yielding strength V_y [kN]	16823	15847	2741	2455
Initial lateral stiffness K_i [kN/m]	292945	268652	84304	76661
Effective lateral stiffness K_e [kN/m]	263963	239767	84304	76661
Second-segment slope percentage α_1 [-]	0.3490	0.3570	0.76	0.77
Strength ratio $\mu_{strength}$ [-]	2.232	2.276	2.85	2.39
Effective seismic Weight W [kN]	29471	29471	29471	29471
C_m [-]	1.000	1.000	1.000	1.000
Target displacement δ_t [m]	0.159	0.166	0.085	0.070
Target-displacement's base shear V_t [kN]	25598	24380	6113	4733

Furthermore, the capacity curves together with their corresponding idealized curve are plotted and shown in Figure 9-56 and Figure 9-57. It can be appreciated that the target displacement for the X direction lands in a post-yield branch with a reduced slope, evidencing the damage that the Maule earthquake excitation should impose in this direction at the base of the columns.

Additionally, in the Y direction, it can be seen that the target displacement showed lands in the post-cracking elastic branch, as shown in Figure 9-57. Hence, this confirms the fact that there was a reduction in the elastic stiffness imposed by the Maule earthquake excitation in the Y direction, but not sufficient to reach the post-yield branch.
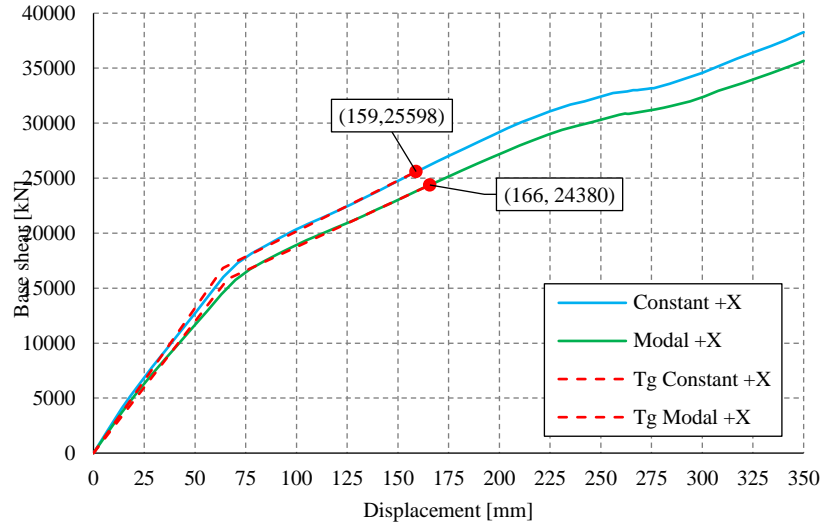
Figure 9-56: Target displacements for Building A capacity curves in the X direction.
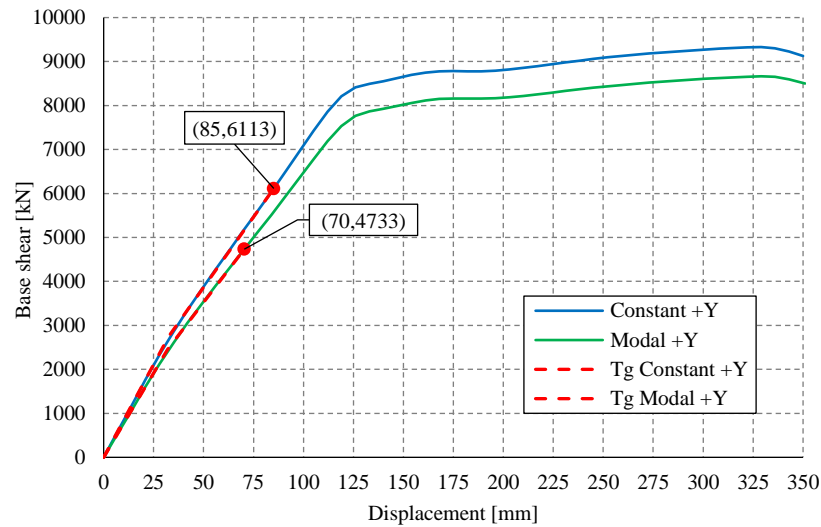
Figure 9-57: Target displacement for Building A capacity curves in the Y direction.

To have a clearer picture of the response of the structure, the local response of the columns is commented on to explain further the previous conclusions. For the sake of comparison, the columns selected are the ones previously shown to exemplify the hysteretic response by performing the nonlinear dynamic analysis, and they correspond to the columns G-4 and M-4, as shown in Figure 9-6.

To compare the pushover results versus the nonlinear dynamic ones, the moment-rotation diagrams (M-ϑ) are plotted up to the target displacement computed for each pushover analysis and then overlapped with the hysteretic results previously obtained.

In the case of column G-4, the comparison is shown in Figure 9-58 and Figure 9-59.

Figure 9-58: Comparison of the pushover analysis results versus the hysteretic results for Column G-4 in the X direction.

As shown in Figure 9-58, the monotonic curves coming from the pushover analyses agree with the peaks shown for the hysteretic response at the G-4 column's base, and it can be seen that rotations reached during the hysteretic response do not overcome the target-displacement's demand. It can be stated that the demand imposed by the target displacement method might be overestimating the state of damage that should be found at the columns' base as a consequence of the Maule earthquake excitation in the X direction.

This goes in agreement with the conservative nature of a static analysis procedure as the pushover analysis that tries to capture the nonlinear dynamic response of the structure. Thus, these results verify the nonlinear dynamic results found in the X direction, since the hysteretic response remains bounded by a more conservative procedure.

Furthermore, when looking at the response in the Y direction the pushover analyses show just a post-cracking slope that is quite close to the slopes found for the hysteretic response. Additionally, the target-displacement's demand coming from the Maule earthquake spectrum in the Y direction does not impose a displacement on the structure that yields a state of damage at the columns' base.

These results agree with the hysteretic response obtained by the nonlinear dynamic analysis since in both cases the behavior remains linear with a similar slope, as shown in Figure 9-59. Moreover, the Y direction should exhibit a more linear behavior than the X direction, as previously shown in 9.1.5.5, and the shift shown in the figure for the hysteretic response is directly related to the damage that the section suffered due to the excitation in the X direction.

Figure 9-59: Comparison of the pushover analysis results versus the hysteretic results for Column G-4 in the Y direction.

In the case of column M-4 that represents one of the less damaged columns, the comparison of the results are shown in Figure 9-60 and Figure 9-61. It can be appreciated that in the X direction's response the hysteretic loops remain close to the elastic branch of the moment-rotation diagrams from the pushover analyses and show a small incursion on the post-elastic branch, unlike column G-4. The damage showed hysteretic response falls quite far from the computed state of damaged imposed by the target displacement method, confirming what was previously said for the excitation X for columns G-4 and the conservative nature of the method.

Furthermore, the comments given for the response in the Y direction for columns G-4 for apply for the results obtained throughout the pushover analyses in column M-4.

Figure 9-60: Comparison of the pushover analysis results versus the hysteretic results for Column M-4 in the X direction.

126
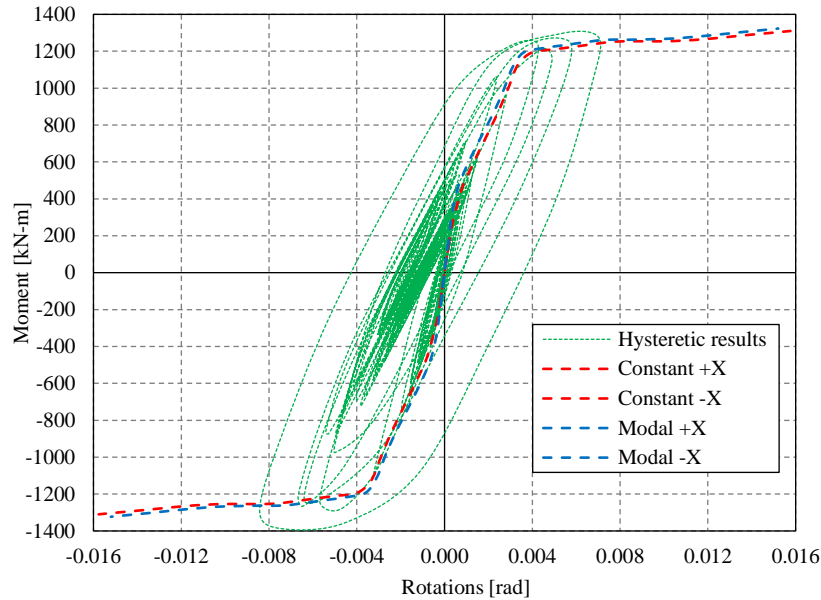
Figure 9-61: Comparison of the pushover analysis results versus the hysteretic results for Column M-4 in the Y direction.

Now for the sake of completeness, the evaluation of the capacity curves throughout the target displacement method are shown for Building B. The parameters corresponding to each pushover analysis are listed in Table # 9-5

Table # 9-5: Target displacement parameters for Building B's capacity curves.

Pushover analysis	Constant +X	Modal +X	Constant +Y	Modal +Y
Modification factor C_0 [-]	1.050	1.074	1.014	1.015
Modification factor C_1 [-]	1.220	1.206	1.000	1.000
Modification factor C_2 [-]	1.000	1.000	1.000	1.000
Spectral acceleration S_a [g]	1.457	1.274	0.380	0.248
Effective fundamental period T_e [s]	0.605	0.629	1.076	1.129
Fundamental period T_i [s]	0.578	0.602	1.076	1.129
Effective yielding strength V_y [kN]	13140	12288	2429	2302
Initial lateral stiffness K_i [kN/m]	236437	211748	70883	64289
Effective lateral stiffness K_e [kN/m]	215690	193918	70883	64289
Second-segment slope percentage α_1 [-]	0.347	0.358	0.740	0.735
Strength ratio $\mu_{strength}$ [-]	2.51	2.35	3.55	2.45
Effective seismic Weight [kN]	22673	22673	22673	22673
Cm [-]	1.000	1.000	1.000	1.000
Target displacement δ_t [m]	0.171	0.161	0.112	0.080
Target-displacement's base shear V_t [kN]	21373	19066	6495	4401

Furthermore, the capacity curves together with their corresponding idealized curve are plotted and shown in Figure 9-62 and Figure 9-63. The columns selected to compare the results as previously done for Building A, correspond to G-11 and G-8. That are the columns previously shown to exemplify the hysteretic response by performing the nonlinear dynamic analysis, as shown in Figure 9-23.

To compare the pushover results versus the nonlinear dynamic ones, the moment-rotation diagrams (M-ϑ) are plotted up to the target displacement computed for each pushover analysis and then overlapped with the hysteretic results. The comparison for column G-11 is shown in Figure 9-64 and Figure 9-65, whereas for column G-8 is shown in Figure 9-66 and Figure 9-67. It is worth to mention that the given remarks for the columns' response for Building A apply to the columns' response for Building B.
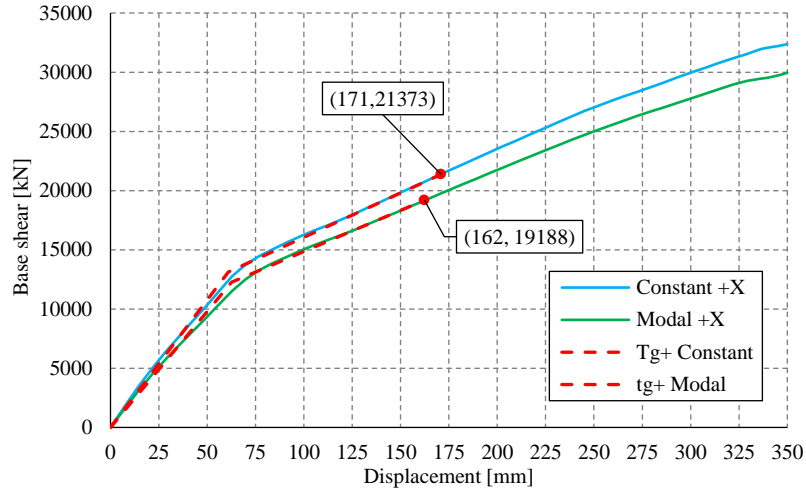
Figure 9-62: Target displacements for Building B capacity curves in the X direction.
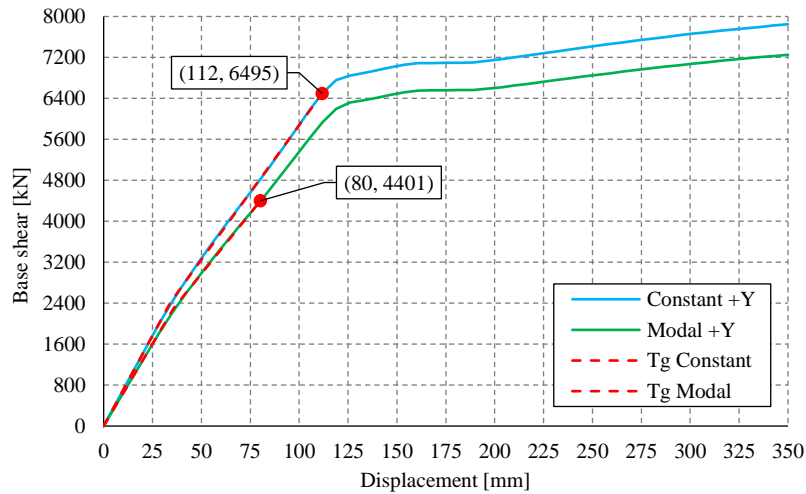
Figure 9-63: Target displacements for Building B capacity curves in the Y direction.
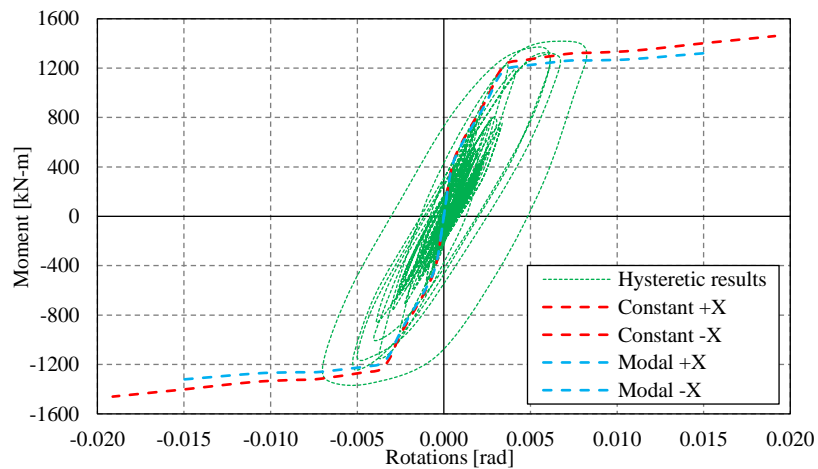
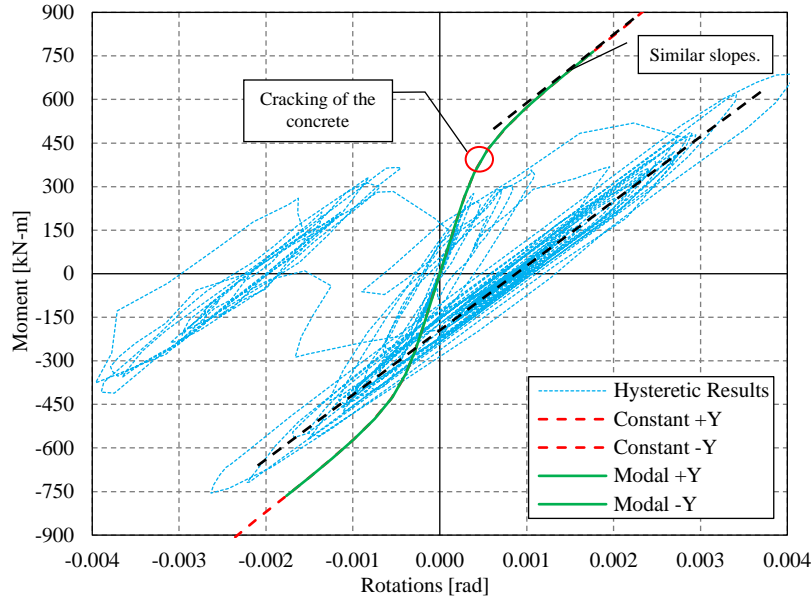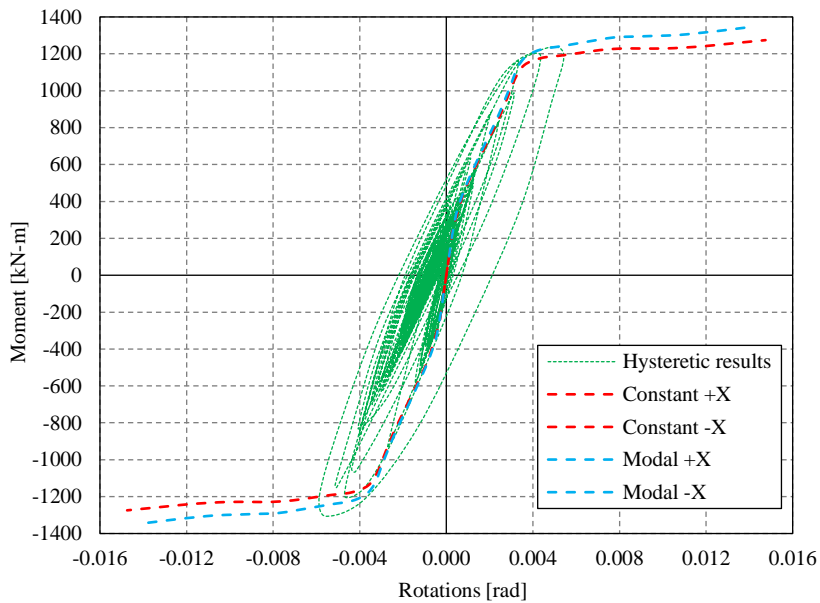Figure 9-64: Comparison of the pushover analysis results versus the hysteretic results for Column G-11 in the X direction.

128
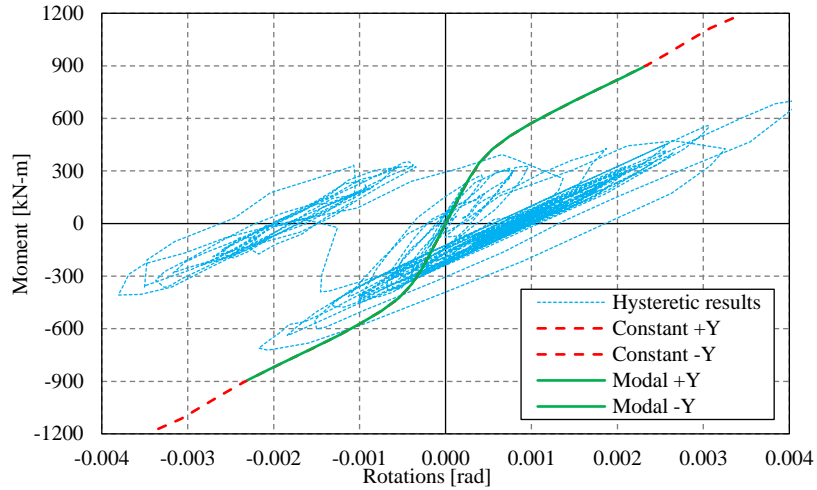
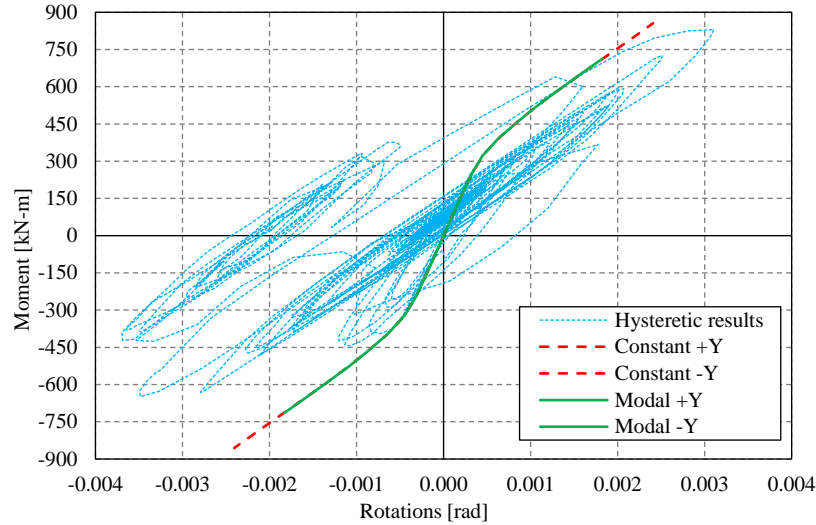Figure 9-65: Comparison of the pushover analysis results versus the hysteretic results for Column G-11 in the Y direction.
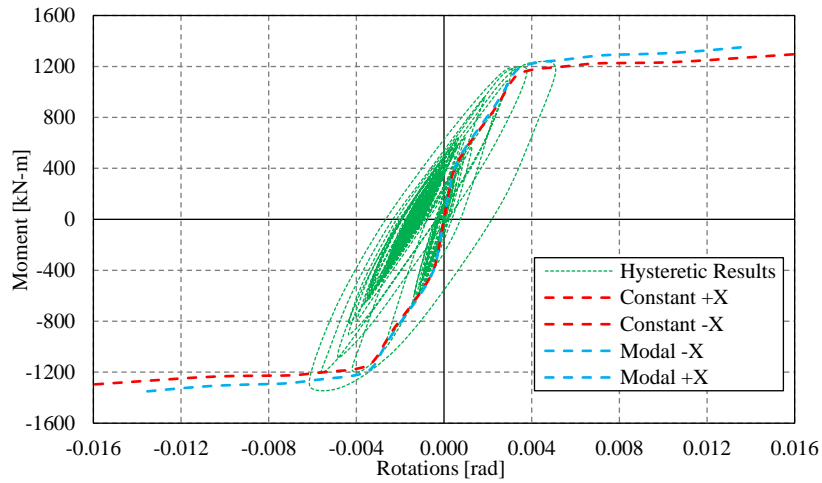
Figure 9-66: Comparison of the pushover analysis results versus the hysteretic results for Column G-8 in the X direction.
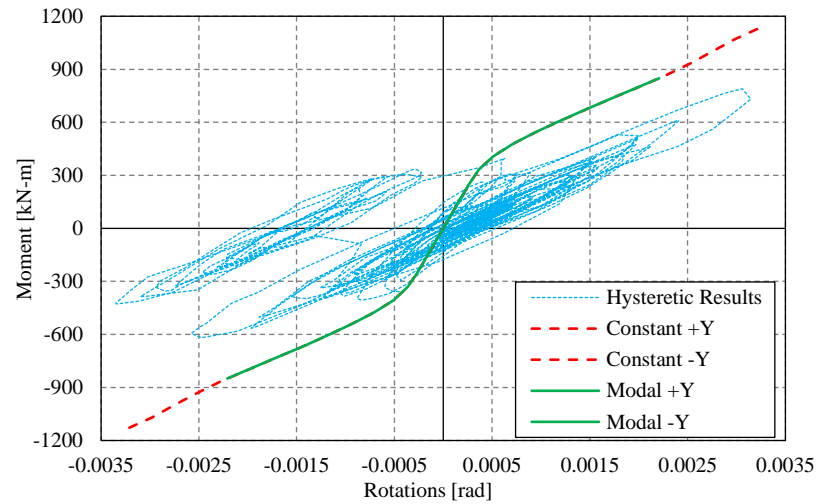
Figure 9-67: Comparison of the pushover analysis results versus the hysteretic results for Column G-8 in the Y direction.

10 Conclusions.

By developing two numerical models representing the structure under study and including the horizontal combination of the seismic components, the vulnerability of the structure was assessed. The evaluation of the structure was carried out by applying a linear analysis using the ULS load combinations to verify the structural elements, and a nonlinear direct-integration analysis to capture the post-elastic behavior of the structure followed by a nonlinear pushover analysis to verify the results obtained. For the sake of simplicity, the conclusions apply to both parts of the structure (Building A and B), as the observed dynamic response and the results of the analyses for both buildings were similar.

Additionally, it is worth mentioning the disadvantages observed when modeling the structure and how they affect its response. In fact, the model lacks a clear way to take into account the contribution from the column-beam connection to the structure's stiffness. However, by modeling the connection taking the two possible extremes (clamped-hinged), it is possible to bound the real response of the structure between these two limits. Another disadvantage is related to the modeling of the cladding panels since it was found that the selected modeling was not sophisticated enough to capture the failure at the connection.

10.1 Dynamic response.

When the dynamic behavior of the structure is observed, the modeling of the beam-column connection only affects the dynamic response in the X longitudinal direction and its torsional mode. It is noticeable that the large increments take place on the accelerations for the modes in the X direction and torsional one when the connection is considered clamped. These increments cannot be considered negligible, since the inclusion of a clamped connection almost doubles the acceleration in the X direction, while in the torsional mode it increases between 38 - 45%

The response spectra related to the Maule earthquake and the one to Chilean code agree in terms of spectral acceleration for periods larger or equal to 0.71 s. When looking at the two possible models of the connection, the X direction modes have a range of periods from 0.641 s to 0.974 s. And for the torsional modes, the periods range from 0.798s to 0.974. This leads to thinking that in an intermediate situation between clamped and hinged, the modal periods would lie beyond 0.71 s. Hence, the reason why the structure suffered some damage is not related to the fact of the Maule earthquake spectral accelerations exceeded those coming from the code spectrum. Instead, the problem relies on the normative exclusion of a combination of horizontal components when employing seismic actions. Furthermore, the structure in the Y direction behaves very flexibly with a period larger than 1.20 s. Hence, the internal forces developed by seismic actions in this direction were not significant.

10.2 Linear procedures.

From the point of view of linear analysis, the first thing that can be observed is the application of the horizontal combination of seismic excitation, which for the case study in [2] were excluded during its evaluation. The reason behind its exclusion is due to the difference that exists between the two lateral-force systems, where the code only requires the designer to combine such components in case of having clear torsional irregularities and/or two frame systems in non-parallel directions.

In terms of global response, the established displacement limit set equal to 15 cm, is not verified if the horizontal combination of the seismic actions is employed. The displacements go beyond 20% of the threshold requested. Therefore, none of the two buildings is classified as safe according to NCh2369-2003.

For the columns' interaction diagrams, the Chilean code load combinations satisfy the condition of the P-M demand, where the internal forces remain within the interaction diagram, thus verifying the design. However, when the Maule seismic forces are included, the central columns at the expansion joint exceed

more than 20% of their capacity, whereas those placed on axis 4 and 11 exceed 10%. Furthermore, when looking at the columns that report some damage, the columns placed in axes 4 and 11 between axes F and I (as shown in Figure 4-1) match with those that the linear analysis procedure predicts to fail under the Maule earthquake solicitation.

Due to the modeling of the beam-column connection, it is difficult to assess in which situation the beams should satisfy the checks prescribed by the code. For this reason, in the case of beams, their resistance at both ends is evaluated by looking at the two opposite situations (clamped and hinged). Regarding the positive bending strength, all beams comply with the strength check, independently of the connection modeling. This becomes more evident when observing the section which includes the prestressing cables, because probably the desired behavior of the beam was to be hinged. Moreover, when the negative bending strength is observed, it is even more evident the intended hinged behavior since these ULS actions, for any type of seismic input, exceed up to 7 times the computed strength.

Furthermore, the linear procedures were not able to capture the failure of the cladding panels with the employed model. However, this may be related to the difference in the dynamic response of the supporting substructure and the response of the building in the Y direction. It can be hypothesized that the substructure that barely comes out from the ground for a height equal to 3.30 m might have a significantly shorter period with respect to the structure in the Y direction (>1.20 s). Then, this difference in response could have caused a considerable differential displacement between the ends of the panels, thus causing their failure.

10.3   Nonlinear procedures.

After performing a comprehensive analysis of the behavior of the fiber hinges in SAP2000, the key parameter to evaluate the post-elastic response of the structure was the length of the plastic hinge. It was selected based on the criteria of observing the damage that took place at the columns' base and by estimating it using empirical equations proposed by the standards. Comparing the equations' estimation with the observed plastic length during the seismic event in terms of global and local behavior, it was concluded that selecting the length related to damage caused by the Maule earthquake was appropriate.

By observing the structure's dynamic response under the action of the Maule earthquake's accelerograms, the displacement results indicate that the maximum displacement imposed by the Chilean norm is not overcome. This result seems to be in contrast to what was previously said in 10.2. However, the Chilean standard imposes a S_o factor in Eq.(6-5) for soil type III when using linear procedures, which takes into account the interaction of this type of soil with structure. To have a fair comparison, the effects of soil-structure interaction with a detailed foundation soil profile should be included in the modeling to capture the real displacement and to state if the code prescription overestimates the displacements.

With respect to the results of the nonlinear dynamic analyses in terms of hysteretic response, it can be appreciated that the damage developed during the analysis in columns F, G, H, and I in axis 4 and 11 agree with those observed during the seismic event. Nevertheless, the columns' hysteretic response in the X direction for those placed between axis 4 and 11, showed some damage during analysis, unlike the real case.

These results lead to the conclusion that the beam-column connection is closer to a hinged type behavior than clamped for the columns between axis 4 and 11. The support length for the columns in axis 4 and 11 is larger than that from the axis in between, and this support length is directly related to the amount of damage and to the stiffness of the columns. Hence, this difference in support length at the connection could be related to the fact that certain columns suffered larger damage with respect to others.

From the perspective of the pushover analyses, the hysteretic response obtained previously remains bounded by the prescribed Target displacement demands. When looking in the X direction, the monotonic curves coming from the pushover analyses agree with the peaks shown for the hysteretic response of the assessed columns, but these reached a larger rotation than the loops of the hysteretic response. The reason behind this might be related to the demand imposed by the target displacement method, which might overestimates the state of damage that should be found at the columns' base as a consequence of the Maule earthquake excitation in the X direction.

This goes in agreement with the conservative nature of a static analysis procedure as the pushover analysis tries to capture the nonlinear dynamic response of the structure. Thus, these results confirm the nonlinear dynamic results found in the X direction, since the hysteretic response remains bounded by a more conservative procedure.

Moreover, in the Y direction the pushover analyses show just a post-cracking slope that is quite close to the slopes found for the hysteretic response. Additionally, the target-displacement's demand coming from the Maule earthquake spectrum in the Y direction does not impose a displacement on the structure that yields a state of damage at the columns' base.

Furthermore, it can be observed that the frequency components of the Maule earthquake are considerably high, though its epicenter was located at 341 km from the structure. Hence, this supports the showed hysteretic behavior results and the target displacement obtained in the Y direction, whose hysteretic behavior remained basically elastic during the whole analysis, and the showed reduction in stiffness was due to the damage suffered in the X direction. This is directly related to the fact that the structure in the Y direction is very flexible; thus, the earthquake was not able to excite the structure in such direction compared to the X direction.

11 References

[1] D. P. Delgado Romero and F. H. Mancini de Barbieri, "NON-LINEAR ANALYSIS OF AN INDUSTRIAL REINFORCED CONCRETE STRUCTURE DAMAGED DURING 2010 CHILE EARTHQUAKE," Politecnico di Milano, 2019.

[2] J. U. B. Moehle, R. U. C. Riddell, and R. U. C. Boroschek, "8.8 Chile Earthquake of February 27, 2010," *EERI Spec. Earthq. Rep.*, vol. 10, no. June, pp. 1–20, 2010.

[3] D. Ugalde and D. Lopez-Garcia, "Analysis of the seismic capacity of Chilean residential RC shear wall buildings," *J. Build. Eng.*, vol. 31, no. March, p. 101369, 2020, doi: 10.1016/j.jobe.2020.101369.

[4] R. Jünemann, J. C. de la Llera, M. A. Hube, L. A. Cifuentes, and E. Kausel, "A statistical analysis of reinforced concrete wall buildings damaged during the 2010, Chile earthquake," *Eng. Struct.*, vol. 82, pp. 168–185, 2015, doi: 10.1016/j.engstruct.2014.10.014.

[5] R. A. Salgado and S. Guner, "A comparative study on nonlinear models for performance-based earthquake engineering," *Eng. Struct.*, vol. 172, no. April 2017, pp. 382–391, 2018, doi: 10.1016/j.engstruct.2018.06.034.

[6] Instituto Nacional de Normalizacion, "NCh433-1996 - Diseño sísmico de edificios," p. 77, 1996.

[7] Universidad de Chile, "OBTENCION DE REGISTROS V2 , ESTANDAR CDMG," Blanca Encalada 2002, Santiago, Chile, 2010.

[8] Instituto Nacional de Normalizacion, "NCh2369-2003 Diseño sismico de estructuras e instalaciones industriales," 2003.

[9] Instituto Nacional de Normalizacion, "NCh430-2007 Hormigón armado - Requisitos de diseño y cálculo," 2007.

[10] Instituto Nacional de Normalizacion, "NCh204-2006 Acero - Barras laminadas en calietne para hormigon armado," 2006.

[11] ACI Committee 318, "318M-14: Building Code Requirements for Structural Concrete and Commentary," 38800 Country Club Drive Farmington Hills, MI 48331, 2014.

[12] M. Lee Marsh, I. G. Buckle, and E. Kavazanjian, *LRFD Seismic Analysis and Design of Bridges - Reference Manual*, no. FHWA-NHI-15-004. One Penn Plaza, New York, NY 10119: U.S. Department of Transportation Federal Highway Administration, 2014.

[13] I. Computers & Structures, *TECHNICAL NOTE MATERIAL STRESS-STRAIN CURVES*. 2008.

[14] J. B. Mander, M. J. N. Priestley, and R. Park, "Theoretical stress-strain model for confined concrete," *J. Struct. Eng*, vol. 114, no. 8, pp. 1804–1826, 1988, doi: 10.1061/(ASCE)0733-9445(1988)114.

[15] T. Tak, M. Sozen, and N. . N. Nielsen, "Reinforced concrete response to simulated earthquakes," *J. Struct. Div.*, vol. 12, pp. 2557–2573, 1970.

[16] I. Computers & Structures, *CSI Analysis Reference Manual*. 2017.

[17]   ASTM International, "Standard Specification for Deformed and Plain Carbon-Steel Bars for Concrete Reinforcement," *AASHTO*, vol. M31, p. 6, 2016.

[18]   M. J. N. Priestley, G. M. Calvi, and K. M.J., *Displacement-Based Seismic Design of Structures*, vol. 1, no. 2. Pavia, Italy: Fondazione EUCENTRE, 2007.

[19]   ASTM International, "Standard Specification for Steel Strand, Uncoated Seven-Wire for Prestressed Concrete," pp. 1–5, 2006.

[20]   Instituto Nacional de Normalizacion, "NCh1537-2009 Diseño estructural - Cargas permanentes y cargas de uso," Santiago de Chile, 2009.

[21]   S. K. Kunnath, A. M. Reinhorn, and Y. J. Park, "ANALYTICAL MODELING OF INELASTIC SEISMIC RESPONSE OF R/C STRUCTURES," *J. Struct. Eng*, vol. 116, no. 4, pp. 56–79, 1990.

[22]   I. Computers & Structures, "Concrete Frame Design Manual Concrete Frame Design Manual ACI 318-14." p. 77, 2017.

[23]   Instituto Nacional de Normalizacion, "NCh3171-2010 Diseño estructural - Disposiciones general y combinaciones de cargas." Matias Cousiño N°64, 6° Piso, Santiago, Chile, p. 14, 2010.

[24]   Y. Wang, Y. Peng, and J. Dong, "Fiber hinge approach for nonlinear analysis of structural members accounting for local buckling under large deformation," *IOP Conf. Ser. Mater. Sci. Eng.*, vol. 397, no. 1, 2018, doi: 10.1088/1757-899X/397/1/012040.

[25]   S. Bae and O. Bayrak, "Plastic hinge length of reinforced concrete columns," *ACI Struct. J.*, vol. 106, no. 2, pp. 233–237, 2009.

[26]   ASCE/SEI, *Seismic Evaluation and Retrofit of Existing Buildings*. 1801 Alexander Bell Drive Reston, Virginia, 20191-4382: The American Society of Civil Engineers, 2017.

[27]   L. Martinelli and M. G. Mulas. (2020). "EC8 and NTC2018 Pushover methods for non-linear seismic analysis." [PowerPoint slides].